CDF/EXOTIC/THESIS/PUBLIC/8932
V2
07/27/2007

SEARCH FOR HEAVY, LONG-LIVED PARTICLES THAT DECAY TO PHOTONS IN $p\bar{p}$ COLLISIONS AT $\sqrt{s} = 1.96$ TEV

A Dissertation

by

PETER WAGNER

Submitted to the Office of Graduate Studies of
Texas A&M University
in partial fulfillment of the requirements for the degree of

DOCTOR OF PHILOSOPHY

August 2007

Major Subject: Physics

SEARCH FOR HEAVY, LONG-LIVED PARTICLES THAT DECAY TO PHOTONS IN $p\bar{p}$ COLLISIONS AT $\sqrt{s} = 1.96$ TEV

A Dissertation

by

PETER WAGNER

Submitted to the Office of Graduate Studies of
Texas A&M University
in partial fulfillment of the requirements for the degree of

DOCTOR OF PHILOSOPHY

Approved by:

Chair of Committee,	David Toback
Committee Members,	Richard Arnowitt
	Teruki Kamon
	Sherry Yennello
Head of Department,	Edward Fry

August 2007

Major Subject: Physics

ABSTRACT

Search for Heavy, Long-Lived Particles That Decay to Photons

in $p\bar{p}$ Collisions at $\sqrt{s} = 1.96$ TeV. (August 2007)

Peter Wagner, B.S., Johannes Gutenberg Universität, Mainz

Chair of Advisory Committee: Dr. David Toback

This dissertation presents the results of the first search for heavy, neutral, long-lived particles that decay to photons at a hadron collider. We use a sample of γ+jet+missing transverse energy events in $p\bar{p}$ collisions at $\sqrt{s} = 1.96$ TeV taken with the Collider Detector at Fermilab. Candidate events are selected based on the arrival time of a high-energy photon at the electromagnetic calorimeter as measured with a timing system that was recently installed. The final result is that we find 2 events, using 570 ± 34 pb^{-1} of data collected during 2004-2005 at the Fermilab Tevatron, consistent with the background estimate of 1.3 ± 0.7 events. While our search strategy does not rely on model-specific dynamics, we interpret this result in terms of cross section limits in a supersymmetric model with $\widetilde{\chi}_1^0 \rightarrow \gamma \widetilde{G}$ and set a world-best $\widetilde{\chi}_1^0$ mass reach of 101 GeV/c^2 at $\tau_{\widetilde{\chi}} = 5$ ns. We can exclude any γ+jet+missing transverse energy signal that would produce more than 5.5 events.

"So, throw off the bowlines.

Sail away from the safe harbor.

Catch the trade winds in your sails."

- Mark Twain (1835-1910)

ACKNOWLEDGMENTS

The work that goes into a dissertation simply cannot be accomplished without the support of other people. This is particularly true for High Energy Physics where the analysis is done at an experiment which encompasses a collaboration of hundreds of researchers, each doing invaluable work. Unfortunately, within the frame of a few dissertation pages, I can only mention the people that I was directly working with.

My journey in the field began with my studies at Texas A&M University. The first year was sponsored by the Deutsche Akademische Austauschdienst which would surely not have been possible without the persistence and support from Jens Lassen and Petra Wacker in Mainz. Once I arrived in Texas I was lucky to experience such support and patience from both faculty and staff. This is certainly necessary to make an international student feel comfortable and productive in a place that seemed so unfamiliar in the beginning. Still in my mind is George Kattawar's "No matter what question you have you'll always find an open door," when I was standing in his office wet to the fingertips after biking through one of Texas' rain showers. Especially, I would like to thank Peter McIntyre and his family who not only hosted my colleague David Haubrich and me as alien guests during our first weeks, but who also helped us acquire our first furniture and our first apartment, and finally introduced a new way of life to us. Once I settled in, it soon was time for my qualifying exams which happened in quick succession and were quite out of schedule for all the professors involved. I would like to thank Ergin Sezgin, Dick Arnowitt and Chris Pope who made their time free to supervise them. Particular thanks go to Dick Arnowitt who introduced in his lectures the world of Quantum Fields to me and showed all the subtleties of the "Standard Model." I would like to thank my preliminary and defense exam

committee members Sherry Yennello and Teruki Kamon for the time they invested and the interest they showed in my research work.

Every student who begins an analysis with the CDF collaboration at Fermilab requires help for the endless hours of learning the tools and debugging code. Ray Culbertson was certainly the prime person to ask any open question that had to do with photons at CDF, Stntuple software, or data processing. I never left his office without a solution to my problem. During my writing of the EMTiming simulation Soon-Yung Jun gave great advice about the intricacies of the CDF calorimeter simulation. Invaluable also are the long hours that Bob Blair spent teaching me a non-standard CES shower simulation in which he had to dig up almost forgotten knowledge from the beginning years at CDF. I would also like to thank Stephen Mrenna and Howard Baer for their help on Monte Carlo event generators. On the technical side I would like to thank the ROOT team that developed the framework that helped produce every histogram in my research years. Even on New Year's Eve, my questions were always answered promptly and helpfully. I would like to thank Henry Frisch for hosting me at the University of Chicago and inviting me to meetings in which I got many invaluable insights in how to do experiments and analyses, and in the professional way of working at "U. of C."

This analysis would surely not have been possible if our hardware, the EMTiming system was not so thoroughly tested, smoothly installed and well maintained. I would like to thank Vadim Khotilovich, Vyacheslav Krutelyov, Sungwon Lee and Maxim Goncharov of the Texas A&M group at Fermilab who assisted - and still assist - so well in the maintenance of the system. Particular thanks to Dervin Allen, and his team of Lewis Morris and Jamie Grado, who supervised the installation and helped the whole project to move so quickly from design to the fully installed system. Special thanks also to the godparents Andrea Messina, Howard Budd and Franco Bedeschi

who helped the analysis paper so quickly through the collaboration.

Most grateful, however, I am to Dave Toback who was certainly the best supervisor I could wish for. He always had an open ear to whatever research question I had. Not rarely this ended up in long and informative conversations that lasted hours during which I hope to have tapped a bit of his vast knowledge. If I will ever make it to a research scientist it is very much him who brought me there. It was his leadership, courage, and organizational skills that made everything possible from the design and installation of the EMTiming hardware to fixing the last typos in our analysis paper. Damned if I can't write journal papers by now!

On the personal side I would like to thank Alexei Safonov and his Russian friends, as well as my friends in Chicago for making the evening hours such a great time. I would also like to thank the Italian crew for the fantastic dinners and more at the "Roma House." Many thanks to Lucas Naveira and Matt Cervantes who make me always feel welcome in College Station, and my friend David Haubrich with whom I shared all the highs and lows of the first years of our graduate life. Many thanks also to Carsten Rott for the great, but much too short, time we had together at CDF.

Finally, I would like to thank my parents, Elke and Rainer, as well as my grandparents, Hilde and Adolf, for the support they have always given me in whatever I did. Even over the long distance they are still with me in what I think and do. And last but surely not least, to Julia, who makes my years in Chicago so wonderful.

TABLE OF CONTENTS

CHAPTER Page

I INTRODUCTION 1

A. Introduction 1
B. Theory 3
1. Supersymmetry 3
2. Gauge Mediated Supersymmetry Breaking 5
a. Theory 5
b. Collider Phenomenology 9
C. Overview of the Search 17
D. Outline of the Dissertation 20

II THE FERMILAB TEVATRON, THE CDF DETECTOR AND THE EMTIMING SYSTEM 21

A. The Fermilab Tevatron 21
B. The CDF Detector 24
C. The EMTiming System 29

III PHOTON IDENTIFICATION AND TIMING 36

A. Standard Photon Identification Variables 36
B. PMT Spikes 39
C. Incident Angle Distribution of Photons from Heavy, Long-Lived Particles 43
D. Photon Identification Variable Distributions and Efficiencies 47
E. The Quality of the Transverse Shower Profile in the CES . 55
F. Measurement of the Collision Time and Position 61
1. Track Clustering Procedure 63
2. Vertexing Performance 65
3. Correlation between Collision Position and Time . . . 73
G. The Corrected Photon Time 75
1. EMTiming Calibration 81

CHAPTER Page

2. Event-Based Time Corrections for the Vertex Time and Position . . . 84
3. Intrinsic EMTiming System Resolution . . . 85
4. Monte Carlo Simulation . . . 87

IV TRIGGERS, DATASETS AND EVENT PRESELECTION . . . 92

A. Definition of Other Objects . . . 92
1. Missing E_T . . . 92
2. Jets . . . 94
B. Triggers and Data Sets . . . 96
C. Event Preselection . . . 98

V BACKGROUNDS . . . 102

A. Standard Model Backgrounds: Prompt Photons . . . 105
B. Non-Collision Backgrounds . . . 111
1. Beam Halo . . . 116
2. Cosmic Rays . . . 121
C. Background Estimation and Methods . . . 123

VI ACCEPTANCES TO GMSB EVENTS AND THEIR SYSTEMATIC UNCERTAINTIES . . . 127

A. Simulated Acceptance and Efficiencies for GMSB Models . 128
B. Estimation of the Systematic Uncertainties . . . 130
1. Time Measurement . . . 131
2. Photon ID Efficiency . . . 132
3. Jet Energy . . . 132
4. Initial and Final State Radiation . . . 133
5. Parton Distribution Functions . . . 133
6. Renormalization Scale . . . 134

VII OPTIMIZATION AND EXPECTED SEARCH SENSITIVITY . 135

VIII DATA, CROSS SECTION LIMITS AND FINAL RESULTS . . 146

CHAPTER Page

A. The Data 146
1. Event 191534, 3062764 151
2. Event 198583, 15031322 158
B. Parametrization of the Acceptance × Efficiency 165
C. Model-Independent Cross Section Limits and GMSB Exclusion Regions 171

IX CONCLUSION 176

A. Summary of the Search 176
B. Future Prospects 177

REFERENCES 180

APPENDIX A: EMTIMING ONLINE MONITORING RESULTS 190

APPENDIX B: IDENTIFICATION VARIABLES FOR ELECTRONS 193

APPENDIX C: TRACK REQUIREMENTS AND CORRECTIONS FOR SIMULATED TRACKS 196

A. Track Requirements 196
B. Additional Corrections for Simulated Tracks 197
C. Systematic Bias in the Track t_0 Measurement 198

APPENDIX D: TIMING AND CORRECTIONS FOR PLUG PHOTONS . . 202

APPENDIX E: NON-COLLISION BACKGROUNDS FOR PLUG PHOTONS 214

APPENDIX F: PHOTON POINTING AT CDF 218

VITA 224

LIST OF FIGURES

FIGURE Page

1 Feynman diagrams of the dominant tree production processes at the Fermilab Tevatron for the GMSB model line from SPS 8. 10

2 In (a) the NLO σ_{prod} of $\widetilde{\chi}_1^+\widetilde{\chi}_1^-$ pair and $\widetilde{\chi}_1^\pm\widetilde{\chi}_1^0$ production at the Tevatron and the the LHC, and in (b) the ratio of NLO to LO cross sections ("K-factors"), both as a function of the average $\widetilde{\chi}_1^\pm/\widetilde{\chi}_2^0$ mass. 11

3 The E_T of the highest-E_T photon and the $\not\!\!E_T$ in simulated GMSB events where at least one $\widetilde{\chi}_1^0$ decays inside the detector, for an example point of $m_{\widetilde{\chi}} = 90$ GeV/c^2 and $\tau_{\widetilde{\chi}} = 10$ ns. 13

4 The schematics of a long-lived $\widetilde{\chi}_1^0$ decaying into a $\widetilde{G}$ and a photon inside the CDF detector. 15

5 In (a) the fraction of events ("efficiency" in the figure) in which a $\widetilde{\chi}_1^0$ decays in the detector ($t_{\text{corr}} \geq 0$) as a function of the $\widetilde{\chi}_1^0$ event lifetime (τ_{evt}). 16

6 The 95% C.L. exclusion region for GMSB searches with the ALEPH detector at LEP [19] as a function of $\widetilde{\chi}_1^0$ mass and lifetime for the SPS 8 choice of parameters [29]. 19

7 In (a) an aerial view [49] of the Fermilab accelerator complex with the Main Injector in the foreground and the Tevatron in the back. . . 23

8 In (a) a photograph [53] and in (b) an elevation view [51] of the CDF II detector. 25

9 In (a) a schematic drawing of a wedge in the central calorimeter, including the EM and CES subsystems [53]. 27

FIGURE Page

10 In (a) the schematics of the EMTiming system including the pulse descriptions. In (b) a schematic diagram of the energy and time measurement of a particle that showers into a tower of the calorimeter using a PMT. 32

11 A schematic diagram of the CEM splitter. 33

12 A schematic diagram of the signal processing on TB and ASD. . . . 34

13 The EMTiming system response as a function of the energy deposited in a tower, separately for CEM and PEM, for a data sample of jets. 35

14 The magnitude of the PMT asymmetry for a the full photon+$\not\!\!E_T$ sample that contains both PMT spikes and real photons in (a), and the asymmetry for electrons from pure $W \to e\nu$ events in (b). . . 41

15 In (a) the difference between the $\not\!\!E_T$ and the E_T of the photon, in (b) its time distribution and in (c) the difference in ϕ between the photon and the $\not\!\!E_T$ in events with $|\mathrm{PA}| > 0.6$. 42

16 The definitions of the α and β incident angles using schematic diagrams of a long-lived $\widetilde{\chi}_1^0$ decaying to a photon and a $\widetilde{G}$ in the CDF detector in the (r,z)- and the (r,ϕ)-planes. 44

17 The distribution of the incident angles α and β and the total incident angle $\alpha \oplus \beta$ at the front face of the central calorimeter for simulated photons from $\widetilde{\chi}_1^0$'s in a GMSB model ($m_{\widetilde{\chi}} = 110$ GeV/c^2). 46

18 The ID variable distributions for photons in a GMSB model with $m_{\widetilde{\chi}} = 110$ GeV/c^2 produced with the CDF MC, normalized to 1. 51

19 A continuation of Fig. 18 for the remaining photon ID variables in Table IV. 52

20 The total efficiencies for the standard photon ID requirements (except for the CES-χ^2) for photons in the fiducial portion of the CEM vs. incident angles α and β. 53

FIGURE Page

21 The relative efficiencies for each ID variable separately, using the order of the cuts in Table IV. 54

22 A continuation of Fig. 21 for the remaining photon ID variables in Table IV. 55

23 A continuation of Figs. 21 and 22 for the remaining photon ID variables in Table IV. 56

24 A comparison of the CES-χ^2 distributions for a photon of energy 50 GeV that propagates from a fixed vertex into a fixed tower in the CEM (wedge 0, tower 1) at 0° incident angle, simulated with G3WS, and the distribution from the CDF MC separately for strips (a), wires (b) and combined (c). 58

25 The CES-χ^2 distributions for photons simulated with G3WS with the same settings as in Fig. 24, but at different incident angles. . . . 60

26 A comparison of the CES-χ^2 efficiency as a function of incident angles α and β. 61

27 A comparison of the CES-χ^2 efficiency as a function of incident angle between several χ^2 cuts of 20, 30, 40 and 50, simulated with G3WS. 62

28 The t_0 and z_0 of the reconstructed highest Σp_{T} vertex in $W \to e\nu$ events without allowing the electron track to participate in the vertexing. 68

29 The difference in t and z between two arbitrarily selected sets of tracks from the same reconstructed vertex in a $W \to e\nu$ dataset with the electron track removed from the vertexing. 69

30 The difference in t (a) and in z (b) between electron track and the highest Σp_{T} reconstructed vertex without the electron track participating in the vertexing. 70

31 In (a) and (b) the resolution distributions reported by the clusters. . 72

FIGURE Page

32 The difference between well measured electron tracks and clusters that are potentially a combination of two separate collisions (vertex RMS > 0.6 cm, see Fig. 31). 73

33 The clustering efficiency as a function of the number of tracks using (a) the subset method and (b) the window method, and (c) as a function of the Σp_{T} of the tracks using the window method. . . 74

34 The mean vertex time as a function of the z position of a collision at CDF, as measured with the space-time vertexing algorithm. 76

35 A comparison between MC (solid) and data (points) for the timing information for electrons from a $W \rightarrow e\nu$ sample after cumulatively applying the various corrections (left side) and a comparison of the corrections themselves (right side). 80

36 A MC simulation of the vertex time and position effects that contribute to the RMS of the raw data and their impact on the final timing resolution using a $W \rightarrow e\nu$ MC sample. 81

37 The functional form (a) of the slewing correction as a function of the energy sum of the PMTs (in ADC counts [74]) and (b) of the C_{energy}-corrected time as a function of the PMT energy asymmetry of an example tower in the CEM from an example run. 85

38 The difference in the arrival times of electrons, that pass the requirements in Table XXIII, from $Z \rightarrow ee$ decays, corrected for the TOF but not the vertex t_0. 88

39 The RMS of the fully corrected arrival time versus the electron EM energy from a electron data sample produced with the requirements shown in App. B without the E_T cut. 88

40 The functional form of the TDC efficiency as a function of energy sum of the PMTs of an example tower in ADC counts [74] with the data of an example run. 92

41 The simulated time of arrival of photons from $\widetilde{\chi}_1^0$'s in a GMSB model with $\tau_{\widetilde{\chi}} = 10$ ns and $m_{\widetilde{\chi}} = 110$ GeV/c^2 after all corrections. 93

FIGURE Page

42 The $t^{\gamma}_{\rm corr}$ distribution of photon candidates for the `W_NOTRACK` sample. 106

43 The electron $t_{\rm corr}$ in a sample of $W \to e\nu$ events. 109

44 The fractional difference between the number of events on the negative and the positive side of the $t_{\rm corr}$ distribution of electrons in the $W \to e\nu$ sample. 111

45 The mean time of arrival of electrons from various subsamples of $W \to e\nu +$ jets events where each entry reflects a different combination of the electron E_T, jet E_T and $\not\!\!E_T$ event requirements. . 112

46 The $t_{\rm corr}$ distribution mean and RMS of electrons from $W \to e\nu$ events, where the wrong vertex is picked, as a function of the tower-η where -9 (+9) corresponds to $\eta = -1$ ($\eta = +1$). 112

47 A view in the r-ϕ plane along the beam direction and the calorimeter towers in the η-ϕ plane for a cosmic ray background candidate. . 114

48 In (a) an illustration of a beam halo event. 116

49 The separation of cosmic and beam halo backgrounds in the $\gamma+\not\!\!E_T$ sample without tracks. 117

50 In (a) the time distribution of photons from beam halo candidate events separated into different photon towers in η. 120

51 Kinematic distributions of the beam halo subsample indicating that it is from non-collision sources. 121

52 The time of arrival for beam halo events with a vertex ($\Sigma p_{\rm T} >$ 1 GeV/c), before (shaded) and after (histogram with error bars) subtracting the vertex t_0. 122

53 Plots showing that the cosmics subsample is from non-collision sources. 124

54 The expected 95% C.L. cross section limit as a function of the photon E_T, the $\not\!\!E_T$, jet E_T and $\Delta\phi(\not\!\!E_T, \text{jet})$ requirement for a GMSB example point ($m_{\tilde{\chi}}$ = 100 GeV and $\tau_{\tilde{\chi}}$ = 5 ns) while all other requirements are fixed at their optimized values. 139

FIGURE Page

55 The expected 95% C.L. cross section limit as a function of the $t^{\gamma}_{\rm corr}$ and the vertex $\Sigma p_{\rm T}$ requirement, which is shown for completeness, for a GMSB example point ($m_{\widetilde{\chi}}$ = 100 GeV and $\tau_{\widetilde{\chi}}$ = 5 ns). 140

56 The predicted kinematic distributions in the signal region after the preselection and optimized requirements. 146

57 The predicted time distribution in the full time window (a) and around the signal region (b), after passing the preselection and optimized kinematic cuts. 147

58 The $t^{\gamma}_{\rm corr}$ distribution including control and signal regions, after all but the timing cut for all backgrounds, the expected signal and the observed data. 151

59 The same as Fig. 56, but including the data in the signal region. . . . 152

60 A view in the r-ϕ plane along the beam direction and the calorimeter towers in the η-ϕ plane for event 191534, 3062764. 154

61 In (a) the track p_T of all tracks with hits in the silicon and/or COT as a function of their η and ϕ. 157

62 A view in the r-ϕ plane along the beam direction and the calorimeter towers in the η-ϕ plane for event 198583, 15031322. 161

63 The CES energy distribution in the seed tower of the photon. 164

64 The same distributions as in Fig. 61, but for event 198583, 15031322; see that figure for detailed descriptions. 165

65 The distribution of the transverse mass of the electron and the $\not\!\!E_T$ in $W \to e\nu$ events simulated with the CDF MC sample used in Section III.G.2. 166

66 The p_T/m distribution of the $\widetilde{\chi}^0_1$ for $m_{\widetilde{\chi}}$ = 40 GeV/c^2, 80 GeV/c^2 and 140 GeV/c^2. 169

67 The relative difference of the $A \cdot \epsilon$ between the fit functions (predicted) and the MC simulation. 171

FIGURE Page

68 A comparison of the $A \cdot \epsilon$ between the fit functions and the MC simulation as a function of $\widetilde{\chi}_1^0$ lifetime for $\widetilde{\chi}_1^0$ masses 67 GeV/c^2 (a), 80 GeV/c^2 (b), 94 GeV/c^2 (c) and 113 GeV/c^2 (d). 172

69 The expected and observed cross section limits as a function of the $\widetilde{\chi}_1^0$ lifetime at a mass of 100 GeV/c^2 (a) and as a function of the $\widetilde{\chi}_1^0$ mass at a lifetime of 5 ns (b). 174

70 The contours of constant cross section limit, using the $A \cdot \epsilon$ interpolation, for the observed number of events. 175

71 The expected and observed exclusion region using the interpolation function, along with the most stringent published LEP limits from ALEPH [19]. 176

72 The dashed lines show the prediction of the exclusion limit after a scaling of the background prediction and the uncertainties for a luminosity of 2 fb^{-1} and 10 fb^{-1} respectively. 180

73 The fraction of all events with a time recorded in a tower with more than 6.25 GeV (3 GeV) energy deposited, as shown by the monitoring system. 193

74 The rate at which an energy deposit of less than 0.2 GeV causes a time to be recorded in the TDC for each tower in the CEM and PEM ("fake firings"), as shown by the monitoring system for the same run as shown in Fig. 73. 194

75 The mean t_0 of the negatively charged simulated tracks (*TStnTrack::T0Cot()*) as a function of (a) their $1/p_T$ before any corrections, (b) their η after applying the p_T dependent corrections. . . . 201

76 The same as in Fig. 75 but for positively charged simulated tracks. . 202

77 The difference between the reconstructed, simulated track t_0 and the true vertex t_0 as a function of the true vertex t_0 after the corrections that are described in App. C for all simulated tracks that pass the basic requirements in Table VI. 203

FIGURE Page

78 A comparison between MC (solid) and data (points) for the timing information for plug electrons from $W \to e\nu$ samples after cumulatively applying the various corrections (left side) and the corrections themselves (right side). 206

79 A MC simulation of the vertex time and position effects for plug electrons from a $W \to e\nu$ MC sample that contribute to the RMS of the "raw" time and their impact on the final timing resolution. . . 207

80 The functional form (a) of the slewing correction as a function of the energy sum of the PMTs of adjacent towers (in ADC counts [74]) and (b) of the C_{energy}-corrected time as a function of the PMT energy asymmetry of an example tower in the PEM from an example run. 208

81 The fully corrected time before applying the "ring-corrections" as a function of tower energy, tower number (integrated over ϕ) and vertex position from a part of the calibration data on the left and plug electrons from $W \to e\nu$ events on the right side. 210

82 The t_{corr} after applying the "ring-corrections" as a function of tower energy, tower number (integrated over ϕ) and vertex position from part of the calibration sample on the left and plug electrons from $W \to e\nu$ events on the right side. 211

83 The difference in the arrival times of the decay electrons, that both pass the requirements in Table XXIII, from a data sample of $Z \to ee$ events, corrected for the TOF but not the vertex t_0. 213

84 The RMS of the fully corrected arrival time versus the electron EM energy from a plug electron data sample produced with the requirements shown in App. B without the E_T requirement. 214

85 The functional form of the TDC efficiency as a function of energy sum of the PMTs of an example tower in the PEM in ADC counts [74] with the data of an example run. 215

86 The time distribution of photon candidates in the MET_PEM sample that pass the photon ID requirements in Table XXVII in events that have no vertex. 218

FIGURE Page

87 The time distribution of photon candidates in the MET_PEM sample that pass the requirements in Table XXVII for both sides of the detector. 219

88 An illustration of the impact parameter b in a plane perpendicular to the beam (z) axis for a photon that is created at a displaced vertex indicated with a star. 222

89 The relationship between $t_{\rm corr}$ and the impact parameter (b) of a photon from $\widetilde{\chi}_1^0 \rightarrow \gamma\widetilde{G}$ decays in a GMSB model with $m_{\widetilde{\chi}}$ = 110 GeV/c^2 and $\tau_{\widetilde{\chi}}$ = 10 ns. 223

90 A comparison of the expected exclusion regions as a function of $\widetilde{\chi}_1^0$ mass and lifetime for the GMSB model at 2 fb^{-1} luminosity for a $\gamma + \not{E}_T + \geq 1$ jet analysis with photon pointing and timing. . . . 224

LIST OF TABLES

TABLE Page

I The $\widetilde{\chi}_1^0$ masses and lifetimes relevant for this search and their translation to the GMSB parameters in accordance with the GMSB SPS model 8 convention [29]. 10

II Overview of the EMTiming system hardware and performance. . . . 31

III The standard photon selection requirements used at CDF to identify high-E_T photon candidates. 37

IV The cumulative number of simulated events after each ID requirement for the highest E_T photon in the event that comes from a $\widetilde{\chi}_1^0$. 48

V The sample requirements to select electrons from $W \to e\nu$ events to validate the ID efficiency of simulated photons as a function of α and β. 49

VI The set of requirements for tracks to be included in the vertex reconstruction. 64

VII The RMS of the corrected time distribution after cumulatively correcting for the effects shown in the first column for electrons in the data and MC using a sample of $W \to e\nu$ events (see Fig. 35) [73]. 79

VIII The contributions of physics and hardware effects, and the uncertainty of their corrections, to the RMS of the EMTiming system taken from a $W \to e\nu$ MC sample (see Fig. 36 and the MC histograms in Fig. 35). 82

IX Triggers that contribute to the `W_NOTRACK` dataset and all their requirements. 99

X The photon, jet, vertex and global event requirements used to obtain the preselection sample of $\gamma + \not\!\!E_T + \geq 1$ jet events. 102

TABLE Page

XI Event reduction for the preselection $\gamma + \not{E}_T + \geq 1$ jet dataset. 103

XII Summary of the event reduction for a GMSB example point at $m_{\widetilde{\chi}} = 100$ GeV and $\tau_{\widetilde{\chi}} = 5$ ns as it passes the preselection cuts of Table X. 131

XIII Summary of the systematic uncertainties on the acceptance and production cross section for an example GMSB point at $m_{\widetilde{\chi}} = 94$ GeV and $\tau_{\widetilde{\chi}} = 10$ ns. 133

XIV The optimized requirement values for a selected number of GMSB parameter points. 142

XV The observed number of events in each control region after all optimized requirements, except the timing cut. 143

XVI The acceptance and expected cross section limits for selected GMSB points with the final selection requirements. 144

XVII Summary of the expected and observed number of events from the background estimate after the event preselection and each requirement from the optimization, separated for each background, and the expected number of signal events. 149

XVIII The data selection criteria and the total, cumulative event efficiency for an example GMSB model point at $m_{\widetilde{\chi}} = 100$ GeV/c^2 and $\tau_{\widetilde{\chi}} = 5$ ns, shown for completeness as it is presented in Ref. [43]. 150

XIX The event selection requirements and the observed values of event 191534, 3062764. 155

XX The event selection requirements compared to the observed values of event 198583, 15031322. 162

XXI The 95% C.L. cross section limit as a function of the hypothetically observed number of events and the Poisson probability for this number of events based on the no-signal hypothesis. 174

TABLE Page

XXII The expected improvement for various luminosities for a GMSB example point at $m_{\widetilde{\chi}} = 100$ GeV/c^2 and $\tau_{\widetilde{\chi}} = 5$ ns assuming all backgrounds and their uncertainty fractions scale linearly with luminosity. 181

XXIII Central and plug electron ID requirements. Note that "q" is the charge of the electron. 197

XXIV The RMS of the corrected time distribution after cumulatively correcting for the effects shown in the first column for PEM electrons taken from data and MC using $W \rightarrow e\nu$ samples (see Fig. 78) [73]. 205

XXV The contributions of physics and hardware effects for the plug, and the uncertainty of their corrections, to the RMS of the EMTiming system taken from a $W \rightarrow e\nu$ MC sample (see Figs. 79 and the MC histograms in 78). 208

XXVI Triggers that contribute to the MET_PEM dataset and their requirements. 217

XXVII The selection requirement for plug photons. 217

XXVIII Photon pointing parameters for the CDF detector [96]. 221

CHAPTER I

INTRODUCTION

A. Introduction

Among the zoo of elementary particles, long-lived species with lifetimes on the order of nanoseconds are quite rare [1]. The most recently discovered, the neutral, strange K_L-meson, lead not only to the discovery of a new quantum number but also to the discovery of its violation ("CP-violation") by Cronin and Fitch in 1964 [2]. This opened a new field in elementary particle physics that is still delivering exciting results in B-physics [3]. Today, there are good theoretical and experimental reasons to believe that new fundamental theories exist in nature that predict the existence of a yet undiscovered heavy, neutral, long-lived particle.

Today the standard model (SM) of particle physics [1] is widely accepted as a correct description of the fundamental particles and their interactions via the strong, electromagnetic and weak forces. However, as it has been explored in recent years it has become apparent that for theoretical reasons [4, 5] this model must be incomplete. For instance, the calculation of the Higgs mass requires an ultraviolet cut-off to be regularized [5]. An interpretation of this cut-off is new dynamics at that energy scale. The magnitude of the corrections to the Higgs mass at higher loop orders depends not only sensitively on the highest mass particle that couples to the Higgs, but also on the choice of this cut-off value (unlike the corrections to other boson and fermion masses). If, for example, the only new dynamics are believed to enter at the Planck energy

---

This dissertation follows the style of Physical Review D.

scale, then the corrections are 30-times higher than the Higgs mass. This problem, known as the "naturalness problem," can be elegantly solved with new particles and interaction terms that allow for all the mass correction terms to identically cancel ("Supersymmetry," SUSY) [5].

A number of experimental observations, both at the small distance scales of elementary particles as well as the large scales of cosmology, also suggest revisions of the SM are necessary. However, there is no model that can naturally account for all of them. The observation of neutrino oscillations [6] suggests that neutrinos are not massless as the SM implies. While this can be incorporated into the SM with a small extension called the "see-saw mechanism" [7], the interpretation of a potential 3.4σ deviation [8] of the negative muon anomalous magnetic moment [9] from the SM is not clear [8]. On cosmological scales, the structure of the cosmic microwave background suggests that 22% of the universe is dark matter [10], and favors the existence of a non-baryonic particle as a dark matter candidate [11]. While such a particle is not predicted by the SM, SUSY models provide a favored candidate [11]. For major SUSY models that also incorporate gravitational interactions ("Supergravity"), the measurement of the muon anomalous magnetic moment has provided the impetus to focus on the "coannihilation region" [12] which will be testable at the Large Hadron Collider (LHC) [12].

Supergravity models, however, do not provide an explanation for another potential hint that occurred during the 1992-1995 data taking period of the Fermilab Tevatron proton-antiproton ($p\bar{p}$) collider at a center-of-mass energy of $\sqrt{s} = 1.96$ TeV. A series of unusual events were observed [13, 14], of which the '$ee\gamma\gamma\not{E}_T$' [15] candidate event was extensively studied [13], that was calculated to have a very small probability to come from SM processes.

In its wake, SUSY models that predict photons in final states gained favor [16], in

particular gauge mediated supersymmetry breaking (GMSB) [17, 18] as described in the next section. To summarize, a major feature of this model is that it predicts heavy, neutral SUSY particles (neutralinos, $\widetilde{\chi}_1^0$) that decay to photons and undetectable gravitinos ($\widetilde{G}$) that cause an energy imbalance. While there have been searches at previous collider experiments [19] for these particles, no corroborating evidence has been uncovered. However, while $\widetilde{\chi}_1^0$'s can naturally occur with lifetimes on the order of nanoseconds and more, most of these searches have assumed negligible lifetimes. This dissertation presents the first direct search for heavy, neutral, long-lived particles, like the $\widetilde{\chi}_1^0$, that decay to photons at a hadron collider. It is also the first search that uses the arrival time information of the photon. The sensitivity of this analysis extends the previous world's best limits.

B. Theory

The search for heavy, neutral, long-lived particles that decay to photons is motivated by the desire to understand the fundamental theory of nature that reduces to the SM. A major model is GMSB, a variation of SUSY models, although there are recent models that also predict these types of particles [20]. This section introduces the concepts and main features of the minimal supersymmetric model (MSSM), and the next section outlines the phenomenology of GMSB and compares it to other SUSY models.

1. Supersymmetry

There are both theoretical and experimental reasons to believe that SUSY is the theory that reduces to the successful SM at low energies. SUSY is well described in the literature, e.g. in Refs. [4] and [5]. It solves the naturalness problem described

above by requiring each fermionic SM particle to have bosonic counterparts (chiral supermultiplet) with the same number of chiral degrees of freedom, and vice versa (gauge supermultiplet) [21]. The bosonic counterparts to the SM fermions get an "s" prefix ("lepton" → "slepton," "quark"→ "squark") and the fermionic counterparts to the SM gauge bosons get an "ino" suffix ("gauge boson" → "gauginos"). The MSSM is minimal in the sense that it contains only one such supermultiplet. However, it has 105 unknown, independent mass, angle and phase parameters.

Each particle is assigned a quantum number,

$$R = (-1)^{3(B-L)+2s}$$

known as "R-parity," where B (L) is its baryon (lepton) number and s is its spin. This quantity is defined to be conserved in most models (even parity for all SM particles and the Higgs boson, odd parity for their superpartners), which in particular causes the decay of a superpartner to a SM particle to be forbidden unless another SUSY particle is emitted. In this case, therefore, the lightest SUSY particle (LSP) must be stable. In most models it is a neutral, non-baryonic particle, that becomes a dark matter candidate in cosmological models (as there are significant constraints on charged candidates [11, 22]).

The many MSSM model parameters are constrained by experimental bounds on flavor changing neutral currents and CP-violating effects, in particular by the non-observation of the $\mu \to e\gamma$ process [5, 23]. With these constraints the gauge coupling constants of the SM can be extrapolated to have the same values at a scale of $\sim 10^{16}$ GeV [5].

As none of the superpartners have been observed, SUSY must be broken [5]. If it is broken at tree level some of the superpartner masses would be lighter than their SM counterparts. However, if SUSY is broken at very high energies, in a "hidden

sector" that introduces SUSY-breaking interactions to the "visible" MSSM gauginos and scalars, then all SUSY counterparts are either heavier than their SM counterparts or are too weakly interacting for a direct detection, for example in cosmic rays [24]. There are many ways SUSY-breaking interactions can occur. Each distinguishes the SUSY models into mainly gravity mediated SUSY breaking ("Supergravity") [25] models where they are non-renormalizable interactions of gravitational strength, and gauge mediated SUSY breaking (GMSB) models. While there have been numerous searches for each of these [1], there are compelling reasons to consider GMSB models, as will be explained in the next section.

2. Gauge Mediated Supersymmetry Breaking

a. Theory

Gauge mediated SUSY breaking (GMSB) [5, 17, 18] is a model of SUSY in which the breaking mechanism originates in a "hidden sector" and is not further specified. It is then "mediated" to the visible MSSM sector by scalar and fermion "messenger fields" that transform under the SM gauge interactions. The breaking mechanism causes fields that couple to the messenger fields to acquire a vacuum expectation value. The messenger fields thus become massive and give masses to the MSSM SUSY fields dynamically via loop corrections. The hidden sector contains particles at a mass scale of $\sqrt{F} \sim 10$ TeV/c^2, while the messenger sector mass scale is $M_{\rm mess} \sim$100 TeV/c^2. To avoid color and charge breaking $M_{\rm mess}$ is required to be $>\sqrt{F}$ and to realize SUSY breaking at low energy it must be $\lesssim 10^{16}$ GeV/c^2. The free parameters of the minimal GMSB model are: the messenger mass scale $M_{\rm mess}$, the number of messenger fields $N_{\rm mess}$, a parameter $\Lambda \sim F/M_{\rm mess}$ that determines the MSSM gaugino and scalar masses, the ratio of the neutral Higgs vacuum expectation values, $\tan(\beta)$, and the

sign of the higgsino mass parameter sign(μ).

The GMSB model is compelling for various reasons [26]:

- As the messenger interactions are flavor-independent it intrinsically suppresses flavor-changing, neutral currents and CP-violating processes to SM levels.
- It naturally predicts high energy photon events at the Tevatron like the $ee\gamma\gamma\not{E}_T$ event.
- SUSY breaking can occur at any energy between the SM and the Planck mass scale. If it occurs at low energy then it is likely that the messenger group has the SM gauge symmetries [27].
- The model is highly predictive with only five free parameters in its minimal version, that allow for experimental results to have a powerful impact on the falsification or validation of the model.

Phenomenologically, the MSSM scalars and gauginos gain masses according to their gauge coupling strength, by construction, which typically causes the squarks and gluinos to be heavier than the gauginos and sleptons. The gaugino masses also scale like $(\Lambda \cdot N_{\text{mess}})$ whereas the scalar SUSY masses scale like $\sqrt{\Lambda \cdot N_{\text{mess}}}$. The weakly interacting $\widetilde{G}$ is the LSP with a mass range of $\sim$eV/c^2 to $\sim$GeV/c^2. The next-to LSP (NLSP) is the lightest neutralino ($\widetilde{\chi}_1^0$) for models with $N_{\text{mess}} = 1$ and low $\tan(\beta)$ ($\lesssim 30$), and it is a right handed slepton (mostly $\tilde{\tau}_1$) for models with $N_{\text{mess}} \geq 1$ or $\tan(\beta) \gtrsim 30$ [28].

In this analysis we consider a GMSB model with an $\widetilde{\chi}_1^0$ NLSP that decays via $\widetilde{\chi}_1^0 \rightarrow \gamma\widetilde{G}$ with a branching ratio of $\sim$100%. As there are many GMSB parameter combinations that match this phenomenology, representative "model lines" have been identified that cover specific characteristics of SUSY models (e.g., GMSB models with

an $\widetilde{\chi}_1^0$ NLSP) with only one free parameter that sets the particle masses. We choose this analysis to follow the Snowmass Points and Slopes (SPS) model line 8 [29]:

$$\begin{aligned} M_{\mathrm{M}} &= 2\Lambda \\ \tan(\beta) &= 15 \\ \mathrm{sgn}(\mu) &= 1 \\ N_{\mathrm{M}} &= 1 \end{aligned}$$

where Λ and an additional parameter ($c_{\widetilde{G}}$) that controls the $\widetilde{G}$ mass and the $\widetilde{\chi}_1^0$ lifetime are both allowed to vary. As lower values of Λ are excluded at 95% confidence level (C.L.) in previous collider experiments [19], we consider Λ in a range where squarks and gluinos have masses of ∼600-800 GeV, and the sleptons and gauginos have masses of ∼100-300 GeV [18].

As the coupling of the $\widetilde{\chi}_1^0$ to the $\widetilde{G}$ is predicted to be very weak because of the nature of the gravitational interactions, the lifetime of the NLSP can be on the order of many nanoseconds or more. Both the $\widetilde{\chi}_1^0$ lifetime ($\tau_{\widetilde{\chi}}$) and the $\widetilde{G}$ mass can be approximated by [18]

$$\tau_{\widetilde{\chi}} \sim 0.434 \left(\frac{100\ \mathrm{GeV}/c^2}{m_{\widetilde{\chi}}}\right)^5 \left(\frac{\sqrt{F}}{100\ \mathrm{TeV}/c^2}\right)^4 \mathrm{ns} \tag{1.1}$$

$$m_{\widetilde{G}} \sim 2.5 \left(\frac{\sqrt{F}}{100\ \mathrm{TeV}/c^2}\right) \mathrm{eV}/c^2, \tag{1.2}$$

which determines the $\widetilde{\chi}_1^0$ lifetime uniquely from the $\widetilde{\chi}_1^0$ mass (in GeV/c^2) for a given F (in (TeV/c^2)^2). However, as the hidden sector is largely unknown, there may be more than one SUSY breaking scale (F_s). While this is not part of the minimal GMSB model it is easily taken into account by varying $c_{\widetilde{G}} = F_S/F$ independently. This allows for an independent variation of the $\widetilde{\chi}_1^0$ lifetime ($\tau_{\widetilde{\chi}} \sim c_{\widetilde{G}}^2$).

GMSB models are subject to cosmological constraints [30] as all SUSY particles produced in the early universe decay to the $\widetilde{G}$ LSP, while its annihilation rate is small due to its weak coupling which causes an overproduction of $\widetilde{G}$'s compared to cosmological observations: If the $\widetilde{G}$'s are too light ($\lesssim$1 keV/c^2) then they can destroy the nuclei produced during the Big Bang Nucleosynthesis and can lead to a cosmic microwave background that is different from observations [30]. If they are heavy ($\gtrsim$1 keV/c^2) then, while they are a warm dark matter candidate [31], their density can cause the universe to overclose if there is no dilution mechanism. There are various solutions to these problems:

- If the $\widetilde{\chi}_1^0$ lifetime is $\sim 10^4$ s then inflation causes the $\widetilde{\chi}_1^0$ density to freeze out and $\widetilde{G}$ are not thermally produced in the early universe. Then the $\widetilde{G}$ mass is expected to be $\sim$100 GeV/c^2 and it is a cold dark matter candidate [30], similar to SUGRA models [5].

- $\widetilde{G}$ with a mass of $\lesssim$GeV/c^2 (corresponding to a short-lived $\widetilde{\chi}_1^0$) are thermally produced in the early universe and inflation dilutes their density. While then the $\widetilde{G}$ can not be a dark matter candidate, axinos [32] can be a dark matter candidate that can also couple weakly to the $\widetilde{\chi}_1^0$ and the γ [33].

- Studies [34] that take both inflation and messenger particle decays into account that dilute the $\widetilde{G}$'s, expect $\widetilde{G}$'s with a mass of $\sim$1-1.5 keV/c^2 to be thermally produced in the early universe after inflation. Then the $\widetilde{G}$ can be a warm dark matter candidate which is favored in models of galaxy structure formation [31].

In the model line used in this search the $\widetilde{G}$ mass is $\sim$0.5-1.0 keV/c^2, as shown in Table I.

b. Collider Phenomenology

In $p\bar{p}$ collisions SUSY particles can only be pair-produced due to R-parity conservation. At the Tevatron, with $\sqrt{s} = 1.96$ TeV, gaugino pair-production dominates [35], since strongly interacting squarks and gluinos are too heavy to be produced. Individually, $\widetilde{\chi}_2^0\widetilde{\chi}_1^\pm$ and $\widetilde{\chi}_1^+\widetilde{\chi}_1^-$ production, as shown in Fig. 1, contribute 45% and 25% of the GMSB production cross section ($\sigma_{\rm prod}$), respectively. The leading-order (LO) production cross sections [36] are corrected to next-to LO (NLO) using the theoretically obtained NLO/LO ratio ("K-factor") [37] which is a function of the $\widetilde{\chi}_1^0$ mass for $\widetilde{\chi}_1^\pm$ pair and $\widetilde{\chi}_1^\pm\widetilde{\chi}_2^0$ production with values between 1.1-1.3 for the mass range considered. Both the NLO $\sigma_{\rm prod}$ and the K-factors are shown in Figure 2a and b. Since the $\widetilde{\chi}_1^0$ lifetime only scales with the $\widetilde{G}$ mass for a fixed $\widetilde{\chi}_1^0$ mass [17] the $\sigma_{\rm prod}$ is independent of the $\widetilde{\chi}_1^0$ lifetime. Figure 2c shows for comparison the NLO $\sigma_{\rm prod}$ of $\tilde{e}_R$ pairs. The production mechanism $p\bar{p} \to \tilde{e}_R^-\tilde{e}_R^+ \to e^-e^+\widetilde{\chi}_1^0\widetilde{\chi}_1^0 \to e^-e^+\gamma\gamma\widetilde{G}\widetilde{G}$ is favored to explain events like $ee\gamma\gamma\not{E}_T$ [16]. For comparison, in the SPS 8 model the $\tilde{e}_R$ mass is $\sim$100 GeV/c^2 at $m_{\widetilde{\chi}} = 70$ GeV/c^2 and $\sim$150 GeV/c^2 at $m_{\widetilde{\chi}} = 110$ GeV/c^2, which covers large parts of the "favored parameter region" of the $ee\gamma\gamma\not{E}_T$ event. In this range the NLO $\sigma_{\rm prod}$ of slepton pairs is $\sim$10% of the $\sigma_{\rm prod}$ of gaugino pairs. Table I summarizes the GMSB model parameters, the resulting $\widetilde{\chi}_1^0$ mass and lifetime, and the next-to-leading order (NLO) $\sigma_{\rm prod}$ for example points for the SPS 8 model line.

Table I: The $\widetilde{\chi}_1^0$ masses and lifetimes relevant for this search and their translation to the GMSB parameters in accordance with the GMSB SPS model 8 convention [29]. Also included are the NLO production cross sections ($\sigma_{\rm prod}$). Since the $\widetilde{\chi}_1^0$ lifetime only scales with the $\widetilde{G}$ mass for a fixed $\widetilde{\chi}_1^0$ mass [17, 18] the $\sigma_{\rm prod}$ is independent of the $\widetilde{\chi}_1^0$ lifetime. Note the different unit for the $\widetilde{G}$ mass.

$m_{\widetilde{\chi}}$ (GeV/c^2)	$\tau_{\widetilde{\chi}}$ (ns)	$m_{\widetilde{G}}$ (eV/c^2)	Λ (GeV/c^2)	K-factor	NLO $\sigma_{\rm prod}$ (pb)
67	10	121	51500	1.23	1.26
80	10	199	60500	1.21	0.518
80	20	280	60500	1.21	0.518
100	5	248	74000	1.19	0.162
113	5	341	83000	1.18	0.0824

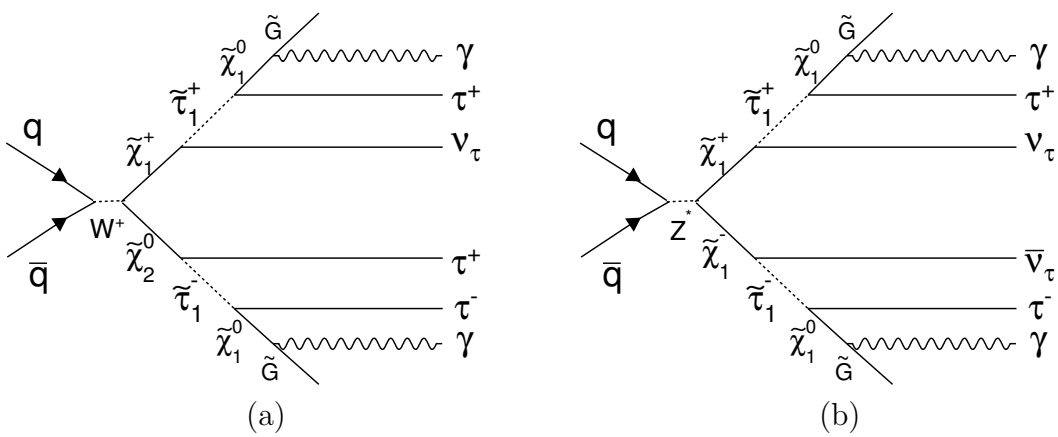

Figure 1: Feynman diagrams of the dominant tree production processes at the Fermilab Tevatron for the GMSB model line from SPS 8. In (a) $\widetilde{\chi}_1^{\pm}\widetilde{\chi}_2^0$ (45%) and in (b) $\widetilde{\chi}_1^+\widetilde{\chi}_1^-$ pair production (25%). The taus and second photons, if available, can be identified as energy deposits in the detector, known as jets. Note that only one choice for the charge is shown. The remaining processes are slepton (τ_1, e_R, μ_R) pair-production with roughly equal proportions.

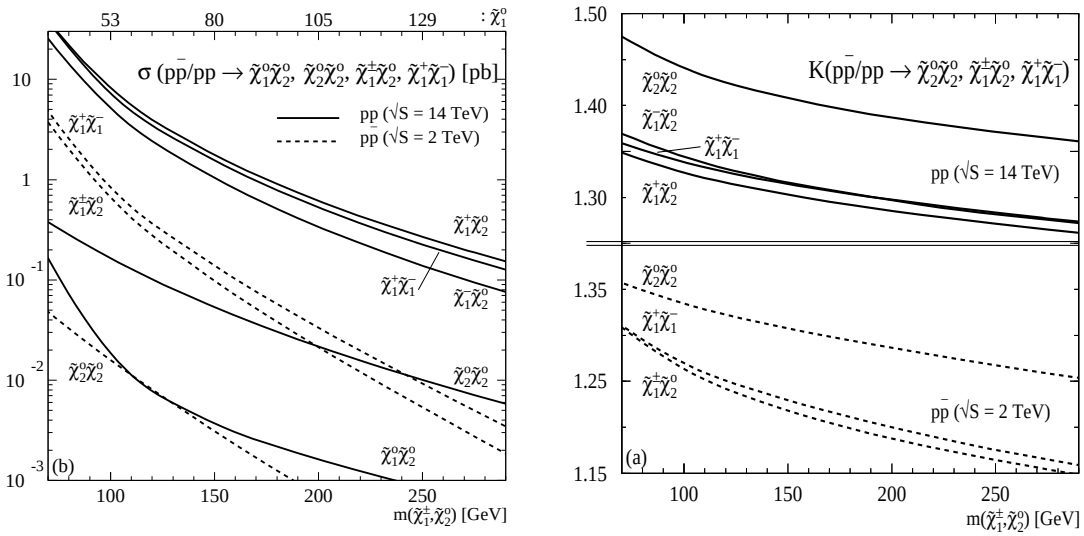

(a) (b)

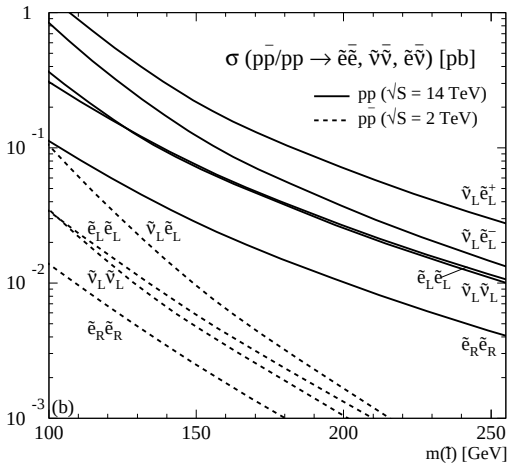

(c)

Figure 2: In (a) the NLO $\sigma_{\rm prod}$ of $\widetilde{\chi}_1^+\widetilde{\chi}_1^-$ pair and $\widetilde{\chi}_1^\pm\widetilde{\chi}_1^0$ production at the Tevatron and the the LHC, and in (b) the ratio of NLO to LO cross sections ("K-factors"), both as a function of the average $\widetilde{\chi}_1^\pm/\widetilde{\chi}_2^0$ mass. The K-factors are used in calculating the NLO $\sigma_{\rm prod}$ from the LO cross sections, provided by the PYTHIA event generator [36]. The $\widetilde{\chi}_1^\pm$ and $\widetilde{\chi}_2^0$ masses are almost identical in the scenario chosen in Ref. [29]. In (c) the NLO $\sigma_{\rm prod}$ for slepton pairs that are the favored process to explain events like $ee\gamma\gamma\not{E}_T$ [16]. All figures are taken from Ref. [37].

GMSB events can be identified in a detector that surrounds the collision. As shown in Fig. 1, each gaugino promptly decays to a $\widetilde{\chi}_1^0$ in association with taus whose prompt hadronic decays can be identified as jets [38, 39]. Each $\widetilde{\chi}_1^0$ decays into a photon and a weakly interacting $\widetilde{G}$ which occurs either inside or outside the detector volume depending on the $\widetilde{\chi}_1^0$ decay length and the detector size. As both the $\widetilde{\chi}_1^0$ and the $\widetilde{G}$ are weakly interacting they can leave undetected and give rise to an energy imbalance ("missing" energy) in the detector that translates to missing transverse energy ($\not\!\!E_T$) at a hadron collider [15]. Figure 3 shows that most events are expected to have a photon E_T of ∼30 GeV and a $\not\!\!E_T$ of ∼30 GeV for an example GMSB point. Depending on how many of the two $\widetilde{\chi}_1^0$'s decay inside the detector, due to their large decay length, the event has the signature $\gamma\gamma + \not\!\!E_T$ or $\gamma + \not\!\!E_T$, with one or more additional jets from the tau decays. This analysis focuses on the $\gamma + \not\!\!E_T$ case which is expected to be more sensitive to nanosecond lifetimes as discussed below and in more detail in Ref. [40].

The arrival time of photons from nanosecond lifetime $\widetilde{\chi}_1^0$'s at the detector allows for a good separation from prompt (SM) photons. Figure 4a illustrates the decay of a $\widetilde{\chi}_1^0$ into a photon and a $\widetilde{G}$ in a detector after a macroscopic decay length. Only the photon is identified and deposits energy in the detector. A suitable separation variable is [40]:

$$t_{\rm corr} \equiv (t_f - t_i) - \frac{|\vec{x}_f - \vec{x}_i|}{c} \tag{1.3}$$

where $t_f - t_i$ is the time between the collision t_i and the arrival time t_f of the photon, and $|\vec{x}_f - \vec{x}_i|$ is the distance between the position of the photon in the detector and the collision point. Essentially, $t_{\rm corr}$ is the photon arrival time corrected for the collision time and a "time-of-flight" that is calculated from the collision position and the position of the photon in the detector. Prompt photons will produce $t_{\rm corr} \equiv 0$

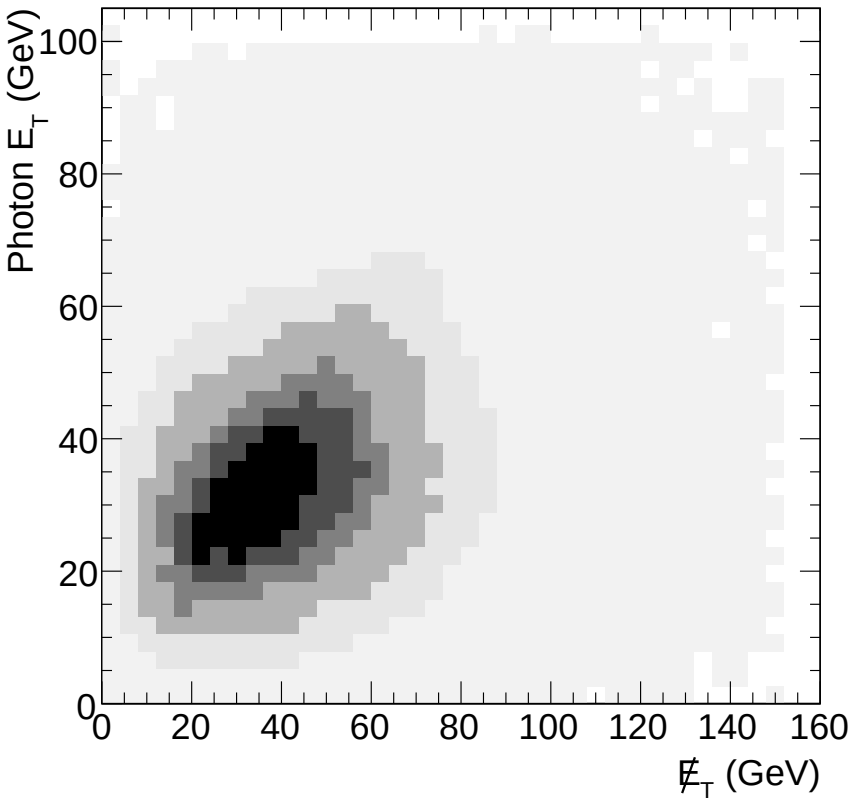

Figure 3: The E_T of the highest-E_T photon and the $\not{E}_T$ in simulated GMSB events where at least one $\widetilde{\chi}_1^0$ decays inside the detector, for an example point of $m_{\widetilde{\chi}} = 90$ GeV$/c^2$ and $\tau_{\widetilde{\chi}} = 10$ ns.

while photons from long-lived particles will appear "delayed" ($t_{\rm corr} > 0$), for perfect measurements. Figure 4b shows the distribution of $t_{\rm corr}$ for GMSB signal and prompt background for an example GMSB points where the $t_{\rm corr}$ resolution is assumed to be 1 ns.

The sensitivity to GMSB models is determined by two quantities: the number of events produced in the collisions (proportional to both the number of $p\bar{p}$ collisions and $\sigma_{\rm prod}$) and the acceptance, defined as the ratio of events that pass all event selection and time requirements to all events produced. The optimal sensitivity is determined by balancing the ability to both detect signal events and the rejection of SM, instrumental and other backgrounds. In this search the sensitivity is dominated by the fraction of $\widetilde{\chi}_1^0$'s that decay in the detector volume. Figure 5a shows the fraction of $\widetilde{\chi}_1^0$ that decay in the detector as a function of the $\widetilde{\chi}_1^0$ lifetime, from a toy Monte Carlo (MC) simulation. While only a small fraction of $\widetilde{\chi}_1^0$'s with a long lifetime decay to photons inside the detector ($\sim$1% at $\tau_{\rm evt} = 10$ ns), all of these photons pass a large timing requirement of $t_{\rm corr} > 5$. For a given lifetime this fraction depends mainly on the boost of the $\widetilde{\chi}_1^0$. Figure 5b shows the relation between the $\widetilde{\chi}_1^0$ boost and the photon $t_{\rm corr}$. Photons that pass a large timing requirement are decay products from $\widetilde{\chi}_1^0$'s with low boost (1-1.5). A highly boosted $\widetilde{\chi}_1^0$ that decays in the detector typically does not contribute to the acceptance because it tends to produce a photon traveling in the same direction as the $\widetilde{\chi}_1^0$. Thus, the photon's arrival time is indistinguishable from promptly produced photons. At small boosts the decay is more likely to happen inside the detector, and the decay angle is more likely to be large, which translates into a larger delay for the photon as well as a high incident angle of the photon at the face of the detector. This effect is discussed in detail in Section III.C. The acceptance as a function of $\widetilde{\chi}_1^0$ mass and lifetime is discussed in detail with a full CDF detector simulation in Section VIII.B. With an understanding of the types of events that are

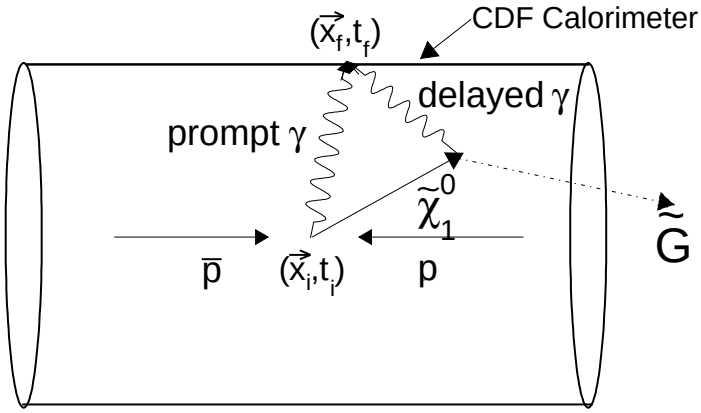

(a)

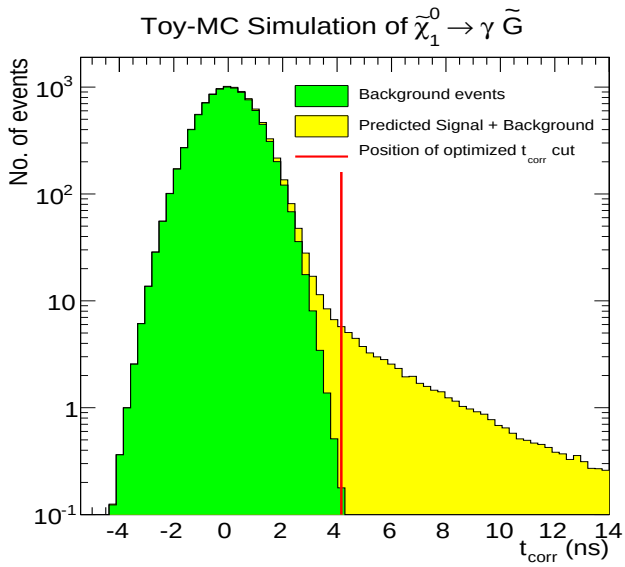

(b)

Figure 4: The schematics of a long-lived $\widetilde{\chi}_1^0$ decaying into a $\widetilde{G}$ and a photon inside the CDF detector. While the $\widetilde{G}$ leaves undetected the photon travels to the detector wall and deposits energy in the detector. A prompt photon would travel directly from the collision point to the detector walls. Relative to the collision vertex time, the photon from the $\widetilde{\chi}_1^0$ would appear "delayed" in time. Note that the lifetime of the $\widetilde{\chi}_1^0$ may be long enough for it to leave the detector, giving rise to $\not{E}_T$. Figure (b) compares the simulated distributions of the photon arrival time, corrected as described in the text, from prompt SM background and GMSB production with $m_{\widetilde{\chi}} = 110$ GeV/c^2 and $\tau_{\widetilde{\chi}} = 10$ ns. They can be well separated with an arrival time requirement, as indicated with the red line.

straightforwardly separated from SM backgrounds we proceed with an overview of the search.

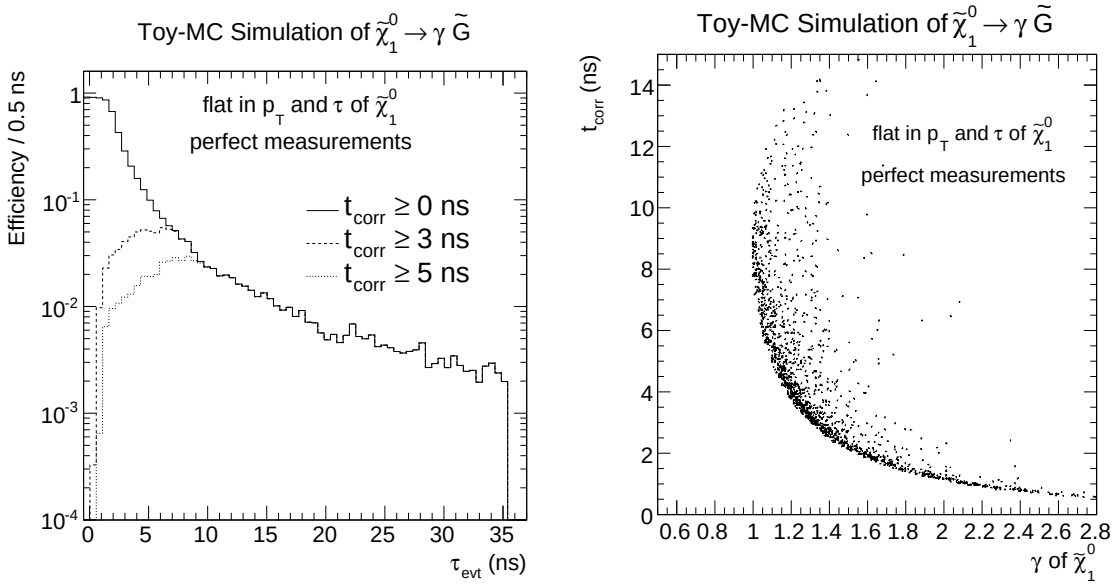

(a) (b)

Figure 5: In (a) the fraction of events ("efficiency" in the figure) in which a $\widetilde{\chi}_1^0$ decays in the detector ($t_{\rm corr} \geq 0$) as a function of the $\widetilde{\chi}_1^0$ event lifetime ($\tau_{\rm evt}$). This is modeled with a toy MC simulation using a perfect photon $t_{\rm corr}$ resolution and a flat $\widetilde{\chi}_1^0$ p_T distribution. Also shown are events with decay photons of medium and large timing requirements. For prompt decays *i.e.* low $\tau_{\rm evt}$ all $\widetilde{\chi}_1^0$ decay in the detector (a small difference shows up as a binning effect), but only a very small fraction of photons pass a large timing requirement. At large $\tau_{\rm evt}$ only few events stay in the detector, however if a $\widetilde{\chi}_1^0$ is long-lived and decays in the detector, it also passes a large timing requirement. Note that the true shape of the distribution depends on the $\widetilde{\chi}_1^0$ boost. In (b) $t_{\rm corr}$ as a function of the $\widetilde{\chi}_1^0$ boost for a $\widetilde{\chi}_1^0$ lab frame lifetime of 8.5 ns $\leq \tau_{\rm evt,L} \leq$ 9.0 ns. In the region 1.0 $<$ boost $<$ 1.5 $\widetilde{\chi}_1^0$'s remain in the detector and can produce a large $t_{\rm corr}$. The $\widetilde{\chi}_1^0$'s with high boost are more likely to decay outside the detector or, if they do not, produce low $t_{\rm corr}$ as the photon likely emanates in flight direction of the $\widetilde{\chi}_1^0$. Thus, events with the largest $t_{\rm corr}$ are produced by $\widetilde{\chi}_1^0$'s with large lifetimes and low boosts.

C. Overview of the Search

This dissertation presents the first search for neutral, heavy, long-lived particles that decay to photons at a hadron collider. The search is performed with a new photon timing system and novel analysis techniques. It uses 570 ± 34 pb^{-1} of data collected in $p\bar{p}$ collisions at $\sqrt{s} = 1.96$ TeV at the CDF detector between December 2004 and November 2005. This analysis preselects events that contain a photon with an arrival time that is significantly delayed compared to prompt production ("signal time window") to select photons from long-lived $\widetilde{\chi}_1^0$'s, and $\not\!\!E_T$ and a high-E_T jet ("$\gamma + \not\!\!E_T + \geq 1$ jet"), in an attempt to identify events that contain cascade decays from $\widetilde{\chi}_1^{\pm}$ and/or $\widetilde{\chi}_2^0$, as shown in Fig. 1. The time requirement provides the major background rejection factor.

For this signature the main backgrounds can be separated into two types of sources: collision and non-collision background. The former are from SM sources like strong interaction (QCD) processes while the latter are from (a) photon candidates that are emitted by cosmic ray muons as they traverse the detector and (b) muons that are emitted by collider beam particles that hit the beam pipe upstream of the detector, travel almost parallel to the beam direction and finally scatter into the detector ("beam halo") to produce an energy deposit that is reconstructed as a photon. The search is performed as a blind analysis, *i.e.* without looking into the signal time window to avoid a possible bias. The window is defined before the final event requirements are determined based on the signal and background expectations alone. The background rates are estimated from control time regions from the same $\gamma + \not\!\!E_T + \geq 1$ jet data sample using the $t_{\rm corr}$ distribution shapes of the backgrounds. The contribution of each background to the signal time window is estimated using a fit of the known shapes of each of the backgrounds in control regions outside this win-

dow. A MC simulation is used to model the GMSB event dynamics in the detector, and to estimate the signal expectations. An estimation of the number of background events as well as the acceptance to GMSB models in the signal time window for various final event selection requirements then allows for a calculation of the most sensitive combination of event requirements for a potential GMSB signal. The final event requirements are found using an optimization of this sensitivity to extend the limits beyond the current $\widetilde{\chi}_1^0$ mass and lifetime region shown below and towards the favored $\widetilde{G}$ mass region $1.0 < m_{\widetilde{G}} < 1.5$ keV/c^2.

The strategy of this search is also chosen to be robust and sufficiently independent of the specific GMSB model dynamics. This effectively makes the search sensitive to any model that produces a large mass particle decaying to a similar final state, in particular to models other than GMSB that produce events such as $ee\gamma\gamma\not{E}_T$.

This is both the first search for heavy, long-lived particles that decay to photons at a hadron collider and also the first direct search for those particles using timing. Other experiments have searched for prompt [41, 42] and nanosecond lifetime [19] particles using non-timing techniques, all with a null result. Figure 6 shows the results using the ALEPH detector at LEP from direct searches in high energy e^+e^- collisions for GMSB $\widetilde{\chi}_1^0$ and indirect searches for sleptons and charginos in $e^+e^- \to \tilde{\ell}\tilde{\ell} \to \ell\tilde{\chi}_1^0\ell\tilde{\chi}_1^0$ and $e^+e^- \to \tilde{\chi}_1^+\tilde{\chi}_1^- \to W^{*-}\tilde{\chi}_1^0 W^{*+}\tilde{\chi}_1^0$ decay channels that yield a lifetime dependent limit on the $\widetilde{\chi}_1^0$ mass of ∼60-98 GeV/c^2. Separately shown is the impact from Higgs searches in $e^+e^- \to hZ$ and $e^+e^- \to hA$ on the $\widetilde{\chi}_1^0$ in this model with an indirect limit at around 90 GeV/c^2 [19]. There are limits from other LEP collaborations [19] but they are unpublished as of this writing.

The results of the full analysis presented here have been submitted for publication in Phys. Rev. Lett. [43].

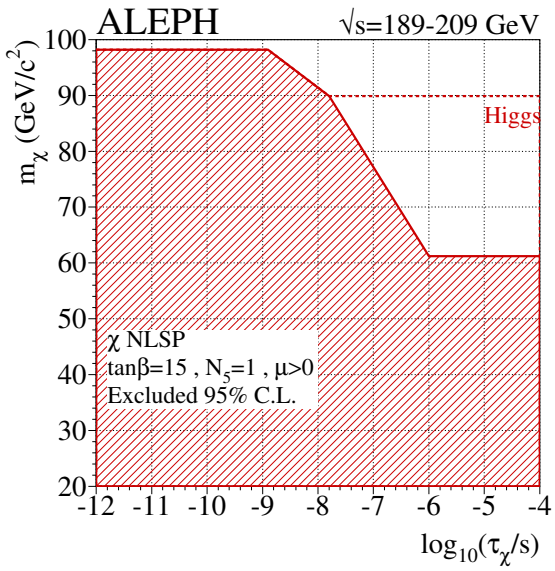

Figure 6: The 95% C.L. exclusion region for GMSB searches with the ALEPH detector at LEP [19] as a function of $\widetilde{\chi}_1^0$ mass and lifetime for the SPS 8 choice of parameters [29]. The shaded region is from direct searches for a GMSB $\widetilde{\chi}_1^0$ up to $\tau_{\widetilde{\chi}}$ ~100 ns using pointing techniques and from searches for sleptons and charginos for longer $\widetilde{\chi}_1^0$ lifetimes [19]. The dashed line shows the indirect upper exclusion limit on the $\widetilde{\chi}_1^0$ from searches for the Higgs boson; $\widetilde{\chi}_1^0$ masses of less than 90 GeV/c^2 in GMSB models are excluded. There are comparable limits from other LEP collaborations [19] but they are unpublished as of this writing.

D. Outline of the Dissertation

The structure of this dissertation is as follows: Chapter II describes the Tevatron accelerator complex and the CDF detector, in particular the recently installed timing system in the electromagnetic calorimeter ("EMTiming") that is used to identify photons and measure their arrival time. Chapter III motivates and describes how photons are identified at CDF. Also described are modifications to the standard identification to maintain a high efficiency for identifying photons from heavy, long-lived particles that often arrive at the calorimeter at unusual incident angles as would be expected from low-boost $\widetilde{\chi}_1^0$ decays. The chapter further describes the corrected photon time measurement and a simulation of the system that is used to estimate the GMSB signal expectations. Chapter IV discusses the event selection starting with the $\gamma + \not\!\!E_T +$ jets preselection criteria, and describes the data sample. The various background sources as well as their estimation methods are described in Chapter V. Chapter VI describes the MC generation of GMSB events and corrections to take into account effects that are not simulated, as well as systematic uncertainties on the acceptance. Chapter VII describes the optimization procedure and shows the expected sensitivity. The signal region is unblinded in Chapter VIII, and the data events observed in the signal region are discussed and compared to background expectations. A parameterization of the acceptance as a function of $\widetilde{\chi}_1^0$ mass and lifetime is presented as it allows for a model-independent description of the sensitivity. Chapter IX concludes with the final results and a discussion of future prospects for similar analyses with more data.

CHAPTER II

THE FERMILAB TEVATRON, THE CDF DETECTOR AND THE EMTIMING SYSTEM

This chapter introduces the Fermilab accelerator complex and the CDF detector used to produce and study high energy proton-antiproton collisions. The subsystems of each that are most important for this analysis are described. The timing system in the electromagnetic calorimeter at CDF ("EMTiming") is described in a separate section in detail as it is a central component in this analysis.

A. The Fermilab Tevatron

The Fermilab Tevatron accelerator complex [44–46] is a superconducting synchrotron of 1 km radius that collides protons and antiprotons with a center-of-mass energy of $\sqrt{s} = 1.96$ TeV. Figure 7 shows its main constituents including the proton and antiproton production, their acceleration up to 150 GeV in the main injector and the Tevatron "main ring" [44] where both particle types are accelerated from 150 GeV to 980 GeV and collided.

When protons and antiprotons are injected into the Tevatron they are collected ("coalesced") into 36 proton and antiproton "bunches" that each typically contains $\sim 3 \cdot 10^{11}$ and $\sim 3 \cdot 10^{10}$ particles, respectively. They counter-rotate in the Tevatron ring ("a store") and collide at each of the two focus points, BØ and DØ in Fig. 7 that are surrounded by the CDF and the DØ detectors, respectively. Within the Tevatron, each bunch is accelerated in one of the many radio-frequency (RF) cavities of 53 MHz, called "buckets" [1]. The 36 bunches are "injected" in groups of 12 ("a train") such

[1]Note that this frequency corresponds to a time separation between each bucket of ∼18 ns.

that within each train the bunches are separated by 21 RF buckets, corresponding to a collision time separation of 396 ns. While ideally only buckets that participate in the collision contain protons and antiprotons, it can happen that the buckets adjacent to these buckets contain a small fraction of beam particles and collide accidentally. For this small fraction of events the "satellite collisions" time is shifted by 18 ns, and multiples thereof.

The smallest data-taking unit is a "run" [47] which is defined by an uninterrupted time interval as part of a store for which no change in detector setup or data-acquisition occurred. While a store usually lasts for ∼2-3 days there are typically many runs per store, each rarely lasting longer than a day.

The profile of the proton-antiproton interaction region is well approximated by a Gaussian distribution with a typical RMS of 30 cm along the beam (z) and 30 μm in the transverse direction (x-y). The interaction time variation is also Gaussian with an RMS of ∼1.28 ns. The average number of collisions per event varies between 0.4 and 4.4 [48].

(a)

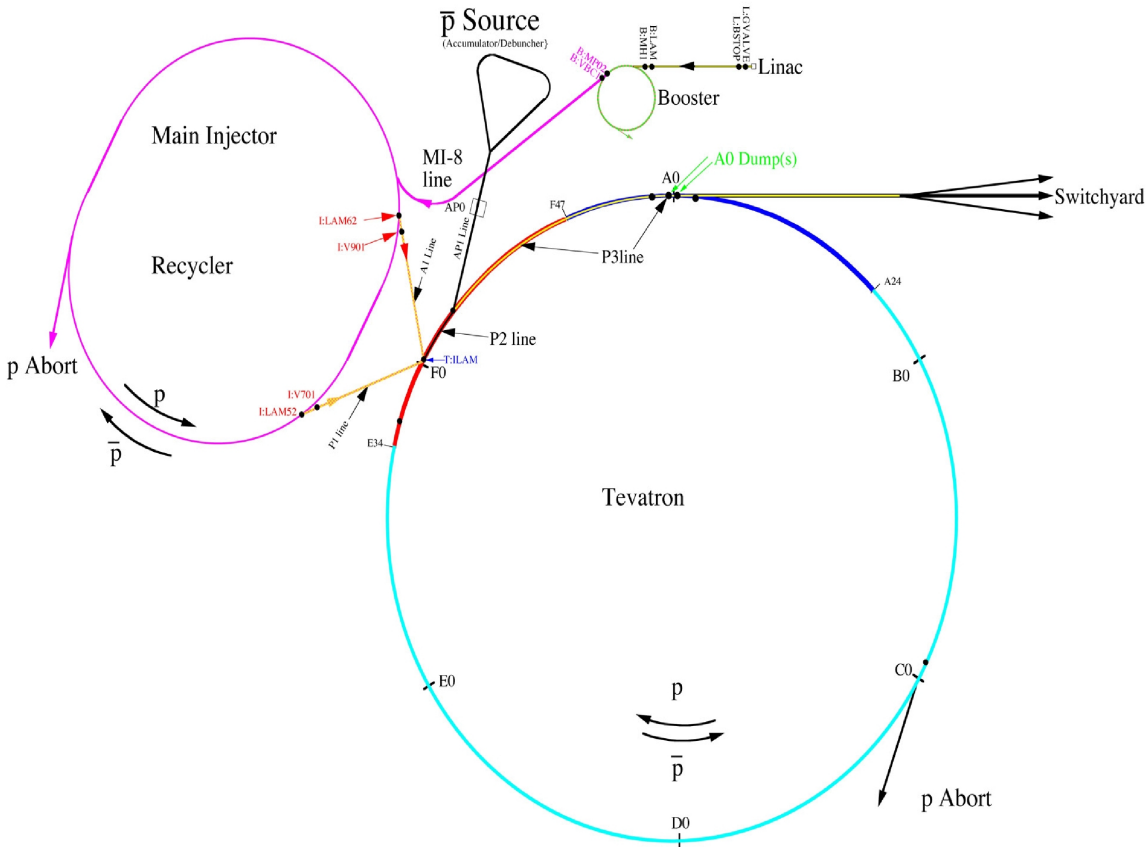

(b)

Figure 7: In (a) an aerial view [49] of the Fermilab accelerator complex with the Main Injector in the foreground and the Tevatron in the back. In (b) an illustration of the Fermilab accelerator chain [44]. The CDF detector is situated at the B0 point on the right.

B. The CDF Detector

The CDF detector for the data taking period 2002-2006 ("CDF II") is an azimuthally and forward-backward symmetric [50], general-purpose magnetic spectrometer with the most probable collision point occurring at its center. Figure 8 shows both a photograph of the detector and a schematic drawing of the major detector components. While a detailed description can be found at Refs. [45, 51, 52], the components salient for this analysis are presented here.

To give an overview, the CDF collision region is surrounded by various systems to measure the full trajectory, 4-momentum and charge of particles. The inner part of the detector has tracking systems that consist of a silicon microstrip system for, e.g., precision measurements of the decay vertices of b-hadrons at a radial range of 1.5 cm to 28 cm and an open-cell wire drift chamber ("Central Outer Tracker," COT) described below. To measure charged particle trajectories they are both immersed in a 1.4 T magnetic field that is generated by a superconducting solenoid of 1.5 m radius and 4.8 m length. Segmented electromagnetic (EM) and hadronic (HAD) sampling calorimeters and muon identification systems are situated outside the solenoid to further provide particle identification and energy measurements.

The COT covers the region $|z| < 155$ cm and a radius between 40 and 137 cm and is sensitive to charged particle tracks with a pseudo-rapidity of $|\eta| < 1$ [50]. Their trajectory is measured using ionizing "hits" in 96 wires that are organized into 8 alternating axial superlayers, providing (r, ϕ) information, and $\pm 2°$ stereo superlayers, providing r, ϕ and z information, with the innermost layer being stereo. With a hit resolution of 140 μm the COT can typically measure the track momentum with a resolution of $\frac{\sigma(p_T)}{p_T^2} \approx 0.0017(\mathrm{GeV}/c)^{-1}$ [45], and the track z position at the beamline with a resolution of 0.22 cm. The time information of each hit allows for a t_0

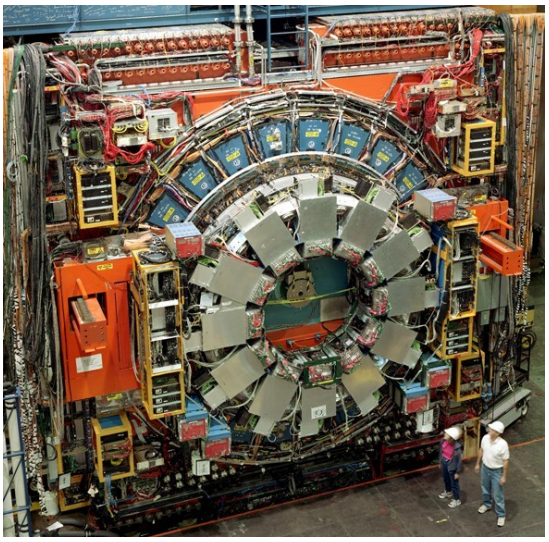

(a)

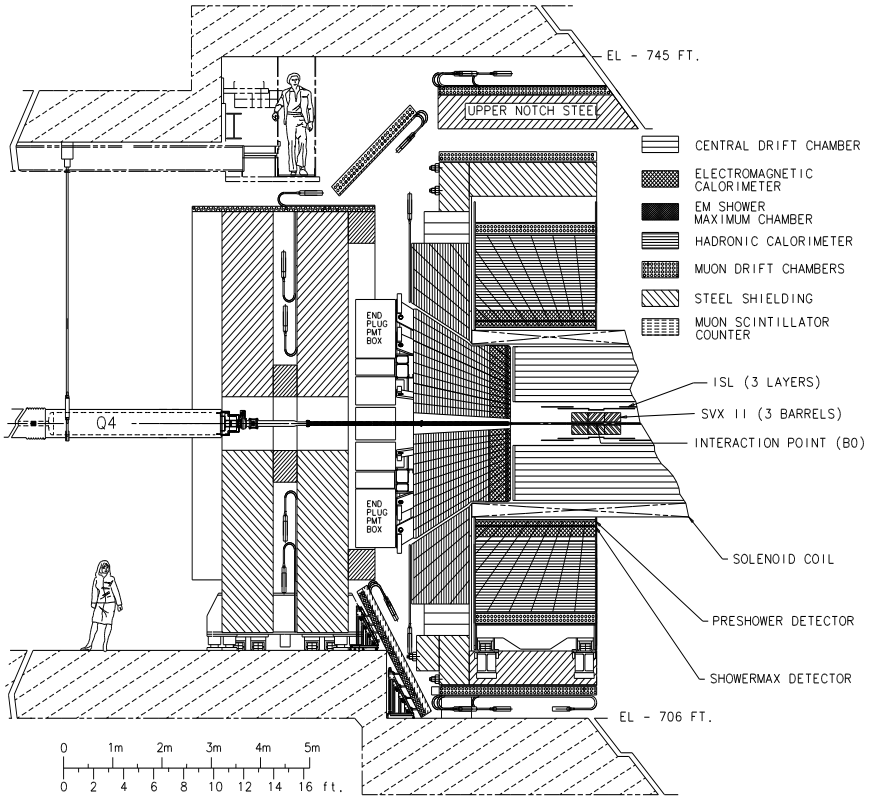

(b)

Figure 8: In (a) a photograph [53] and in (b) an elevation view [51] of the CDF II detector. In this analysis, the "central drift chamber" (COT) is used for track identification and timing and the calorimeter systems for photon identification and timing, with a newly installed system in the EM part. The muon drift chambers are used for cosmic ray muon rejection.

measurement of the track with a resolution of 0.27 ns (see Section III.F) and also provides $\frac{\mathrm{d}E}{\mathrm{d}x}$ information that helps identify charged particles.

The calorimeter systems [51] measure the energy deposited by particles in a range of $|\eta| < 1.0$ ("central") and $1.1 < |\eta| < 3.64$ ("plug") using towers projective to the most probable collision position in the center of the detector. Most towers cover 15° in ϕ and between 0.10 and 0.13 units in η, where all towers of the same ϕ are collectively called a "wedge." The central electromagnetic calorimeter (CEM) shown in Fig. 9a uses 23 lead and polystyrene scintillator layers alternating in the radial direction, each with ∼5 mm thickness and having a total of $21X_0$ (radiation lengths) to fully contain the energy of cascade showers from EM particles like photons and electrons. Light deposited in the scintillators is read out by two phototubes on opposing sides of each tower and provides an energy measurement with a resolution of $\frac{\sigma(E)}{E} = \frac{13.5\%}{\sqrt{E_T}} \oplus 2\%$. A proportional strip and wire chamber (CES) is located at a depth of $\sim 6X_0$, corresponding to the shower maximum of electrons and photons [54]. The CES consists of 256 cathode strips, that run in ϕ direction and measure the position and profile in z, and 128 anode wires per wedge, that run in z direction and measure the position and profile in ϕ of the shower ("a CES cluster"). The typical shower profile of prompt photons and electrons is Gaussian with a width of 1.5-2.0 cm. The central HAD calorimeter has the same tower/wedge geometry as the EM but with iron sampling instead of lead. It measures showers of hadronic particles (jets) with an energy resolution of $\frac{\sigma(E)}{E} \approx 0.1E_T + 1.0$ GeV [38]. The plug calorimeters are sampling scintillator calorimeters with one phototube per tower readout up to $|\eta| = 3.64$ where each tower covers 7.5° in ϕ, 12 towers for each plug. The EM part (PEM) has an energy resolution of $\frac{\sigma(E)}{E} = \frac{16\%}{\sqrt{E}} \oplus 1\%$, the HAD part an energy resolution of $\frac{\sigma(E)}{E} = \frac{80\%}{\sqrt{E}} \oplus 5\%$. During beam operations the calorimeter

systems integrate the energy deposited in each tower over a time interval of 132 ns that contains the collision time.

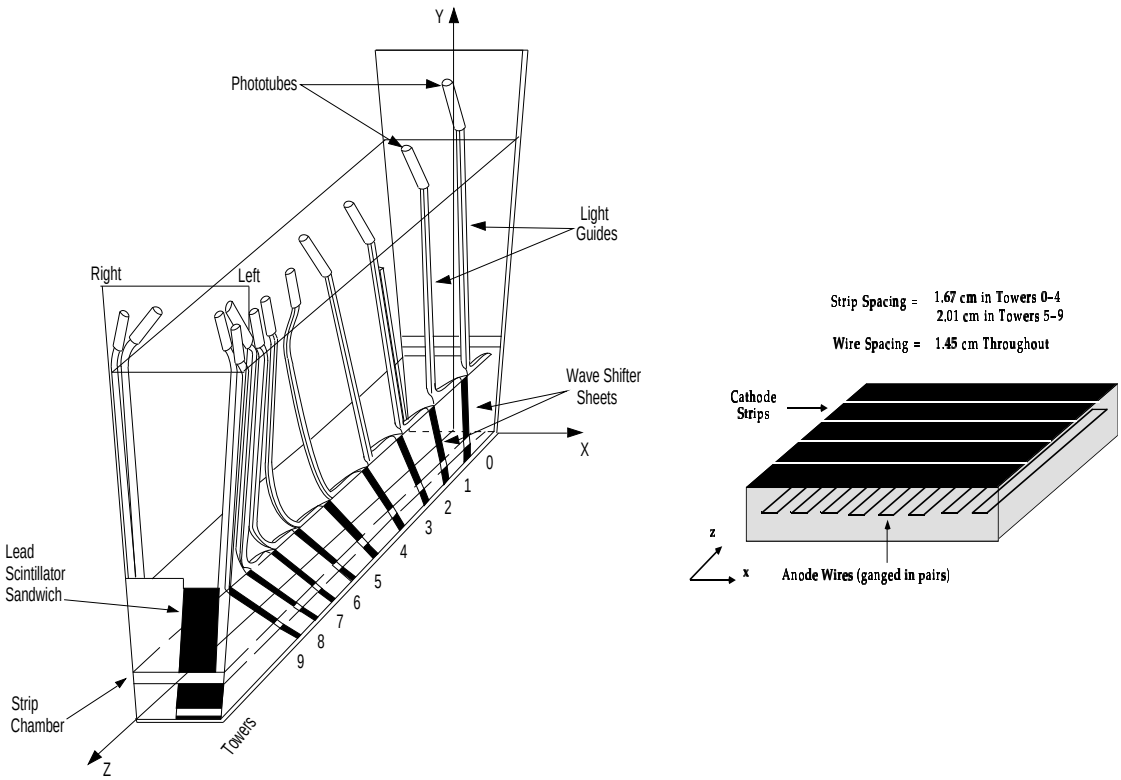

(a) (b)

Figure 9: In (a) a schematic drawing of a wedge in the central calorimeter, including the EM and CES subsystems [53]. In (b) a schematic drawing of the CES subsystem showing strips and wires [53].

The muon identification system is located behind the calorimeter and is used in this analysis to reject events with cosmic ray muon contamination. In the region $|\eta| < 0.6$, planar drift chambers inside (CMU) and outside (CMP) the return yoke of the magnet detect muons with $p_T > 1.4$ GeV and $p_T > 2.2$ GeV, respectively. Drift chambers with a conical geometry (CMX) detect muons with $0.6 < |\eta| < 1.0$, "Intermediate Muon Detectors" cover the region $1.0 < |\eta| < 1.5$. Typically a muon

is identified via a COT track that is matched to an energy deposit ("stub") in one or more muon systems. However, if a muon from a cosmic ray shower traverses the detector coming from outside the detector instead of from the collision, it is likely that there is no track reconstructed to a muon stub. This case is described in detail in Section V.B.2 as part of the cosmic ray background rejection.

The beam luminosity is measured using low-mass gaseous Cherenkov luminosity counters (CLC) [55] to estimate the amount of collision data. Two modules of 48 counters each are situated along the p and the $\bar{p}$ direction at $3.7 < |\eta| < 4.7$. An empty bunch crossing is observed if there are fewer than two counters with signal above threshold in either module. As the number of $p\bar{p}$ interactions in a bunch crossing follows Poisson statistics the luminosity is determined by the inelastic cross section ($\sigma_{in} \sim 60$ mb [56]) and the measured fraction of empty bunch crossings. The systematic error on the luminosity is estimated to be 6% with major contributions to the CLC acceptance from the precision of the detector simulation and the event generator (4.4%) and the calculation of the inelastic cross section (4.0%) [55]. The instantaneous luminosity for the data used in this analysis was in the range 8 to $160 \cdot 10^{30}$ cm^{-2} s^{-1}, with an integrated luminosity of 570 ± 34 pb^{-1}.

The CDF detector is a well understood measuring instrument and there exist standard identification criteria for photons, electrons, muons, taus, b-quarks, jets and $\not\!\!E_T$. The photon identification criteria are discussed in Chapter III, the criteria for other objects like $\not\!\!E_T$ and jets in Chapter IV. The detector is also sensitive to non-collision backgrounds such as cosmic ray muons and instrumental "beam halo" [57] that can produce energy deposits in the calorimeters and mimic photons from the collision. These are discussed in Chapter V.

C. The EMTiming System

The EMTiming system [58, 59] plays a central role in this analysis as it measures the arrival time of photons and helps separate potential GMSB signal candidate events from background sources. In many ways it was built in response to the CDF $ee\gamma\gamma\not\!\!E_T$ candidate event [13] that featured two high-E_T photons, a central electron, an electron candidate in the plug EM calorimeter that passes all but the tracking requirement and significant $\not\!\!E_T$. While only an estimated $\sim 10^{-6}$ of such events are expected from SM processes (like $WW\gamma\gamma \rightarrow e\nu e\nu\gamma\gamma$) it may be that the event is due to other rare conditions like two overlapping collisions or an overlapping cosmic ($\sim 10^{-9}$ expected events). Since one of the photons and the plug electron candidate in this event had no arrival time information, in many ways the EMTiming system was built to help verify that in future events that all particles come from the primary collision. Alternatively, the system can also be used to reject events with energy deposits that might be due to cosmic-ray or beam-related contamination.

The system was installed and commissioned in Fall 2004. It covers the central and both plug regions of the calorimeter in the region $|\eta| < 2.1$, and measures the arrival time in each tower where particles (like photons, electrons or jets) deposit an energy of at least $\sim$3-4 GeV [59]. Note that while this section describes the full EMTiming system, in this analysis only photons in the central part are considered for reasons described later.

The photon arrival time in the calorimeter is measured using the electronic signal from the energy of the EM shower. As shown Fig. 10a, the EMTiming system attaches to the outputs of photomultiplier tubes (PMTs) that collect the light from the particle interaction with the EM calorimeter and effectively convert the energy deposited into an analog signal. As shown in the figure, this signal is sent via a coaxial cable

attached with "LEMO" brand connectors to a transition board (TB). The TBs serve as an interface to Amplifier-Shaper-Discriminator boards (ASDs) that convert the analog signal to a low-voltage differential signal (LVDS) and send it to fixed-start time-to-digital converters (TDCs) for the time measurement that are then read out by the data acquisition system. While both the TB and ASD boards are situated at the detector, within 40 ft of the PMTs, the TDC boards are in 220 ft distance as part of the data-acquisition readout equipment. Table II summarizes both the hardware setup and the performance of the system. Next, the signal path and the several hardware pieces are discussed in detail.

Figure 10b shows a schematic of a photon that interacts by showering into an EM calorimeter tower. As the shower develops the scintillator layers in the tower collect the light and send it into photomultiplier tubes (PMTs). Since there are 2 PMTs on opposite sides of each tower in the CEM detector as shown in Fig. 9a, there are twice as many towers in the PEM, that as it features only one PMT per tower. The resulting PMT analog signal shape has a rise time, measured from 10% to 90% of the voltage maximum, of $\sim$10 ns ($\sim$6 ns) for the CEM (PEM) and a full width-half mean signal length of $\sim$50 ns. Note that the energy readout of both PMTs in the CEM tower is correlated in the CEM, but the PMTs in two adjacent towers are independent in the PEM.

The CEM and PEM have different PMT readout schemes, as shown in Table II [60]. The PMT bases in the CEM, designed for the 1985 collider run, only provide an anode output for an energy measurement via a LEMO connector while the PEM was designed for the 2001 collider run with a possible timing upgrade, and provides an "AMP" connector unit for each PMT dynode. In the CEM consequently a custom-designed, inductive "splitter" board branches off $\sim$15% of the anode signal energy. As shown in Fig. 11 the anode cable is connected, via LEMO connector, to

a printed circuit board where the primary line, used for the energy measurement, is separated from its shield, passed through a small circular ferrite and reconnected to its shield. A secondary wire is wound around the ferrite so that the signal from the PMT anode induces a voltage for timing use, and is reconnected to a ∼30 ft coaxial cable that leads to the TB. In the PEM the dynode outputs from each PMT are collected in AMP sockets in groups of 16 (containing two adjacent wedges of one plug side) and sent via 25 ft cables to the TBs.

Table II: Overview of the EMTiming system hardware and performance.

	CEM	PEM
Coverage	$\|\eta\| < 1.0$	$1.1 < \|\eta\| < 2.1$
PMT	Hamamatsu R580	Hamamatsu R4125
Physical tower segmentation	$\Delta\phi = 15°$, $\Delta\eta \approx 0.1$	$\Delta\phi = 7.5°$, $\Delta\eta \approx 0.1$
Tower readout	2 PMTs per tower	1 PMT per tower
PMT→ASD readout method	Analog splitter, both PMTs from a single tower combined	Dynode, PMTs from two adjacent towers combined
Total number of PMTs/ASD channels	956/478	768/384
Number of TB/ASD/TDC boards	32/32/8	16/16/4
Energy threshold (50% efficiency point)	3.8±0.3 GeV	1.9±0.1 GeV
Threshold width	1.4±0.2 GeV	0.6±0.1 GeV
Timing resolution at asymptotic energies	600±10 ps	610±10 ps

Both CEM and PEM cables are connected to the TB with LEMO connectors. The corresponding ASD board is directly connected to the TB. Figure 12 shows the circuit schematics of a single channel on a TB and ASD board pair. The notable feature on the TB is the *RC* circuit on the TB board that helps reduce reflections

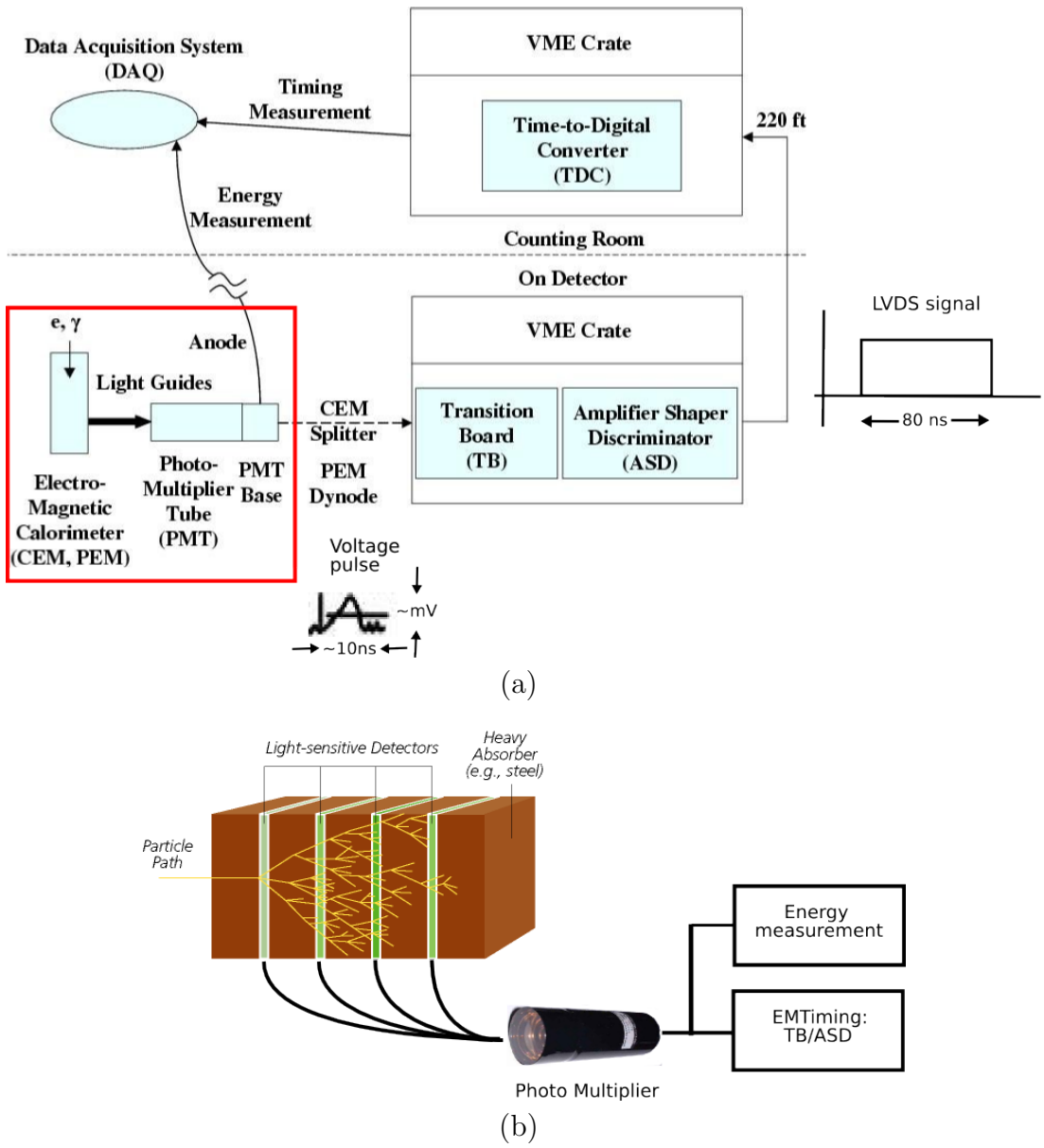

Figure 10: In (a) the schematics of the EMTiming system including the pulse descriptions. In (b) a schematic diagram of the energy and time measurement of a particle that showers into a tower of the calorimeter using a PMT. In the central wedge there are two PMT tubes that attach to opposite sides each as shown in Fig. 9a. Note that the CES sub-detector is not shown here.

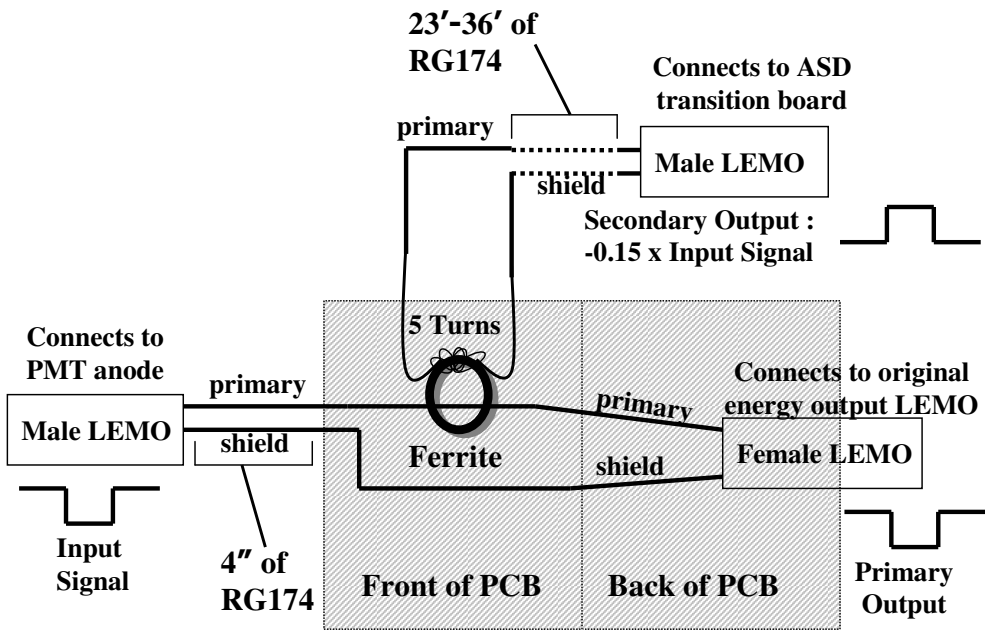

Figure 11: A schematic diagram of the CEM splitter. "RG174" refers to the coaxial cable and "LEMO" refers to the connector type. While the primary output is used for the energy measurement, the secondary output with the inverted PMT signal leads to the TBs for the time measurement.

back to the PMT that would be, in turn, reflected at the PMTs electric "open" end and can cause a second, erroneous signal to be sent. The rate at which multiple hits are recorded is typically negligible but can be as high as one in 10^5 collisions for a few towers [61]. However, this effect is easily removed by considering only the first timing hit. On the ASD the amplified signals of two PMTs are summed and compared to a 2 mV threshold which corresponds to ∼3-4 GeV energy deposit. If this signal is about the threshold, the ASD sends an LVDS pulse of (70 ± 10) ns output width, that shows little sensitivity to noise, through a long 220 ft cable. The ∼100 mV LVDS pulse has a rise time of ∼50 ns after traveling this length, which shows negligible data loss at an input signal length of 70 ns when it arrives at the TDC. The TDC finally records the arrival time of this signal, and is read out for each event as part of the data-acquisition system [51].

Figure 13 shows the performance of the EMTiming system using a sample of hadron jets [38] measured in the detector [59]. The top plot shows the efficiency, the fraction of the number of events with a time recorded in the TDC to all events as a function of the tower energy, for CEM and PEM, and includes all channels. The efficiency as a function of tower energy can be described with an error function. The system is 100% efficient for tower energies above ∼5 GeV (∼3 GeV) with thresholds of 3.8±0.3 GeV (1.9±0.1 GeV) and widths of 1.4±0.2 GeV (0.6±0.1 GeV) in the CEM (PEM). The distribution of the threshold in Fig. 13 (as well as the online monitoring results as shown in App. A) illustrate the uniform performance of the system. During the data-taking period of this analysis (∼20000 PMT · months) there was only 1 channel marked bad which was due to a LEMO socket not soldered correctly on the TB. The system timing resolution is discussed at the end of the next chapter, in conjunction with the description of the identification of photons and its comparison to expectations from promptly produced photons.

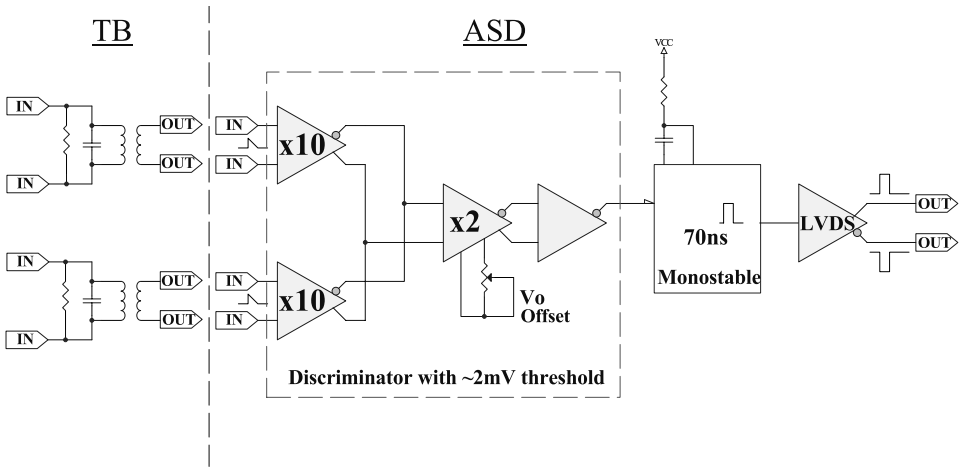

Figure 12: A schematic diagram of the signal processing on TB and ASD. The RC circuit on the TB ($R = 150\Omega,\ C = 12$ pF) in parallel with a transformer (1:1) helps reduce potential noise and reflection problems at the input. The amplifiers and comparators on the ASD effectively sum the two PMT signals and discriminate on the leading edge with a ∼2 mV threshold.

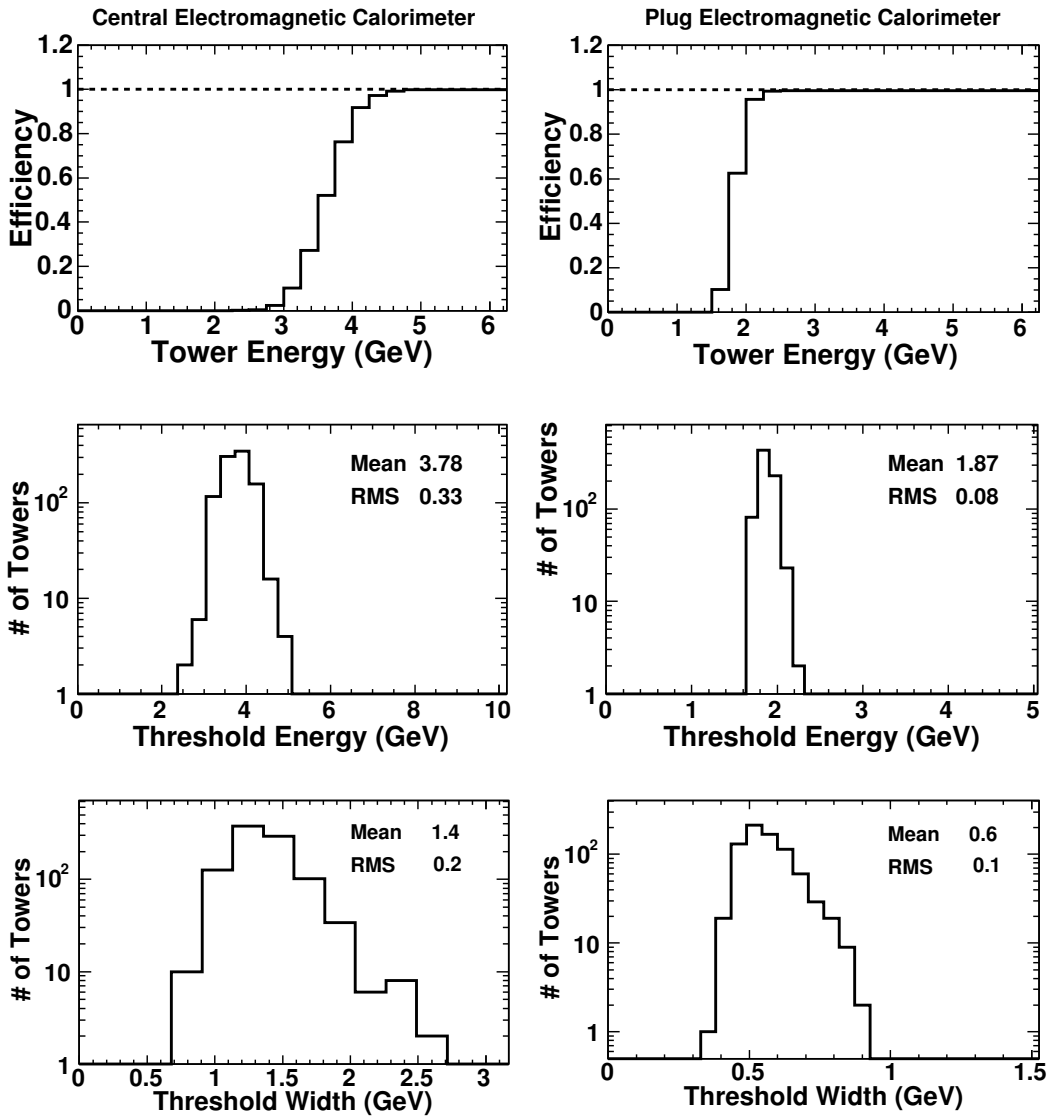

Figure 13: The EMTiming system response as a function of the energy deposited in a tower, separately for CEM and PEM, for a data sample of jets. The top plot shows the efficiency (the fraction of events with a time recorded in the TDC to all events), the bottom two rows show histograms of the energy threshold and threshold width of individual towers (all values in GeV), and indicate the uniformity of the system. There are 956 towers in the CEM and 768 in the PEM.

CHAPTER III

PHOTON IDENTIFICATION AND TIMING

This chapter describes the timing and the identification of photons, the primary object in this search. As photons from heavy, long-lived particles are not expected to hit the calorimeter coming directly from the collision point and can have a large incident angle at the face of the calorimeter, there is the possibility of an inefficiency for some of the standard photon identification (ID) requirements. After reviewing the standard photon ID variables, the efficiency of each ID variable is investigated as a function of incident angle. Since the quality of the transverse shower shape at the calorimeter is not simulated correctly in the CDF detector simulation ("CDF MC") [62] it is treated in a separate section and is finally removed from the ID criteria. Also introduced is a simple requirement that removes PMT high-voltage discharges ("PMT spikes") with ∼100% rejection power that can mimic a photon by coinciding with prompt, low-energy deposits in the calorimeter.

In the second part of this chapter, the full $t^{\gamma}_{\mathrm{corr}}$ calculation is described in detail that separates photons from various background sources. This includes the measurement of the photon arrival time by the EMTiming system and a new vertex algorithm that simultaneously determines the position and the time of the collision. The chapter concludes with a description of a full simulation of the EMTiming system in Section III.G as well as its validation by comparing data and MC. The simulation will be used in Chapter VI for the GMSB acceptance and sensitivity estimate.

A. Standard Photon Identification Variables

The CDF detector has been used to identify high-energy photons for over 20 years; the ID criteria described in this section are well established and standardized. Refs. [13,

14, 63] lists sources that contain good reviews for more details. The criteria are summarized in Table III.

Table III: The standard photon selection requirements used at CDF to identify high-E_T photon candidates. Note that all but the last requirement is retained in this search. See Table X for the final requirements.

Requirement
$E_T > 30$ GeV
Fiducial: $\lvert X_{\rm CES}\rvert < 21$ cm and 9 cm $< \lvert Z_{\rm CES}\rvert < 230$ cm
$\frac{E_{\rm Had}}{E_{\rm Em}} < 0.125$
$E^{\rm Iso}_{\rm R=0.4} < 2.0 + 0.02 \cdot (E_T - 20)$
$N_{\rm trks} = 0$ or $N_{\rm trks} = 1$ and $p_T < 1.0 + 0.005 \cdot E_T$
$\Sigma p_{\rm T}$ of tracks in a 0.4 cone $< 2.0 + 0.005 \cdot E_T$
$E^{\rm cluster}_{\rm 2nd\ strip\ or\ wire} < 2.34 + 0.01 \cdot E_T$
CES $(\chi^2_{\rm Strips} + \chi^2_{\rm Wires})/2 < 20$

In this analysis only photons in the central region ($|\eta| < 1.0$) are considered for two main reasons: (a) the central region provides the most powerful variables to identify photons, in particular as these photons traverse the COT tracking volume, and (b) the timing system has been fully validated in the central. A photon is identified as an energy deposition in one EM calorimeter tower ("seed") with only a small amount of leakage ("shoulder") into an adjacent tower of the same wedge. A set of one seed and its two adjacent shoulder towers is referred to as an "EM cluster" and constitutes a photon candidate. The seed tower is required to exceed 3 GeV. Then, the CES in this tower is searched for a cluster and, if found, the centroid of the CES profile is used to determine the position of the photon. The photon shower position is required to lie within 21 cm of the tower center in r-ϕ (CES $|X| < 21$ cm) and well away from the calorimeter tower edges, the gap at $|\eta| < 0.05$

and other uninstrumented regions [60] which lead to a fiducial region fraction of ∼80% ($9 < \mathrm{CES}|Z| < 230$ cm). The photon E_T is calculated from the energy deposited in the seed and one shoulder tower of the EM-cluster with respect to the position of the vertex with the highest scalar p_T-sum (Σp_{T}) of associated tracks.

The following photon identification criteria have been developed to separate real photons from $\pi^0 \to \gamma\gamma$ decays, hadronic jets and electrons:

- Hadronic Leakage ($\frac{E_{\mathrm{Had}}}{E_{\mathrm{Em}}}$): the ratio of energy deposited in the HAD compartment of the towers in the cluster to that in the electromagnetic part and is required to be less than 0.125. This rejects hadronic backgrounds from jets that usually deposit most of their energy in the hadronic part.

- Calorimeter Isolation: This requirement rejects EM clusters that contain π^0 decays as part of a jet that can deposit significant energy nearby. The isolation energy is defined as the difference between the sum of the energy of all EM and HAD towers within a cone of 0.4 in η-ϕ space around the photon and the energy of the photon cluster itself and is required to be less than 2.0 GeV. This requirement becomes less restrictive with higher E_T as the jets become more collimated. Also applied is a correction to take into account potential energy leakage into the cracks between the wedges. If there are additional reconstructed vertices, the mean energy per tower of 356.3 MeV from extra "underlying events" (see Section IV.A.2), is subtracted for each additional vertex that can otherwise increase the isolation energy of the photon.

- Track rejection: Since showers from electrons in the EM calorimeter are similar to those from photons, photon candidates are rejected if a track points to the EM cluster with a p_T of more than 1 GeV/c, but becoming less restrictive with higher photon E_T.

- Track isolation: As a jet likely contains charged particles along with π^0's, the Σp_{T} of all tracks coming from the vertex associated to the photon within a cone of 0.4 around the seed tower is required to be less than 2 GeV/c, becoming less restrictive with higher photon E_T.

- 2nd CES cluster rejection: To reject photon pairs from π^0 decays as part of jets, the CES of the seed tower is searched for a 2nd-highest energy cluster. If one is found it is required to be less than 2.34 GeV, becoming less restrictive with higher photon E_T.

- CES ($\chi^2_{\mathrm{Strips}} + \chi^2_{\mathrm{Wires}}$): The lateral shower shape of the photon at shower maximum as measured in the CES strips and wires is compared to that from test beam data using a χ^2 test and typically required to be less than 20. As the previous requirement, it helps reject photon pairs from π^0 decays as part of jets.

The next section describes a new photon ID variable that is designed to reject PMT high voltage discharges. While this variable is not part of the standard photon ID criteria, a simple requirement is motivated that will be used to identify photons in this search. Then, each ID requirement is studied to see if it can be used unchanged for the search. The main concern is the unusual incident angle at the calorimeter of photons from heavy, long-lived particles (see Fig. 4a) as shown in Section III.C.

B. PMT Spikes

This section describes a new photon ID variable that is designed to reject against non-collision photon candidates. It is used in this search to identify photons in addition to the criteria shown in the previous section.

High-energy photon candidates can be caused by a high-voltage breakdowns ("spike") between the photocathode and the surrounding material (μ metal shield

and white paper wrapping on the lightguide-to-phototube transition piece) in one of the two PMTs in the tower. These events can be misidentified as photons if they overlap with a low-energy deposit from collision sources. Figure 14 shows the energy asymmetry of PMTs in a tower which is defined as

$$\mathrm{PA} = \frac{E_1 - E_2}{E_1 + E_2} \tag{3.1}$$

where E_1 and E_2 are the energies in PMT 1 and 2, respectively. The figure compares photons with an EM energy > 10 GeV that pass the identification requirements shown in Table III in events with $\not\!\!E_T > 30$ GeV and electrons from $W \to e\nu$ events that are required to pass the requirements described in App. B. It shows that PMT spikes cause a high PMT asymmetry and can be efficiently rejected by requiring $|\mathrm{PA}| < 0.6$. While most events with PMT spikes have a high asymmetry, their asymmetry magnitude is mainly less than 1. The reason is that a PMT spike can overlap with a soft particle from the collision that deposits energy in the same tower, e.g. a π^0. This causes most PMT spikes to have a measured time that is consistent with the collision, as shown in Fig. 15. The figure also confirms that these are non-collision events as the photon is in opposite direction of the $\not\!\!E_T$ and its $E_{_T}$ is of roughly the same magnitude. The PA requirement will be used to identify photons throughout the search in addition to the requirements described in the previous sections. As the rate of this background is small and as this requirement has a rejection power of $\sim$100% PMT spikes are neglected in the background estimate.

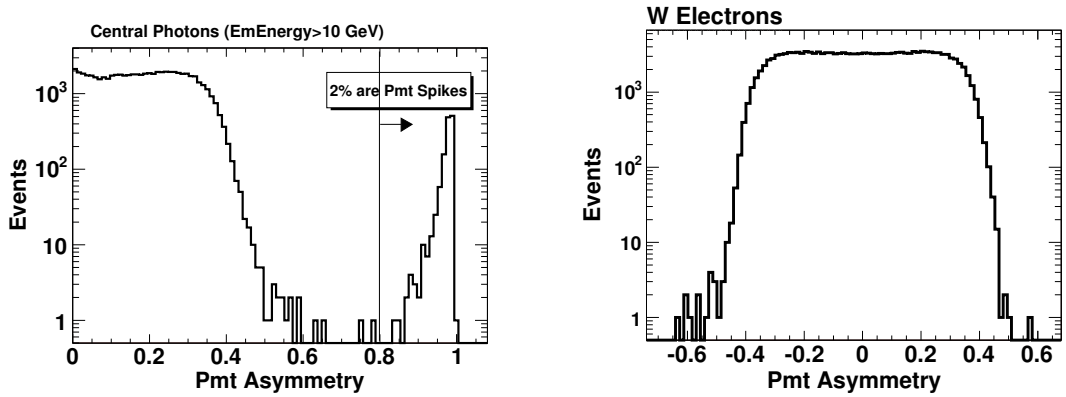

(a) (b)

Figure 14: The magnitude of the PMT asymmetry for a the full photon+$\not\!\!E_T$ sample that contains both PMT spikes and real photons in (a), and the asymmetry for electrons from pure $W \rightarrow e\nu$ events in (b). PMT spikes can be removed by requiring the asymmetry to be less than 0.6.

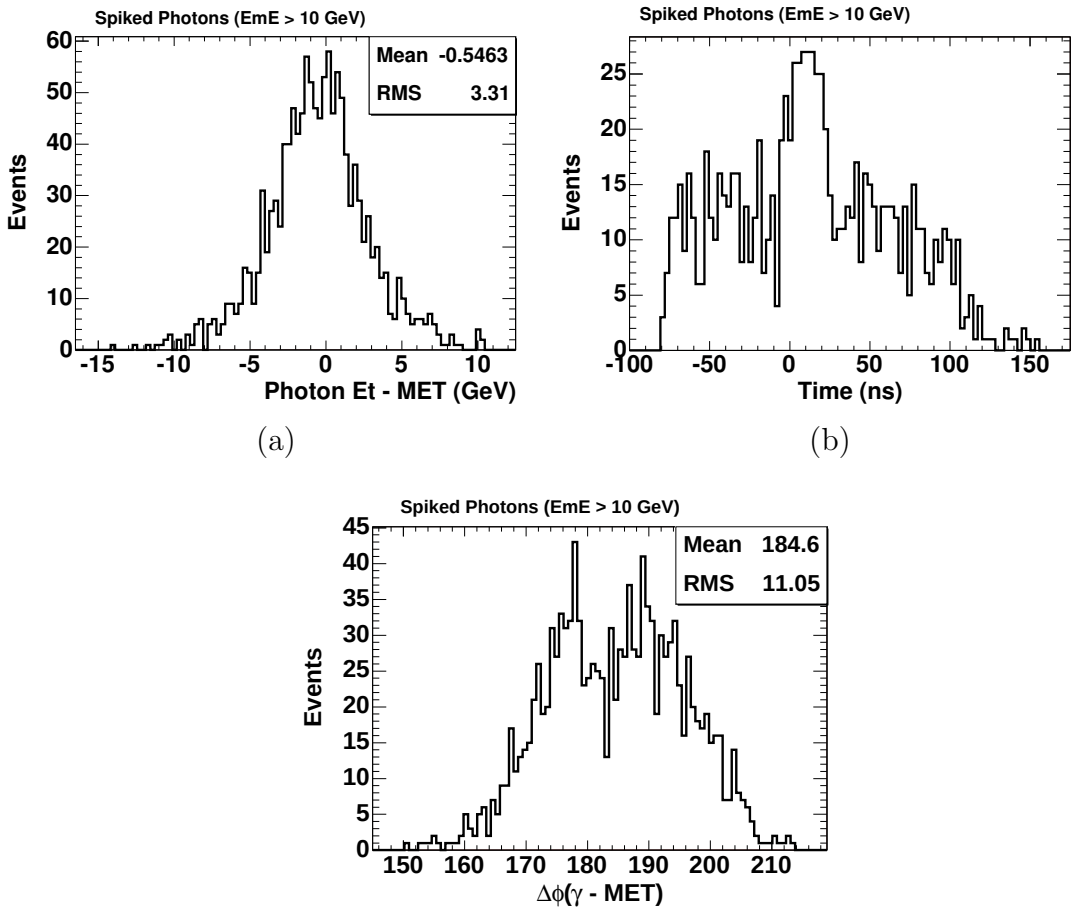

Figure 15: In (a) the difference between the $\not\!\!E_T$ and the E_T of the photon, in (b) its time distribution and in (c) the difference in ϕ between the photon and the $\not\!\!E_T$ in events with $|\mathrm{PA}| > 0.6$. PMT spikes are a non-collision source as they lie roughly opposite the $\not\!\!E_T$ and have roughly the same $\not\!\!E_T$. Most PMT spikes have a measured time consistent with the collision as they overlap with a soft particle.

C. Incident Angle Distribution of Photons from Heavy, Long-Lived Particles

Photons from heavy, long-lived particles can be produced far from the collision position. When they interact with the calorimeter they can have an incident angle much larger than photons from the collision position for which the standard ID variables were developed. In this section, the incident angles of a photon at the calorimeter are defined and the simulated distributions of photons from long-lived particles are compared to prompt photons directly emitted from the collision point.

The photon incident angle is defined as the angle between the momentum vector of the photon and the momentum vector a prompt photon would have if it came from the center of the detector, $z = 0$, and arrived at the same location at the front face of the calorimeter, as shown in Fig. 16. The projection of the incident angle onto the (r, ϕ)-plane is called β, its projection onto the (r, z)-plane α, where z is the axis along the beam. This distinction is made because, as shown later in detail, a change in α affects the ID efficiency of the CES strips subdetector while a change in β affects the efficiency in the CES wires subdetector (see Section II.B and Fig. 9 for a detailed description of the CES).

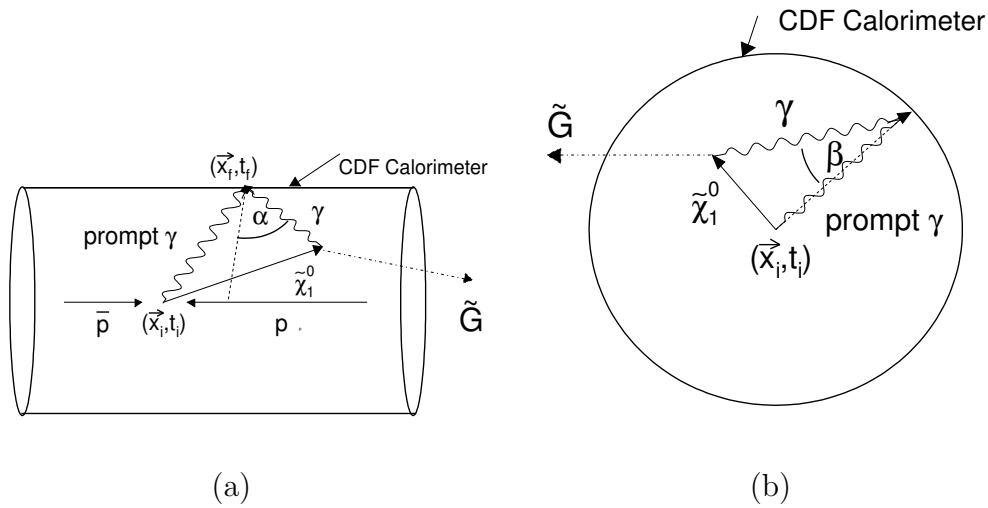

Figure 16: The definitions of the α and β incident angles using schematic diagrams of a long-lived $\widetilde{\chi}_1^0$ decaying to a photon and a $\widetilde{G}$ in the CDF detector in the (r,z)- and the (r,ϕ)-planes. The $\widetilde{\chi}_1^0$ emanates from the collision at $(\vec{x}_i, t_i)$ and after a time τ it decays. While the $\widetilde{G}$ leaves the detector the photon travels to the detector wall and deposits energy in the EM calorimeter where its final location $\vec{x}_f$ and arrival time t_f can be measured. A prompt photon would travel directly from $\vec{x}_i$ to $\vec{x}_f$. As the calorimeter towers point to the center of the detector ($\vec{x}_i = 0$) the incident angle of the photon is measured with respect to the dashed line that extends from the calorimeter tower where the photon hits, to the center of the detector; α and β are the incident angles at the front face of the calorimeter in the (r,z)- and the (r,ϕ)-plane respectively. The photon shower measurement in the CES strips is affected by changes in α, the measurement in the CES wires by changes in β. Note that for prompt production α can vary as the vertex position varies, but β is always $\ll 1°$.

Figure 17 compares the incident angle distribution for prompt, SM-like photons, simulated as decay products of $\widetilde{\chi}_1^0$'s with $m_{\widetilde{\chi}} = 110$ GeV/c^2 in the GMSB SPS 8 framework with $\tau_{\widetilde{\chi}} = 0$ ns, to photons from $\widetilde{\chi}_1^0$'s with $\tau_{\widetilde{\chi}} = 10$ ns. Also shown is the distribution for a photon after a requirement on its corrected arrival time ($t^{\gamma}_{\rm corr}$), measured with the EMTiming system, of $2 < t^{\gamma}_{\rm corr} < 10$ ns, similar to a typical final analysis requirement. (Both the MC simulation and the photon arrival time measurement are described in detail later in Section III.G.) The prompt distributions have a maximum at 0° and extend to ∼18° in α while β is 0 as the beam has negligible extent in the x-y plane. The incident angle α variation is due to the vertex position (z_0) variation within the requirement of $|z_0| < 60$ cm; the towers point to the center of the detector, so the angle extends out to ∼18° ≈ arctan(60 cm/183 cm) where 183 cm is the radius from the beamline to the CES.

The maximum of the $\alpha \oplus \beta$ GMSB distribution for a $\widetilde{\chi}_1^0$ lifetime of 10 ns is at around 10°, extending out to maximum angles of ∼60° and ∼40° in α and β respectively with a large fraction of photons arriving at angles between 0 and 40° total incident angle. The distribution is largely independent of $m_{\widetilde{\chi}}$ and $\tau_{\widetilde{\chi}}$ (tested for the range $90 < m_{\widetilde{\chi}} < 150$ GeV/c^2 and $10 < \tau_{\widetilde{\chi}} < 35$ ns). The photon arrival time requirement shifts the maximum of the distribution from ∼10° to ∼25°. As the incident angles of photons from long-lived particles are much larger than for prompt photons, the distributions and efficiencies of all the ID variables must be studied. The CES-χ^2 is considered separately in Section III.E as it is the variable most susceptible to incident angle variation and as it is not simulated correctly in the CDF MC.

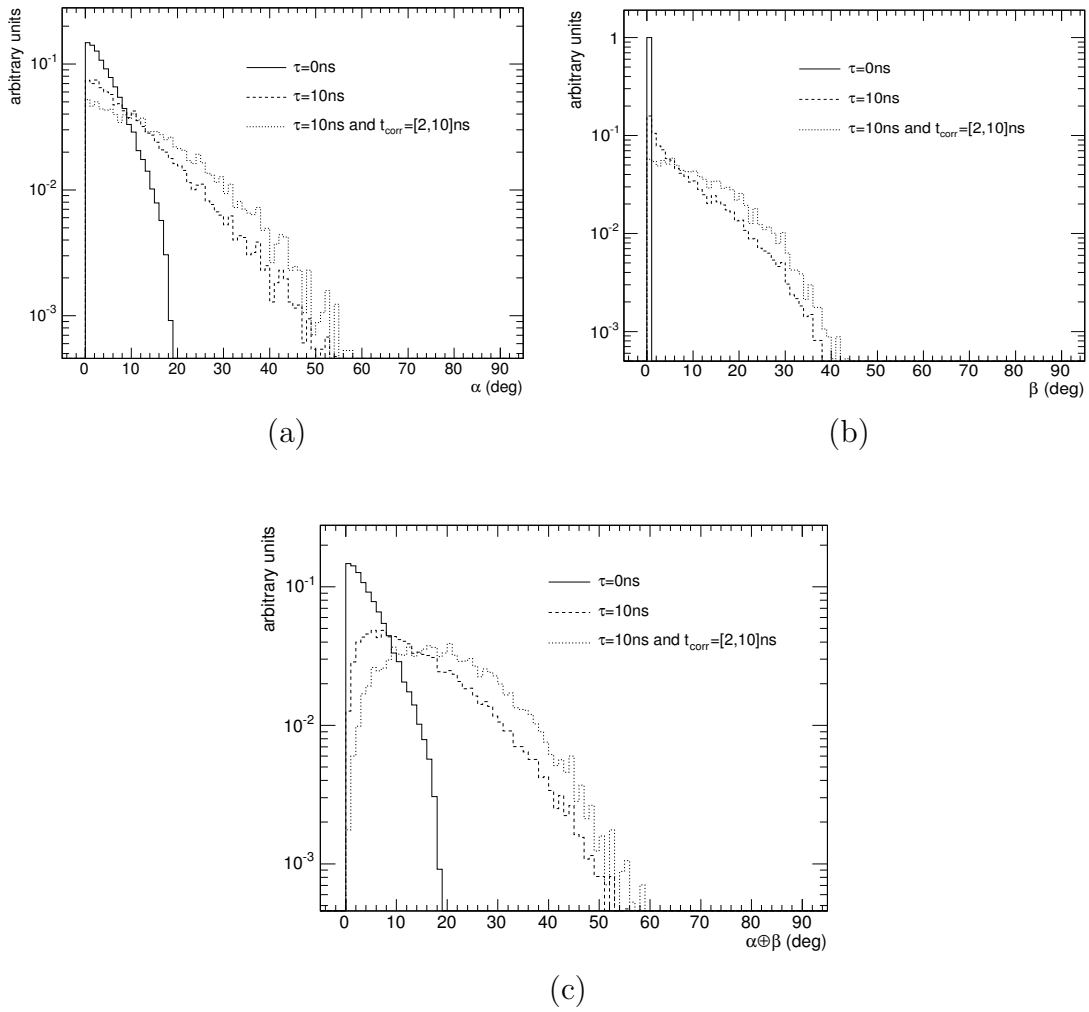

Figure 17: The distribution of the incident angles α and β and the total incident angle $\alpha \oplus \beta$ at the front face of the central calorimeter for simulated photons from $\widetilde{\chi}_1^0$'s in a GMSB model ($m_{\widetilde{\chi}} = 110$ GeV/c^2). "Prompt" photons from $\widetilde{\chi}_1^0$'s with a lifetime of 0 ns (solid) are compared to photons from $\widetilde{\chi}_1^0$'s with a lifetime 10 ns (dashed). The dotted histogram shows the distribution for a lifetime of 10 ns for photons with a $t_{\rm corr}$ between 2 and 10 ns. For α, while prompt photons have incident angles up to 20° with a maximum at 0° the distribution for photons from long-lived $\widetilde{\chi}_1^0$'s extends out to 60°, with a large fraction between 0° and 40°. For β the angle is always zero for prompt production, but can extend to 40° in the long-lived case.

D. Photon Identification Variable Distributions and Efficiencies

This section investigates the standard photon ID variable distributions and their efficiencies as a function of incident angles α and β using the MC simulation. To validate the simulation its distributions are compared to those from an electron sample from $W \rightarrow e\nu$ data as (1) it is easy to create a pure electron sample and (2) electrons shower in the calorimeter similarly to photons. The following data samples are created:

- Photons from heavy, long-lived GMSB $\widetilde{\chi}_1^0$'s are simulated using a MC sample with $m_{\widetilde{\chi}} = 110$ GeV/c^2 and $\tau_{\widetilde{\chi}} = 10$ ns. The highest E_T photon with $E_T > 30$ GeV is selected if it is the decay product of a $\widetilde{\chi}_1^0$ and if it passes the ID requirements shown in Table IV. Events with a jet within $\Delta R = 0.7$ of the photon are not considered, as a jet can deposit significant energy in the calorimeter within $\Delta R = 0.7$ of its center and can cause a bias in the photon isolation energy measurement.

- Prompt photons are simulated using a MC sample with exactly the same settings as above, but with $\tau_{\widetilde{\chi}} = 0$ ns.

- A data sample of electrons from $W \rightarrow e\nu$ events is collected with an integrated luminosity of 145.7 pb^{-1}. Electrons are required to pass the requirements listed in Table V.

- A MC sample of $W \rightarrow e\nu$ events where the electron passes the same requirements as the data sample above.

Figures 18 and 19 show the distributions of the photon ID variables using both MC GMSB samples. A visual comparison shows that the differences are, on average, very small. This is confirmed quantitatively in Table IV which summarizes the

Table IV: The cumulative number of simulated events after each ID requirement for the highest E_T photon in the event that comes from a $\widetilde{\chi}_1^0$. As the fiducial cuts do not help separating photons from the various backgrounds, these numbers are used to find the corresponding cumulative efficiencies after the fiducial cuts and the relative efficiencies ($N_{\text{pass this cut and all previous}}/N_{\text{pass all previous cuts}}$). The uncertainties are statistical only. As confirmed visually with the distributions in Figs. 18 and 19, there are only small differences between the samples.

Requirement	cumulative # of events		cumulative efficiency (%)		relative efficiency (%)	
	$\tau_{\widetilde{\chi}}$ =0 ns	$\tau_{\widetilde{\chi}}$ =10 ns	$\tau_{\widetilde{\chi}}$ =0 ns	$\tau_{\widetilde{\chi}}$ =10 ns	$\tau_{\widetilde{\chi}}$ =0 ns	$\tau_{\widetilde{\chi}}$ =10 ns
Central ($\lvert\eta\rvert < 1.1$)	101179	90813				
$E_T > 30$ GeV	81730	69788				
Fiducial: $\lvert X_{\text{CES}}\rvert < 21$ cm and 9 cm $< \lvert Z_{CES}\rvert < 230$ cm	64997	44632				
$\frac{E_{\text{Had}}}{E_{\text{Em}}} < 0.125$	64499	44115	99.23±0.03	98.84±0.05	99.23±0.03	98.84±0.05
$E^{\text{iso}}_{0.4\text{ cone}} < 2.0 + 0.02 \cdot (E_T - 20)$	63171	42554	97.19±0.06	95.34±0.10	97.94±0.06	96.46±0.09
$N_{\text{trks}} = 0$ or if $N_{\text{trks}} = 1$ then $p_T < 1.0 + 0.005 \cdot E_T$	61629	41963	94.82±0.09	94.02±0.11	97.56±0.06	98.61±0.06
Σp_T of tracks in a 0.4 cone $< 2.0 + 0.005 \cdot E_T$	60820	41392	93.57±0.10	92.74±0.12	98.69±0.05	98.64±0.06
$E^{\text{cluster}}_{\text{2nd strip or wire}} < 2.4 + 0.01 \cdot E_T$	60718	41333	93.42±0.10	92.61±0.12	99.83±0.02	99.86±0.02

Table V: The sample requirements to select electrons from $W \to e\nu$ events to validate the ID efficiency of simulated photons as a function of α and β. For more detail on the standard electron requirements see App. B. These are slightly different from the requirements shown in the sense that topological and global event cuts in combination with loose calorimetry but tight track quality requirements are used. These produce a sample that contains electrons with (1) high purity but (2) a low bias for calculating the efficiency of photon cuts vs. incident angle. The vertex reconstruction algorithm is described in Section III.F and uses tracks passing the requirements listed in Table VI.

CEM Electron
$E_T > 30$ GeV
Fiducial: $\lvert X_{\rm CES}\rvert < 21$ cm and 9 cm $< \lvert Z_{\rm CES}\rvert < 230$ cm
$p_T > 50$ GeV or $0.9 < \dfrac{E}{p} < 1.1$
Track traverses $\geq$3 stereo and $\geq$3 axial COT superlayers with 5 hits each
Additional requirements to reject electrons from $\gamma \to ee$
Global Event Cuts
$\not\!\!E_T$ >30 GeV
Exactly 1 vertex with $N_{\rm trks} \geq 4$ and $\lvert z\rvert < 60$ cm
Transverse mass of the electron and $\not\!\!E_T$: $50 < m_T < 120$ GeV

relative efficiencies ($N_{\text{pass this cut and all previous}}/N_{\text{pass all previous cuts}}$) and cumulative efficiencies ($N_{\text{pass this cut and all previous}}/N_{\text{pass fiducial}}$) where $N_{\text{pass fiducial}}$ denotes the number of events with a photon that is in the fiducial part of the CES which ensures that the ID criteria can be reliably applied. The ID criteria are ∼1.5% less efficient for a lifetime of 10 ns than for prompt, dominated by the difference in the isolation distribution. While this number is typical for comparisons between data and MC and it is taken as a systematic uncertainty on the photon efficiency. Note that this uncertainty is small compared to the other uncertainties on the overall GMSB acceptance in Section VI.B. While the ID requirements show slight inefficiencies at large incident angles ($> 50°$), only very few events are produced there.

Figures 20, 21, 22 and 23 show the relative efficiency of each ID variable as a function of incident angles α and β along with the results from the electron sample [64]. The efficiencies at low incident angles are similar for electrons from the $W \to e\nu$ data sample and the MC photons from long-lived particles for all ID variables. For large angles, where real data is not available, all the ID variable efficiencies are roughly flat as a function of α and β, except the energy isolation which falls slightly in β from ∼98% to ∼90% at 50° accounting for the small difference noted above. This small drop is caused at large incident angles where the photon shower traverses into the wedge or tower neighboring the seed tower. While the neighboring tower energy (in η) is used in the cluster energy sum, the neighboring wedge is used in the energy isolation calculation and makes the photon appear non-isolated. This causes the total efficiency as a function of incident angle to fall from ∼94% to ∼80% (see Fig. 20) at angles $> 50°$. Since the simulation appears to reproduce the data well and no requirement is overly inefficient with the exception of the energy isolation at very large angles which is well understood, all the requirements can be left unchanged for the search. The variation of the efficiency as a function of angle is taken into account by

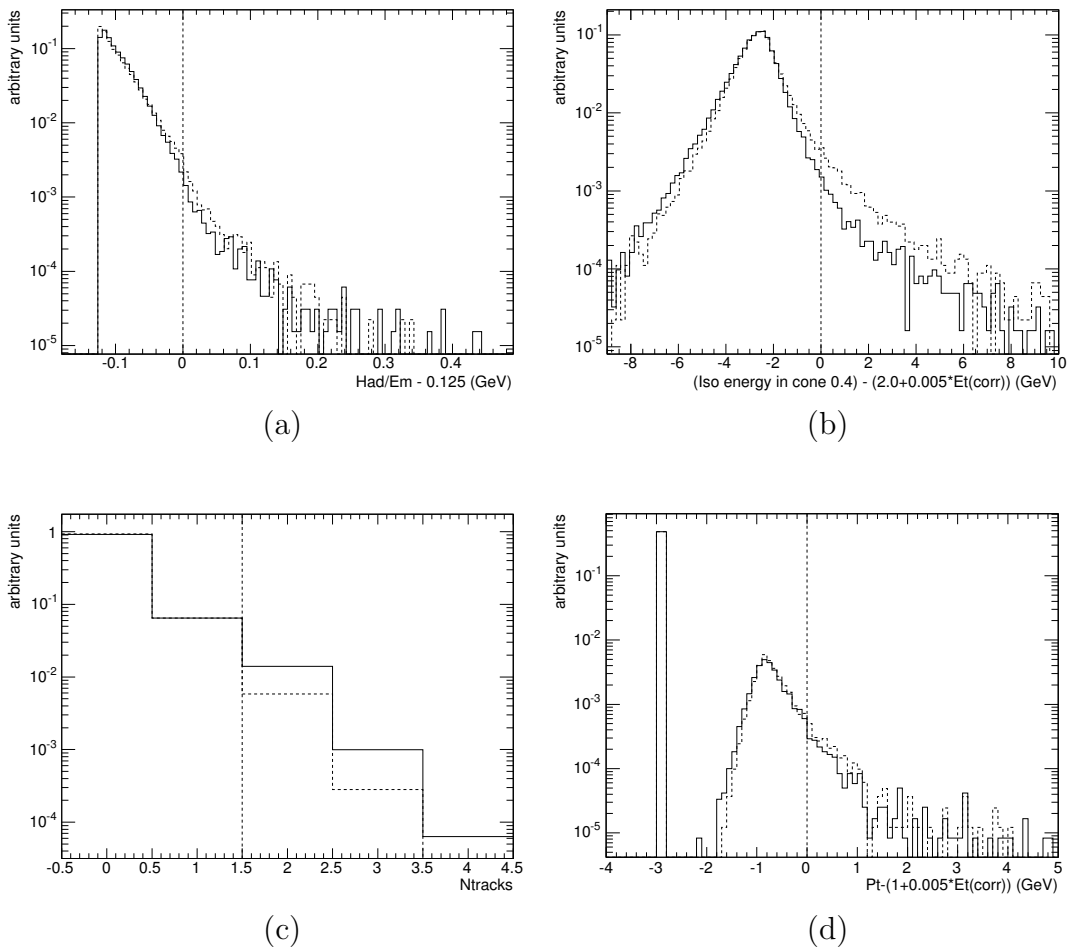

Figure 18: The ID variable distributions for photons in a GMSB model with $m_{\widetilde{\chi}} = 110$ GeV/c^2 produced with the CDF MC, normalized to 1. The plots compare the distributions of prompt photons, simulated as decay photons from $\widetilde{\chi}_1^0$'s with a lifetime of 0 ns (solid) to photons from long-lived $\widetilde{\chi}_1^0$'s with a lifetime of 10 ns (dashed). A value of <0 means that it passes the corresponding cut. The bin left of the distributions in Fig. (d) collects the photons that have no track associated. The distributions for all ID variables do not change significantly between the prompt and the long-lived case except for slight deviations in the energy isolation in Fig. (b).

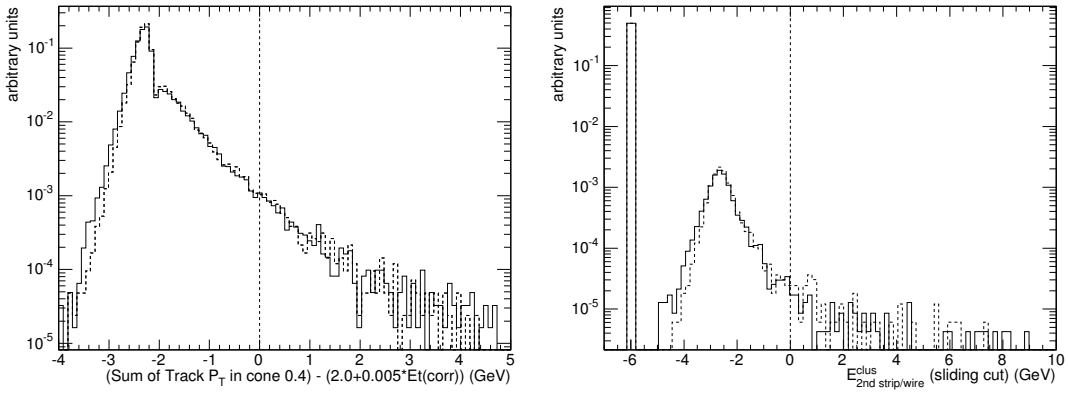

(a) (b)

Figure 19: A continuation of Fig. 18 for the remaining photon ID variables in Table IV. The bin left of the distributions in Fig. (b) it shows the photons that have no 2nd cluster.

assigning a 5% systematic uncertainty to the overall ID efficiency for any simulated GMSB point. While the simulation of the ID variables is well understood and can be used to estimate efficiencies at large incident angles, the CES-χ^2 requirement is believed not to be simulated correctly in the CDF MC and is discussed in the next section.

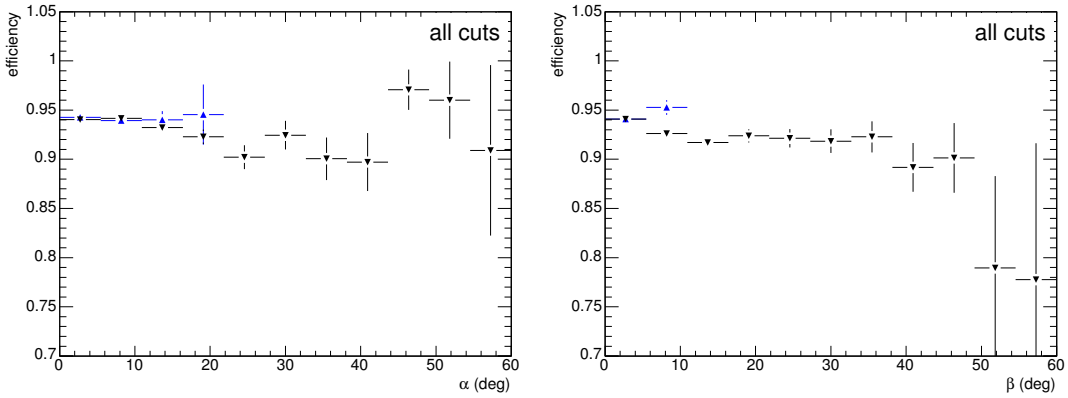

(a) (b)

Figure 20: The total efficiencies for the standard photon ID requirements (except for the CES-χ^2) for photons in the fiducial portion of the CEM vs. incident angles α and β. The efficiencies from MC using photons in a GMSB model ($m_{\widetilde{\chi}} = 110$ GeV/c^2, $\tau_{\widetilde{\chi}} = 10$ ns) (black) are compared to the efficiencies obtained from data using electrons from a $W \rightarrow e\nu$ sample that pass the loose requirements in Table V (blue). The efficiency falls slightly by ∼15% from 0 to 60° in β, which mainly comes from the energy isolation as discussed in the text. Figures 21, 22 and 23 show the efficiencies for each requirement separately.

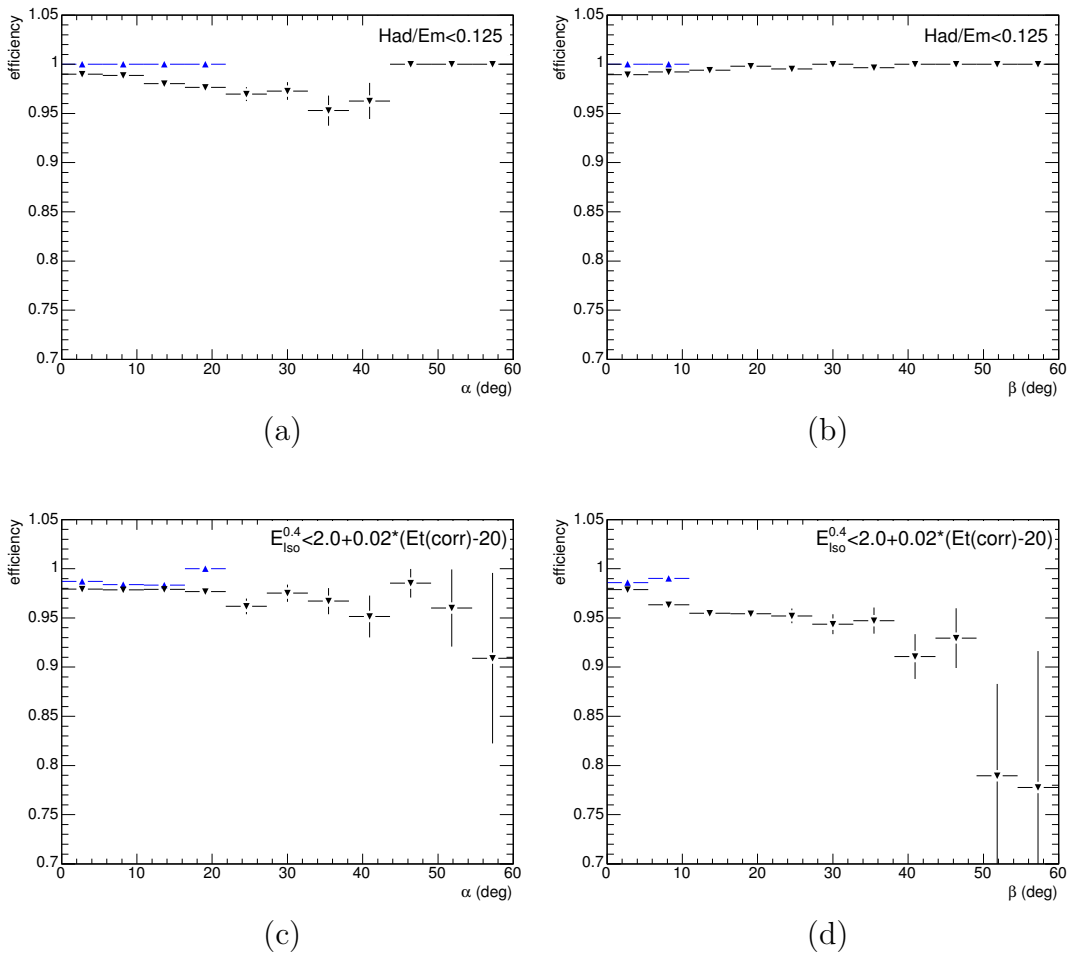

Figure 21: The relative efficiencies for each ID variable separately, using the order of the cuts in Table IV. The photon MC (reversed triangles) and the electron data sample (upright triangles) generally match well in all shown ID variables in the range for which data is available and are roughly flat except the energy isolation in β (see Fig. (c) and (d)).

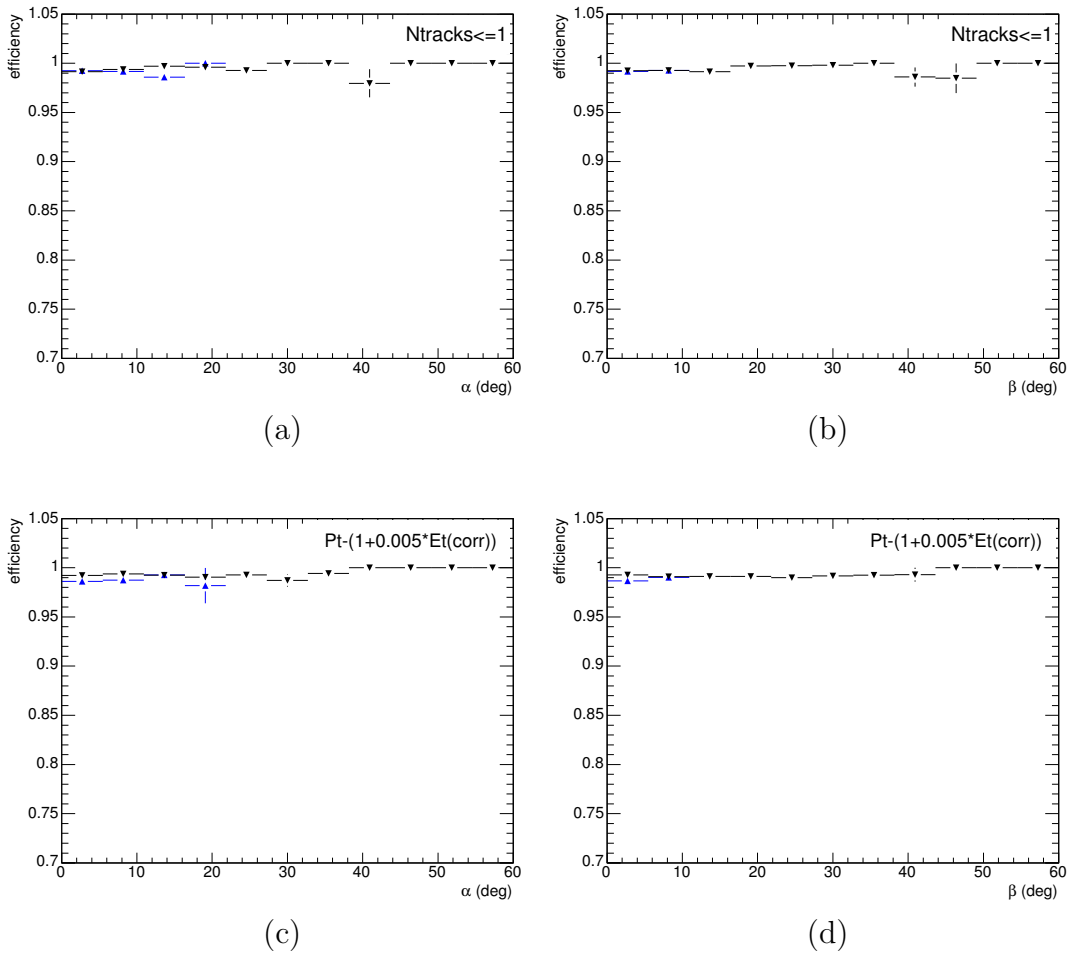

Figure 22: A continuation of Fig. 21 for the remaining photon ID variables in Table IV.

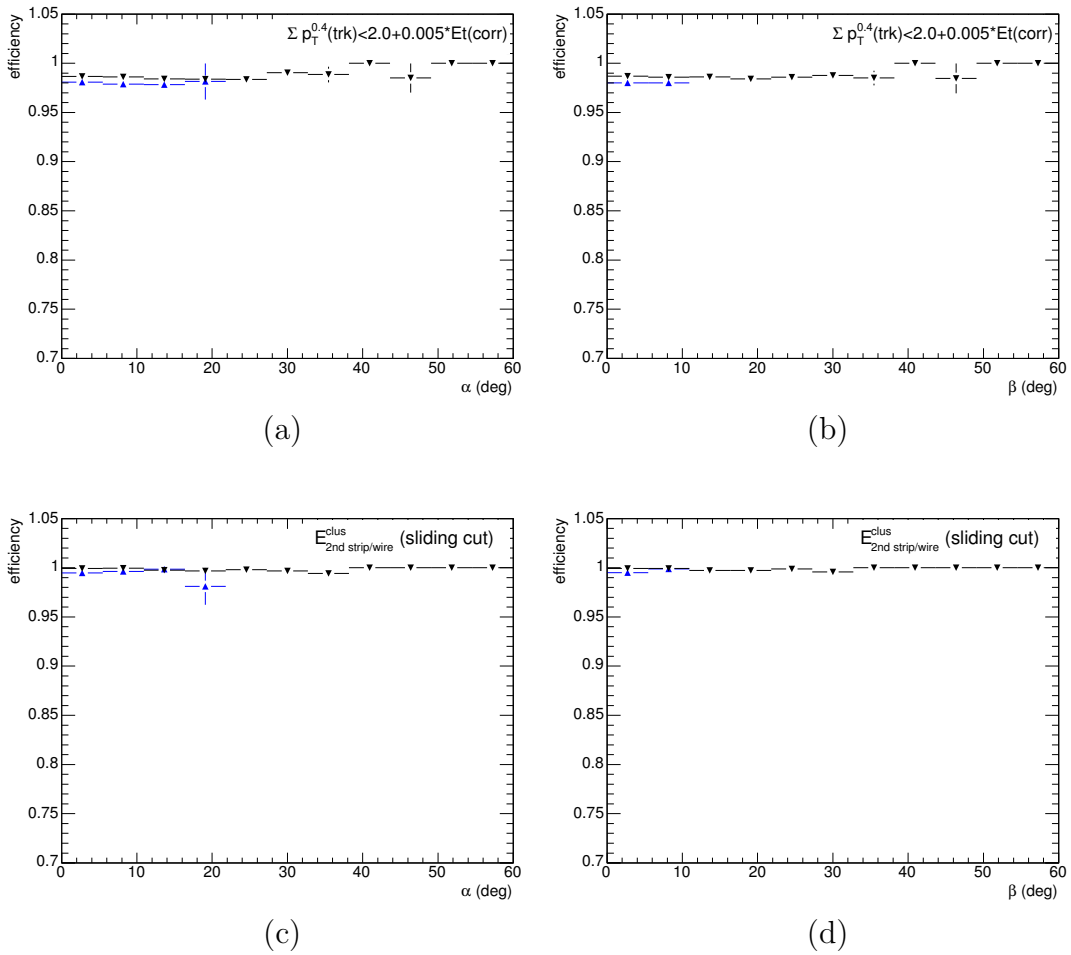

Figure 23: A continuation of Fig. 21 and 22 for the remaining photon ID variables in Table IV.

E. The Quality of the Transverse Shower Profile in the CES

Since the standard CDF MC (called "cdfSim" in the figures) does not correctly simulate the CES-χ^2 distribution this section discusses a full GEANT [65] simulation of the calorimeter (Geant 3 Wedge Simulation, "G3WS") [66] and its predictions for the requirements efficiency. The CDF MC simulates the CES to particles as follows: it extrapolates the trajectory of the particles from the radius at the solenoid to the CES. Then it picks the transverse shower shape from a template that was produced from test beam data based on its z and ϕ position at the CES, independent of its incident angle. Hence, while the position of the CES cluster is realistic, which is important for the 2nd CES cluster-E_T ID requirement, the shape of the shower in the CES is not reliable for particles with displaced vertices and large incident angles at the calorimeter. In contrast, G3WS produces the CES shower measurement based on a full calorimeter shower simulation [67]. An energy-corrected χ^2 is calculated by comparing the shower profile in 11 strips and 11 wires, centered around the strip and wire with the highest energy deposit, to expectations from test beam data. Figure 24 compares the normalized CES-χ^2 distributions using G3WS for 50 GeV photons, that enter into a fixed tower in the CEM (wedge 0, tower 1) from a fixed vertex, and the CES-χ^2 distribution from prompt photons in the CDF MC. While G3WS is expected to simulate the effects of the shower correctly as a function of incident angle correctly, it shows a significant discrepancy at low incident angles where both should match, an effect that is not properly understood [68]. Thus, we expect G3WS to underestimate the χ^2 requirement efficiency.

Figure 25 compares the normalized χ^2 distributions from G3WS at different incident angles. The shower for a particle that hits the CES at a large α (β) angle should appear spread out in z (ϕ) direction due to the projection whereas the shower

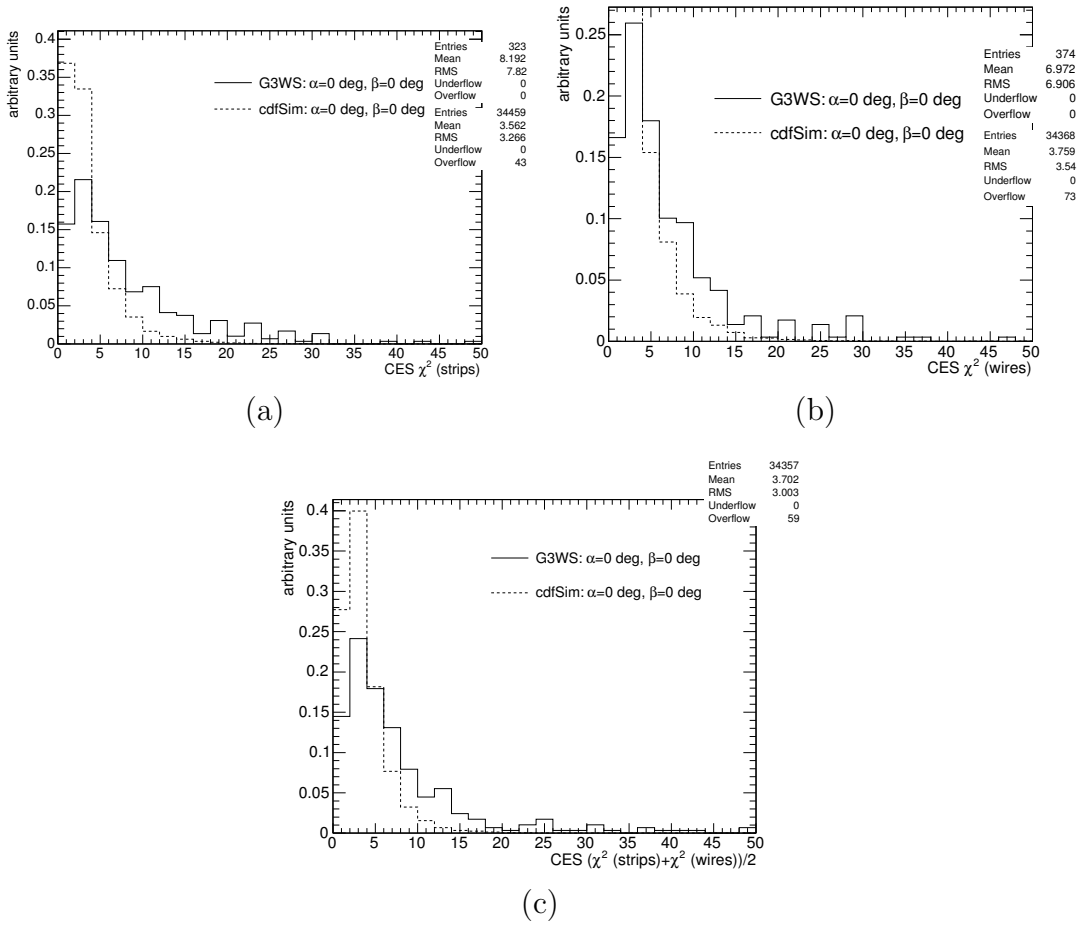

Figure 24: A comparison of the CES-χ^2 distributions for a photon of energy 50 GeV that propagates from a fixed vertex into a fixed tower in the CEM (wedge 0, tower 1) at 0° incident angle, simulated with G3WS, and the distribution from the CDF MC separately for strips (a), wires (b) and combined (c). If simulated correctly, both should yield the same distributions, however, there is clearly a mismatch, in particular in the strips. This leads to an overestimate of the combined χ^2 and to an underestimate of the χ^2 efficiency for G3WS.

projection in ϕ (z) should remain unaffected, causing only the strips-χ^2 (wires-χ^2) to get large. This is seen in Fig. 25 for a variation in α from 0 to 50° (a and b) and a variation in β between 0 and 60° (c and d). The individual changes in strips and wires propagate to the total χ^2 in Fig. 25e and f.

Figure 26 shows the CES-χ^2 efficiency for the standard photon ID cut $(\chi^2_{\text{Strips}} + \chi^2_{\text{Wires}})/2 < 20$ as a function of α and β of photons from the CDF MC, G3WS and of electrons from the CDF MC and data. The following can be observed: Within the range of incident angle variation from the vertex variation, as explained in Section III.D, both the electron data sample and the electron MC sample show no angle dependence. Their efficiencies match well within error which gives confidence in the CDF MC results. The CDF MC sample with photons from $\widetilde{\chi}_1^0$'s with $\tau_{\widetilde{\chi}} = 10$ ns shows a constant average efficiency that extends out to ∼50°. This is because the shower shape is not accurately simulated. The G3WS distribution shows that the CES-χ^2 efficiency of photons of energy 50 GeV is constant at low angles, but then falls off rapidly at high angles as expected. Using a fit with an error function, the average efficiency at low incident angles is found to be only $(90.6 \pm 0.8)\%$ for α and $(89.7 \pm 0.7)\%$ for β (from the fit). The same fit finds threshold values at 58° and 63° for α and β respectively. While the statistical uncertainty on this fit is small, there is unfortunately no good way of estimating the systematic uncertainties on the threshold. And since the distributions in Figure 24 appear to overestimate the width of the χ^2 distribution, there is good reason to believe that the threshold values are probably higher than those observed.

In Figure 27 the possibility of loosening the CES-χ^2 requirement is investigated to gain back efficiency or to make the efficiency flat as a function of α and β. For any CES-χ^2 cut a drop in efficiency is observed at a finite angle, so that it is not expected to approach the cut efficiency of prompt photons even if the cut is relaxed.

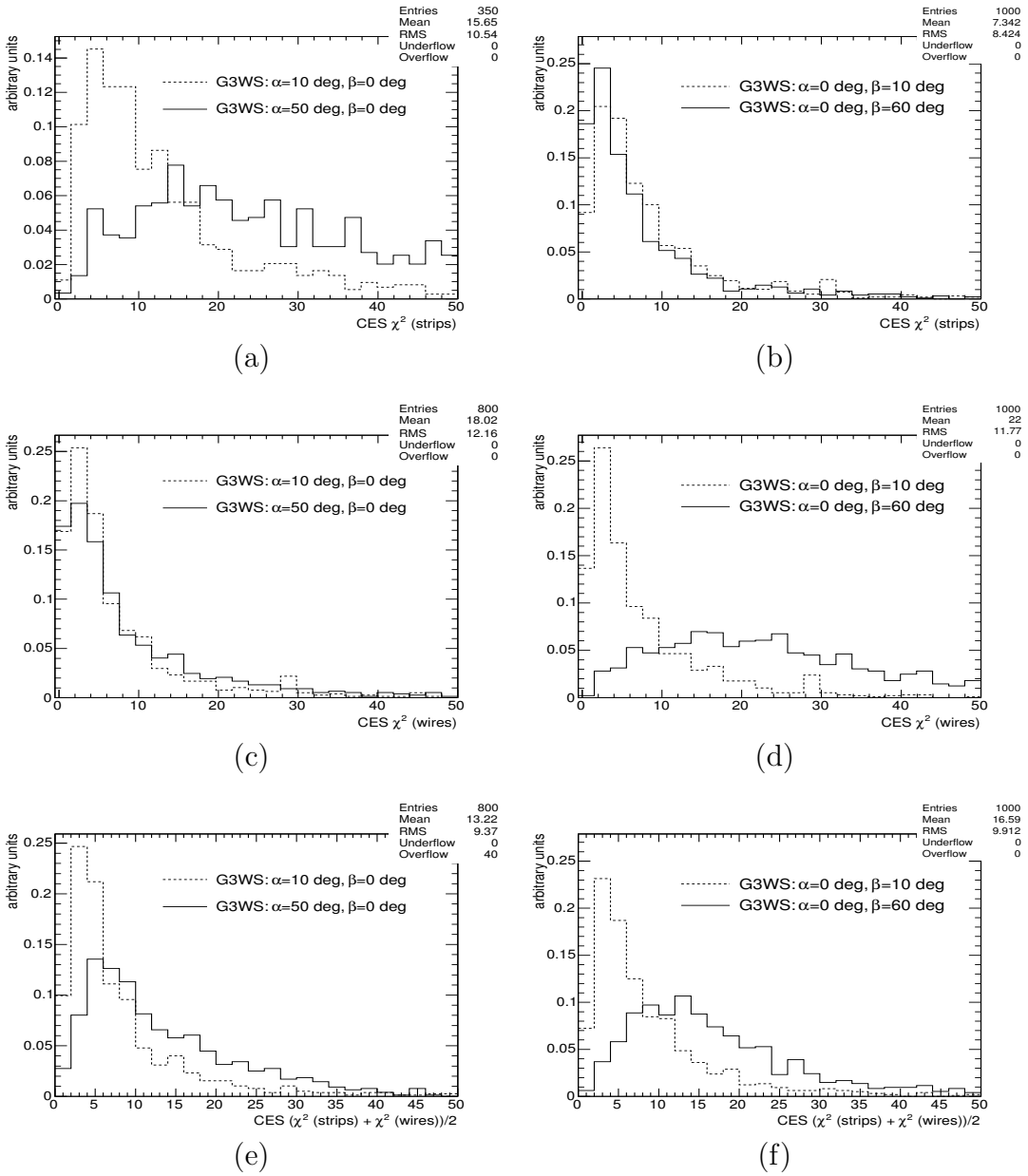

Figure 25: The CES-χ^2 distributions for photons simulated with G3WS with the same settings as in Fig. 24, but at different incident angles. The figures in the left column show the distributions in the strips, wires and combined for incident angles of $\alpha = 10°$ (solid) and $\alpha = 50°$ (dashed), with $\beta = 0°$; the figures in the right column for $\beta = 10°$ (solid) to $\beta = 60°$ (dashed), with $\alpha = 0°$. As expected a change of α affects the strips only, a change in β only the wires. Figures (e) and (f) show that the individual effects propagate to the combined CES-χ^2 distribution.

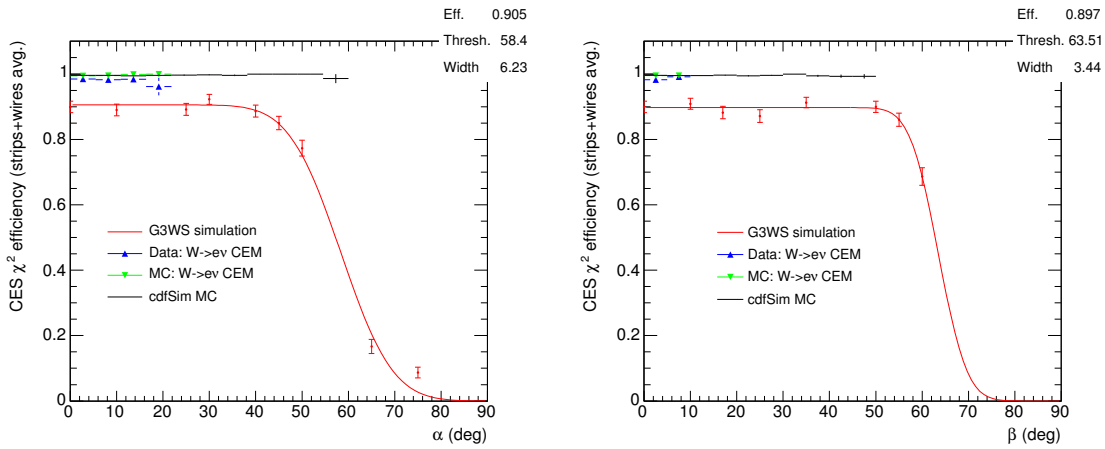

(a) (b)

Figure 26: A comparison of the CES-χ^2 efficiency as a function of incident angles α and β. Separately shown are the results for a $W \rightarrow e\nu$ data sample (blue, upright triangles), a $W \rightarrow e\nu$ CDF MC sample (green, inverted triangles) and a GMSB MC sample simulated with the CDF MC (black), and the efficiency simulated with G3WS, with vertical error bars indicating the statistical uncertainty. G3WS, which simulates the angle-dependence of the shower in the CES, shows that the efficiency drops rapidly beyond $\sim$40° for α and $\sim$50° for β respectively. While the drop is expected, its location is not clearly understood as there is evidence that the G3WS does not accurately simulate the χ^2 distribution. Also shown is a fit to the G3WS points using an error function, with the fit parameters in the upper right box.

To summarize, an efficiency loss at high incident angles is confirmed in the simulation and appears to be a sharp fall-off.

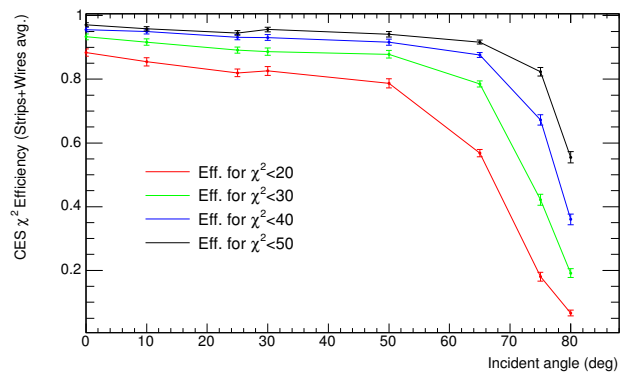

Figure 27: A comparison of the CES-χ^2 efficiency as a function of incident angle between several χ^2 cuts of 20, 30, 40 and 50, simulated with G3WS. For any cut the efficiency curve turns over at an angle of $\lesssim 70°$.

While the CDF MC and the G3WS simulation disagree in their calculation of the CES-χ^2, the G3WS, which fully simulates the CES shower shape, shows the expected efficiency drop at large incident angles. Thus, the photon CES-χ^2 requirement is removed for robustness reasons. This has the further advantages that it no longer produces a loss in efficiency, that a separate CES simulation is not needed to calculate its efficiency and that there is a negligible mass and lifetime dependent systematic uncertainty. The primary drawback is that doing so increases the background in searches for new physics. However, the impact of this depends critically on the final form of the analysis; it is less of a problem for searches with high-E_T photons as the backgrounds are dominated by:

- photon production in QCD processes with misreconstructed $\not\!\!E_T$. As this background contains real photons this requirement has no rejection power.

- electrons without a reconstructed track. In this case the requirement has no

rejection power as electron and photon shower shapes are similar.

- jets that are misreconstructed as photons due to $\pi^0 \to \gamma\gamma$ decays. In this case the requirement provides only little rejection at high E_T as the two photons are highly boosted and mostly appear as a single shower in the CES.

Thus, the primary rejection is against cosmic ray and beam halo sources. If, after all event requirements, these are not a major background then the requirement can be removed. This is the case in this search, as will be shown in Chapter VII.

F. Measurement of the Collision Time and Position

This section describes a space-time vertex reconstruction using COT tracks. It has been developed to measure the time at which the collision occurs and the photon time-of-flight. Along with the photon arrival time as measured by the EMTiming system, this allows for a calculation of t_{corr} as defined in Eq. 1.3 with a resolution of 0.65 ns for a correctly assigned vertex (see Section III.G), which is a powerful discrimination variable between photons from long-lived particles and other photon sources. A misreconstructed or misassigned vertex leads to an increase of the RMS of t_{corr} on the order of the interaction time variation of 1.3 ns as shown in Fig. 28a.

While existing vertexing algorithms [69] can reconstruct the vertex position (z_0), necessary to calculate the photon E_T and track isolation ID variables, it is important for a proper t_{corr} estimate to separate the photon vertex from another vertex that lies close in space but happens at a different time (t_0). This is a significant problem at high instantaneous luminosities where two or more collisions can occur in one event and can lie close to each other in position and/or time. Misassigned vertex events are a dominant contribution to the background estimate in the signal region as will be discussed in detail in Section V.A.

This section begins with a discussion of the new vertexing algorithm and its performance. Then it describes the efficiency for finding an accurately reconstructed vertex and parameterizes it as a function of the number and the Σp_{T} of the tracks used in its construction. Finally, as an application, the correlation between the collision time and position are measured. Note that throughout this section a "vertex" refers to the true underlying collision, whereas the term "cluster" refers to the clustered set of tracks that constitute the reconstructed vertex. Each track is required to pass the requirements listed in Table VI designed to remove potentially problematic tracks from the vertexing. They are the standard CDF requirements for COT tracks [70] described in detail in App. C, but with additional timing quality requirements, e.g., on the $\frac{\mathrm{d}E}{\mathrm{d}x}$ to reject slow protons that likely have a mismeasured t_0.

Table VI: The set of requirements for tracks to be included in the vertex reconstruction. These are the standard track requirements [70], described in App. C, but with additional quality requirements on the t_0 measurement and on the $\frac{\mathrm{d}E}{\mathrm{d}x}$ of positively charged tracks to reject slow protons that likely have a mismeasured track t_0.

$p_T > 0.3$ GeV/c
$p_T > 1.4$ GeV/c or $\frac{\mathrm{d}E}{\mathrm{d}x} < 20$ keV/cm, only if charge> 0
$\lvert\eta\rvert < 1.6$
$\lvert z_0\rvert < 70$ cm
$\mathrm{Err}(z_0) < 1$ cm
$\lvert t_0\rvert < 40$ ns
$0.05 < \mathrm{Err}(t_0) < 0.8$ ns
Traverses $\geq$3 stereo and $\geq$3 axial COT superlayers with 5 hits each

1. *Track Clustering Procedure*

The clustering procedure identifies a set of tracks that are close to each other in both space and time. The algorithm can be separated into three ideas: (1) the identification of a set of tracks and their assignment to proto-clusters, (2) the determination of the best-fit values for the cluster parameters using an expectation maximization (EMAX) technique [71], and (3) the adjustment of the number of clusters by merging and splitting clusters that are close to each other.

The clustering begins with a simple algorithm that assigns tracks to a cluster: The highest-p_T track becomes the "seed" of a cluster, and any lower-p_T tracks are assigned to it if they lie within three times the expected RMS of the cluster, *a priori* defined to be 0.6 ns and 1.0 cm for t_0 and z_0, respectively. The highest-p_T track from the remaining set of tracks is then picked as a second seed and tracks are assigned to it, and so forth until no tracks are left.

After all clusters are defined the parameters of each cluster are calculated using the EMAX procedure. It is based on the assumptions that (a) each track has a finite probability to be a member of a vertex and (b) the track density in a vertex is described by a Gaussian shape. The EMAX procedure begins by computing the total probability density function (PDF) of all tracks with coordinates $x = (t_0, z_0)$ to belong to the cluster to which they were assigned. Each cluster is described by a Gaussian PDF with an assumed mean position and time $\mu = (\mu_t, \mu_z)$ and a 2x2 covariance matrix M:

$$\mathrm{PDF} = \frac{1}{(2\pi)||M||^{1/2}} \exp\left\{-\frac{1}{2}(x-\mu)^T M^{-1}(x-\mu)\right\} \tag{3.2}$$

where $(x-\mu)^T$ denotes the transposed vector $(x-\mu)$. Each cluster is also assigned a weight w according to the number of tracks assigned to it. To summarize, the i-th

cluster is described by the variables $\lambda_i = (\vec{\mu}_i, \vec{M}_i, \vec{w}_i)$.

An iterative procedure then varies the parameters of all clusters simultaneously at each iteration step n, such that it maximizes the probability that all tracks belong to a set of clusters with parameters, equivalent to a likelihood fit. The expected probability for the k-th track at position x_k to originate from the i-th cluster at step n is represented by:

$$P(x_k|\lambda_{i,n}) = \frac{P(x_k|\mu_{i,n}, M_{i,n})w_{i,n}}{\sum_{j=1}^{N} P(x_k|\mu_{j,n}, M_{j,n})w_{j,n}} \tag{3.3}$$

where $P(x_k|\mu_{i,n}, M_{i,n})$ is the PDF for the k-th track in vertex i shown in equation 3.2 and N is the total number of clusters. At the next step the parameters $\lambda_{i,n}$ are adjusted by re-calculating them from the coordinates of each track and the cluster parameters from the current iteration step as follows:

$$\mu_{i,n+1} = \frac{\sum_k P(x_k|\mu_{i,n}, M_{i,n})x_k}{\sum_k P(x_k|\mu_{i,n}, M_{i,n})}$$
$$M_{i,n+1} = \frac{\sum_k P(x_k|\mu_{i,n}, M_{i,n})[x_k - \mu_{i,n+1}][x_k - \mu_{i,n+1}]^T}{\sum_k P(x_k|\mu_{i,n}, M_{i,n})}$$
$$w_{i,n+1} = \frac{\sum_k P(x_k|\mu_{i,n}, M_{i,n})}{N}$$

where i runs over all clusters, k over the tracks and n is the iteration number. The iteration procedure stops when the parameters change by less than one percent.

If, during the EMAX procedure, the means of two clusters are within both 3 cm in z and 1.8 ns in t or two clusters share the same set of tracks, then the clusters are merged. In this case one cluster gets killed and the clustering starts over again with the $n = 1$ state. The algorithm does not implement a splitting procedure for two reasons: (a) the initial seeding described above is designed to likely overestimate the number of clusters and (b) splitting a cluster, e.g. based in a too large RMS, can result in two clusters that both do not pass the final requirements and would reduce

the clustering efficiency. Having two clusters merged that are close in both space and time does not affect the time correction much, as described in Section III.G. For the analysis the resulting parameters of the cluster with the highest Σp_{T} of associated tracks is used as the primary vertex. The final event selection will require this vertex to have a $\Sigma p_{\mathrm{T}} > 15$ GeV/c and at least 4 tracks ("good vertex").

2. Vertexing Performance

In this section the cluster resolution and the reconstruction efficiency are measured using an inclusive $W \to e\nu$ data sample, corresponding to an integrated luminosity of 370 pb^{-1}. This sample is chosen both because (a) the electron track can be used to measure the vertexing performance as it identifies the correct event vertex and (b) the electron t_{corr} distribution is expected to look similar to photons as both interact similarly in the calorimeter. To reduce measurement bias and to increase the statistics, events are only required to contain an electron that passes the loose selection criteria described in App. B. In order to properly measure the performance for events with photons this study removes the electron track from the vertexing and, as in the search, the primary vertex is chosen to be the highest Σp_{T} cluster that has at least 4 tracks.

Figure 28 shows the reconstructed cluster distributions for the sample in z and t. Both are Gaussian and centered at zero with an RMS of 25 cm and 1.28 ns, respectively. The falloff in Fig. 28b at $|z| \simeq 70$ cm is due to the requirement that all tracks have $|z| < 70$ cm to be well measured (see Table VI). Note that in the search the vertex will be required to have $|z| < 60$ cm. There is a non-Gaussian excess around zero that comes from events that contain more than one vertex. In this case the clustering has merged two vertices that are close to each other, which most likely happens at $z = 0$ cm as will be shown below.

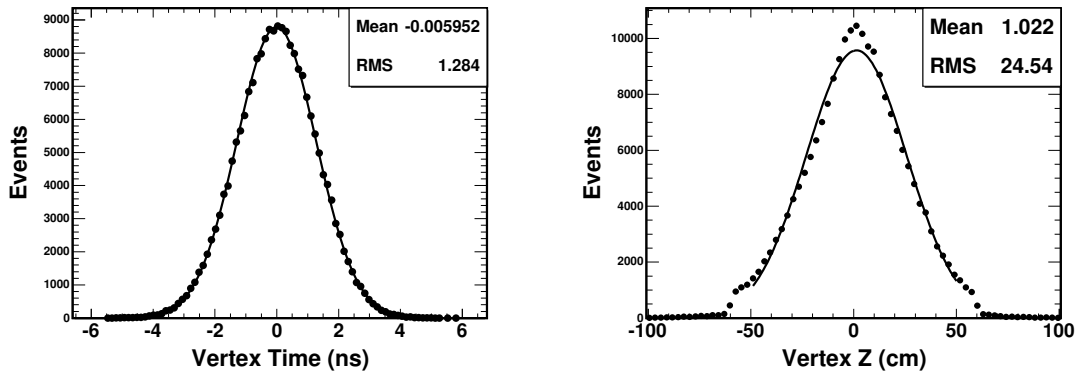

(a) (b)

Figure 28: The t_0 and z_0 of the reconstructed highest Σp_{T} vertex in $W \to e\nu$ events without allowing the electron track to participate in the vertexing. The collision distribution in t has an RMS of 1.28 ns, in z an RMS of 25 cm. The non-Gaussian excess at $z = 0$ cm comes from cases in which two vertices that lie close to each other and have been merged. The falloff at $|z| \simeq 70$ cm is due to the requirement that all tracks have $|z| < 70$ cm to be well measured.

The vertexing resolution as measured by the algorithm is estimated by using a sample of events with only one reconstructed vertex. For each event the tracks in the vertex are randomly divided into two random groups, and then separately put through the vertexing algorithm. Figure 29 shows the distance between the two clusters, divided by $\sqrt{2}$ to take into account the two measurements, which is equivalent to the uncertainty on the mean z and t of each vertex. The secondary Gaussian in Fig. 29b indicates cases where two different vertices have been combined into one cluster and is discussed further below. Also shown is the t_0 difference divided by the resolution reported by the cluster to see how well the algorithm reports its own resolution. The resolution for both z and t is underestimated by $\sim$20%.

As a check for a potential measurement bias of z or t compared to the true vertex coordinates due to clustering, Fig. 30 shows the difference in time and position between the reconstructed cluster and the electron track that is not included

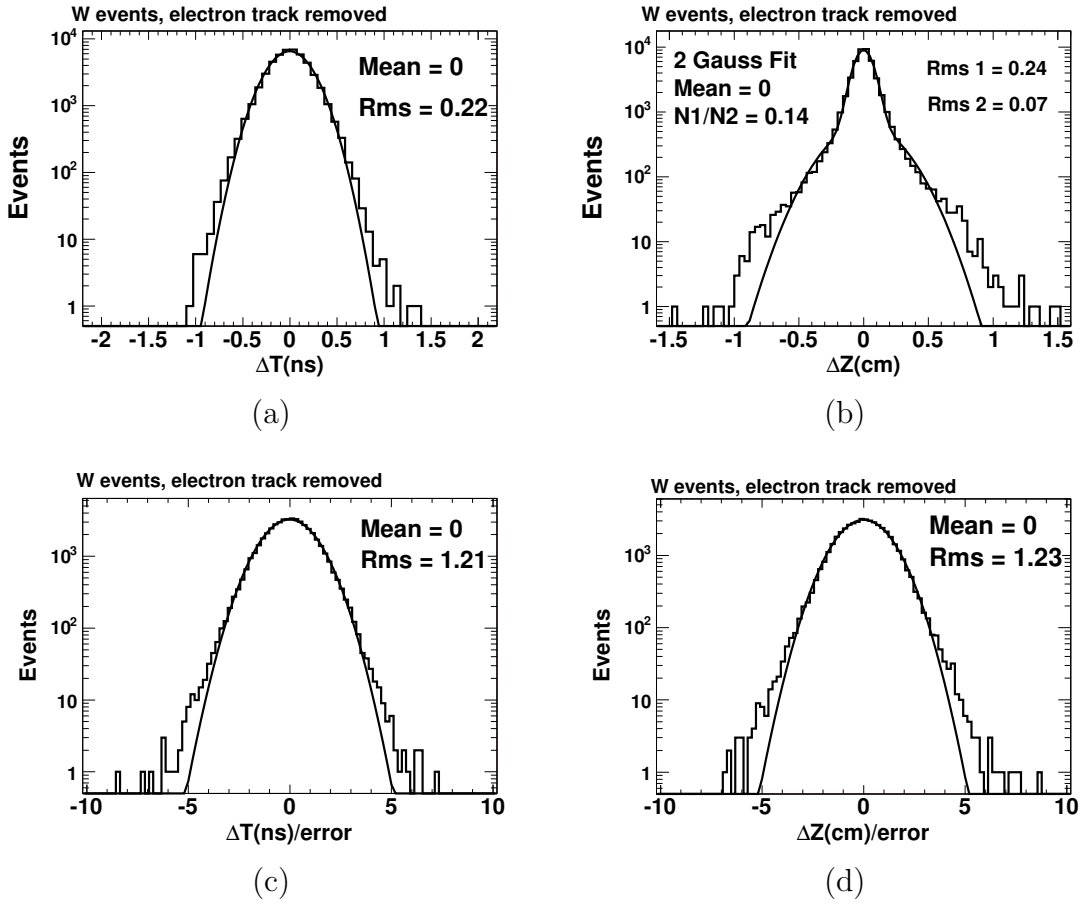

Figure 29: The difference in t and z between two arbitrarily selected sets of tracks from the same reconstructed vertex in a $W \rightarrow e\nu$ dataset with the electron track removed from the vertexing. This is a measure of the vertex resolution. Note that the factor of $\sqrt{2}$ is already taken out. The lower plots show the RMS normalized to the uncertainty reported by the cluster. The cluster errors are underestimated by $\sim$20%.

in the vertexing. The distributions are well described by two Gaussians that are both symmetric and centered at zero, indicating no measurement bias. The primary Gaussian distributions contains events where the reconstructed cluster is the vertex that produced the electron. Its RMS is dominated by the resolution of the electron track position and time. The secondary Gaussian distributions contain events where the electron originates from a second vertex in the event. As a sidenote, the track resolution can be estimated by subtracting the widths of the primary distributions in Figs. 29c and d (0.22 ns in t and 0.07 cm in z) from the RMS shown in Fig. 30. This leads to COT track resolution measurements of $\sim$0.27 ns in t and $\sim$0.22 cm in z.

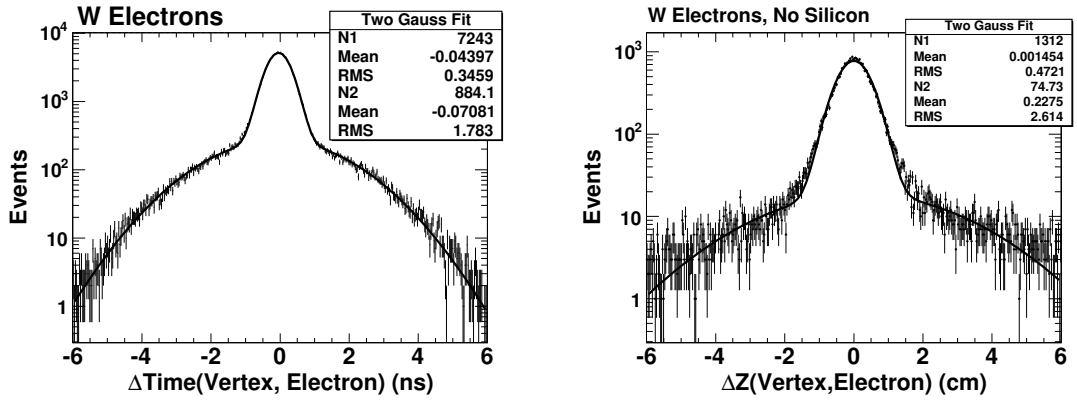

(a) (b)

Figure 30: The difference in t (a) and in z (b) between electron track and the highest Σp_{T} reconstructed vertex without the electron track participating in the vertexing. The distributions are centered at zero, indicating that there is no bias in the clustering procedure. The secondary Gaussian contains events where the electron originates from a second vertex in the event.

Figure 31 shows the resolutions reported by the clustering algorithm. As expected the uncertainty on the mean t_0 in (c) and z_0 in (d) drops like the square-root of the number of tracks in the vertex. The second peak in the RMS distribution in z (Fig. 31b) indicates that there are cases when two different vertices are combined in

one cluster. To investigate a potential concern that the merging causes a mismeasurement of the vertex time, Fig. 32 shows the t_0 difference between the electron track and the cluster for the cases with a large RMS in z (RMS $>$ 0.6 ns). As there is no substantive difference between this distribution and the one for all vertices that is shown in Fig. 30a it can be concluded that there is no bias or degradation of the resolution. This effect does not occur in the time distribution as the vertex resolution in z ($\sim$0.07 cm) is small compared to the RMS (25 cm) and thus the requirement in z is much tighter.

The efficiency of the vertex reconstruction algorithm is investigated using two separate methods. The efficiency as a function of the number of tracks is determined by selecting events that contain good clusters with a high track multiplicity and then taking various random subsets of the tracks that belong to this cluster to see if they alone could produce a good cluster ("subset method"). Figure 33a shows the ratio of subset samples in which a good cluster is reconstructed compared to all cases tried for a given set of tracks as a function of the number of tracks in the various subsets. The inset shows that the algorithm is over 90% efficient if 4 tracks are present, where the inefficiency is likely caused by the algorithm reconstructing two clusters with each $<$4 tracks, and 100% efficient by 6 tracks (note that the algorithm requires at least 4 tracks).

A second method that also allows for a measurement of the efficiency as a function of the Σp_{T} is to count tracks only in a 2 cm $\times$ 2 ns window around the electron track ($\sim$10 σ in each direction) in events with one or fewer clusters ("window method"). While this result is not biased by selecting cases with a known good vertex, the disadvantage is that not all tracks are, for resolution reasons, in the window, resulting in a known under-counting of the number of tracks. Figure 33b shows that the efficiency as a function of the number of tracks in the vertex yields the same result as

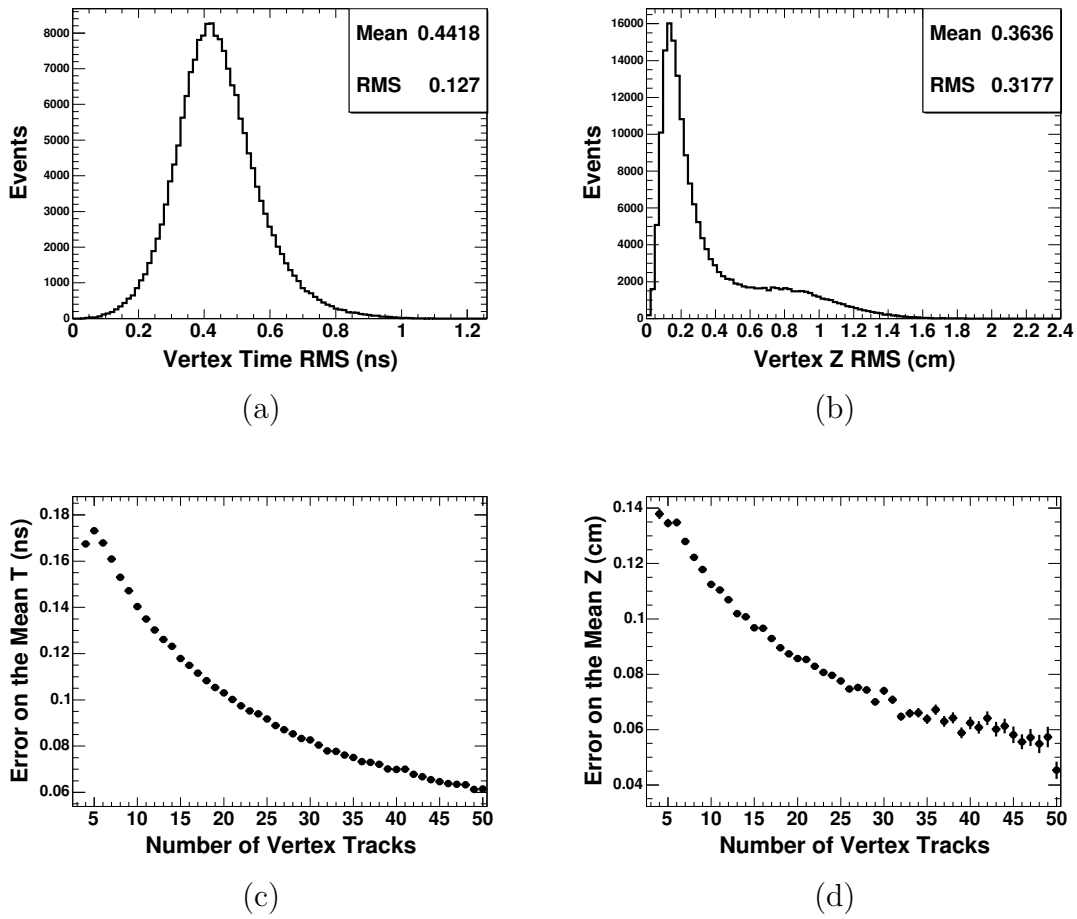

Figure 31: In (a) and (b) the resolution distributions reported by the clusters. The second peak at $z = 0.8$ cm indicates that the assumed true resolution is not selected optimally and that there are cases when two vertices close in z are combined into a single cluster. As discussed in the text this does not affect the final analysis. In (c) and (d) the uncertainty on the mean t_0 and z_0 drops like the square-root of the number of tracks in the vertex.

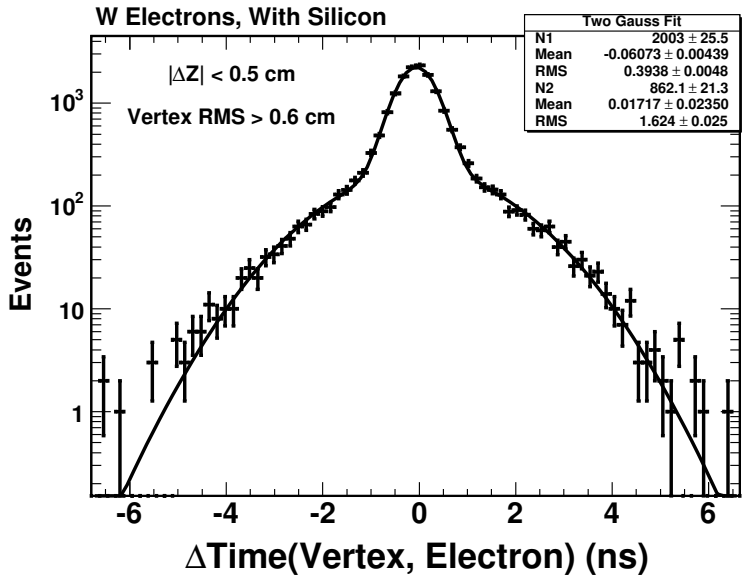

Figure 32: The difference between well measured electron tracks and clusters that are potentially a combination of two separate collisions (vertex RMS > 0.6 cm, see Fig. 31). There is no substantive difference between this plot and Fig. 30a indicating no timing bias or resolution deficiency in the clustering algorithm.

the subset method, which gives confidence in the results as a function of Σp_{T}. The efficiency plateaus at a Σp_{T} of 5 GeV/c.

It is important to note that these numbers are sample-dependent. If, for instance, a sample is chosen that is biased towards a higher average track p_T then the efficiency might be larger as a function of the number of tracks. Or, if a sample contains many high-p_T tracks, the efficiency as function of Σp_{T} might plateau earlier. Since the vertex selection criteria for the search require $\Sigma p_{\mathrm{T}} > 15$ GeV/c as described later, the efficiency will be 100%.

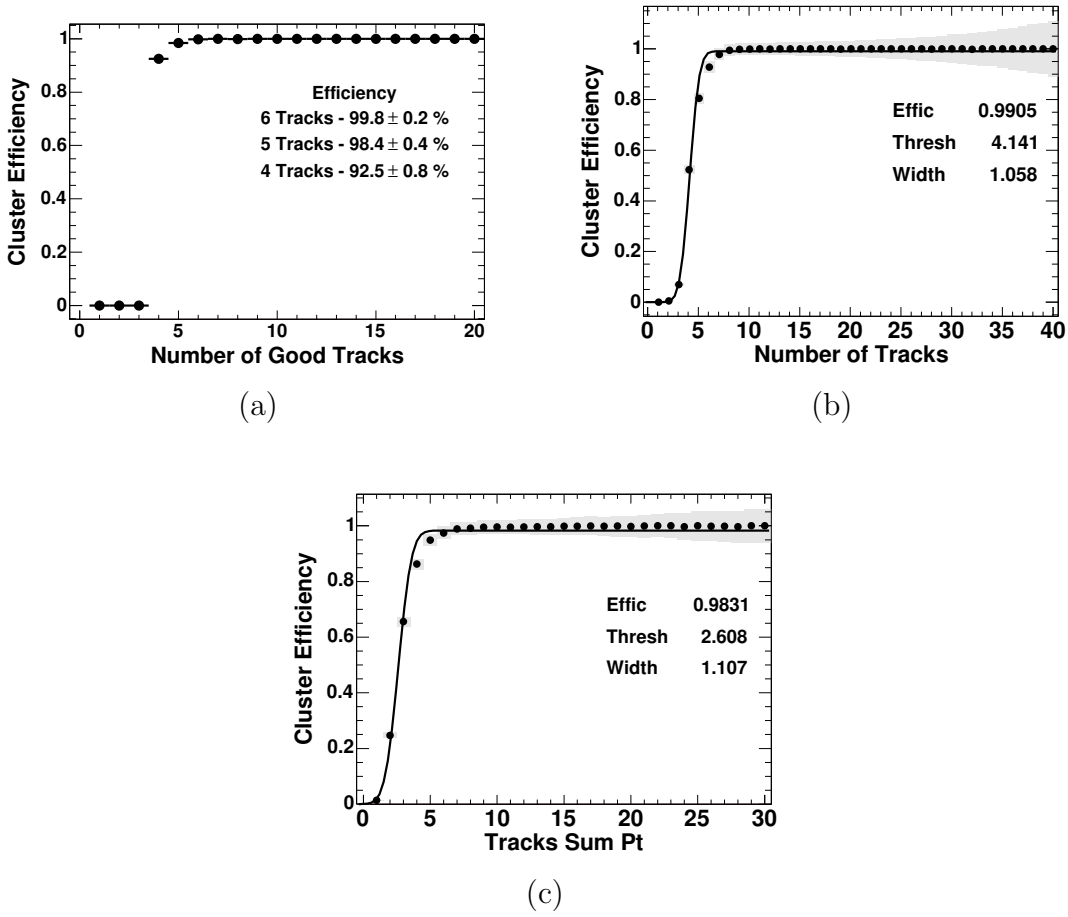

Figure 33: The clustering efficiency as a function of the number of tracks using (a) the subset method and (b) the window method, and (c) as a function of the Σp_{T} of the tracks using the window method. The similar results for the window and the subset method as a function of the number of tracks gives confidence in the window method for the Σp_{T} plot. Note that a cluster is required to have at least 4 tracks.

3. *Correlation between Collision Position and Time*

The collision position and time distributions are determined by the proton and antiproton bunch structure. A small difference between their bunch widths in z cause a slight correlation between the vertex position and time. Figure 34 shows that the vertex time decreases as one moves from the negative to the positive side along the z direction [50].

The proton and antiproton bunch widths are well approximated by Gaussians, in z denoted σ_p and $\sigma_{\bar{p}}$. The bunch propagation in position (z) and time (t) can be expressed as

$$F_p \sim \exp\left\{\frac{-(z-ct)^2}{2\sigma_p^2}\right\},$$
$$F_{\bar{p}} \sim \exp\left\{\frac{-(z-ct)^2}{2\sigma_{\bar{p}}^2}\right\}. \tag{3.4}$$

The probability distribution function of the collision position and time is therefore approximated by

$$F_{p-\bar{p}} \sim \exp\left\{\frac{-(z-ct)^2}{2\sigma_p^2} - \frac{(z+ct)^2}{2\sigma_{\bar{p}}}\right\}. \tag{3.5}$$

The average collision time is found by setting $\frac{\mathrm{d}F_{p-\bar{p}}}{\mathrm{d}t} = 0$

$$\Rightarrow \quad ct = z\frac{\sigma_{\bar{p}} - \sigma_p}{\sigma_{\bar{p}} + \sigma_p}. \tag{3.6}$$

If $\sigma_{\bar{p}}$ and σ_p are not equal this results in a linear correlation between the collision time and position as seen in Fig. 34. Combined with the RMS of the vertex z position from Fig. 28b, which can be estimated from Eq. 3.5 for a constant t as $\sigma_{\bar{p}}\sigma_p/\sqrt{\sigma_{\bar{p}}^2 + \sigma_p^2}$, the bunch widths can be estimated to be $\sigma_p \approx 55$ cm and $\sigma_{\bar{p}} \approx 60$ cm. While this result is based on a simplified bunch shape model, it is comparable to the values from Tevatron bunch length studies of $\sigma_p \approx 50$ cm and $\sigma_{\bar{p}} \approx 70$ cm [72].

Note that while this effect is not simulated in the CDF MC, there is negligible difference between data and MC simulation as the corrected photon arrival time takes the measured vertex z_0 and t_0 into account. However, if the wrong vertex is selected, there is a variation in the RMS of the $t^{\gamma}_{\rm corr}$ distribution as described in Section V.A. This effect is taken into account as a systematic uncertainty on the background and the acceptance estimate.

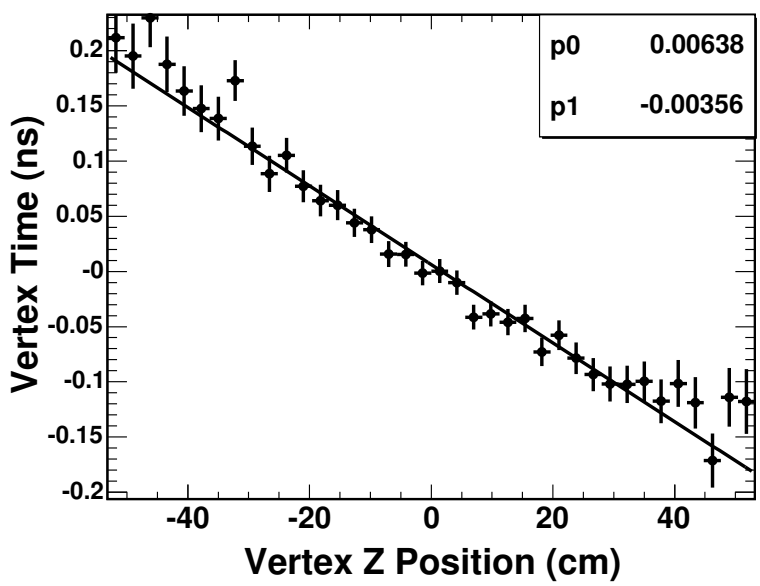

Figure 34: The mean vertex time as a function of the z position of a collision at CDF, as measured with the space-time vertexing algorithm. This correlation effect is due to the difference between the proton and antiproton bunch widths and is consistent with expectations from accelerator performance.

G. The Corrected Photon Time

As shown in Section I.B.2 the corrected photon arrival time, $t_{\rm corr}$, is an effective variable in the discrimination of GMSB signal from prompt SM photons and other backgrounds. It is based on the arrival time as measured by the EMTiming TDCs along with the space-time vertex reconstruction that provides the collision time and the photon TOF measurement as described in the previous section. This section discusses the arrival time of the photon as measured by the EMTiming TDCs and various corrections that center the distribution at zero and reduce its RMS. Finally, it discusses a simulation of the EMTiming system and how well it reproduces the data, in combination with the vertex algorithm.

The time of arrival recorded by the EMTiming system TDCs, $t_{\rm raw}$, is an integer that lies between 560 and 590 ns for a prompt particle and has a 8 ns variation due to several effects. This is shown in Fig. 35(a) using electrons from simulated $W \to e\nu$ events that pass the event requirements described below. Each effect is taken into account in calibrations and vertex-based corrections such that the corrected time is given by [59]:

$$\begin{aligned} t_{\rm corr} &= t_{\rm raw} + C_{\rm calibs} + C_{\rm vertex} \quad \text{where} \\ C_{\rm calibs} &= C_{\rm start} + C_{\rm energy} + C_{\rm asymmetry} + C_{\rm run} \quad \text{and} \\ C_{\rm vertex} &= C_{\rm TOF} - t_{\rm vertex} \ , \end{aligned} \tag{3.7}$$

where the $t_{\rm corr}$ will be referred to as "fully corrected time." The corrections $C_{\rm calibs}$ take into account the time the PMT signal needs to travel to the TDC ($C_{\rm start}$), an energy-dependent ("slewing") effect due to the fixed-height ASDs ($C_{\rm energy}$) and an effect due to energy difference deposited in the two PMTs ($C_{\rm asymmetry}$), as described in Section II.C. They are determined from fits for each channel that are obtained

from a calibration procedure on high statistics jet data samples and that do not vary over a period of months. Also applied are small run-dependent corrections C_{run} due to temperature variations of some cables. Each of those effects is described in Section III.G.1. They are effectively $\langle t_{\text{raw}} \rangle + C_{\text{calibs}} = \langle t_f - t_i - \frac{|\vec{x}_f - \vec{x}_i|}{c} \rangle$ for prompt photons (compare Eq. 1.3) where $\langle$ and $\rangle$ indicate averages over the calibration period. The C_{vertex} term comprises both the vertex time (t_{vertex}) and the position (as TOF corrections, C_{TOF}) that are entirely measured from and applied to the event data as described in Section III.G.2.

To visualize the effects and as a check, the time distribution after each term is applied, is shown in Fig. 35. The contribution to the raw time of the RMS of each term is summarized in Table VII. The uncertainties due to each effect are estimated using a combination of data and MC simulation, described below in detail. They are shown in Fig. 36 and summarized in Table VIII. After all terms are applied the time resolution for electrons from $W \to e\nu$ events is 0.63 ns (0.64 ns) for MC (data), dominated by the intrinsic resolution (0.5 ns), the precision of the TDC output (0.29 ns) and the vertex t_0 resolution (0.25 ns).

In Section III.G.3, an intrinsic EMTiming resolution is derived using a $Z \to ee$ data sample and is put *ad-hoc* into the MC as this hardware effect is not simulated. This makes the argumentation for the correctness of the MC simulation circular, in the sense that, given the intrinsic resolution from data, the MC simulation reproduces the data results.

The EMTiming system is simulated as part of a modified CDF detector simulation that is described in Section III.G.4. It is run, independently, after event generation and standard CDF simulation. Its purpose is mainly to reproduce the arrival time of prompt, isolated particles with a robustness that allows it to be used to measure the arrival time of photons from long-lived particles. Thus, the emphasis

is not on a detailed reproduction of the hardware but on a correct reproduction of the data results at each correction step found with prompt electrons.

Unless otherwise noted, electrons from a $W \to e\nu$ event sample are used in this section because (a) their arrival time distribution is expected to look similar to photons as they interact similarly with the calorimeter and (b) the vertex of the electron is well known from its track which allows for reliable vertex and TOF corrections. The data correspond to an integrated luminosity of 145.7 pb^{-1}, and the event selection is similar to the final analysis: Events are required to have $\not\!\!E_T > 25$ GeV, and at least one vertex, reconstructed as shown in Section III.F, that is required to contain more than 2 tracks with a $\Sigma p_{\mathrm{T}} > 2$ GeV/c, and to have $|z_{\mathrm{vtx}}| < 60$ cm. An electron that passes the requirements described in App. B with an $E_T > 20$ GeV is required to match the vertex using $|z_{\mathrm{track}} - z_{\mathrm{vertex}}| < 2$ cm and $|t_{\mathrm{track}} - t_{\mathrm{vertex}}| < 1.3$ ns to ensure the right vertex correction to the arrival time. The same requirements are applied to both the $W \to e\nu$ data and MC sample.

Table VII: The RMS of the corrected time distribution after cumulatively correcting for the effects shown in the first column for electrons in the data and MC using a sample of $W \to e\nu$ events (see Fig. 35) [73]. The last row shows the fully corrected RMS.

Correction	MC (ns)	Data (ns)
Before corrections (raw)	8.10	
Calibrations (energy dependent)	1.48	1.62
Vertex t_0	0.75	0.75
Vertex Position (TOF)	0.63	0.64

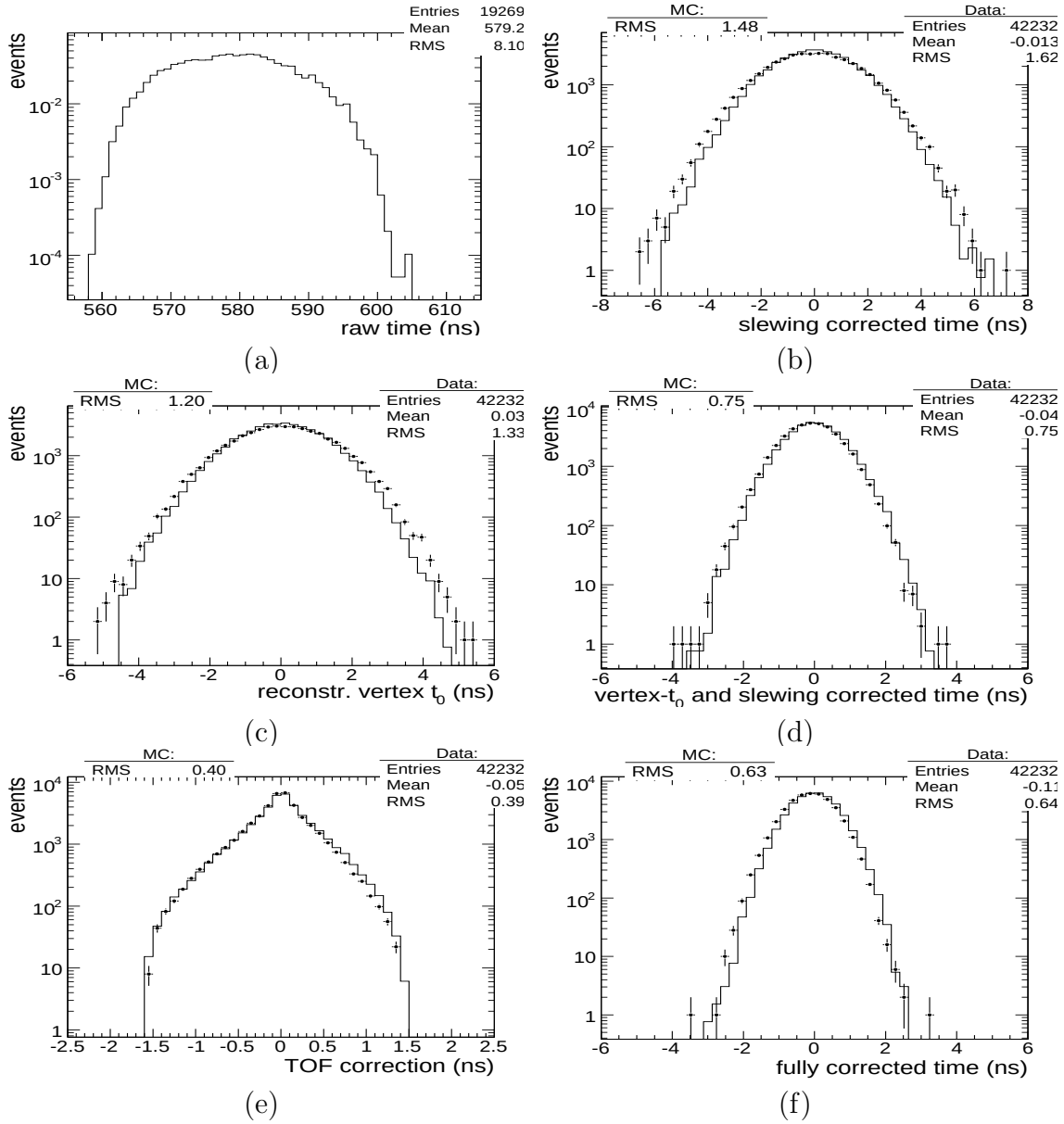

Figure 35: A comparison between MC (solid) and data (points) for the timing information for electrons from a $W \to e\nu$ sample after cumulatively applying the various corrections (left side) and a comparison of the corrections themselves (right side). Figure (a) shows the raw time as it comes out of the TDC (MC only) [73]. Figure (b) shows the time after the calibration corrections, Figure (c) shows the vertex t_0 correction, Figure (d) the time after this correction, Figure (e) the TOF correction and Figure (f) the TOF corrected, i.e. the fully corrected time. In all cases the distributions are well centered around 0 and the resolutions of data and MC fit well with a fully corrected RMS of 0.64 ns. The mean of the fully corrected data of -0.11 ns is likely due to small correlations between the variables and can be corrected e.g. by improved run-dependent corrections. The two outliers with corrected times beyond 2 ns have been studied and are most probably from a cosmic ray contamination of the sample.

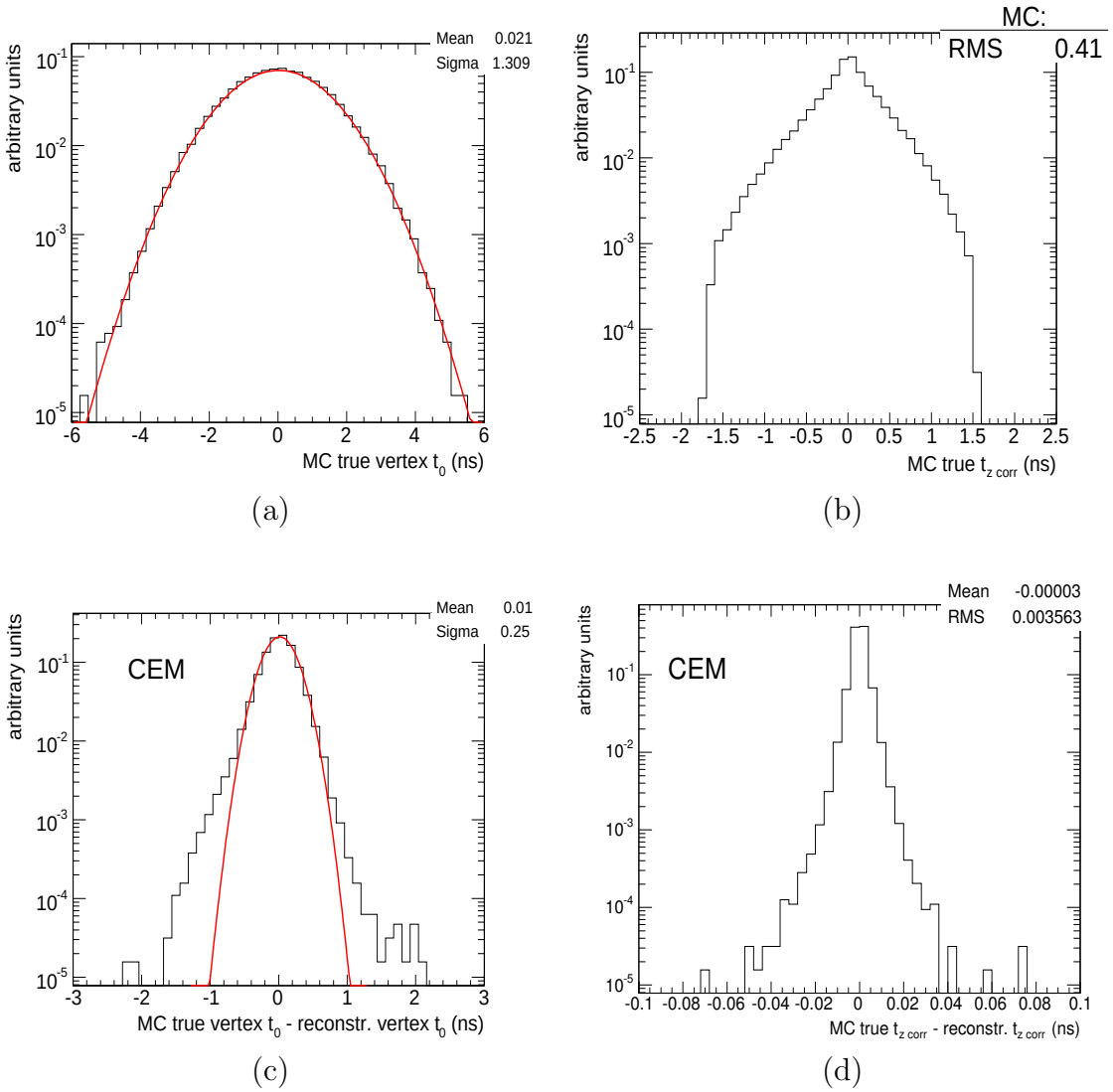

Figure 36: A MC simulation of the vertex time and position effects that contribute to the RMS of the raw data and their impact on the final timing resolution using a $W \rightarrow e\nu$ MC sample. Figures (a) and (b) show the MC values for the collision time and the time distribution originating from the spread of the primary vertex in the z-direction, respectively. The contributions to the raw time RMS are 1.3 ns from the vertex t_0 and 0.41 ns from the TOF correction. Similarly, Figures (c) and (d) show the difference between the reconstructed vertex information and the true values; a measure of the final resolution of these quantities. The resolution of the time correction from the vertex z_0 measurement is negligible with 0.004 ns, the resolution of the vertex t_0 is 0.25 ns. The non-Gaussian tails in (c) are due to the track t_0 calculation being biased towards a vertex t_0 of 0 ns as described in App. C.C.

Table VIII: The contributions of physics and hardware effects, and the uncertainty of their corrections, to the RMS of the EMTiming system taken from a $W \to e\nu$ MC sample (see Fig. 36 and the MC histograms in Fig. 35). The dominant contribution is the slewing effect as part of the calibrations as described next.

Effect	Contribution to Raw RMS (ns)	Uncertainty of Correction (ns)
Calibrations (energy dependent)	7.9	0.5
Vertex t_0	1.20	0.25
Vertex Position	0.40	< 0.1
TDC integer conversion	0.29	0.29
Total	8.10	0.63

1. *EMTiming Calibration*

As described in Eq. 3.8, the raw time as it comes out of the EMTiming system, t_{raw}, is corrected for several effects (C_{calibs} in Eq. 3.8), some of which can be obtained from *in-situ* calibrations using high statistics jet data samples:

- There is a constant offset between the average time of arrival of the energy deposited in the calorimeter and the recorded TDC start time (see Fig. 10). This constant, C_{start}, has a value on the order of ∼580 ns and a variation that is dominated by the overall cable lengths that can differ over 5 m between towers, corresponding to a C_{Start} variation of ∼10 ns and more.

- As the ASDs use fixed-threshold discriminators for the PMT pulses, the start time of the timing hit is dependent on the rise time of the pulse which in turn depends on the energy of the incoming particle ("slewing"). Figure 37a shows t_{raw} as a function of the tower energy (sum of the PMT energies) ("slewing curve"). At high energies it asymptotes to C_{start} as the rise time of the energy pulse becomes effectively infinite.

  The shape of the slewing curve is well described by the following empirically derived formula:

  $$C_{\text{energy}} = \frac{A_1}{\ln(x)} + \frac{A_2}{x^2}$$

  where A_1 and A_2 are constants and x is the sum of the two PMT energies.

- Figure 37b shows the C_{energy}-corrected time as a function of the energy asymmetry of the PMTs in a tower defined as in Eq. 3.1. In the CEM the PMTs lie on opposite sides of the same tower, thus if the incident position of the photon is closer to either PMT, the PMT asymmetry becomes greater and the time that the light needs to get from the incident photon to either PMT is shorter.

This leads to a correlation between the recorded time and the PMT asymmetry which can be corrected with the following, empirically derived formula:

$$C_{\text{asymmetry}} = B_0 + B_1 \cdot \text{PA} + B_2 \cdot \text{PA}^2$$

where B_1, B_2 and B_3 are constants.

The parameters for all three effects are produced in one calibration procedure and are collectively referred to as "slewing calibrations/corrections."

Run-dependent corrections (C_{run}) are applied separately to take into account variations in the CDF DAQ clock relative to the interaction time. The calorimeter systems are synchronized to the CDF DAQ clock which in turn is set by the Tevatron clock. It is generally assumed that the shifts on the order of ∼1-2 ns are caused by changes in the properties of the material of the cable that transfers the clock signal, due to temperature variations outside. While the calibrations average over this effect, it has to be taken into account in the analysis. They contribute an RMS of 0.43 ns to the calibration corrections.

After all of the above corrections, equivalent to $\langle t_{\text{raw}} \rangle + C_{\text{calibs}} = \langle t_f - t_i - \frac{|\vec{x}_f - \vec{x}_i|}{c} \rangle$, the time distribution is centered at zero with an RMS of ∼1.62 ns, as shown in Fig. 35b. The next section describes the vertex and the TOF corrections that effectively take into account the t_i and the $\frac{|\vec{x}_f - \vec{x}_i|}{c}$ of Eq. 1.3 measured for each event.

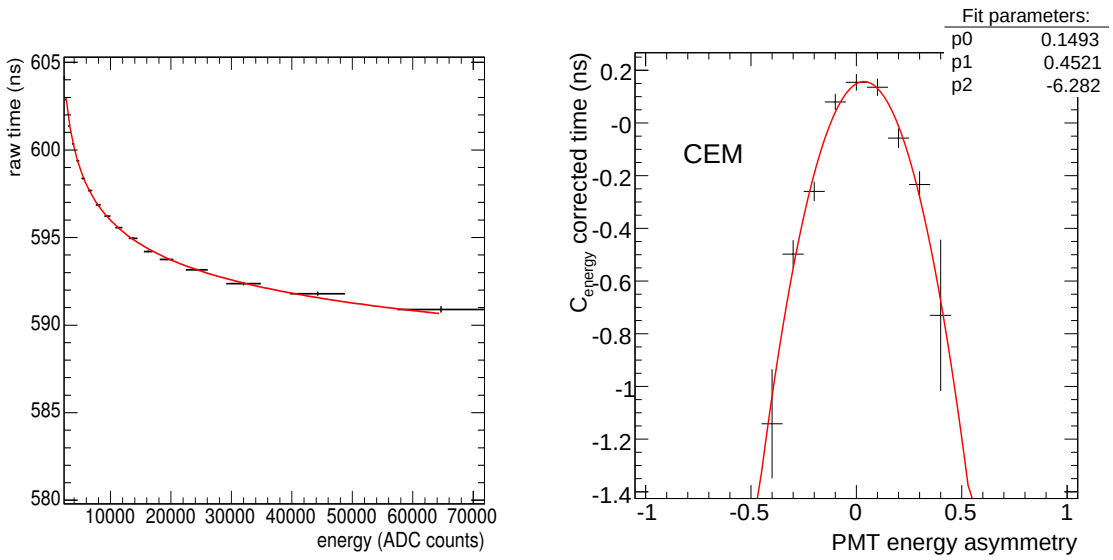

(a) (b)

Figure 37: The functional form (a) of the slewing correction as a function of the energy sum of the PMTs (in ADC counts [74]) in a range between 2 GeV and 24 GeV (b) of the C_{energy}-corrected time as a function of the PMT energy asymmetry of an example tower in the CEM from an example run. In (a) the raw times are energy dependent due to the fixed height discrimination slewing of the ASD and lie between 560 ns and 590 ns for a prompt particle. The shape of the parabolic fit in (b) is due to the PMT/tower setup and is explained in the text.

2. *Event-Based Time Corrections for the Vertex Time and Position*

While the calibration method assumes that the vertex always lies at the center of the detector, the t_{corr} calculation takes into account, event-by-event, the collision position and time variation (see C_{vertex} in Eq. 3.8). The time distributions and corrections for the PEM are shown in App. D for completeness.

The event collision time, t_{vertex}, is measured by the vertexing algorithm discussed in Section III.F and subtracted off. Figure 36a shows the typical distribution of t_{vertex} for the MC $W \rightarrow e\nu$ sample with the default $\sigma = 1.3$ ns. Figure 36c shows a comparison of the vertex reconstructed time and the true generated collision time. The RMS is a measure of the t_{vertex} resolution of the MC W sample which is 0.25 ns. This makes up the largest non-EMTiming contribution to the final t_{corr} resolution. The non-Gaussian tails in this distribution are due to the track t_0 calculation being biased towards a vertex t_0 of 0 ns as shown in App. C.C which does not affect this analysis as it occurs at a low rate. The reconstructed t_{vertex} distribution is shown in Fig. 35c and the time distribution after this and the slewing correction is shown in Fig. 35d with an RMS of 0.75 ns.

The TOF correction is estimated using the measured collision position from the COT and the known calorimeter tower position of the electron in η. Figure 36b shows the TOF correction needed to compensate for the collision position being different from $z = 0$ if the spread of the vertex position is $\sigma_z = 28$ cm, from the MC $W \rightarrow e\nu$ sample. The mean corrected TOF is centered at 0 with an RMS of 0.41 ns. Figure 36d shows the time difference of the TOF between the true and measured vertex z-position for the MC sample. The small RMS shows that the resolution of the TOF correction is negligible at 0.004 ns assuming that the vertex is correctly picked. The time distribution from the reconstructed vertex has an RMS of 0.39 ns as shown in Fig. 35e.

After this correction the RMS of the fully corrected timing distribution is 0.64 ns for electrons as shown in Table VII and visualized in Fig. 35f. The mean of the fully corrected data distribution of -0.11 ns in Fig. 35f is described in Section V.A.

Next the intrinsic resolution is discussed and measured. It is implemented *ad-hoc* into the MC simulation that is described afterwards in detail.

3. Intrinsic EMTiming System Resolution

The intrinsic EMTiming resolution can be estimated using the t_{corr} difference of electrons in a data sample of $Z \to ee$ events, as shown in Fig. 38. The events are required to have two electrons that pass the criteria listed in App. B. While the vertex position and time measurement cancels out in the difference and the TOF measurement has a negligible measurement uncertainty, the RMS is ∼0.84 ns after correcting for the TOF as shown in the previous section. From this one gets a resolution of $\sigma_{\mathrm{EMTiming}} = 0.84\ \mathrm{ns}/\sqrt{2} = 0.59$ ns. After subtracting off the contribution to the RMS from the TDC that rounds the time to integers ($1/\sqrt{12} \approx 0.29$ ns) and the resolution for the TOF correction (see Fig. 36d, negligible), one gets an "intrinsic" EMTiming system resolution of 0.5 ns. If this value is put into the MC simulation, taking into account its variation as a function of energy derived from data (see Fig. 39, in particular for EM clusters with low energy) the data plots after each correction can be reproduced as shown in Fig. 35 which is a confirmation of its correctness. Similarly the corrected time RMS of 0.64 ns can be estimated from the intrinsic, the vertex t_0 resolution and the rounding effect $(0.5 \oplus 0.25 \oplus 0.29)$ ns. The simulation itself is described in the next section.

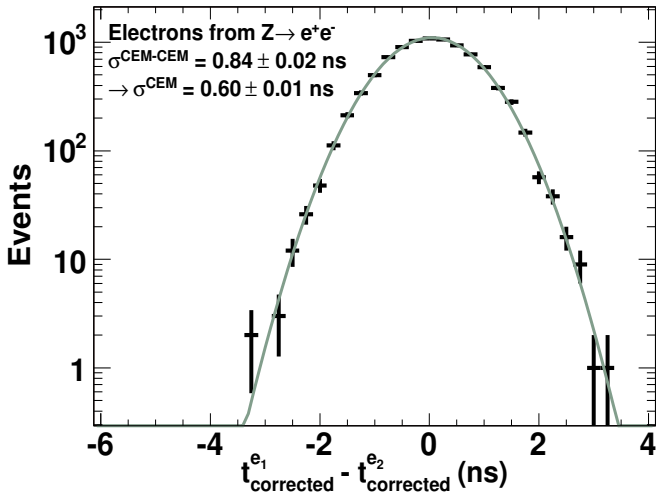

Figure 38: The difference in the arrival times of electrons, that pass the requirements in Table XXIII, from $Z \rightarrow ee$ decays, corrected for the TOF but not the vertex t_0. The distribution is centered at 0 ns with an RMS of ∼0.84 ns which indicates an intrinsic EMTiming system resolution of 0.5 ns as explained in the text.

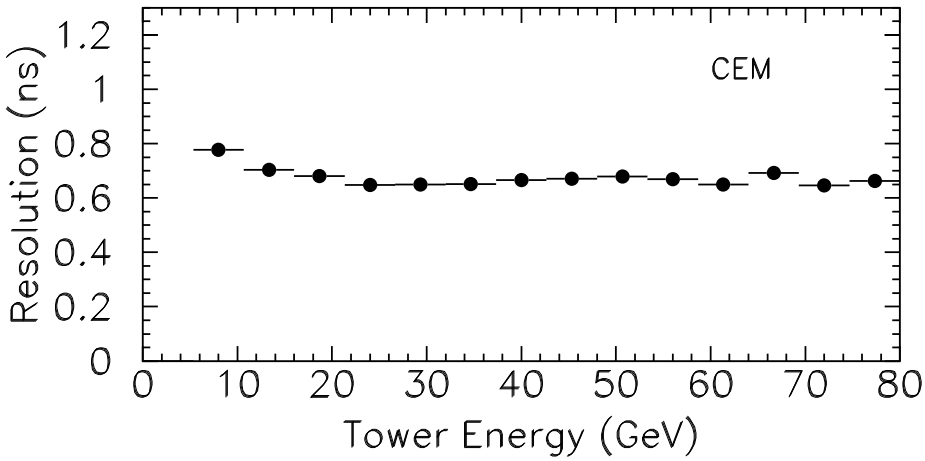

Figure 39: The RMS of the fully corrected arrival time versus the electron EM energy from a electron data sample produced with the requirements shown in App. B without the E_T cut. This effect is simulated by varying the intrinsic EMTiming resolution as a function of the EM energy of the incident particle with an RMS of 0.5 ns at an EM energy of 25 GeV. Note that the intrinsic resolution as a function of energy is found by folding the value in the figure with the TDC and the TOF resolution (negligible).

4. Monte Carlo Simulation

This section describes the simulation of the EMTiming system response to high energy particles. It begins with the generation of the true time of arrival, then the simulation of the effects at the calorimeter, and finally the correction for the TOF and vertex time. Each step is first summarized and then described in detail:

(i) Generate an event including the production, decay and propagation of the particle through the detector as well as the simulation of the vertex t_0 and z_0

(ii) Calculate the true arrival time for a particle at the calorimeter

(iii) Check to see if it hits an EMTiming-instrumented part of the detector

(iv) Smear the corrected arrival time for the intrinsic resolution (see Section III.G.3)

(v) Check to see if it has enough energy to create a hit (see Section III.G.1)

(vi) Convert the arrival to a raw time using the slewing curve (see Fig. 37a)

(vii) Truncate the raw time to an integer to simulate the TDC output format of real data

As previously mentioned, this analysis uses the CDF MC [62] in combination with the PYTHIA event generator [36] to model the GMSB signal described in Section I.B.2, as well as the $W \rightarrow e\nu$ events. The detector simulation propagates each particle through the tracking volumes using GEANT [65], and creates ("digitizes") the hits in the calorimeter using GFLASH [75]. It is modified for the simulation of the EMTiming system, developed specifically for this analysis.

The PYTHIA event generator is a parton-shower simulation that produces the vertex, center-of-mass energy, all initial particles and their decays as long as they are not related to the detector material. Given the momenta of the particles the CDF detector simulation propagates them through the detector volume, taking into account material effects.

As the EMTiming module is not part of the calorimeter simulation, the final simulated arrival time of a particle at the calorimeter, taking into account the vertex time and TOF, t_{arrival}, is obtained using information generally available in the MC generated files, i.e. true vertex information and true particle information. It can be expressed as follows:

$$t_{\text{arrival}} = t_{\text{prod}} + \frac{|\vec{x_f} - \vec{x}_{\text{prod}}|}{|\vec{v}_{\text{part}}|} \tag{3.8}$$

where $\vec{v}_{\text{part}}$ is the velocity of the particle, $\vec{x}_{\text{prod}}$ and t_{prod} are the position and time of its production vertex and $\vec{x}_f$ is its final position at the CES (r = 184.15 cm [51]). As the energy threshold of the timing system is on the order of 2-3 GeV (see Section II.C) the curvature of a charged particle in the magnetic field is negligible and one can calculate t_{arrival} by extrapolating the particle trajectory as a straight line from $\vec{x}_{\text{prod}}$ (either as part of a decay or directly), to the position $\vec{x}_f$. The value of t_{arrival} is then given by the vertex time plus the TOF of the particle. The true vertex time information, t_{prod}, takes into account the simulation of the primary vertex position and time, t_{event} (see Figs. 36a and b), and, if it is a decay vertex, the actual time the decay parent needed to propagate through the detector volume. As the slewing calibration corrections assume that particles come from the center of the detector, $\vec{x}_{\text{event}} = \vec{0}$, at $t_{\text{event}} = 0$ ns, t_{arrival} is corrected for the TOF of the particle that it would have if it came from $\vec{0}$. The corrected arrival time, $t^{\text{corr}}_{\text{arrival}}$, is then:

$$t^{\text{corr}}_{\text{arrival}} = t_{\text{arrival}} - \frac{|\vec{x}_f|}{c} \ . \tag{3.9}$$

For a prompt particle this is equivalent of $(t_{\text{vertex}} - C_{\text{TOF}})$ (compare Eq. 3.8), however for decay particles it correctly takes into account the travel time of the decay parent.

Next the simulation checks if the particle hits the detector. While this is typically straightforward there are few pathological cases dominated by when the energy deposit happened in the neighboring tower rather than the tower calculated in $\vec{x}_f$. In this case the same timing information is assigned to the neighboring tower. Particles that do not deposit energy in the calorimeter or that have a decay vertex outside the detector volume are ignored. Note that in the case of multiple particles arriving at the same tower, only the first hit in time is used. Considering the resolution of the system this is a good approximation for jets. In this case there is no handle available to decide which particle actually triggered the timing system as the fraction of energy left in the EM calorimeter is not known. However, this is only critical if the energies of the particles that hit the same tower are around threshold (see Sec. III.G.1), which is not used in this analysis.

If the particle passes the above requirements the intrinsic EMTiming resolution (see Section III.G.3) is implemented as a Gaussian smearing of $t^{\text{corr}}_{\text{arrival}}$ and $\sim$0.5 ns, depending on its energy-dependence derived from jet data (see Fig. 39).

Once a set of towers with potential timing hits is obtained, the amount of deposited energy is tested to see whether it can produce a timing hit. The hit probability is determined using the energy turn-on curves determined tower-by-tower from jet data. Figure 40 shows the hit efficiency dependence on the energy sum of the PMTs of an example tower in the CEM [74]. The threshold for all CEM towers lies consistently at $\sim$3.5 GeV deposited energy with widths of $\sim$1 GeV (see Section II.C). The run dependence of the threshold curves is negligible unless a channel is broken (broken energy measurement or broken time measurement). In this case the channel is flagged bad in the calibration tables and no timing hits are registered.

If a tower is determined to have a hit, then the generated time is converted to a "raw time" using the inverted slewing curves (see Section III.G.1) and truncated to an integer to simulate the TDC for the output of real data. In this manner MC events can be easily processed by the standard data analysis tools, by applying the corrections as shown in Eq. 3.8. Note that the same slewing curve is used further downstream in the process when applying the slewing corrections to reconstruct t_{corr}. Figure 41 compares the simulated time of arrival of photons for an example GMSB point at $m_{\widetilde{\chi}} = 110$ GeV$/c^2$ and $\tau_{\widetilde{\chi}} = 10$ ns to the simulated arrival time of electrons from W's, after all timing corrections, normalized to 1. Clearly visible is the exponential tail in the GMSB distribution. The fraction of GMSB events with $t > 2$ ns is 53.3%.

The next chapter describes the datasets, trigger and the event preselection.

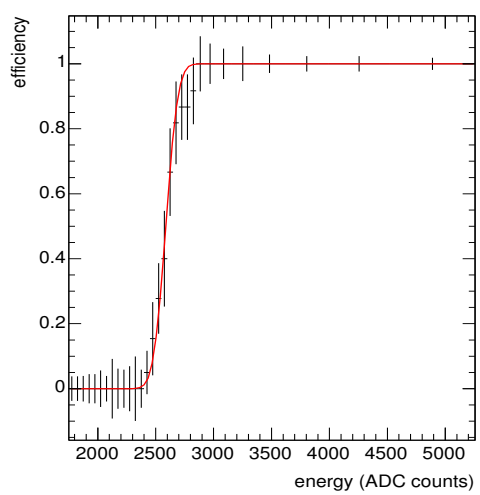

Figure 40: The functional form of the TDC efficiency as a function of energy sum of the PMTs of an example tower in ADC counts [74] with the data of an example run. In this case the threshold is around 7.0 GeV for the energy sum and the width around 1.2 GeV. Note that the energy is here given by the energy sum of the PMTs instead of the usual geometric average as this is the quantity that the fixed height discriminator triggers on. Thus, the tower typically fires at 3.5 GeV of deposited energy.

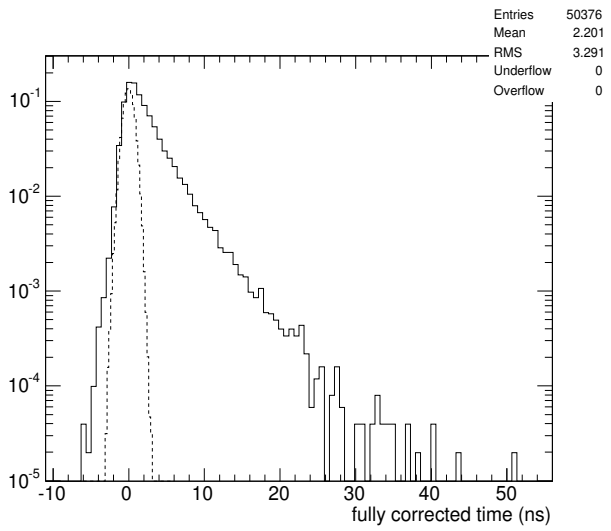

Figure 41: The simulated time of arrival of photons from $\widetilde{\chi}_1^0$'s in a GMSB model with $\tau_{\widetilde{\chi}} = 10$ ns and $m_{\widetilde{\chi}} = 110$ GeV/c^2 after all corrections. The dashed histogram shows the prompt distribution of electrons from $W \to e\nu$ events (taken from Fig. 35(f)). Both distributions are normalized for better comparison.

CHAPTER IV

TRIGGERS, DATASETS AND EVENT PRESELECTION

The $\gamma + \not\!\!E_T + \geq 1$ jet analysis provides the best sensitivity to heavy, neutral particles with nanosecond lifetimes. As previously described, the event selection is done in two stages: (1) a $\gamma + \not\!\!E_T + \geq 1$ jet "preselection" sample is defined and (2) the event selection is optimized to determine the final event requirements. While the photon identification was described in Sections III.A-III.E, this chapter describes both the jet and $\not\!\!E_T$ identification in detail, and then the online selection (triggers) and the datasets for this search. Finally, the event preselection criteria are motivated and described that are used in combination with the simulated GMSB acceptance (see Chapter VI) as a starting point for an optimization of the sensitivity to the GMSB signal (see Chapter VII).

A. Definition of Other Objects

Events are selected based on the presence of a high-E_T photon, described in Sections III.D-III.E, significant $\not\!\!E_T$ and at least one jet. The full set of preselection requirements for the search are summarized in Table X.

1. Missing E_T

At CDF, as in other collider experiments, the collision occurs with approximately no momentum in the plane transverse to the collision. By conservation of momentum the vector sum of the momenta of the final state particles are approximately zero in the transverse plane. However, particles that do not interact with the calorimeter, like the SM neutrino, the GMSB $\widetilde{G}$ or the $\widetilde{\chi}_1^0$ before decaying, cause an energy imbalance of the detected particles. As the momentum in the z direction of the acccelerated protons

and antiprotons at a hadron collider is shared among its constituents ("partons"), the momentum of the colliding partons is not known. Hence, only the transverse component of the imbalance can be inferred. The $\not\!\!E_T$ is defined as the negative of the vector sum of the transverse energy in all calorimeter towers with $|\eta| < 3.6$. It is calculated using the total deposited energy in the calorimeter relative to the highest-Σp_{T} vertex z-position, and the x and y coordinates of the vertex that are taken from the beamline position recontructed by the silicon microstrip system.

There are both non-collision and collision background sources that can cause $\not\!\!E_T$. While the transverse energy of all produced particles is expected to be conserved in collisions, this is not true for instrumental or cosmic ray backgrounds that can produce energy deposits in a small region of the calorimeter, as will be described in detail in Section V.B. The $\not\!\!E_T$ in collision backgrounds presumably comes from two sources: QCD processes and electroweak $W \to e\nu +$ jets processes. QCD processes (γj and jj with one photon reconstructed as a jet) have no intrinsic $\not\!\!E_T$. However, $\not\!\!E_T$ can be misreconstructed by mismeasuring the photon and/or jet energies in the calorimeter. This can occur, for example, when energy is deposited in an uninstrumented region of the detector or when there is a muon in the event that deposits only little energy in the calorimeter and is not reconstructed [13]. While the fraction of QCD events with a mismeasured $\not\!\!E_T$ of $\gtrsim$30 GeV is typically $\sim$1/1000 [13], the total QCD cross section is large, on the order of $\sim$1000 pb, such that it is potentially a major background. The other SM source is real $\not\!\!E_T$ from SM $W \to e\nu +$ jets events where the electron is misidentified as a photon, for example by producing a photon from bremsstrahlung in the tracking volume, and the ν leaves undetected to cause the $\not\!\!E_T$. As the cross section of $W \to e\nu +$ jets events in the central calorimeter region is on the order of $\sim$10 pb it has a minor contribution compared to QCD processes after the event selection requirements.

2. Jets

The term "jets" typically refers to the hadronization of a high energy quark or gluon that is produced in the collision. Since at CDF jets are identified as clusters of energy in the calorimeter, π's from the hadronic decays of taus [39] and the energy deposits from electrons and photons are also reconstructed as jets. In particular, both the second photon and the two taus that are predicted to be produced in GMSB models in the cascade decays from $\widetilde{\chi}_2^0\widetilde{\chi}_1^{\pm}$ and $\widetilde{\chi}_1^+\widetilde{\chi}_1^-$ (see Fig. 1) can be identified as jets. While it increases the acceptance to GMSB events, the jet requirement also reduces non-collision backgrounds which typically only produce a photon (see Chapter V).

This search requires at least one jet in the central or plug calorimeter to have an E_T of 30 GeV. The jet is required to deposit energy in a region of detector-$|\eta| < 2.1$ to reduce backgrounds from proton and antiproton dissociations at high η that are not part of the parton collision.

Jets are identified as clusters of energy in the calorimeter, using a standard jet-cone algorithm [76]. Calorimeter towers are grouped within 0.7 in $\eta - \phi$ space ("0.7 cone") around a seed tower with $E_T > 1$ GeV, and the cluster centroid and E_T are iteratively recalcuated until convergence. Jets with an overlap of $> 50\%$ are merged. The E_T is calculated from the sum of all calorimeter towers within the 0.7 cone and corrected for several effects that include [38]:

- η-dependency of the detector response (relative energy corrections). This corrects for the calorimeter response near the gaps at $\eta = 0$ and $\eta = 1.1$ and the difference between the central and plug calorimeter response. Implicitly included are corrections for the η dependence of the transverse spread of calorimeter showers, and of the gluon radiation and multiple parton interactions. The systematic uncertainty of the E_T measurement is taken from the difference of

the measured jet p_T in dijet events ("dijet balance"). It varies with the p_T and η of the jet and lies between 0.5% and 1.5% in the region $|\eta| < 2.1$.

- Multiple interactions: energy from additional collisions in the same event ("pile-up") can be deposited in the 0.7 cone of the jet cluster causing the jet E_T to be overmeasured. The jet E_T is corrected using an average value of $<E_T^{vtx}>$ (GeV) $= 0.01793 + 1.056 \cdot N_{\text{vtx}}$ where N_{vtx} is the number of reconstructed vertices [48]. After the correction an uncertainty on the slope of the parametrization of 150 MeV remains per additional vertex.

- Absolute energy scale: the calorimeter response from the jet does not perfectly relate to the energy of the original particles in the jet. The uncertainties come from the ability to model the data, in particular the calorimeter response to single particles (∼3%), differences in hadronization modelling (1%) and stability of the calorimeter calibrations (0.5%).

- Underlying event: detector independent corrections are needed to take into account interactions from spectator quarks and initial state gluon radiation (ISR) that deposit energy that is not related to the jet caused by the hard interaction. Differences in MC generators are taken as a systematic uncertainty on the jet energy of 0.32 GeV.

- Energy out-of-cone (OOC): Jet energy that is often deposited outside the jet cone, due to radiation and hadronization effects, is corrected in a detector independent way. While this effect is corrected on average, a systematic uncertainty is taken to be the difference between simulation and data which is ∼5% at ∼30 GeV and decreases with increasing E_T.

B. Triggers and Data Sets

At the Tevatron a collision occurs every 396 ns in the center of the CDF detector corresponding to a 7.6 MHz $p\overline{p}$-bunch crossing rate. A three-level trigger system [51] selects a small fraction of collision candidate events with an output rate of ∼40 Hz in realtime during data-taking using a fixed set of requirements. The level 1 trigger is synchronous and has a decision time of 4 μs with a buffering of 42 beam crossings. It accepts events based on calorimeter, tracking and muon detector information with an output rate of ∼10 kHz. At level 2, calorimeter tower clustering is performed and additional tracking information from the silicon detector is used to reduce the rate to ∼200 Hz. At level 3, a computer farm performs event reconstruction and 3D track reconstruction.

For this analysis events are selected by a single set of 3-level trigger requirements summarized in Table IX, that are referred to as the `W_NOTRACK` trigger. It only requires a photon candidate and $\not\!\!E_T$. As the name indicates it was originially used as a backup trigger for selecting $W \to e\nu$ events in the central and plug calorimeter without relying on tracking measurements. It is used in this analysis mainly because it is the only trigger available that allows for a photon selection without any isolation or CES-χ^2 requirements that might be inefficient for photons from long-lived particles (see Section III.E).

At Level 1, events are required to have energy deposited in an EM-calorimeter trigger tower [77], in the central or plug, that measures more than 8 GeV and has a $\frac{E_{\rm Had}}{E_{\rm Em}} < 0.125$ to help reject hadronic jets, as well as a $\not\!\!E_T$ of 15 GeV. At Level 2 the calorimeter clustering selects only central ($|\eta_{\rm max}| = 1.1$) EM-clusters with a seed tower of at least 8 GeV. At Level 3 the photon candidate E_T and $\not\!\!E_T$ requirements are raised to 25 GeV. All events that pass the full set of `W_NOTRACK` trigger requirements

are written to permanent mass storage.

Events from this initial data sample are used in the data-taking period from December 2004, when the EMTiming system became fully functional, until November 2005. Only events from "good runs" are selected with (a) an integrated luminosity of more than 10 nb^{-1} to contain sufficient statistics for a measurement of the run-dependent corrections described in Section III.G.1 and (b) fully functional calorimeter and COT systems (both used for photon identification), as well as muon systems (used for cosmic ray muon rejection). After these requirements the data correspond to an integrated luminosity of (570±34) pb^{-1}.

Table IX: Triggers that contribute to the `W_NOTRACK` dataset and all their requirements. Note that at Level 1 the central and plug requirements are *or*'d. The $|\eta_{\max}| = 1.1$ requirement at level 2 effectively selects only central EM objects.

Object Type	Trigger Type		
	Level 1	Level 2	Level 3
Photon	≥1 EM cluster Central $E_T > 8$ GeV $\frac{E_{\mathrm{Had}}}{E_{\mathrm{Em}}} < 0.125$ Plug $E_T > 8$ GeV $\frac{E_{\mathrm{Had}}}{E_{\mathrm{Em}}} < 0.125$	$\lvert\eta_{\max}\rvert = 1.1$ $E_T > 20$ GeV seed tower $E_T > 8$ GeV	≥1 central EM cluster use 3 towers for $\frac{E_{\mathrm{Had}}}{E_{\mathrm{Em}}}$ $E_T > 25$ GeV $\frac{E_{\mathrm{Had}}}{E_{\mathrm{Em}}} < 0.125$
$\not\!\!E_T$	$\not\!\!E_T > 15$ GeV central $\Sigma E_T > 1$ GeV plug $\Sigma E_T > 1$ GeV		$\not\!\!E_T > 25$ GeV

C. Event Preselection

The sample of $\gamma + \not\!\!E_T + \geq 1$ jet candidate events that passes the `W_NOTRACK` trigger requirements is then processed "offline" where the event characteristics are refined to increase the signal purity and to further reduce the background. To ensure that all selected events pass the trigger with 100% efficiency [78], the events are required to have $\not\!\!E_T > 30$ GeV and a central EM cluster-$E_T > 30$ GeV. The highest-E_T central EM-cluster in the event is required to pass the standard high-E_T photon identification criteria, but without the CES-χ^2 requirement as it is potentially inefficient for the signal (see Section III.E) and with the PMT energy asymmetry requirement of PA $<$ 0.6 to reduce "PMT spikes" (see Section III.B). As the GMSB signal is expected to produce an additional photon and/or taus and to reduce non-collision backgrounds, at least one jet is required with $E_T > 30$ GeV and $|\eta| < 2.1$.

To measure $t^{\gamma}_{\rm corr}$, events in the preselection sample are required to have a vertex reconstructed with the space-time vertex algorithm (see Section III.F). To ensure that the vertexing is fully efficient, a vertex is required to have at least 4 good tracks. The vertex is required to have a $\Sigma p_{\rm T}$ of at least 15 GeV/c ("good vertex") which helps reduce non-collision backgrounds that mostly do not coincide with a real collision event (see Chapter V). Finally, the vertex position in z is required to be at most 60 cm away from the center of the detector so that both the COT tracking and the projective geometry of the calorimeter are maintained.

Additionally, events are rejected if there is evidence that a cosmic ray muon traversed the detector. It often creates a muon stub with a nearby energy deposit in the calorimeter. While this is described in Section V.B.2, note for now that an event is rejected if a photon is reconstructed within an angle of 30° in ϕ of a muon stub [78] ("muon co-stub" cut).

The full preselection sample requirements are listed in Table X. Table XI lists the cumulative number of events which pass each of the successive cuts to create our preselection sample. The final selection requirements after the optimization procedure are shown in Section VII, along with kinematic distributions.

Table X: The photon, jet, vertex and global event requirements used to obtain the preselection sample of $\gamma + \not\!\!E_T + \geq 1$ jet events. Note that we use the standard photon ID requirements as shown in Table III, but with the addition of a requirement on the asymmetry of the PMT energies to reduce "PMT spikes" and without a CES-χ^2 requirement (see Chapter III). The track requirements are listed in Table VI. The μ co-stub cut is explained in detail in the text. The number of events in the data that pass each cut are shown in Table XI, the estimated signal acceptance in Table XII.

Photon
$E_T > 30$ GeV
Fiducial: $\lvert X_{\rm CES}\rvert < 21$ cm && 9 cm $< \lvert Z_{\rm CES}\rvert < 230$ cm
$\frac{E_{\rm Had}}{E_{\rm Em}} < 0.125$
$E^{\rm iso}_{\rm R=0.4} < 2.0 + 0.02 \cdot (E_T - 20)$
$N_{\rm trks} = 0$ or $N_{\rm trks} = 1$ and $p_T < 1.0 + 0.005 \cdot E_T$
$\Sigma p_{\rm T}$ of tracks in a 0.4 cone $< 2.0 + 0.005 \cdot E_T$
$E^{\rm cluster}_{\rm 2nd\ strip\ or\ wire} < 2.34 + 0.01 \cdot E_T$
PMT asymmetry: $\frac{\lvert E_{\rm PMT1} - E_{\rm PMT2}\rvert}{E_{\rm PMT1} + E_{\rm PMT2}} < 0.6$
Jet
$E_T^{\rm jet}$(cone 0.7) > 30 GeV, Jet Corrections level 7
$\lvert\eta^{\rm jet}_{\rm detector}\rvert < 2.0$
Vertex
Highest Σp_T space-time vertex with $N_{\rm trks} \geq 4$
$\Sigma p_{\rm T}$>15 GeV
$\lvert z\rvert < 60$ cm
Global Event Cuts
Event is part of a good run
$\not\!\!E_T > 30$ GeV
μ co-stub cut, $\Delta\phi(\mu{-}{\rm stub}, \gamma)$>30°
Passes the `W_NOTRACK` trigger

Table XI: Event reduction for the preselection $\gamma + \not\!\!E_T + \geq 1$ jet dataset. The total good run-luminosity before any of above cuts, but after the trigger (see Table IX), is (570±34)pb^{-1}. For the individual requirements see Table X.

Selection	No. of Observed Events
$E_T > 30$, $\not\!\!E_T > 30$,	
photon ID and fiducial cuts	119944
Good vertex	19574
≥1 jet with $E_T > 30$ GeV and $\|\eta\| < 2.0$	13097
Cosmics rejection (μ co-stub)	12855

CHAPTER V

BACKGROUNDS

Events with the $\gamma + \not\!\!E_T +$jets final state can be produced by two different background classes: collision and non-collision events. In this chapter each of the backgrounds is described in detail and the background estimation techniques are outlined. To summarize, the number of background events in the final signal time window is estimated solely from data by normalizing the measured time distribution for each background in control time regions where each background dominates and extrapolating into the signal region.

Figure 42 shows the $t_{\text{raw}}+C_{\text{calibs}}$ distribution of photon candidates in the `W_NOTRACK` dataset without vertex requirement that pass the photon selection criteria of Table III, but without the CES-χ^2 requirement. It represents the combination of various backgrounds including prompt events (photon candidates, electrons and jets) and non-collision backgrounds. Note that overlaps of PMT spikes with real jets are described in Section III.B.

Prompt collision events dominate the sample and populate the region around $t = 0$ ns. While it is not important for this search to further distinguish between the prompt photon sources, they mainly consist of events from QCD processes with fake $\not\!\!E_T$ (see Section IV.A.1), with minor contributions of $W \to e\nu +$ jets where the electron emits a high-E_T photon as bremsstrahlung in the tracking volume and the ν causes $\not\!\!E_T$ as described in Section V.A. These events can have large t^{γ}_{corr} and fall in the signal time window due to either Gaussian fluctuations of the measured arrival time or a wrong collision vertex selection. The latter can happen at high instantaneous luminosity when there are multiple collision vertices reconstructed and the wrong vertex is associated to the photon.

The other backgrounds are distributed over the rest of the time range in Fig. 42. These can be subdivided into two separate sources: (a) photon candidates that are emitted by cosmic ray muons as they traverse the detector ("cosmics") and (b) muons that are emitted by beam particles that hit the beam pipe upstream, travel almost parallel to the proton beam direction and finally shower into the calorimeter ("beam halo") to create a photon candidate. Section V.B shows how to separate them and describes each in detail, along with their time distributions. The contributions of each of the backgrounds to the signal time window can then be extrapolated using a fit of the measured shapes of the backgrounds in control regions outside the window of the same dataset.

Throughout this section time shapes are estimated using data from the `W_NOTRACK` trigger during the period when the EMTiming system was fully functional, corresponding to an integrated luminosity of 337 pb^{-1}. Further event selection criteria are described in each section that are used to create subsamples to study each event type separately. Note that, as $t^{\gamma}_{\mathrm{corr}}$ has been validated for all particles that pass the photon ID criteria, the results in Section III.G are also valid for the non-collision energy deposits and the jets from the collision QCD background that are both reconstructed as photons. The backgrounds for $\gamma + \not{E}_T$ events with plug photons are discussed in App. E for completeness.

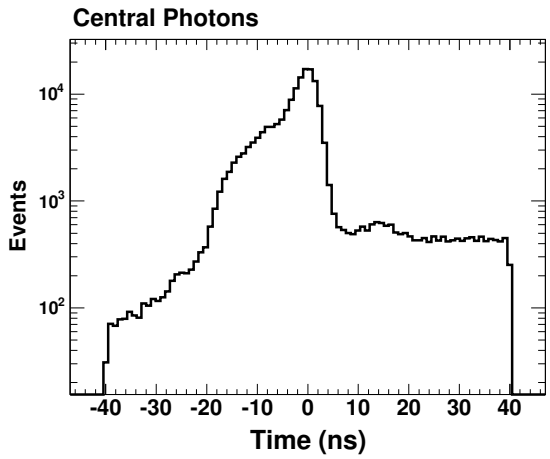

Figure 42: The $t^{\gamma}_{\rm corr}$ distribution of photon candidates for the `W_NOTRACK` sample. The distribution is a superposition of a number of different sources including prompt events (photon candidates, electrons and jets), non-collision backgrounds (cosmic ray and beam halo events and overlaps of PMT spikes with real jets). The sample is dominated by a peak at $t^{\gamma}_{\rm corr} \approx 0$ ns from prompt sources, while the regions with $|t| > 5$ ns are dominated by non-collision backgrounds. Note that the cutoffs at ± 40 ns are due to an artificial $|t^{\gamma}_{\rm corr}| < 40$ ns requirement to enlarge the prompt region.

A. Standard Model Backgrounds: Prompt Photons

Background from prompt photon production in the signal region arises from events in which either the $t^{\gamma}_{\rm corr}$ fluctuates into the signal time window or the wrong collision vertex is selected. This section begins by explaining both background shapes, their contribution to the background rate in the signal region and the systematic uncertainty of this estimate.

To study the $t^{\gamma}_{\rm corr}$ distribution for promptly produced particles, $W \to e\nu$ events from the `W_NOTRACK` sample are selected where an electron is required pass the requirements described in App. B [79]. This method is used because (a) the detector response to these and $\gamma + \not\!\!E_T$ events is identical except that the electron COT track allows for a determination of the correct vertex and (b) this sample has only small contributions from non-collision sources as it is unlikely for these to produce an EM cluster that both matches the position of a track and its momentum, as would be the case for electrons. To closely mimic the vertexing for events with photons, the electron track is dropped from the vertex clustering and the highest-$\Sigma p_{\rm T}$ vertex is picked as the most likely to have produced the "photon." Figure 43a shows the resulting electron $t_{\rm corr}$ distribution. Clearly visible is a double-Gaussian shape with contributions coming from two cases: (a) when the highest-$\Sigma p_{\rm T}$ vertex is the vertex that created the electron and (b) when there was another vertex in the event that has a $\Sigma p_{\rm T}$ greater than the one that produced the electron. This occurs in $\sim$14% of the cases. While this is an interesting number, the fraction of events where the wrong vertex is picked is very sample dependent as it is only based on the probability that the highest-$\Sigma p_{\rm T}$ vertex in the event is the same vertex that produces the photon. For example, as $Z\gamma \to \nu\nu\gamma$ processes produce very few tracks in association with the photon there is a lower probability that the highest-$\Sigma p_{\rm T}$ vertex produces the photon

at high luminosity. As a second example, in $t\bar{t}\gamma \rightarrow \gamma + \text{jets}$ events the photon is very likely to come from the highest-Σp_{T} vertex.

Figures 43b and c show that these events can be separated into right and wrong vertex subsamples by requiring a tight match ($|z_{\text{track}} - z_{\text{vertex}}| < 2$ cm and $|t_{\text{track}} - t_{\text{vertex}}| < 2$ ns) and anti-match between the electron track and the vertex, respectively. In both cases the distributions are Gaussian and centered at zero with an RMS of 0.64 ns for the right vertex selection, reflecting the system resolution as described in Section III.G, and an RMS of ∼2.0 ns when the wrong vertex is selected. This can be understood by combining the RMS of the uncorrected time distribution in Fig. 35b with the RMS of the collision t_0 distribution described in Fig. 28: $\sqrt{1.6^2 + 1.28^2} = 2.05$ ns. The number of events in the signal region can be estimated by simple extrapolation methods as described in detail in Section V.C. Next the systematic uncertainties on both shape estimates are discussed.

The dominant systematic uncertainty on the number of prompt events in the signal region where the right vertex is selected, is the uncertainty on the mean of the distribution. Figure 44 shows the relative difference between the number of events on the negative and positive sides of the time distribution for all electrons with the arrival time shown on the x-axis, or higher in magnitude. While the results are consistent with zero within a 20% error, the distribution is clearly asymmetric for the first bins. This is caused by the distribution not being centered exactly at zero and is taken into account by a systematic uncertainty on the number of prompt background events in the signal region of 20%. While the t_{corr} of the preselection sample is centered at zero, there is a variation of its mean when other requirements are applied. Figure 45 shows the mean t_{corr} of electrons in subsamples of $W + \text{jets}$ events for various electron E_T, jet E_T and $\not{E}_T$ event requirements, similar to what will be done in the optimization as explained in Chapter VII. This variation of up

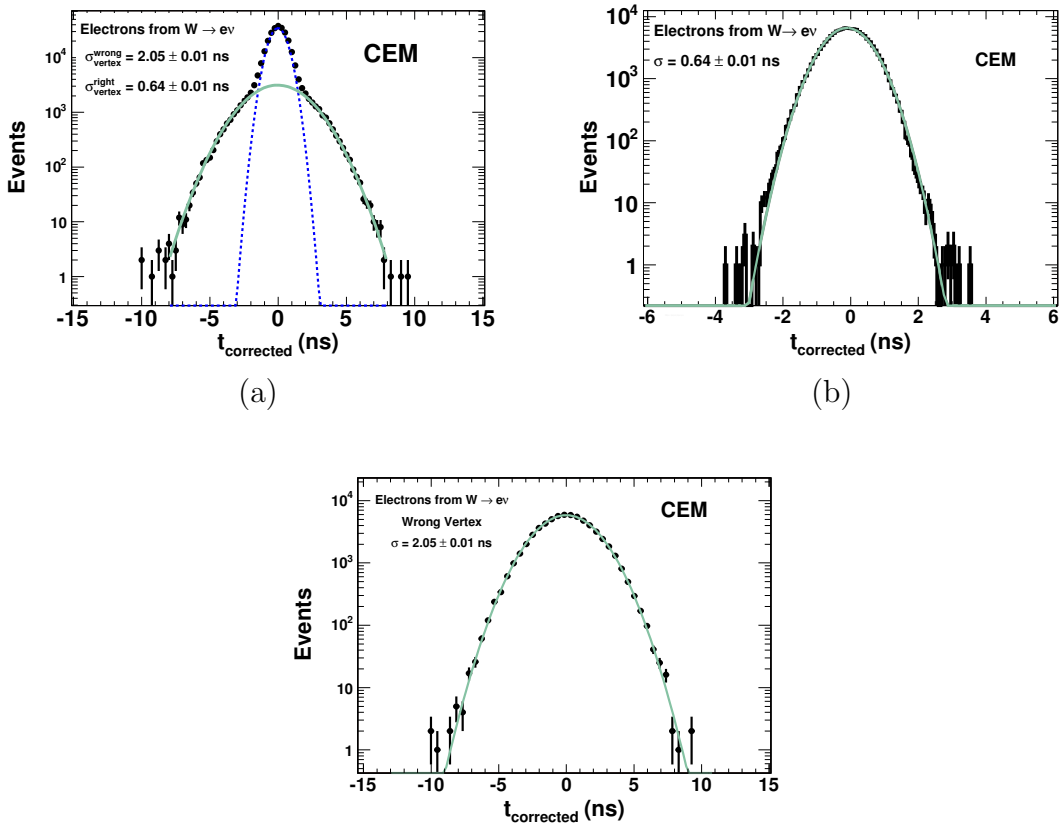

Figure 43: The electron t_{corr} in a sample of $W \to e\nu$ events. The two Gaussians correspond to the cases when the highest-Σp_{T} vertex is associated to the electron track and when it is not. They can be separated by requiring a match (b) and an anti-match (c), respectively, between vertex and electron track in both space and time.

to 0.11 ns is conservatively overestimated to 0.2 ns, and is taken as a systematic uncertainty on the mean of the right vertex distribution. The systematic uncertainty on the RMS of t_{corr} is conservatively overestimated from the fit in Fig. 43b to be 0.02 ns.

The dominant uncertainty on the wrong vertex contribution is due to the variation of the TOF due to the mismeasurement of the vertex position. Figure 46a shows the mean and RMS of the t_{corr} distribution for electrons from $W \to e\nu$ events where the wrong vertex is picked for the timing correction, as a function of tower-η. This variation is expected to be due to a geometric effect in the (wrong) TOF correction. Figure 43 shows that both right and wrong vertex distributions are Gaussian and centered at $z = 0$ cm. As the vertexing has the tendency to merge vertices close to each other in z (see Fig. 28b), wrong vertices lie on average further away from $z = 0$ cm than right vertices. Hence, for a tower at $\eta = 0$ the TOF correction overcorrects and leads to a slightly positive mean time on the order of 0.1 ns which corresponds to a distance of $\sim$5 cm. The higher the tower-η value the steeper the angle between tower and beam axis and the greater the corresponding spread of the TOF correction for this tower. Figure 46b shows that the RMS of t_{corr} increases as a function of the tower-η value from 1.8 ns at $\eta = 0$ to $\sim$2.1 ns. This variation is taken into account as a 0.28 ns systematic uncertainty on the RMS of the wrong vertex contribution to the t_{corr} distribution. As the mean TOF correction for a tower at high η, based on a symmetric Gaussian vertex distribution, is asymmetric and under-corrects on average, the mean TOF correction for these cases is shifted to the negative region as shown in Fig. 46b. This variation is taken into account with a 0.33 ns systematic uncertainty on the mean of the wrong vertex contribution to the t_{corr} distribution. Note that there are small second-order effects like (a) the correlation between vertex position and time that can introduce a slight asymmetry in the RMS between the

negative-η and positive-η towers and (b) the average vertex position as a function of tower that can lead to a slight difference in the mean t_{corr} at central and high-η towers. Both are covered by the estimated systematic uncertainty.

To summarize, the systematic uncertainties on the right vertex contribution are estimated to be 0.2 ns on its mean and 0.02 ns on its RMS. The systematic uncertainties on the wrong vertex contribution are taken to be 0.33 ns on its mean and 0.28 ns on its RMS.

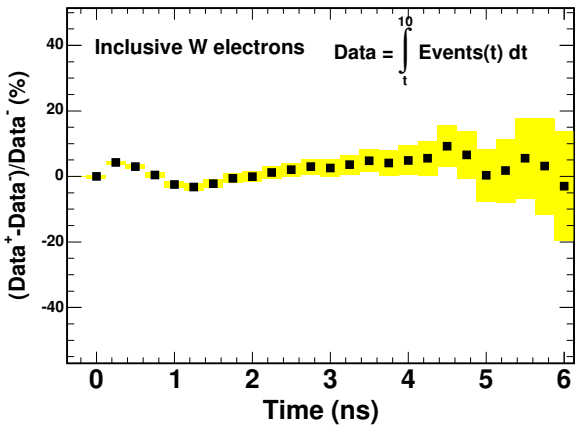

Figure 44: The fractional difference between the number of events on the negative and the positive side of the t_{corr} distribution of electrons in the $W \to e\nu$ sample. The results are well bounded by 20% error and consistent with zero. The deviation from zero in the first bins is due to the distribution not being centered exactly at zero.

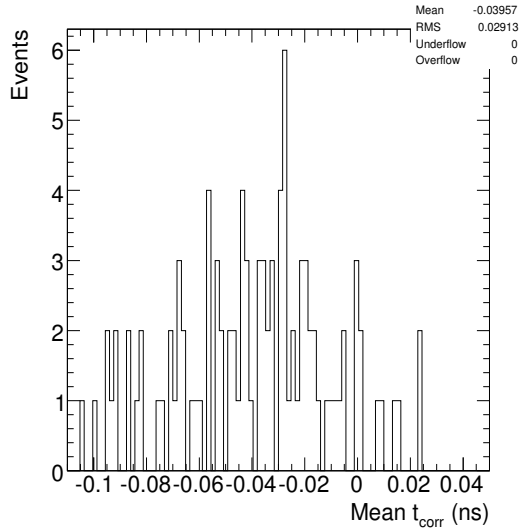

Figure 45: The mean time of arrival of electrons from various subsamples of $W \to e\nu + \text{jets}$ events where each entry reflects a different combination of the electron E_T, jet E_T and $\not\!\!E_T$ event requirements. Small variations of the kinematic requirements can slightly shift the mean of the distribution. While the mean of this distribution is close to zero, the systematic uncertainty on the mean of the primary Gaussian of the prompt time distribution is conservatively overestimated to be 0.2 ns.

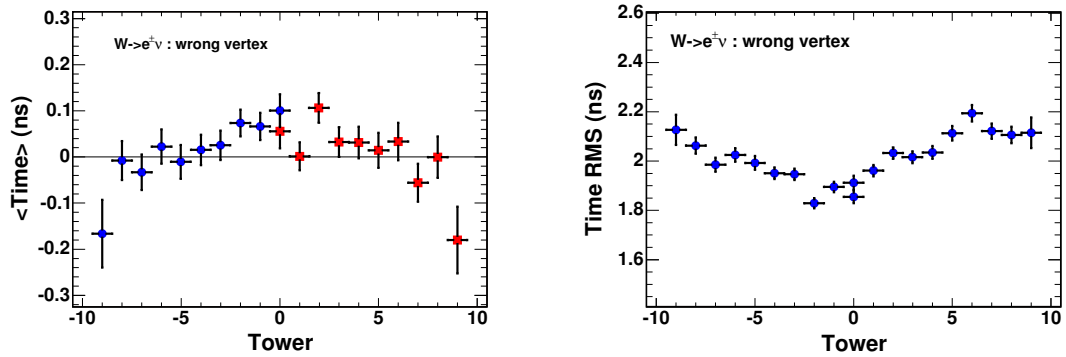

(a) (b)

Figure 46: The t_{corr} distribution mean and RMS of electrons from $W \to e\nu$ events, where the wrong vertex is picked, as a function of the tower-η where -9 (+9) corresponds to $\eta = -1$ ($\eta = +1$). Both distributions originate from a geometric effect that is described in the text, and lead to systematic variations of 0.33 ns on the mean and 0.28 ns on the RMS of the time distribution.

B. Non-Collision Backgrounds

Non-collision photon backgrounds can produce the $\gamma + \not{E}_T +$ jets signature in the detector [57]. They arise from (a) cosmic ray muons interacting with the detector material and (b) bunch interactions with the beam pipe ("beam halo"). This section discusses discusses each background in detail and describes methods for separating each.

It is believed that cosmic rays produce EM clusters that are misidentified as photons either via bremsstrahlung as it traverses the magnet, or via a catastrophic interaction with the EM calorimeter. Figure 47 shows an event with a reconstructed photon candidate that has likely been produced by a cosmic ray particle. The arrow indicates the possible trajectory of the cosmic ray particle as it traverses the detector. As cosmic ray sources interact with the detector and produce a photon randomly in time, their time distribution is constant over the full energy integration window range of 132 ns (see Section II.B).

Beam halo background events arise from particles such as muons created in interactions of proton beam bunches and gas with material near the beam pipe upstream of the CDF detector. As illustrated in Fig. 48a they travel roughly parallel to the original proton beam and can traverse the HAD and/or EM calorimeters where they radiate Bremsstrahlung. While they typically leave a small amount of energy in multiple towers, they can deposit significant energy in a single tower that can mimic a photon. Figure 48b shows the energy deposits of all calorimeter towers up to $|\eta| = 4$ in a grid in η-ϕ space from an example beam halo event; EM energy deposits are indicated in pink, hadronic in blue. Clearly visible is the tower with the photon candidate and the trail of energy deposits in towers along the z direction of the same wedge. Beam halo "photons" typically arrive a few ns earlier than prompt photons.

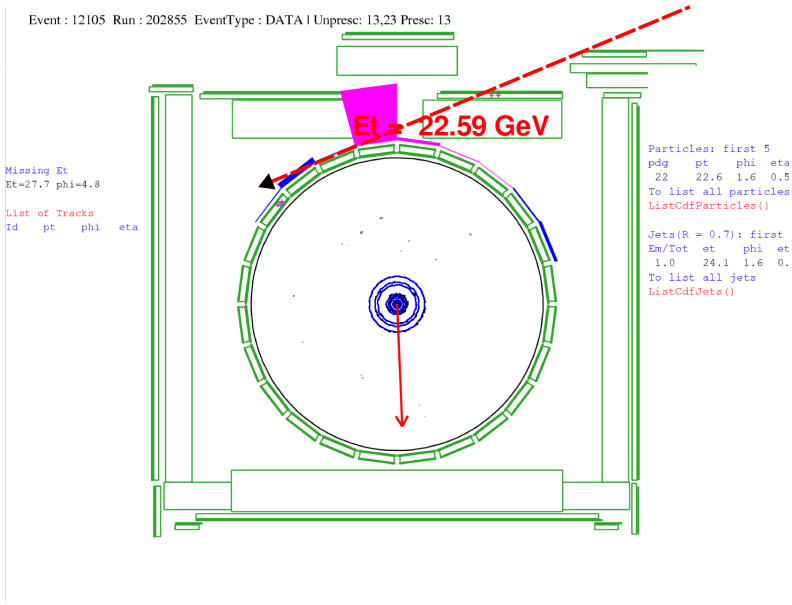

(a)

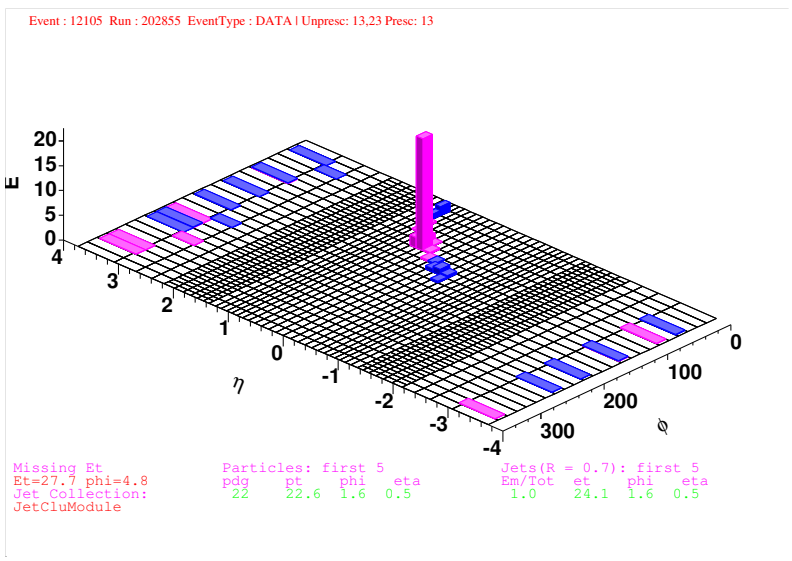

(b)

Figure 47: A view in the r-ϕ plane along the beam direction and the calorimeter towers in the η-ϕ plane for a cosmic ray background candidate. Note that (a) shows no tracks, indicating that this is a non-collision event. Also note that a cosmic ray muon does not necessarily deposit energy in the muon chambers ("muon stubs"). A possible trajectory of the cosmic ray particle is indicated with the red arrow.

However, while the rate is lower, the photon candidate can also have a $t^{\gamma}_{\rm corr}$ of $\sim$18 ns and multiples later and earlier, if the muon was created in an interaction of a satellite bunch (see Section II.B).

To quantify the $t^{\gamma}_{\rm corr}$ distribution of both non-collision backgrounds, a number of features can be used to identify and separate them from each other. Events with cosmic or beam halo photons have significant $\not\!\!E_T$ on the order of the photon E_T, and do not necessarily coincide with a collision. Therefore, the selection of the non-collision sample begins by requiring a photon to pass the photon ID criteria listed in Table X, $\not\!\!E_T > 30$ GeV and additionally no reconstructed vertex. As these events lack a vertex, the photon arrival time is not corrected for the effects described in Section III.G.2.

The primary difference between cosmics and beam halo events is that beam halo muons deposit energy in a series of towers of the same wedge along the z direction in the calorimeter. Figure 49a shows the energy deposited in the EM part of all towers in the same wedge as the photon for the non-collision subsample, and Figure 49b shows the energy deposited in the hadronic part of the plug calorimeter towers in the same wedge as the photon candidate. These distributions motivate a requirement to the EM tower energy of > 0.1 GeV and the HAD tower energy of > 0.1 GeV. This is used to show the correlation between the number of the HAD towers ("nHadTowers") and the number of the EM towers ("seedWedge") in Fig. 49c. While photons from cosmic rays are concentrated around seedWedge = 3, as it is for collision photons, beam halo populates the seedWedge = 16 region; seedWedge = 8 provides a reasonable separation. Figure 49d shows each $t^{\gamma}_{\rm corr}$ distribution in the full integration window, separated using this requirement. The next sections describe the features and time shapes of the beam halo background and cosmic rays separately. The uncertainty on the number of events in the signal region from both non-collision backgrounds are

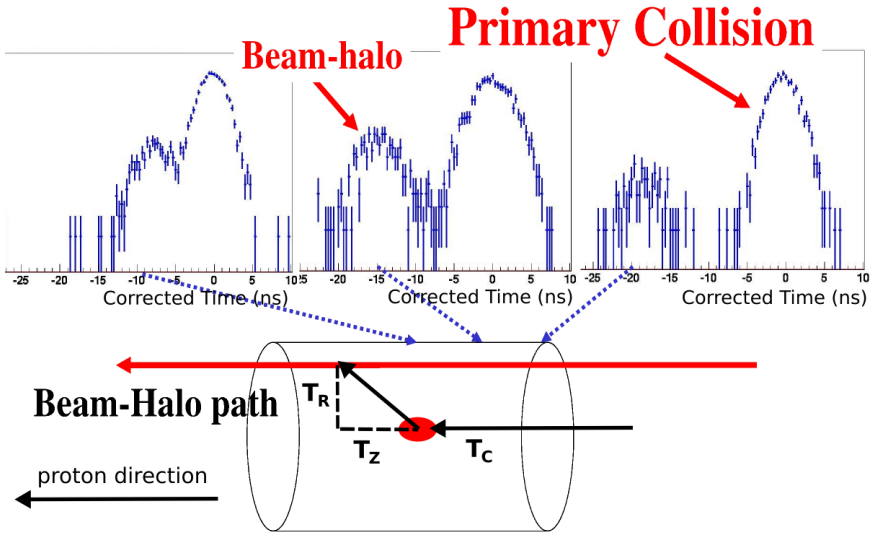

(a)

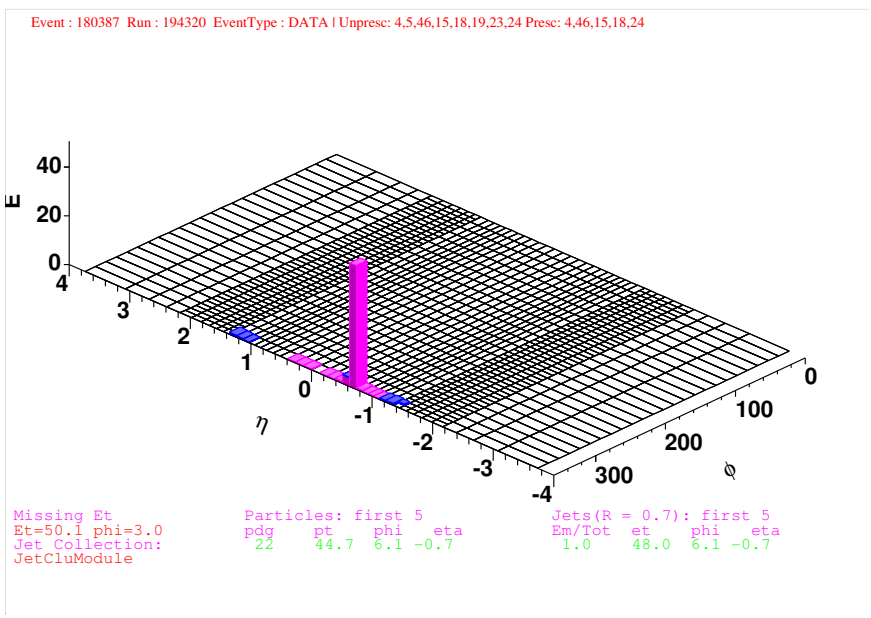

(b)

Figure 48: In (a) an illustration of a beam halo event. The beam halo path is indicated with an arrow. A comparison of the time distributions of prompt collision events and beam halo "photons" that arrive at three example towers in the calorimeter shows that it is harder to separate them the further the tower lies in beam halo direction. In (b) the energy deposits of all calorimeter towers up to $|\eta| = 4$ in a grid in η-ϕ space from an example beam halo candidate event. Beam halo tends to occupy a series of towers in the same wedge along the z direction.

dominated by the statistical uncertainty on the non-collision $t^{\gamma}_{\rm corr}$ distribution.

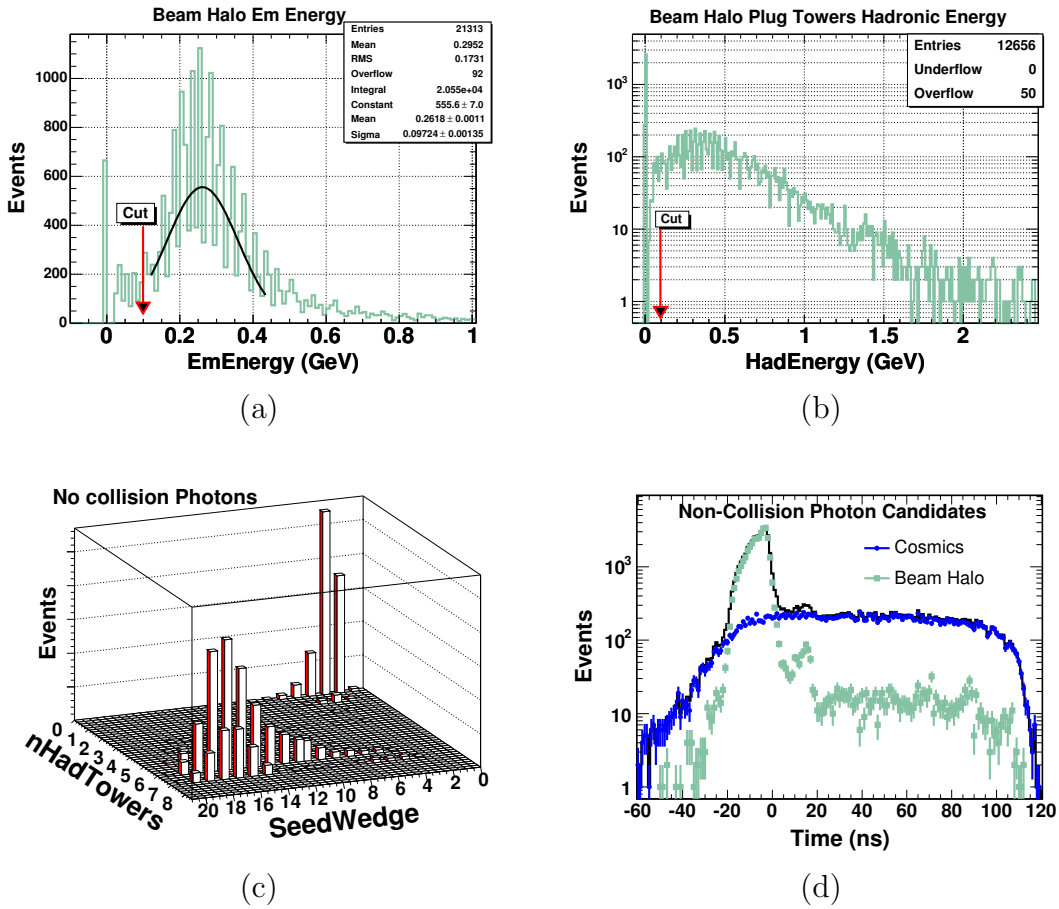

Figure 49: The separation of cosmic and beam halo backgrounds in the $\gamma + \not\!\!E_T$ sample without tracks. Beam halo muons leave a trail in the calorimeter towers in the CEM and plug HAD compartments with tower energies shown in (a) and (b). The requirement of 0.1 GeV for each is a reasonable threshold choice for selecting the number of towers in the CEM and plug-HAD. The correlation in (c) between seedWedge and nHadTowers for the non-collision sample can be used to separate beam halo from cosmic ray backgrounds. The time distribution for each is shown separately in (d).

1. *Beam Halo*

A subsample beam halo events from the non-collision sample described in the previous section is separated from the cosmic ray candidates. These events are required to have (a) energy deposits in multiple towers of the same wedge by the beam halo particle that travels roughly parallel to the beam pipe (nHadTowers > 1 and nEmTowers > 4) and (b) no muon stubs that could indicate a cosmic ray traversing the detector. The arrival time distribution in Fig. 49d shows that (a) in the majority of events the photon candidates typically arrive at the calorimeter at negative $t^{\gamma}_{\rm corr}$ between -15 and 0 ns, and (b) peaks in a distance of ∼18 ns, due to interactions of satellite bunches (see Section II.A). Feature (a) can be understood from geometry as shown in Fig. 48a by comparing the arrival time to a vertex time of $t_0 = 0$ ns. While beam halo muons travel during the time T_Z along the beam line in z and interact with the tower, a collision event would produce a photon at the time T_C that travels from the collision to the calorimeter tower in the time T_R. The hypothetical time it would take the photon for each case to reach the tower is:

$$\begin{aligned} t^{\rm Coll\ Ev}_{\rm arrival} &= T_C + \sqrt{T_Z^2 + T_R^2} \\ t^{\rm BH}_{\rm arrival} &= T_C + T_Z \ . \end{aligned} \tag{5.1}$$

Since the EMTiming system is calibrated on the collision events that have $t^{\gamma}_{\rm corr} \equiv 0$ ns (see Section III.G.1), the beam halo events have a corrected time of:

$$t^{\rm BH}_{\rm corr} = t_{\rm BH} - t_{\rm Coll\ Ev} = T_Z - \sqrt{T_Z^2 + T_R^2}, \tag{5.2}$$

which is always a negative number for beam halo from the primary bunch. Figure 50a shows the $t_{\rm corr}$ of the photon candidates as it hits towers in the CEM with different rapidities. The mean $t_{\rm corr}$ increases from negative to positive rapidities as shown in

Fig. 50b as expected from a particle that traverses the detector in z direction parallel to the proton beam. Figure 50c shows that ∼40 times more muons travel along two out of the 24 wedges (numbered 0 and 23) due to interactions of beam particles with the CDF "Roman Pot" spectrometers that are located upstream close to the proton beam at $\phi \approx 0°$ [80]. This feature helps to reduce beam halo events in the cosmics sample selection below.

The kinematic features of beam halo candidate events are shown in Fig. 51. Since the photon candidate is from a non-collision source, most of the $\not\!\!E_T$ is expected to be caused by the photon E_T and opposite in ϕ to the photon. The photon E_T falls rapidly towards high E_T as expected for collisions of muons in the calorimeter.

The rate at which beam halo events populate the signal time window is small and can be estimated from the shape in Fig. 49d, as described in Section V.C. While for the background estimate the arrival time for collision backgrounds is corrected as shown in Section III.G, Fig. 52 shows that the corrected arrival time for beam halo can be obtained by smearing the uncorrected arrival time with the RMS of the interaction time of 1.3 ns (see Fig. 28) as the collision time is uncorrelated. The figure compares the $t^{\gamma}_{\rm corr}$ in a single tower (tower-$\eta = -5$) of beam halo events with a vertex ($\Sigma p_{\rm T} > 1$ GeV/c), before and after subtracting the vertex t_0 for arrival times between -21 ns and -5 ns. As expected for an arrival time that is not correlated to the collision time, the RMS with the vertex correction is, in quadrature, greater than the RMS without correction by the collision time RMS of 1.3 ns. To conclude, the timing shape in Fig. 49d can be used to estimate the background in the search, after convolution with a Gaussian of RMS of 1.3 ns, representing the collision time distribution.

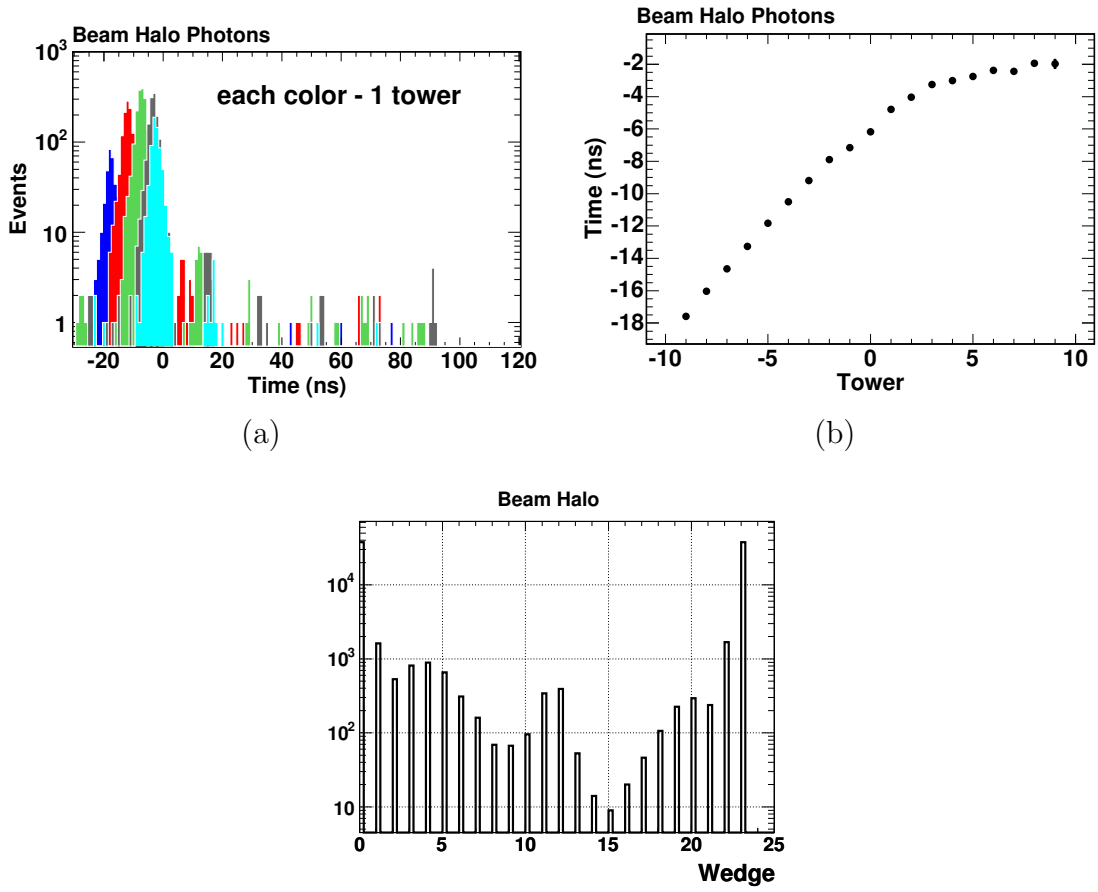

Figure 50: In (a) the time distribution of photons from beam halo candidate events separated into different photon towers in η. Figure (b) shows that the mean arrival time of these photons is later the further this tower is downstream along the proton beam direction, as expected. Figure (c) shows the number of beam halo photon candidates as a function of the ϕ position (note that wedges numbered 0 and 23 are adjacent). Most photons ($\sim$80%) arrive in 2 out of 24 wedges due to interactions of beam particles with the CDF "Roman Pot" spectrometers [80].

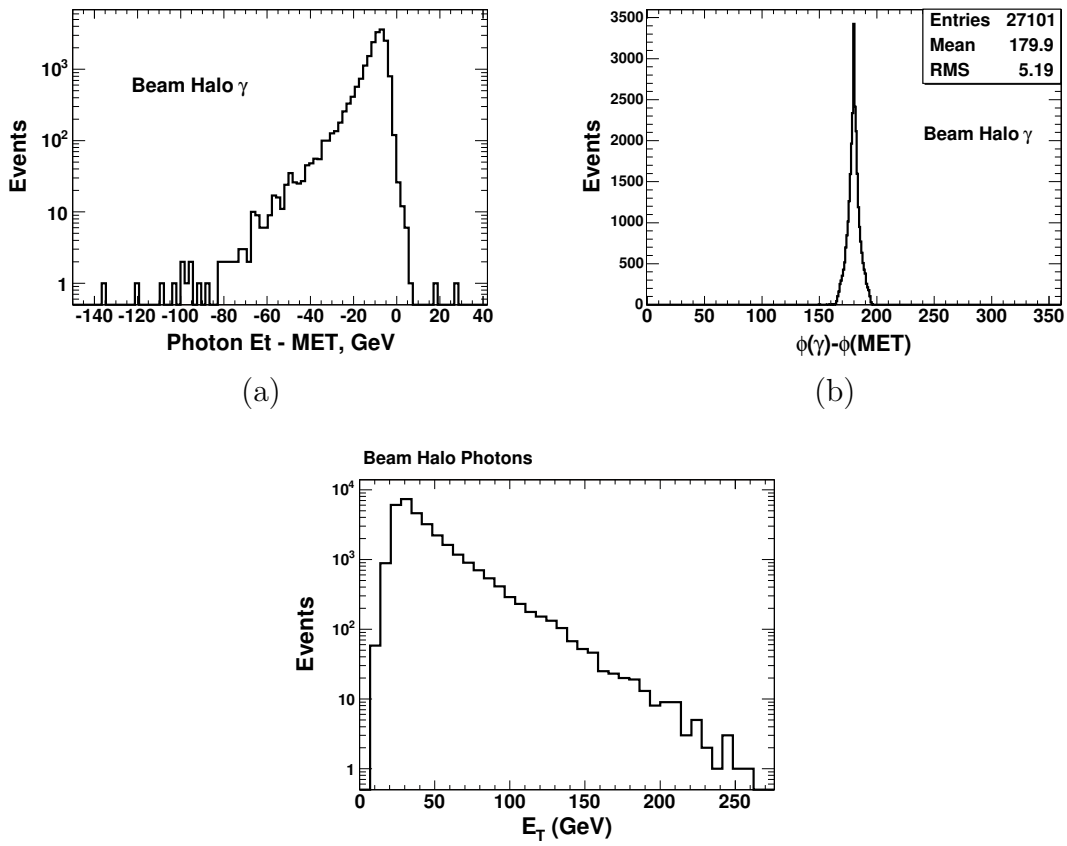

Figure 51: Kinematic distributions of the beam halo subsample indicating that it is from non-collision sources. In (a) the difference between photon E_T and $\not\!\!E_T$ is centered around zero as expected. In (b) the $\Delta\phi$ is centered at 180° as expected as the photon and $\not\!\!E_T$ are back-to-back. In (c) the E_T spectrum of the photon that both falls off rapidly towards high E_T and at low energies as the `W_NOTRACK` trigger is fully efficient only for $E_T > 30$ GeV as described in Section IV.B.

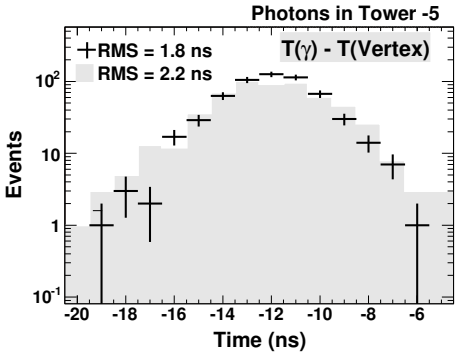

Figure 52: The t_{corr} for beam halo events with a vertex ($\Sigma p_{\mathrm{T}} > 1$ GeV/c), before (shaded) and after (histogram with error bars) subtracting the vertex t_0. The distribution after the vertex correction has an RMS that is by 1.3 ns (the collision t_0 RMS) in quadrature greater compared to before the correction. This is expected for events in which the arrival time and the collision time are uncorrelated.

2. *Cosmic Rays*

A subsample of cosmics events is created from the non-collision sample by removing the beam halo candidates. This is done by rejecting (a) photon candidates in wedges 0 and 23 where beam halo most likely deposits energy and (b) beam halo photon candidates that deposit energy in more than 4 towers of the same wedge (nHadTowers = 0 and nEmTowers < 5). Figure 49d shows that the t^{γ}_{corr} distribution of photons from cosmic rays is mostly uniform as expected. The finite energy integration window causes the photon energy to be increasingly undermeasured as it approaches -30 ns and 100 ns which causes a falloff in the rate in both regions.

As in beam halo events, since most of the $\not{E}_T$ is almost always caused by the photon E_T, it is expected to be opposite in ϕ to the photon, as shown in Fig. 53. Large values for the difference between $\not{E}_T$ and photon E_T comes from muons that deposit additional energy in the same or neighboring wedges as they traverse the detector and can be identified as jets. The photon E_T distribution falls rapidly towards high E_T, as expected, as cosmic muons are less likely to emit bremsstrahlung photons with high energy. A total of 93% of the cosmics candidate events in this sample contain a muon stub. In most of those events the photon is $< 30°$ away from the muon in ϕ as energy deposits from muons that enter the calorimeter at low incident angles are more likely to be reconstructed as photons.

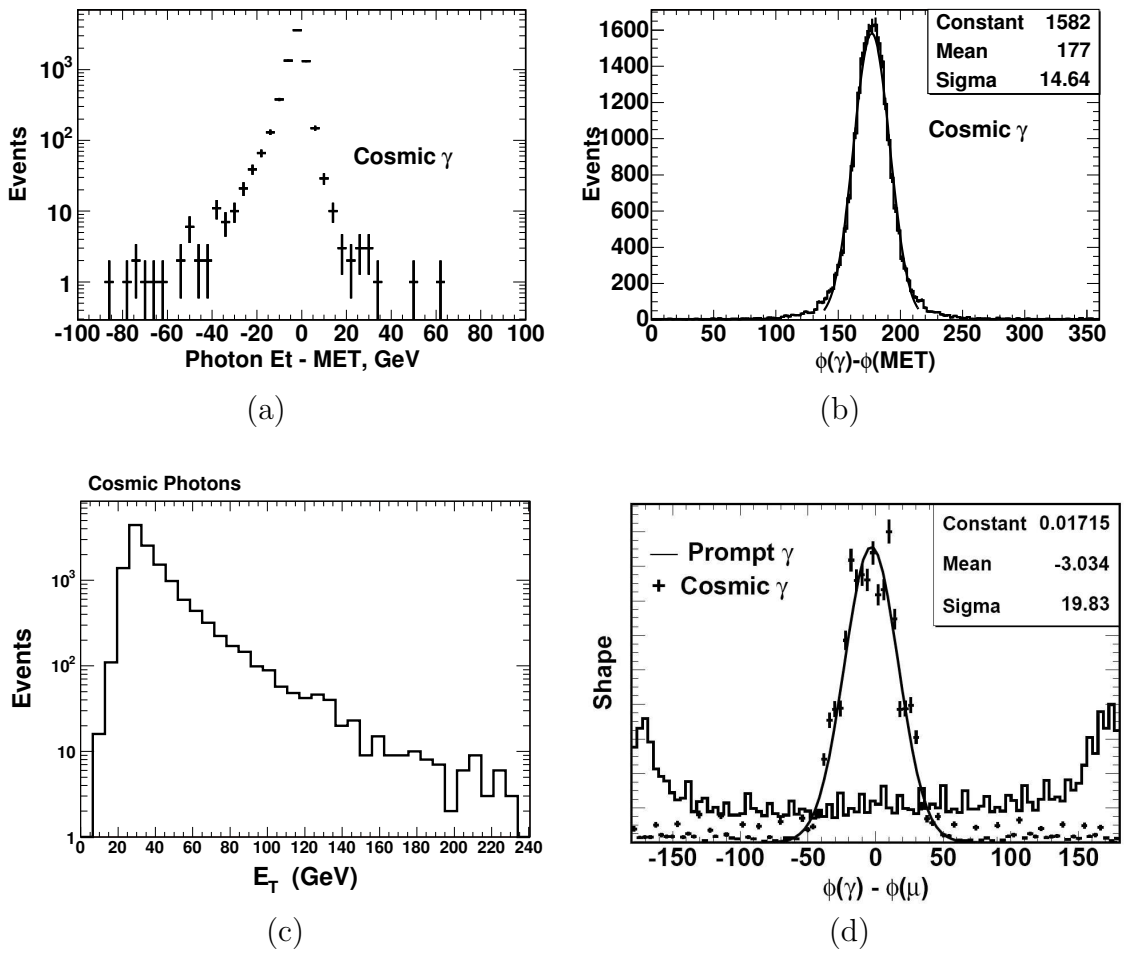

Figure 53: Plots showing that the cosmics subsample is from non-collision sources. In (a) the difference between photon E_T and $\not{E}_T$ is centered around zero as expected. In (b) the $\Delta\phi$ is centered at 180° as expected. In (c) the E_T spectrum of the photon that falls off rapidly towards high E_T, as does the momentum distribution of cosmics, and falls off at low energies as the `W_NOTRACK` trigger is fully efficient only for $E_T > 30$ GeV as described in Section IV.B. In (d) for the events that contain a muon stub (93% out of all cosmics candidates), the difference in ϕ between the photon and the muon stub. Most of those events have $|\Delta\phi| < 30°$ as energy deposits from muons that enter the calorimeter at low incident angles are more likely to be reconstructed as photons.

C. Background Estimation and Methods

In this section the background estimation methods are motivated and described. It begins with a presentation of the main ideas and then moves to the estimation algorithm.

The final signal region of the search for heavy, neutral, long-lived particles is defined by the sample of events that pass a set of final kinematic and time window requirements. The method for determining the number of background events in the signal region is based on data alone using events that pass all but the final time window requirement. The t^{γ}_{corr} distributions of the background sources discussed in the previous sections serve as shape "templates" for each source. The shape templates are normalized to the data in control time regions outside the signal region to estimate the number of background events in the signal time window. The t^{γ}_{corr} requirements on the final sample for both signal and control regions are motivated below. Figure 57a shows all background sources in the full time window using an example set of requirements.

Since the method is based on the t^{γ}_{corr} distributions alone we can create background estimates for a large number of potential signal regions, each corresponding to different sets of kinematic and final timing cuts. In other words, given a sample defined by kinematic cuts alone we can estimate the number of background events in a potential signal time window using sensibly chosen control regions. Thus, we can predict the backgrounds for a large variety of final sets of cuts and use these estimates as part of an optimization procedure described in Chapter VII.

As previously described, the backgrounds can be separated into two classes: collision and non-collision backgrounds such as cosmic rays and beam halo. Figures 43a and 49d, respectively, show the t^{γ}_{corr} shapes of the photon candidates in each back-

ground separately. The region around 0 ns is dominated by collision data, while large positive times are dominated by cosmic rays, and negative times are dominated by beam halo. Using a separate control time region for each of these three backgrounds minimizes the correlation between them in the final background estimate methods.

The cosmics time distribution is essentially constant in time so our control region is defined to be $[25, 90]$ ns and is chosen such that (a) it is well above the beam halo secondary peak at at ~ 18 ns (see Section V.B.1) and (b) does not not include the region close to the end of the ADMEM energy integration gate where the event rate falls sharply. The beam halo control region $[-20, -6]$ ns is chosen such that (a) it contains most of the beam halo events but (b) stays well away from the region dominated by the prompt photon production. The collision data control region is defined to be $[-10, 1.2]$ and is chosen such that (a) we include as much of the collision data as possible to get the ratio of right to wrong vertices as accurately as possible, and (b) allows for a potential signal region above 1.2 ns. While the precise upper time limit of the signal region at 10 ns is not quantitatively motivated, it contains most of a long-lived signal on the order of nanosecond lifetimes as the time distribution falls exponentially (see Fig. 41). Next, the prediction method for each background is described.

The background prediction for each subsample of events after the kinematics-only (e.g. preselection) requirements is done as a two-step process. The first step is to estimate the contributions from the right and wrong vertex collision background and take into account non-collision contamination. The second step is to use the collision shapes to estimate the non-collision backgrounds using a simultaneous fit.

For step 1, the right and wrong vertex background is estimated using the time control window $[-10, 1.2]$ ns (expected to be dominated by collision data), but excluding wedges other than 0 and 23 which contain the bulk of the beam halo con-

tribution. The non-collision contamination is estimated by fitting the beam halo and cosmics templates, separated as described in Section V.B, simultaneously in the control regions $[-20, -6]$ ns (beam halo dominated) and $[25, 90]$ ns (cosmics dominated), and extrapolating to the collision control region $[-10, 1.2]$ ns, where they are subtracted off. The remaining data is then re-fit using the Gaussian functions as shown in Fig. 43a. While the mean and RMS of the functions are fixed, the relative normalization of wrong and right vertex collision events is allowed to float. Then the normalization is scaled by a factor of 24/22 to account for the data in wedges 0 and 23. If we choose the kinematics-only sample to be the dataset that passes the preselection criteria (see Table X) the resulting fraction of wrong vertex events in the kinematics-only sample is $(3\pm1)\%$. The statistical error on the prediction in the signal region is determined by the fit and takes into account the correlation matrix. The systematic uncertainty on the number of events in the signal time window is estimated by varying the mean and RMS of the collision background time shapes. As discussed in Section V.A, the uncertainty on the mean is estimated to be 200 ps (330 ps) and on the RMS to be 20 ps (280 ps) for the primary (secondary) Gaussian distribution.

For step 2, the rate of the non-collision backgrounds is determined. A fit is performed for the normalization in all wedges in the beam halo and cosmic ray time control regions, after subtracting off the expected contamination from collision sources obtained in step 1. The uncertainties on this estimate are dominated by the statistical uncertainty on the non-collision templates and the systematic uncertainty on the prompt background.

With this technique, the background estimation is robust enough to be applied to a variety of kinematic sample requirements. This feature will be used, along with the simulated acceptance of GMSB events discussed in the next chapter, for the

optimization in Chapter VII.

CHAPTER VI

ACCEPTANCES TO GMSB EVENTS AND THEIR SYSTEMATIC UNCERTAINTIES

As there are no set of established GMSB events available, a MC simulation is used to mimic both the event generation and the detector response to allow for an estimation of the sensitivity to GMSB models. For this estimate all GMSB processes are simulated, including those with no direct sensitivity, to produce the best expected 95% confidence level (C.L.) cross section limits [81]. This chapter defines the acceptance, describes how it is estimated, including MC correction factors, and describes and estimates the various sources of the systematic uncertainty.

To map out the sensitivity for GMSB models for the Snowmass Slope choices of $\widetilde{\chi}_1^0$ mass and lifetime parameters (SPS 8) [29] (see Section I.B.2) MC samples are generated at various GMSB model points for $m_{\widetilde{\chi}}$ between 65 GeV/c^2 and 130 GeV/c^2 and $\tau_{\widetilde{\chi}}$ between 0 ns and 40 ns. For each simulated GMSB point the particle properties (mass, branching fractions etc.) are calculated with ISASUGRA [82]. As mentioned in Section I.B.2.b, $\widetilde{\chi}_2^0\widetilde{\chi}_1^{\pm}$ and $\widetilde{\chi}_1^+\widetilde{\chi}_1^-$ production dominates, followed by prompt decays to $\widetilde{\chi}_1^0$'s in association with taus. It will be shown later in Chapter VII that on average $\sim$5% of the GMSB events produced will pass all selection requirements. The size of the MC samples is chosen such that their statistical uncertainty is with $\sim$1% negligible to the combined systematic uncertainty.

A. Simulated Acceptance and Efficiencies for GMSB Models

The total event acceptance, used to estimate the expected sensitivity described later in Chapter VII, is given by:

$$A \cdot \epsilon = (A \cdot \epsilon)_{\text{Signal MC}} \times C_{\text{MC}} \tag{6.1}$$

where A is the fraction of events that pass fiduciality, trigger and kinematic requirements (acceptance), and ϵ the fraction of these events that remain after the t^{γ}_{corr} requirement (efficiency). Both are calculated for each GMSB parameter point based on the preselection requirements and the subsequent stringent requirements determined by the optimization described in Chapter VII. The term C_{MC} is a correction factor to the $(A \cdot \epsilon)_{\text{Signal MC}}$ from the MC simulation for small effects that are not simulated in the MC. While the efficiency loss due to the cosmic ray rejection requirement (see Section V.B.2) is included in this factor, multiple collision effects that are simulated separately in a simplified way.

The fraction of GMSB events lost due to cosmic rays overlapping the signal events causing the events to fail the muon co-stub requirement is not simulated in the MC. This acceptance loss is included in the acceptance calculation as a multiplicative factor C_{MC}. It is estimated to be equal to the efficiency of the muon co-stub requirement measured from the preselection sample by requiring the photons to be within $|t^{\gamma}_{\text{corr}}| <$ 10 ns to select collision events with high purity. There are 12583 events in this sample. As will be shown later this sample has a negligible contribution from cosmics (see the table on p. 149). 12360 events remain after the cosmics rejection cut, giving an efficiency of $C_{\text{MC}} = 12360/12583 = (98.2 \pm 1)\%$, with the error conservatively overestimated by rounding to the nearest percentage.

Multiple collisions in the event can produce extra vertices, one of which can

be picked incorrectly as the event vertex. To take this effect into account in the acceptance calculation, a fake vertex is simulated for each event with a z_0 and t_0 that is randomly selected from a Gaussian of $\sigma_z = 30$ cm and $\sigma_t = 1.3$ ns, respectively. The wrong vertex fraction of events is assumed to be (3±1)%, a number that has been obtained for the preselection sample (see Section V.C). This is a conservative estimate as the average vertex Σp_{T} for GMSB is higher than for QCD events that dominate the SM background. As will be shown later in Section VI.B, while this number varies between samples, it has a negligible impact on the acceptance.

The breakdown of events after passing each of the preselection requirements in Table X for an example GMSB point at $m_{\widetilde{\chi}} = 100$ GeV and $\tau_{\widetilde{\chi}} = 5$ ns is shown in Table XII. The acceptance for other requirements used in the optimization and final event selection are estimated with the same technique and are given in Chapters VII and VIII. The next section presents the estimation of the systematic uncertainties on the signal MC sample.

Table XII: Summary of the event reduction for a GMSB example point at $m_{\widetilde{\chi}} = 100$ GeV and $\tau_{\widetilde{\chi}} = 5$ ns as it passes the preselection cuts of Table X. Note that the efficiency of the μ co-stub requirement is implemented as an MC correction factor, C_{MC}. Other event requirements as part of an optimization procedure are described in Chapter VII.

Requirement	Events passed	$(A \cdot \epsilon)_{\text{Signal MC}}$ (%) ($m_{\widetilde{\chi}} = 100$ GeV and $\tau_{\widetilde{\chi}} = 5$ ns)
Sample events	120000	100.00
Central photon with $E_T > 30$, $\not{E}_T > 30$	64303	53.6
Photon fiducial & ID cuts	46730	38.9
Good vertex	37077	30.9
≥1 jet with $E_T > 30$ GeV and $\lvert\eta\rvert < 2.0$	28693	23.9
μ co-stub cut ($\times C_{\mathrm{MC}}$)	N/A	23.5

B. Estimation of the Systematic Uncertainties

A proper sensitivity estimate must take into account the uncertainties in the luminosity, background, acceptance and GMSB production cross sections. As described in Section II.B, the systematic uncertainty on the luminosity is estimated to be 6% with the dominant contribution from uncertainties on the CLC acceptance from the precision of the detector simulation and the event generator. As described in Section V.C, the uncertainty on the background in the signal region is determined from the understanding of the collision and non-collision sources from the control regions and is estimated from $W \to e\nu$ and non-collision events. The acceptance and cross section uncertainties are estimated in the subsections below. To summarize, the systematic uncertainty on the acceptance-MC sample is estimated to be 8.8% with major contributions from the uncertainty on the time distribution shape and the photon ID efficiency. The uncertainty on the NLO production cross section is estimated from parton distribution (or density) functions (PDFs) and the renormalization scale to be 6.4%. The uncertainties on acceptance and cross section are typically ∼10% and ∼6%, respectively. They are summarized in Table XIII for an example GMSB point of $m_{\widetilde{\chi}} = 94$ GeV and $\tau_{\widetilde{\chi}} = 10$ ns and have negligible variation as $m_{\widetilde{\chi}}$ and $\tau_{\widetilde{\chi}}$ are varied. The optimization and limit setting described in Section VII uses a combined uncertainty of 10% on the acceptance and production cross section. All uncertainties are consistent with a recent GMSB diphoton analysis [41], except the Initial/Final State Radiation (ISR/FSR) uncertainty, as that analysis requires two prompt photons while this analysis requires one delayed photon and a jet making it less sensitive to ISR/FSR. We next summarize the individual uncertainties.

Table XIII: Summary of the systematic uncertainties on the acceptance and production cross section for an example GMSB point at $m_{\widetilde{\chi}} = 94$ GeV and $\tau_{\widetilde{\chi}} = 10$ ns. For the optimization they are combined in quadrature to produce a 10% uncertainty on the acceptance. The estimation procedures are described in detail in the subsections of Section VI.B.

Factor	Relative Systematic Uncertainty (%)
Acceptance:	
$t^{\gamma}_{\rm corr}$ measurement and vertex selection	6.7
Photon ID efficiency	5.0
Jet energy scale	1.0
Initial and Final State Radiation	2.5
Parton Distribution Functions	0.7
Total	8.8
Cross section:	
Parton Distribution Functions	5.9
Renormalization scale	2.4
Total	6.4

1. Time Measurement

There is a systematic uncertainty on the acceptance due to variations in the $t^{\gamma}_{\rm corr}$ distribution. Three types of uncertainties are considered simultaneously: (1) a shift in the mean of the $t^{\gamma}_{\rm corr}$ distribution, (2) a change in the RMS of the $t^{\gamma}_{\rm corr}$ distribution and (3) a change in the fraction of events that have an incorrectly chosen vertex.

As explained in Section V.A, the variation on the mean of the right (wrong) vertex $t^{\gamma}_{\rm corr}$ distribution is conservatively overestimated to be 0.2 ns (0.33 ns). This can shift events into and out of the signal region. The fractional variation in acceptance due to this effect is estimated to be 6.7%. The uncertainty on the RMS of a prompt distribution, as estimated from a fit of electrons from $W \to e\nu$ events, is 0.01 ns as shown in Fig. 43. The magnitude of any effect is conservatively overestimated by doubling the variation. The fractional change in acceptance due to this effect, again

due to events shifting in and out of the signal region, is estimated to be 0.03%. The fraction of events for which the wrong vertex is picked has been estimated to be 3% with an uncertainty of 1% on the fit to the negative time side of the background data distribution as described in Section VI.A. To estimate the impact of this uncertainty on the acceptance the fraction of wrong vertex events from the MC simulation is varied by 1%, obtaining an uncertainty of 0.1%. To estimate the impact on the acceptance from a variation of the wrong vertex fraction depending on the event requirements, the wrong vertex fraction is varied between 0% and 10%, obtaining a variation of $< 1.5\%$. The total systematic uncertainty due to uncertainties on the $t^{\gamma}_{\rm corr}$ distribution is taken to be the orthogonal sum of the uncertainties of each effect and equal to 6.7%. The timing effects form the dominant contribution to the systematic uncertainty on the acceptance.

2. Photon ID Efficiency

As described in Section III.D, the systematic uncertainty on the photon ID efficiency is estimated to be 5.0%.

3. Jet Energy

As the event preselection requires a jet with a corrected $E_T > 30$ GeV we have studied the uncertainty on the acceptance if the jet energy is systematically mismeasured. The jet energy is corrected for several effects as listed in Section IV.A.2 with the known uncertainties on each effect as described therein. One uncertainty that is not part of the corrections is the "splash-out" energy. While the out-of-cone jet energy correction (see Section IV.A.2) takes into account the energy that falls outside a jet cone of 0.7, but within a cone of 1.3, MC samples show that an average additional energy of 0.5 GeV falls outside this cone. Half of this energy is taken as systematic uncertainty.

To conservatively overestimate the acceptance uncertainty, the jet energy is varied by all uncertainties simultaneously in the positive and in the negative energy direction using a standard CDF procedure [83]. The resulting variation in the acceptance is 1.0%.

4. Initial and Final State Radiation

Initial state radiation (ISR) caused by a gluon radiating from an incoming parton or final state radiation (FSR) from an outgoing jet can both make the E_T spectrum of the final state particles softer than expected without radiation. This can cause the photon, the jet or the $\not\!\!E_T$ to be systematically more likely to fail the kinematic requirements. This effect carries a non-negligible theoretical uncertainty and is estimated using the standard CDF procedure by varying the Sudakov parameters as described in [84]. Doing so we find the variation in the acceptance, taken to be the systematic uncertainty, at 2.5%.

5. Parton Distribution Functions

In an event where the proton and antiproton bunches collide it is mostly a single subparticle of the (anti-)proton, a parton (quark or gluon), that participates in the hard collision and produces a high center-of mass energy event. The momentum fraction, described by parton distribution functions (PDFs), that is carried by each of the partons in the proton or antiproton is not perfectly understood. It affects both the rate at which a process happens (the production cross section) and the kinematics of the outgoing final state particles (the acceptance of the event selection criteria).

For each simulated event the MC generator calculates the momentum fraction of the colliding parton using a standardized "PDF-set" by the CTEQ collaboration (CTEQ-5L) [85]. As only the newer PDF-set version CTEQ-6M contains 90% confidence

intervals for each eigenvector, the total uncertainty is estimated using a standard procedure by reweighting the parton momenta of the original CTEQ-5L set and varying the PDFs using the uncertainties from CTEQ-6M as described in [85]. For the example GMSB point the relative uncertainty is $+0.7\%$ -0.5% [86] on the acceptance and $+5.9\%$ -5.3% on the cross section. To be conservative the larger value of each is taken as the systematic uncertainty.

6. Renormalization Scale

While the dominant GMSB production mechanisms are via electroweak processes (see Fig. 1), the probability of QCD processes in the events that occur through gluon emission and higher-order loops depend sensitively on the energy scale at which the process happens. The PYTHIA event generator [62] determines the renormalization scale from the center of mass energy of each event ($\hat{s}$) which can be much larger than the energy scale of the outgoing particle. This can lead to a systematic variation of the NLO production cross section which is estimated with a standard technique of varying the renormalization scale (q) between $0.25{\cdot}q^2$ and $4{\cdot}q^2$ using PROSPINO2 [87]. The variation of the cross section is 2.4% for the example GMSB point which is consistent with the results in [41].

CHAPTER VII

OPTIMIZATION AND EXPECTED SEARCH SENSITIVITY

In this chapter the expected search sensitivity is determined and estimated. Now that the background and the signal acceptances, with uncertainties, are available for a given set of requirements, a procedure to optimize the search sensitivity can be readily employed that allows for a determination of the best event requirements for a prospective GMSB signal before unblinding the signal region.

The sensitivity for various GMSB parameter points is estimated in the form of expected 95% C.L. upper cross section limits (σ_{95}^{exp}) using a Bayesian calculation with a constant cross section prior [88, 89] for the total GMSB production. Each such limit is calculated from the 95% C.L. upper cross section limits ($\sigma_{95}(N_{\text{obs}})$) based on the number of events N_{obs} "observed" in a pseudo-experiment, assuming no GMSB signal exists. For a fixed integrated luminosity of $\mathcal{L} = (570 \pm 34)$ pb^{-1}, $\sigma_{95}(N_{\text{obs}})$ is a function of the number of predicted background events and the $(A \cdot \epsilon)$ of the expected signal for each GMSB parameter point. Both factors depend, in turn, on the specific event requirements thus making $\sigma_{95}(N_{\text{obs}})$ dependent on these requirements (cuts), $\sigma_{95}(N_{\text{obs}}, \text{cut})$. To summarize, $\sigma_{95}(N_{\text{obs}}, \text{cut})$ is determined from:

$$\begin{aligned} 0.95 &= \int_0^{\sigma_{95}(N_{\text{obs}},\text{cut})} \mathrm{d}\sigma \;\; \text{Poisson}(N_{\text{obs}}, \mu_{\text{exp}}(\sigma, \text{cut})) \qquad (7.1) \\ \text{where} \quad \mu_{\text{exp}}(\sigma, \text{cut}) &= N_{\text{exp}}(\text{cut}) + \sigma \cdot \mathcal{L} \cdot (A \cdot \epsilon)(\text{cut}) \end{aligned}$$

is the sum of the number of expected background (N_{exp}) and expected signal events, and Poisson(N_{obs},μ_{exp}) is the normalized Poisson distribution of N_{obs} with mean μ_{exp}. The uncertainties on the signal efficiencies, backgrounds and luminosity are treated as nuisance parameters with Gaussian priors [89].

The expected cross section limit is calculated from $\sigma_{95}(N_{\text{obs}}, \text{cut})$ and takes into

account all possible outcomes of the pseudo-experiments, determined by their relative Poisson-probability To summarize, the expected cross section limit and its RMS are given by:

$$\sigma_{95}^{\rm exp}({\rm cut}) = \sum_{N_{\rm obs}=0}^{\infty} \sigma_{95}(N_{\rm obs}, {\rm cut})\ {\rm Poisson}(N_{\rm obs}, \mu_{\rm exp} = N_{\rm exp}({\rm cut})) \tag{7.2}$$

$$\begin{aligned} {\rm RMS}^2({\rm cut}) &= \sum_{N_{\rm obs}=0}^{\infty} (\sigma_{95}(N_{\rm obs}, {\rm cut}) - \sigma_{95}^{\rm exp}({\rm cut}))^2 \\ &\qquad \cdot\ {\rm Poisson}(N_{\rm obs}, \mu_{\rm exp} = N_{\rm exp}({\rm cut})). \end{aligned} \tag{7.3}$$

Each GMSB point has its optimal values for a set of requirements where $\sigma_{95}^{\rm exp}({\rm cut})$ is minimized. The set of requirements is chosen to be the event kinematic requirements and an additional requirement on the azimuthal angle between $\not\!\!E_T$ and the highest-E_T jet ($\Delta\phi(\not\!\!E_T, {\rm jet})$) which helps reduce events where the $\not\!\!E_T$ is overestimated because of a poorly measured jet: Photon E_T, $\not\!\!E_T$, jet E_T, $\Delta\phi(\not\!\!E_T, {\rm jet})$ and the lower limit on $t_{\rm corr}^{\gamma}$ (the upper limit on $t_{\rm corr}^{\gamma}$ is kept constant at 10 ns as discussed in Section V.C). As an illustration of the optimization, Figures 54 and 55 show the expected cross section limit for a GMSB example point at $m_{\widetilde{\chi}} = 100$ GeV/c^2 and $\tau_{\widetilde{\chi}} = 5$ ns as a function of each requirement while all other requirements are kept fixed at the optimized values.

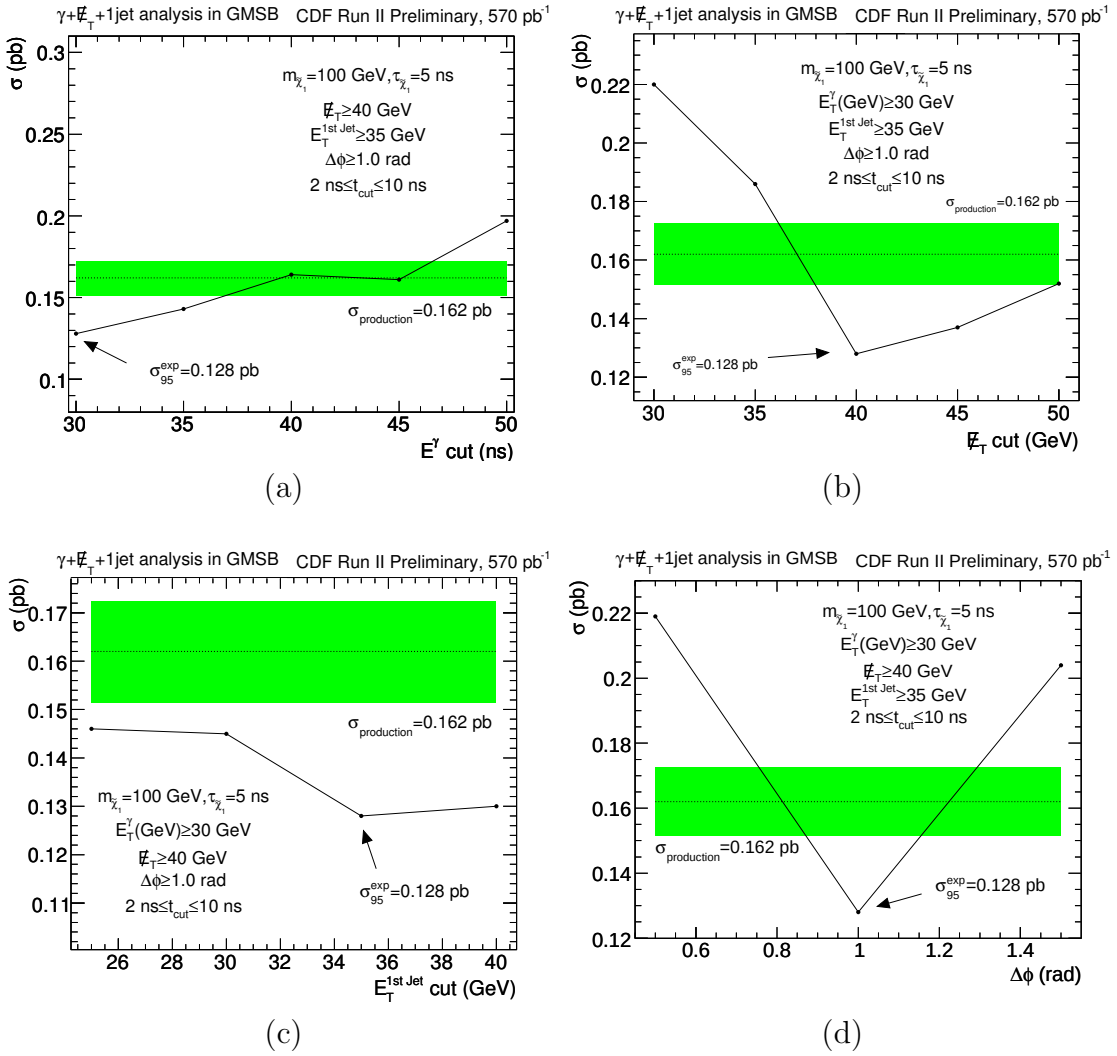

Figure 54: The expected 95% C.L. cross section limit as a function of the photon E_T, the $\not\!\!E_T$, jet E_T and $\Delta\phi(\not\!\!E_T, \text{jet})$ requirement for a GMSB example point ($m_{\tilde{\chi}} = 100$ GeV and $\tau_{\tilde{\chi}} = 5$ ns) while all other requirements are fixed at their optimized values. The optimal requirement is where the expected cross section is minimized. Indicated in green is the 6.5% uncertainty-band for the production cross section (see Table XIII). The arrows show the choices of the final requirements, and the expected cross section limit values. Note that the photon E_T is > 30 GeV as part of the trigger requirements and cannot be lowered further.

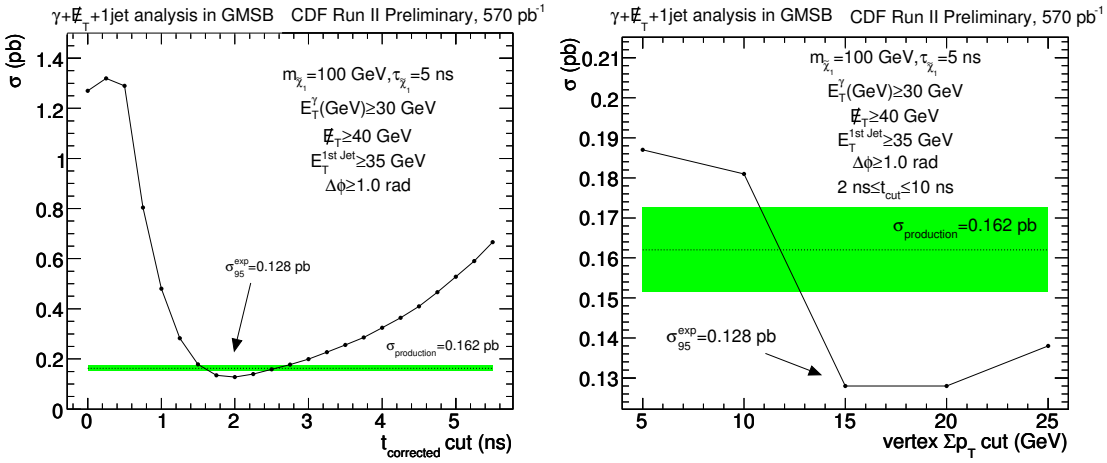

(a) (b)

Figure 55: The expected 95% C.L. cross section limit as a function of the $t^{\gamma}_{\rm corr}$ and the vertex $\Sigma p_{\rm T}$ requirement, which is shown for completeness, for a GMSB example point ($m_{\widetilde{\chi}} = 100$ GeV and $\tau_{\widetilde{\chi}} = 5$ ns). For a more complete description see Fig. 54.

Table XIV lists the selection requirements that minimize $\sigma^{\rm exp}_{95}$(cut), along with the NLO production cross section for each point in the considered GMSB parameter space. There is only small variation in the optimal jet E_T requirement and the lower limit on $t^{\gamma}_{\rm corr}$ while all other requirements are constant over the parameter region $65 < m_{\widetilde{\chi}} < 150$ GeV/c^2 and $0 < \tau_{\widetilde{\chi}} < 35$ ns. A single set of final requirement values is chosen for simplicity before unblinding the signal region, with the expectation that they will yield the largest expected exclusion region. These values are: Photon E_T>30 GeV, jet E_T>35 GeV, $\Delta\phi(\not{E}_T, \text{jet})$>1.0, $\not{E}_T$>40 GeV and $2.0 < t^{\gamma}_{\rm corr} < 10.0$ ns. With this choice, Table XV lists the number of events observed in the three control regions. A total of 506 events are observed in the control regions: 498 in the prompt, 4 in the cosmics and 4 in the beam halo control region. The background estimate for the signal region predicts 1.3±0.7 events with 0.46±0.26 from beam halo, 0.07±0.05 from cosmics and 0.71±0.60 from SM. The wrong vertex is predicted to be chosen in

fraction of (0.50±0.25)% of all SM events, corresponding to 0.32 events. Table XVI shows the optimized expected cross section limits, $(A \cdot \epsilon)$ and NLO production cross section for each GMSB point, along with the predicted background, for the final requirements. In each case a comparison with Table XVI shows only a <4% loss of sensitivity by using one fixed set of requirements. Note that this table also shows the observed cross section limits for completeness, even though the signal region will be unblinded in the next chapter. The same 95% C.L. expected cross section limits will be used to show the excluded GMSB parameter space in Section VIII.C by comparing them to the NLO production cross section throughout the considered parameter space.

Figures 56 and 57 show the distributions of each optimization variable normalized to the number of expected events, after applying all but this optimized cut. The background distribution before unblinding the signal region is compared to the expected signal in the signal region for an example GMSB point at $m_{\widetilde{\chi}} = 100$ GeV and $\tau_{\widetilde{\chi}} = 5$ ns, close to the expected exclusion region limit. Taking into account the uncertainties, this point yields an acceptance of (6.3±0.6)% and 5.7±0.7 events of signal expected. This leads to a cross section limit of 0.128 pb to be compared with a GMSB production cross section of 0.162 pb (see Table I). In the next chapter the signal region is unblinded and limits are set for GMSB models. In addition, the model-independent features are described in detail.

Table XIV: The optimized requirement values for a selected number of GMSB parameter points. All values are quite stable as a function of $m_{\widetilde{\chi}}$ and $\tau_{\widetilde{\chi}}$ with the biggest variation in the jet E_T requirement that slightly increases with $m_{\widetilde{\chi}}$. As the exclusion limit is expected to be close to 100 GeV/c^2, these values were chosen for the final signal region.

	GMSB model $m_{\widetilde{\chi}}$,$\tau_{\widetilde{\chi}}$ (GeV/c^2, ns)										
	67,25	75,3	75,10	75,20	80,20	94,5	94,10	94,20	100,5	100,15	113,5
Photon E_T						30					
$\not\!\!E_T$						40					
Jet E_T	25	35	25	25	25	35	35	35	35	35	40
$\Delta\phi(\not\!\!E_T, \text{jet})$						1.0					
Lower limit on t^{γ}_{corr}	2.0	1.75	2.0	2.0	2.0	2.0	2.0	2.0	2.0	2.0	2.0
Acceptance (%)	0.9±0.1	3.0±0.3	2.6±0.3	1.6±0.2	2.1±0.2	5.3±0.5	3.9±0.4	2.4±0.2	6.3±0.6	3.6±0.4	8.1±0.8
Backgrounds:											
Prompt SM	1.0±0.7	1.6±1.7	1.0±0.7	1.0±0.7	1.0±0.7	0.7±0.6	0.7±0.6	0.7±0.6	0.7±0.6	0.7±0.6	0.7±0.6
Beam Halo	0.4±0.1	0.1±0.1	0.4±0.1	0.4±0.1	0.4±0.1	0.1±0.1	0.1±0.1	0.1±0.1	0.1±0.1	0.1±0.1	0.1±0.0
Cosmics	1.5±0.5	0.5±0.3	1.5±0.5	1.5±0.5	1.5±0.5	0.5±0.3	0.5±0.3	0.5±0.3	0.5±0.3	0.5±0.3	0.2±0.2
σ^{exp}_{95} (pb)	1.12	0.320	0.388	0.650	0.494	0.152	0.204	0.329	0.128	0.222	0.0935
NLO $\sigma_{\text{Signal MC}}$ (pb)	1.26	0.736	0.736	0.736	0.518	0.235	0.235	0.235	0.162	0.162	0.0824

Table XV: The observed number of events in each control region after all optimized requirements, except the timing cut. Chapter VIII presents the data result for the total time window, including the signal region.

Control Region	Dominant Background	Observed Events
$-20 \leq t^{\gamma}_{\text{corr}} \leq -6$ ns	Beam halo	4
$-10 \leq t^{\gamma}_{\text{corr}} \leq 1.2$ ns	SM	498
$25 \leq t^{\gamma}_{\text{corr}} \leq 90$ ns	Cosmics	4

Table XVI: The acceptance and expected cross section limits for selected GMSB points with the final selection requirements. "BH" and "CS" denote beam halo and cosmics background, respectively. The acceptances in the column marked "Fit" are obtained using the interpolation functions described in more detail in Chapter VIII. Note the small loss of sensitivity compared to the optimal cuts in Table XIV. For completeness, both the expected and observed number of events and cross section limits are included from Chapter VII. (continued on the next page)

$m_{\widetilde{\chi}}$ (GeV/c^2)	$\tau_{\widetilde{\chi}}$ (ns)	Acceptance (%) MC	Acceptance (%) Fit	Background	$\sigma_{95}^{\rm exp}$ (pb) MC	$\sigma_{95}^{\rm exp}$ (pb) Fit	$\sigma_{95}^{\rm obs}$ (pb) MC	$\sigma_{95}^{\rm obs}$ (pb) Fit	$\sigma_{\rm prod}$ (pb)
67	1	0.77±008	0.97		1.05	0.826	1.25	0.984	
67	7	1.5±0.2	1.6		0.521	0.512	0.621	0.611	
67	10	1.4±0.1	1.3		0.581	0.610	0.693	0.727	
67	18	0.9±0.1	0.88		0.940	0.914	1.12	1.09	1.26
67	25	0.7±0.1	0.67		1.23	1.20	1.47	1.43	
67	35	0.5±0.1	0.50		1.62	1.61	1.93	1.91	
67	50	0.3±0.0	0.36		2.81	2.23	3.35	2.65	
75	0	0.3±0.0	0.27		2.64	2.95	3.15	3.52	
75	1	1.2±0.1	1.4		0.693	0.585	0.825	0.698	
75	3	2.5±0.2	2.5		0.321	0.318	0.383	0.379	
75	7	2.5±0.2	2.3		0.328	0.342	0.390	0.407	
75	10	2.1±0.2	2.0	1.3±0.7 (2 observed)	0.390	0.404	0.464	0.481	0.736
75	14	1.6±0.2	1.6	SM: 0.71±0.60	0.500	0.499	0.596	0.595	
75	20	1.2±0.1	1.2	BH: 0.46±0.26	0.674	0.651	0.804	0.776	
75	40	0.6±0.1	0.68	CS: 0.07±0.05	1.30	1.18	1.55	1.41	
75	100	0.3±0.0	0.29		2.90	2.80	3.46	3.34	
80	1	1.4±0.1	1.7		0.569	0.479	0.679	0.571	
80	3	3.3±0.3	3.2		0.245	0.254	0.292	0.303	
80	7	3.1±0.3	3.0		0.262	0.269	0.312	0.320	0.518
80	10	2.6±0.3	2.5		0.311	0.316	0.371	0.376	
80	15	1.9±0.2	2.0		0.424	0.408	0.506	0.486	
80	20	1.6±0.2	1.6		0.497	0.505	0.592	0.602	
84	5	3.9±0.4	3.7		0.207	0.216	0.247	0.257	0.402

Table XVI continued.

$m_{\widetilde{\chi}}$ (GeV/c^2)	$\tau_{\widetilde{\chi}}$ (ns)	Acceptance (%) MC	Acceptance (%) Fit	Background	$\sigma_{95}^{\rm exp}$ (pb) MC	$\sigma_{95}^{\rm exp}$ (pb) Fit	$\sigma_{95}^{\rm obs}$ (pb) MC	$\sigma_{95}^{\rm obs}$ (pb) Fit	$\sigma_{\rm prod}$ (pb)
94	0	0.5±0.1	0.47		1.73	1.73	2.06	2.06	
94	1	2.2±0.2	2.4		0.364	0.334	0.434	0.399	
94	3	5.1±0.5	4.8		0.157	0.169	0.187	0.201	
94	5	5.3±0.5	50	1.3±0.7 (2 observed)	0.152	0.160	0.181	0.191	0.235
94	10	3.9±0.4	4.0	SM: 0.71±0.60	0.204	0.199	0.243	0.237	
94	20	2.4±0.2	2.6	BH: 0.46±0.26	0.329	0.313	0.392	0.373	
94	30	1.7±0.2	1.8	CS: 0.07±0.05	0.465	0.435	0.554	0.519	
94	40	1.3±0.1	1.4		0.625	0.560	0.745	0.667	
100	5	6.3±0.6	5.9		0.128	0.136	0.153	0.162	0.162
100	15	3.6±0.4	3.8		0.222	0.212	0.264	0.253	
113	0	0.56±0.1	0.61		1.42	1.31	1.70	1.56	
113	5	8.5±0.9	7.7		0.0944	0.105	0.112	0.125	0.0824
113	10	6.6±0.7	6.4		0.122	0.125	0.145	0.149	

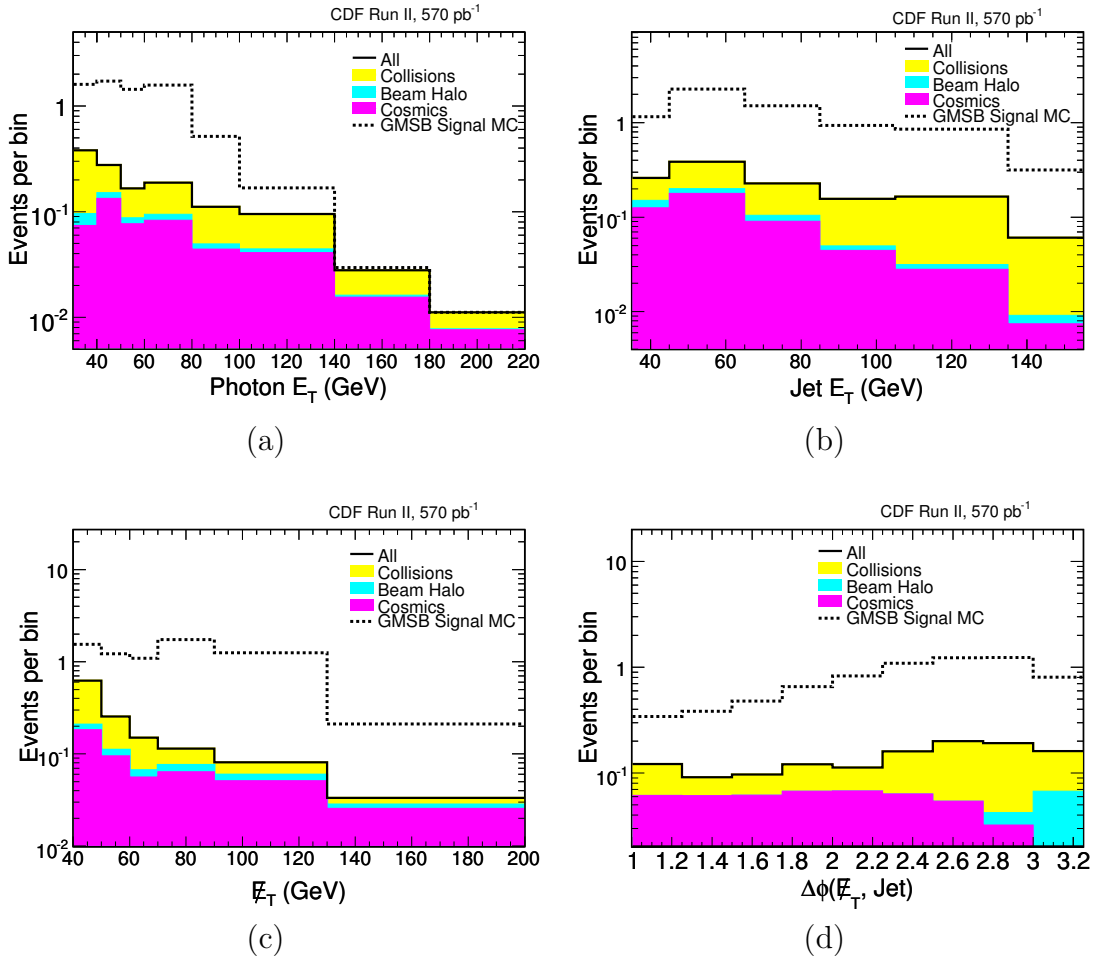

Figure 56: The predicted kinematic distributions for the signal region after the preselection and optimized requirements. The background prediction for the signal region is compared to the expected GMSB signal at an example point of $m_{\widetilde{\chi}} = 100$ GeV and $\tau_{\widetilde{\chi}} = 5$ ns. A total of 1.3±0.7 background events are predicted after all cuts. The MC is normalized to the 5.7±0.7 expected signal events.

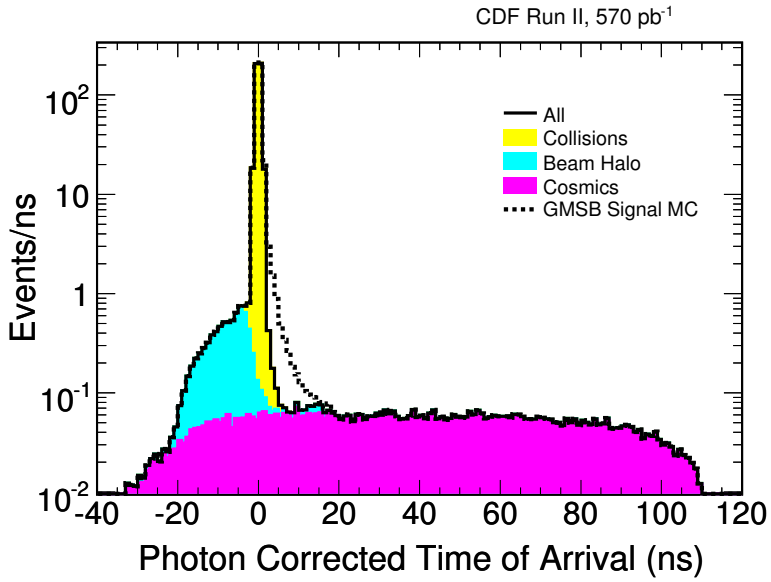

(a)

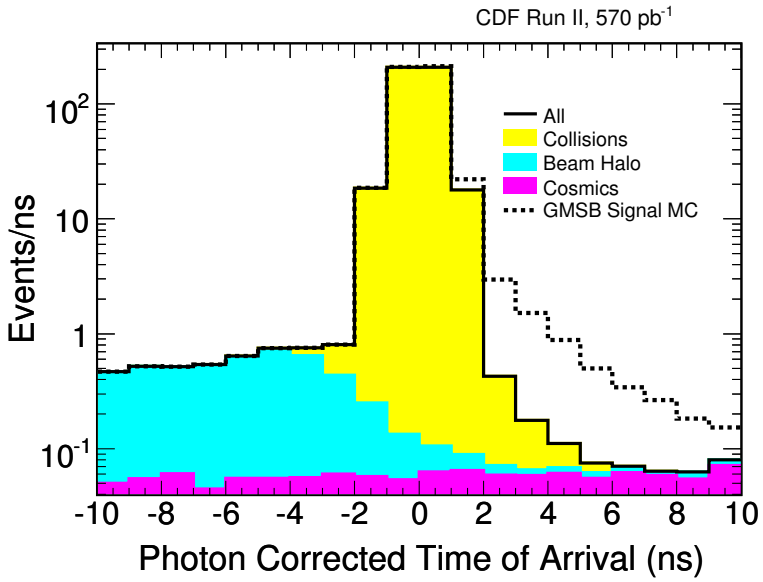

(b)

Figure 57: The predicted time distribution in the full time window (a) and around the signal region (b), after passing the preselection and optimized kinematic cuts. The background prediction for the signal region is compared to the expected GMSB signal at an example point of $m_{\widetilde{\chi}} = 100$ GeV and $\tau_{\widetilde{\chi}} = 5$ ns. A total of 1.3±0.7 background events are predicted after all cuts in the signal region 2ns $\leq t^{\gamma}_{\rm corr} \leq$ 10 ns. The MC is normalized to the 5.7±0.7 expected signal events.

CHAPTER VIII

DATA, CROSS SECTION LIMITS AND FINAL RESULTS

This chapter applies the optimized requirements found in the previous chapter to the dataset and unblinds the signal region. Two events are observed, consistent with the expected 1.3 ± 0.7 events. Both appear to be from the prompt collision background that is expected to dominate. This chapter describes the events in detail and shows exclusion regions for GMSB models. A parametrization of the acceptance using model-independent features allows for a measure of the sensitivity of this search. This is useful for future comparisons to production cross sections in any model that predicts long-lived, heavy, neutral particles that decay via the $\gamma + \not{E}_T$ event selection criteria

A. The Data

After all the kinematic requirements listed in Chapter VII there are 508 events observed in the data. Figure 58a shows the $t^{\gamma}_{\rm corr}$ distribution from data along with the signal expectations and the background shapes, normalized using the control regions. Table XV lists the number of events observed in the three control regions; the normalizations predict 6.2±3.5 events from cosmics, 6.8±4.9 events from beam halo and the rest from SM. To check the background estimation methods, Table XVII lists the expected number of background and signal events for a GMSB example point as each of the optimized requirements is applied one at a time. The uncertainties are large as the predictions are for the loose timing window $1.2 \leq t^{\gamma}_{\rm corr} \leq 10$ ns to allow the background method to make predictions at each stage for comparison. Also note that the bulk of the beam halo and cosmics background is rejected by the timing requirement. At each requirement a GMSB signal would have increased the

number of events observed in the signal region but there is a good agreement between background prediction and the number of events observed. For completeness the acceptance is presented as a function of the cuts in a slightly different order for $m_{\widetilde{\chi}} = 100$ GeV and $\tau_{\widetilde{\chi}} = 5$ ns in Table XVIII, as shown in Ref. [43].

Table XVII: Summary of the expected and observed number of events from the background estimate after the event preselection and each requirement from the optimization, separated for each background, and the expected number of signal events. The asterisk indicates that the expected signal numbers are for a GMSB example point at $m_{\widetilde{\chi}} = 100$ GeV$/c^2$ and $\tau_{\widetilde{\chi}} = 5$ ns. Note that the additional requirement $1.2 < t^{\gamma}_{\rm corr} < 10$ ns is applied at the top line to allow the background estimation methods to use the control regions to make predictions at each stage. The preselection cuts are listed in Table X. The background predictions match well with the observed number of events for each requirement indicating the background estimation methods are reliable. There is no evidence of new physics.

Requirement	Expected Background				Expected	Data
	SM	Beam Halo	Cosmics	Total	Signal*	
Photon, $\not\!\!E_T$, jet preselection cuts and $1.2 \leq t^{\gamma}_{\rm corr} \leq 10$ ns	490.74±295.40	0.27±0.12	1.30±0.49	492.3±295.4	11.7±1.4	398
$\not\!\!E_T > 40$ GeV	162.96±76.19	0.24±0.12	1.17±0.46	164.4±76.2	10.2±1.2	99
Jet $E_T > 35$ GeV	154.52±72.96	0.12±0.08	0.79±0.37	155.4±73.0	9.4±1.1	97
$\Delta\phi(\not\!\!E_T, \text{jet}) > 1.0$	13.07±11.57	0.10±0.07	0.52±0.30	13.7±11.6	8.5±1.0	8
$2 \leq t^{\gamma}_{\rm corr} \leq 10$ ns	0.71±0.60	0.07±0.05	0.46±0.26	1.3±0.7	5.7±0.7	2

There are 2 events in the final signal region, $2 < t^{\gamma}_{\rm corr} < 10$ ns, consistent with the background expectation of 1.3±0.7 events. Figure 58b shows the time window just around the signal window and is also consistent with expectations. Figure 59 shows the kinematic distributions for the background and signal expectations along with the data. There is no distribution that hints at an excess and the data appears to be well modeled by the background predictions alone. The next subsections describe the two events observed in the signal region and compares them to the various signal and background hypotheses.

Table XVIII: The data selection criteria and the total, cumulative event efficiency for an example GMSB model point at $m_{\widetilde{\chi}} = 100$ GeV/c^2 and $\tau_{\widetilde{\chi}} = 5$ ns, shown for completeness as it is presented in Ref. [43]. The listed requirement efficiencies are in general model-dependent. Note, however, that the photon fiducial requirement (74% efficient), the collision fiducial requirement of $|z_0| < 60$ cm as part of the good vertex requirement (95%) and the cosmics rejection requirement (98%) are model-independent and estimated from data.

Preselection Requirements	**Cumulative (individual) Efficiency (%)**
$E^{\gamma}_T > 30$ GeV, $\not\!\!E_T > 30$ GeV	54 (54)
Photon ID and fiducial, $\|\eta\| < 1.0$	39 (74)*
Good vertex, $\sum_{\rm tracks} p_T > 15$ GeV/c	31 (79)
$\|\eta^{\rm jet}\| < 2.0$, $E^{\rm jet}_T > 30$ GeV	24 (77)
Cosmic ray rejection	23 (98)*
Requirements after Optimization	
$\not\!\!E_T > 40$ GeV, $E^{\rm jet}_T > 35$ GeV	21 (92)
$\Delta\phi(\not\!\!E_T, {\rm jet}) > 1$ rad	18 (86)
2 ns $< t^{\gamma}_c <$ 10 ns	6 (33)

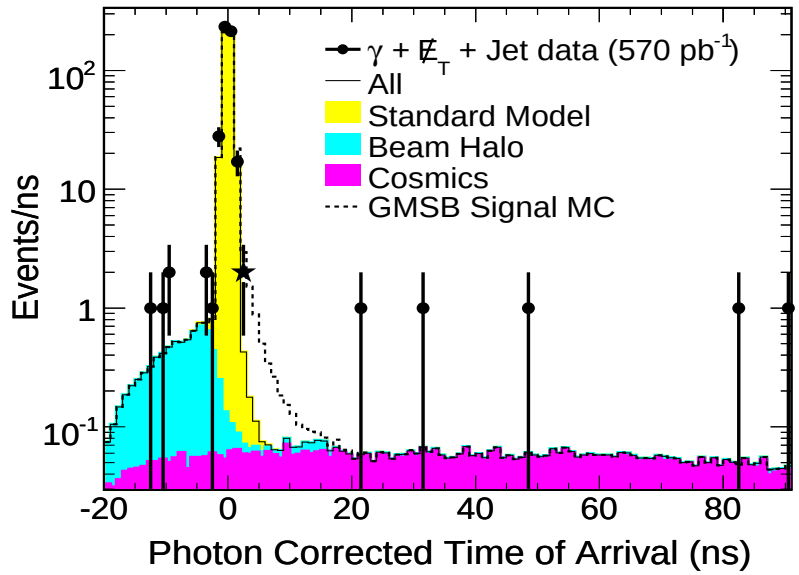

(a)

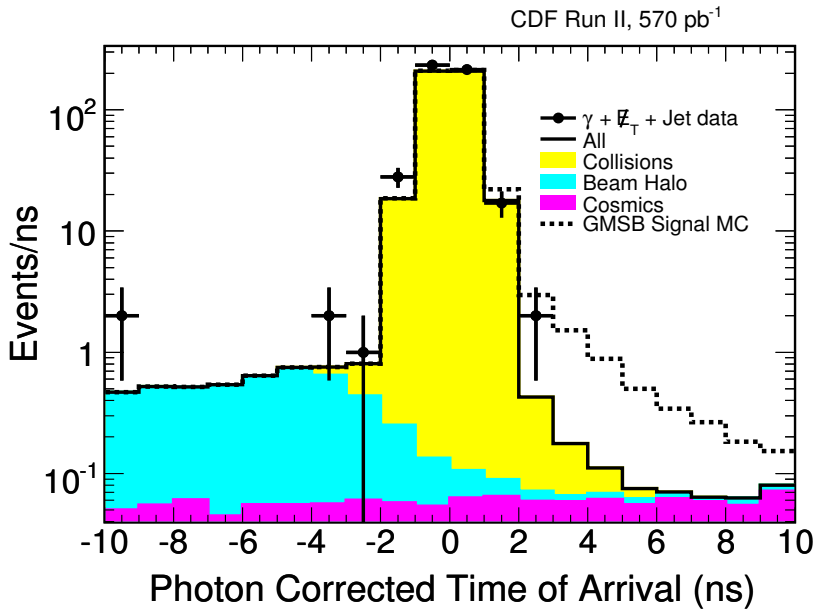

(b)

Figure 58: The $t^{\gamma}_{\rm corr}$ distribution including control and signal regions, after all but the timing cut for all backgrounds, the expected signal and the observed data. A total of 508 events are observed in the full time window where 6.2±3.5 are expected from cosmics, 6.8±4.9 from beam halo and the rest from SM. Two events are observed in the signal region $2 < t^{\gamma}_{\rm corr} < 10$ ns, consistent with the background expectation of 1.3±0.7 events. Table XVII lists the expected number of events for the various sources.

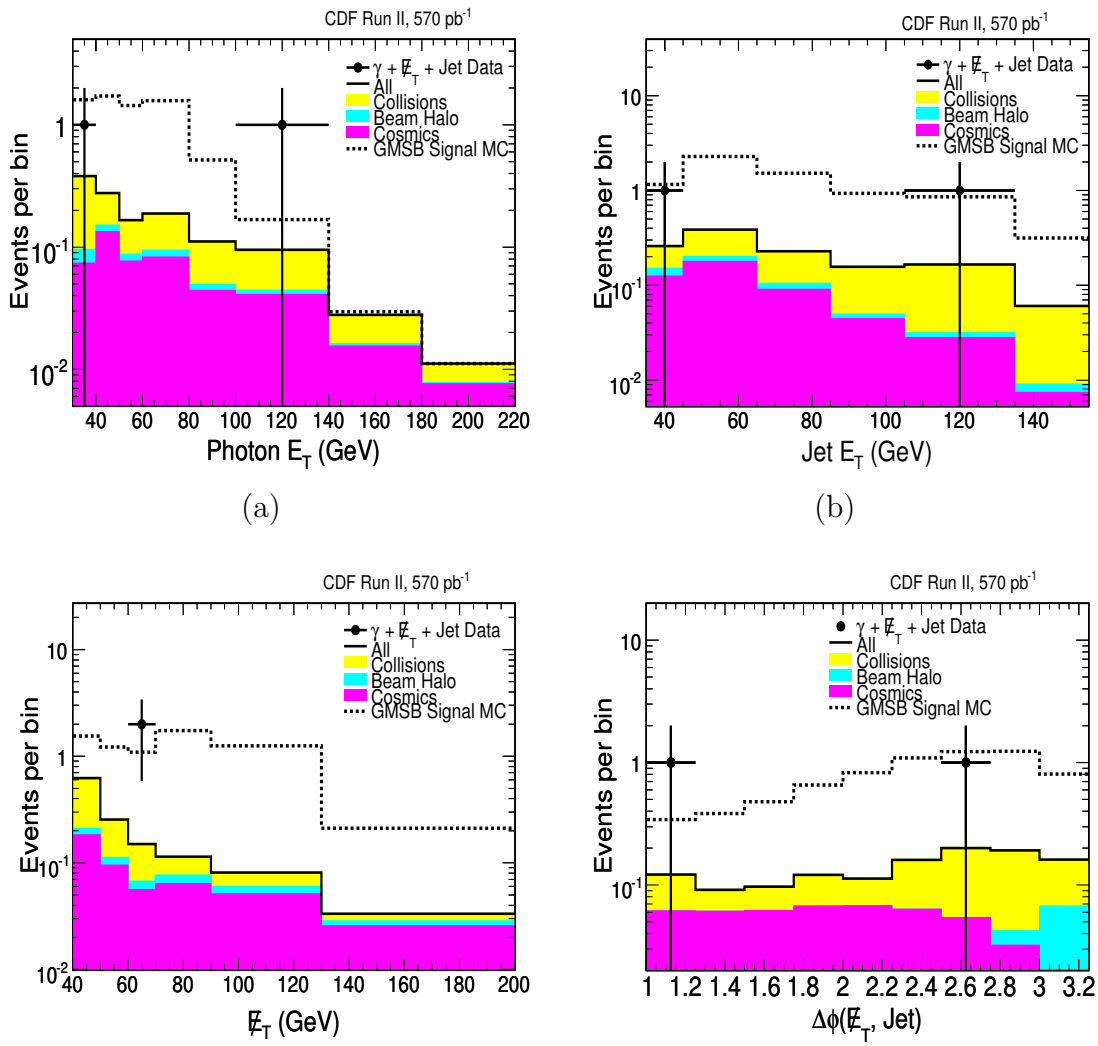

(a) (b) (c) (d)

Figure 59: The same as Fig. 56, but including the data in the signal region. Each variable is plotted down to its optimized requirement value. There is no evidence for new physics.

1. *Event 191534, 3062764*

This section studies the properties of event number 3062764 in run number 191534 for evidence that it comes from GMSB, SM, beam halo or cosmic ray background sources. Table XIX compares the event properties to the selection requirements, and Fig. 60 shows the CDF event displays in both the r-ϕ and the η-ϕ planes. The most striking properties of this event are a $\not\!\!E_T$ of 68.3 GeV, a very high-E_T photon with a corrected time of 2.93 ns and $E_T = 136.3$ GeV, as well as two jets with $E_T =$ 125.6 GeV and $E_T = 60.6$ GeV. Both high-E_T jets are centered in poorly instrumented regions of the calorimeter; one jet at $\eta_{\rm det} = -1.1$, near the cracks between central and plug calorimeter at $\eta_{\rm det} = \pm 1.1$, and the other jet at $\eta_{\rm det} = -0.004$, near the crack between the east and the west side of the calorimeter (around $\eta_{\rm det} = 0$). Both can easily cause grossly mismeasured $\not\!\!E_T$. While the highest E_T jet barely passes the $\Delta\phi(\not\!\!E_T, \text{jet})$ requirement ($\Delta\phi(\not\!\!E_T, \text{jet}) = 1.06$), the $\Delta\phi(\not\!\!E_T, \text{jet})$ for the second-highest E_T jet ($\Delta\phi(\not\!\!E_T, \text{jet}) = 0.59$) would have failed, indicating that the $\not\!\!E_T$ may be mismeasured. As shown in the figure, the $\not\!\!E_T$ points in ϕ between the two jets. Both jets are roughly opposite to the photon in ϕ and do not indicate a recoil to a heavy, neutral particle.

To find more hints that the significant $\not\!\!E_T$ is caused by the energy mismeasurement of the jets or other objects like muons that do not interact with the calorimeter, Figure 61a shows the p_T of all reconstructed tracks as a function of η and ϕ, along with the ϕ of the $\not\!\!E_T$ as a dashed line. The high-p_T track that points to the $\not\!\!E_T$ is most probably misreconstructed as its vertex lies at $z = -135$ cm and has no hit in the TOF detector. It has 5 hits in only 2 COT axial and 2 stereo superlayers whereas 3 axial superlayer are required for a good track (see App. C). It further deposits no energy in the HAD calorimeter and does not extrapolate to any CMU or CMP muon stub

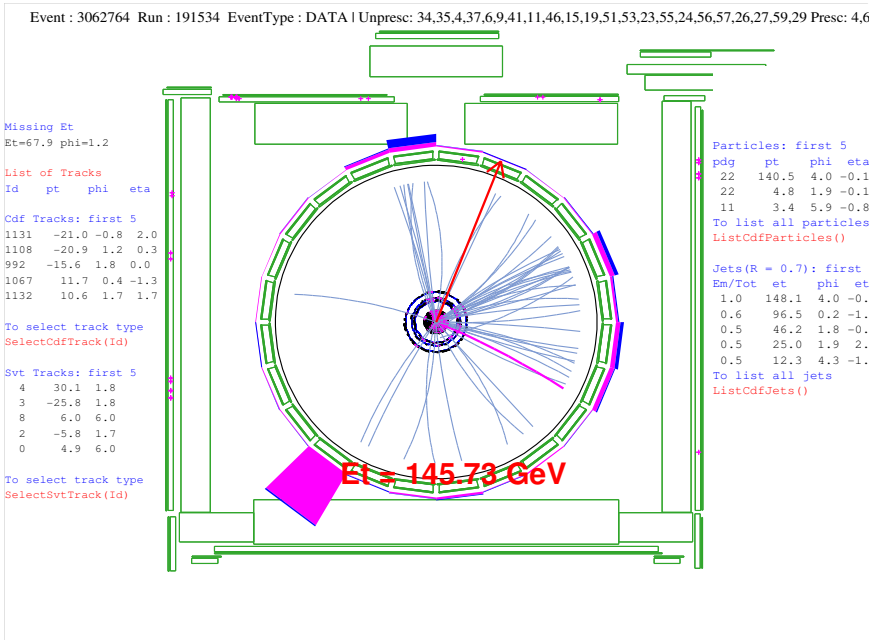

(a)

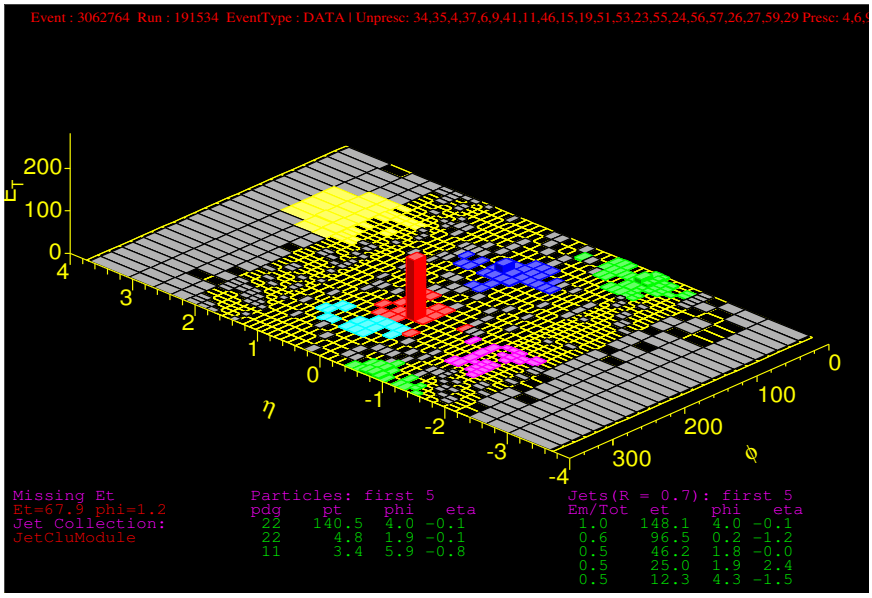

(b)

Figure 60: A view in the r-ϕ plane along the beam direction and the calorimeter towers in the η-ϕ plane for event 191534, 3062764. This event is likely from a QCD process with mismeasured $t^{\gamma}_{\rm corr}$ and mismeasured $\not\!\!E_T$ as both jets are centered in uninstrumented regions of the calorimeter and the highest-E_T jet barely passes the $\Delta\phi(\not\!\!E_T, \text{jet})$ requirement.

Table XIX: The event selection requirements and the observed values of event 191534, 3062764. Measurements that are not part of the requirements are shown in square brackets. The ΣE_T is over all towers in the calorimeter. The z-corrected t_{EMTiming} of jets is the EMTiming-measured time in the highest-E_T tower that is part of the jet cluster, corrected for the z_0 of the primary vertex. (continued on the next page)

Requirement	Value
Photon	
$E_T > 30$ GeV	136.3 GeV
Fiducial: $\lvert X_{\mathrm{CES}}\rvert < 21$ cm	13.26 cm
&& 9 cm $< \lvert Z_{\mathrm{CES}}\rvert < 230$ cm	-15.78 cm
Central	$\eta_{\mathrm{det}} = -0.085$ $\phi = 3.99$
$E_{\mathrm{Had}}/E_{\mathrm{Em}} < 0.125$	0.0226
$E^{\mathrm{Iso}}_{\mathrm{R=0.4}} < 2.0 + 0.02 \cdot (E_T - 20)$	-0.584 GeV
$N_{\mathrm{trks}} = 0$ or $N_{\mathrm{trks}} = 1$ and $p_T < 1.0 + 0.005 \cdot E_T$	$N_{\mathrm{trks}} = 0$
Σp_{T} of tracks in a 0.4 cone $< 2.0 + 0.005 \cdot E_T$	0.463 GeV/c
$E^{\mathrm{cluster}}_{\mathrm{2nd\ strip\ or\ wire}} < 2.34 + 0.01 \cdot E_T$	no 2nd cluster
PMT asymmetry: $\lvert E_{\mathrm{PMT1}} - E_{\mathrm{PMT2}}\rvert/(E_{\mathrm{PMT1}} + E_{\mathrm{PMT2}}) < 0.6$	0.034
2ns $\leq t^{\gamma}_{\mathrm{corr}} \leq$ 10 ns	2.93 ns ($t_{\mathrm{EMTiming}} = 2.60$ ns)
[CES-χ^2]	$\chi^2_{\mathrm{Strips}} = 1.16$ $\chi^2_{\mathrm{Wires}} = 3.48$
[nEmTowers, nHadTowers]	6, 2
[Phoenix track]	no
Jets	
1) $E_T^{\mathrm{jet}} > 35$ GeV	125.6 GeV
$\lvert\eta^{\mathrm{jet}}_{\mathrm{detector}}\rvert < 2.0$	$\eta_{\mathrm{det}} = -1.1$ $\phi = 0.15$
$\Delta\phi(\not{E}_T, \mathrm{jet}) > 1.0$	1.06
[z-corrected t_{EMTiming}]	-0.85 ns
2) $E_T^{\mathrm{jet}} > 35$ GeV	60.6 GeV
$\lvert\eta^{\mathrm{jet}}_{\mathrm{detector}}\rvert < 2.0$	$\eta_{\mathrm{det}} = -0.004$ $\phi = 1.8$
[$\Delta\phi(\not{E}_T, \mathrm{jet})$]	0.59
[z-corrected t_{EMTiming}]	-1.07 ns

Table XIX continued.

Requirement	Value
Vertices	
$N_{\text{trks}} \geq 4$	45
$\Sigma p_{\text{T}} > 15$ GeV/c	94.73 GeV/c
$\lvert z \rvert < 60$ cm	(4.20±0.02) cm
t_0	(−0.34±0.01) ns
Global Event Properties	
raw $\not\!\!E_T > 40$ GeV	68.3 GeV $\phi(\not\!\!E_T) = 1.21$
[$\Sigma \text{E}_{\text{T}}$]	461.7 GeV
μ-stubs	none

although it is fiducial there. A track with $p_{_T} = 20.2$ GeV/c at $(\phi, \eta) = (-0.82, 2.03)$ is only measured in the silicon detectors and is likely misreconstructed as it has no energy in the calorimeter and no CMU or CMP stubs despite being fiducial. While these tracks do not show any indication of an energy mismeasurement of the jets, there is the possibility that a significant neutral fraction (π^0's) of the jet energy is deposited in a crack.

To investigate the possibility that the large $\not\!\!E_T$ is due to a large uncertainty on the jet energy measurement and on the energy deposited by the underlying event, an improved $\not\!\!E_T$ and its uncertainty are estimated. As clustered energy from jets, electrons, muons and photons is typically well-measured, the $\not\!\!E_T$ is recalculated using this energy measurement rather than the vector sum of their energy deposits in the calorimeter towers (see Section IV.A.1). The "corrected" $\not\!\!E_T$ for this event is 44.8 GeV. [90]. The uncertainty on the corrected $\not\!\!E_T$ is also estimated separately for clustered and unclustered energy: The photon $E_{_T}$ is usually well measured (to ∼1% at this $E_{_T}$, see Section II.B) if it is fiducial (as in this event) as it is almost fully

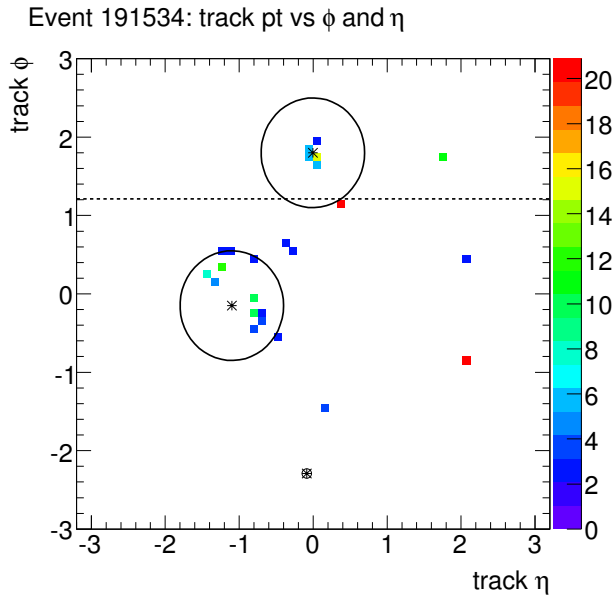

(a)

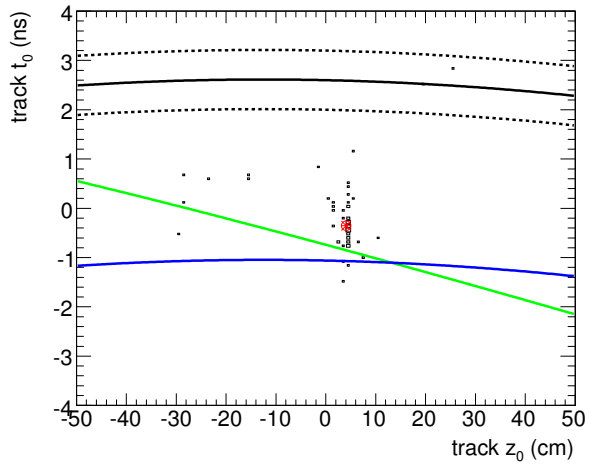

(b)

Figure 61: In (a) the track p_T of all tracks with hits in the silicon and/or COT as a function of their η and ϕ. Indicated with stars are the positions of the reconstructed objects in the event. The primary photon is indicated with a circled star. The big circles around the jets show the cone of 0.7, and the dashed line shows the ϕ position of the $\not\!\!E_T$. The second jet is near the $\not\!\!E_T$. In (b) the points show the distribution of all tracks in the (t_0,z_0)- plane for event 191534, 3062764 that pass the requirements in Table VI, along with the primary vertex position (red star). The solid line indicates the vertex t_0 and z_0 that would be needed to produce $t^{\gamma}_{\rm corr} = 0$ ns, and the dashed lines show its $\pm 1\sigma$ variation. The jets, shown with the blue and green lines along their $t_{\rm corr} = 0$ ns, were most likely produced at the primary vertex.

contained in the EM calorimeter. The jet E_T uncertainty is given by [90]

$$\sigma_{E_T}/E_T = \sqrt{(1.124 \pm 0.006)^2/E_T + (0.062 \pm 0.001)^2}\ , \tag{8.1}$$

which gives $\sigma_{E_T,1} = 11.8\%$ and $\sigma_{E_T,2} = 15.8\%$ for the two jets, respectively. From this 1σ uncertainty the $\not\!\!E_T$ varies by 11.66 GeV (17.1%). This is taken in quadrature with the $\not\!\!E_T$ uncertainty that is given by [90]

$$\sigma_{\not\!\!E_T,x} = (1.03 \pm 0.27) + (0.393 \pm 0.033) \cdot \sqrt{\Sigma \mathrm{E_T}}\ \mathrm{GeV} \tag{8.2}$$

$$\text{and}\ \ \sigma_{\not\!\!E_T,y} = (0.71 \pm 0.27) + (0.422 \pm 0.033) \cdot \sqrt{\Sigma \mathrm{E_T}}\ \mathrm{GeV} \tag{8.3}$$

for the $\not\!\!E_T$ components in x and y direction separately where the $\Sigma \mathrm{E_T}$ is over unclustered energy only [90] which is 276.1 GeV in this event. This leads to a $\not\!\!E_T$ uncertainty of 12.0 GeV and to a combined uncertainty of $\sigma_{\not\!\!E_T} = 16.7$ GeV which is equivalent to a 2.7σ deviation from $\not\!\!E_T = 0$ GeV.

Assuming that the energy in the event is correctly reconstructed, and the $\not\!\!E_T$ is real, it could be caused by a $W \rightarrow e\nu + \text{jets}$ event. However, this event does not show any indication for a track in the silicon detector associated to the photon that could indicate an electron converting in the material between the silicon and COT detectors ("phoenix track") [91]. The transverse mass of the photon and the $\not\!\!E_T$ is 204.8 GeV/c^2, which lies on the tail of the W transverse mass distribution as shown in Fig. 65.

While there are 6 EM and 2 HAD towers with energy in the same wedge of the photon, the event is unlikely caused by beam halo from a satellite bunch: (a) the photon CES-χ^2 is very good (4.6) which indicates that it comes from the center of the detector, and (b) the photon does not lie in wedge 0 or 23 where beam halo is most likely to occur. The event is unlikely from GMSB production as there is no

evidence for muons, electrons or taus in the event.

While this appears to be a SM event with mismeasured $\not\!\!E_T$, it has an unusually large $t^{\gamma}_{\rm corr}$. Figure 61b shows the t_0 and z_0 of both the tracks and the primary reconstructed vertex along with a hypothetical vertex t_0 and z_0 that would be needed to produce $t^{\gamma}_{\rm corr} = 0$ ns for both the jets and the photon and their 1σ variation. The event has one well-measured vertex with a high $\Sigma p_{\rm T}$ of 95 GeV/c that has $z \approx 4$ cm. While the photon arrival time lies 4.5σ away from what one would expect if it is produced from this vertex, the arrival times of both jets are consistent with coming from this vertex. However, it may well be that two collisions occurred in this event and that the photon comes from a second vertex that is not reconstructed.

To summarize, there is no evidence that this event is due to beam halo, cosmics or GMSB sources. The large track activity in this event, as well as the high-$\Sigma p_{\rm T}$ vertex and the high $\Sigma {\rm E_T}$ indicate that it most likely is a QCD event with mismeasured $\not\!\!E_T$ and mismeasured $t^{\gamma}_{\rm corr}$. The $\not\!\!E_T$ points between two high-E_T jets in ϕ that are both centered in poorly instrumented regions of the calorimeter. While there are no high-p_T tracks as part of the jets that point into these regions that would indicate the amount of lost energy, it is likely that the jets are the cause for a $\not\!\!E_T$ mismeasurement. If both the $\not\!\!E_T$ and the $t^{\gamma}_{\rm corr}$ measurement are assumed to be from statistical fluctuations rather than energy deposits in poorly instrumented regions, the combined measurement deviation is calculated to be 5.3σ.

2. *Event 198583, 15031322*

This section studies the properties of event number 15031322 in run number 198583 for evidence that it comes from SM, beam halo or cosmic ray background sources. Table XX compares the event properties to the selection requirements, and Fig. 62 shows the event displays in both the r-ϕ and the η-ϕ planes. The most striking properties of this event are a $\not\!\!E_T$ of 63.6 GeV, a photon with $E_T = 38.5$ GeV, a jet with $E_T = 42.5$ GeV, as well as a low-energy muon candidate with $p_T \approx 1$ GeV/c. The corrected $\not\!\!E_T$ is estimated to be 82.0 GeV with an uncertainty of 11.4 GeV (both calculated using Eqs. 8.1-8.3).

This event is unlikely from beam halo sources as there is no indication of a series of energy deposits in the calorimeter (nEmTowers = 2 and nHadTowers = 0), in particular no significant deposits in wedges 0 and 23. It is unlikely from cosmic ray background sources as the energy depositions in the CES, as shown in Fig. 63 are not broadened as would be expected from a photon with a large incident angle that does not come from the beam direction. The large CES-χ^2 for the wires does not come from a broad shower profile but from the two CES energy depositions close to each other that mislead the fit to the shower shape. Hence, the event is most likely from collision background.

While this event has two reconstructed vertices, both with roughly the same Σp_{T} (see Fig. 64a), it occurred with an instantaneous luminosity of $1.68 \cdot 10^{31}$ cm^{-2} s^{-1} at the low end of the range of this data sample where, on average, 0.54 collisions are expected to occur [48]. The second-highest-Σp_{T} vertex fails the Σp_{T} requirement by only 3.2 GeV/c. If this is the vertex that produced the photon, its t_0 and z_0 would lead to a $t_{\mathrm{corr}} = 1.67$ ns which is well within $\sim 3\sigma$ of the prompt distribution. Similarly, the arrival time of the jet is consistent with this vertex.

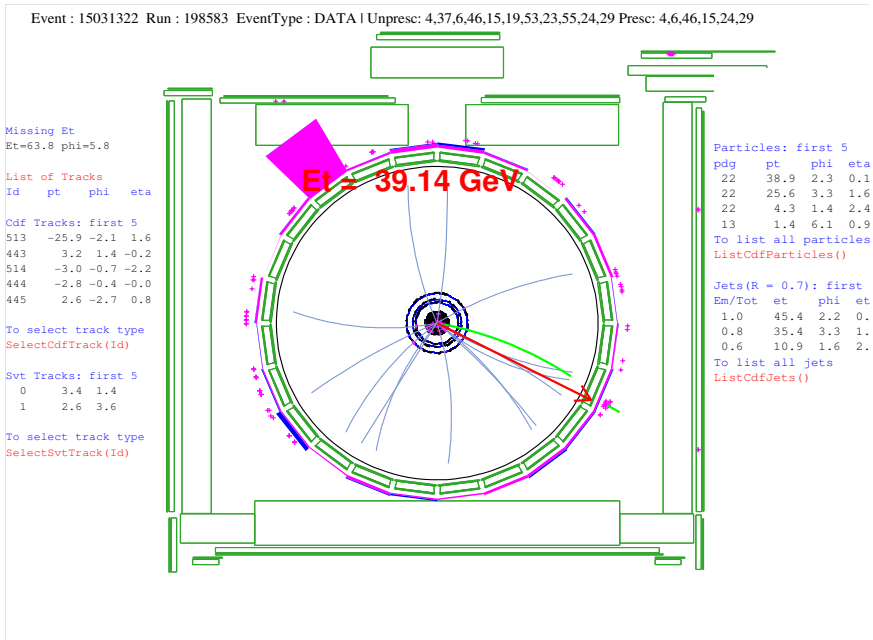

(a)

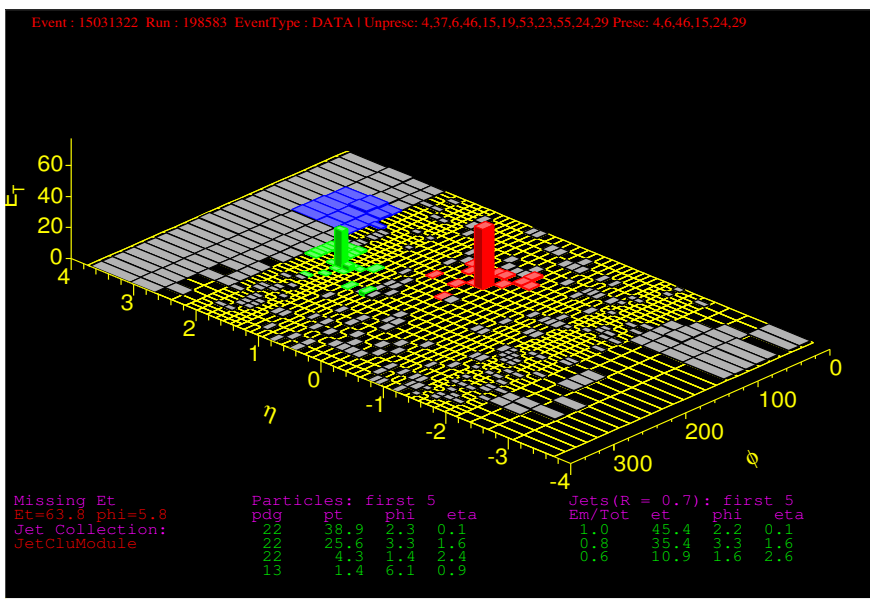

(b)

Figure 62: A view in the r-ϕ plane along the beam direction and the calorimeter towers in the η-ϕ plane for event 198583, 15031322. This event appears to be a $W \rightarrow e\nu + \text{jets}$ event where the electron has lost its track and is misidentified as a photon, the ν causes the $\not\!\!E_T$ and the wrong vertex has been selected causing the large t^{γ}_{corr}.

Table XX: The event selection requirements compared to the observed values of event 198583, 15031322. For detailed comments see Table XIX. (continued on the next page)

Requirement	Value
Photon	
$E_T > 30$ GeV	38.5 GeV
Fiducial: $\lvert X_{\mathrm{CES}}\rvert < 21$ cm	-10.30 cm
&& 9 cm $< \lvert Z_{\mathrm{CES}}\rvert < 230$ cm	10.80 cm
Central	$\eta_{\mathrm{det}} = 0.058$ $\phi = 2.28$
$E_{\mathrm{Had}}/E_{\mathrm{Em}} < 0.125$	0.0037
$E^{\mathrm{Iso}}_{\mathrm{R=0.4}} < 2.0 + 0.02 \cdot (E_T - 20)$	0.514 GeV
$N_{\mathrm{trks}} = 0$ or $N_{\mathrm{trks}} = 1$ and $p_T < 1.0 + 0.005 \cdot E_T$	$N_{\mathrm{trks}} = 0$
Σp_{T} of tracks in a 0.4 cone $< 2.0 + 0.005 \cdot E_T$	0
$E^{\mathrm{cluster}}_{\mathrm{2nd\ strip\ or\ wire}} < 2.34 + 0.01 \cdot E_T$	$E^{\mathrm{cluster}}_{\mathrm{2nd\ strip}} = 0$ $E^{\mathrm{cluster}}_{\mathrm{2nd\ wire}} = 0.545$ GeV ($X_{\mathrm{CES}} = -19.02$ cm)
$\lvert E_{\mathrm{PMT1}} - E_{\mathrm{PMT2}}\rvert/(E_{\mathrm{PMT1}} + E_{\mathrm{PMT2}}) < 0.6$	-0.215
$2\mathrm{ns} \leq t^{\gamma}_{\mathrm{corr}} \leq 10$ ns	3.25 ns ($t_{\mathrm{EMTiming}} = 2.67$ ns)
[CES-χ^2]	$\chi^2_{\mathrm{Strips}} = 0.49$ $\chi^2_{\mathrm{Wires}} = 53.74$
[nEmTowers, nHadTowers]	2, 0
[Phoenix track]	no
Jets	
$E^{\mathrm{jet}}_T > 35$ GeV	42.5 GeV
$\lvert\eta^{\mathrm{jet}}_{\mathrm{detector}}\rvert < 2.0$	$\eta_{\mathrm{det}} = 1.56$ $\phi = 3.31$
$\Delta\phi(\not{E}_T, \mathrm{jet}) > 1.0$	2.51
[$E_{\mathrm{Had}}/E_{\mathrm{Em}}$]	0.823
[z-corrected t_{EMTiming}]	1.29 ns

Table XX continued.

Requirement	Value
Vertices	
1) $N_{\text{trks}} \geq 4$	21
$\Sigma p_{\text{T}} > 15$ GeV/c	15.8 GeV/c
$\lvert z \rvert < 60$ cm	(38.49±0.03) cm
t_0	(−0.63±0.02) ns
2) $N_{\text{trks}} \geq 4$	9
$\Sigma p_{\text{T}} > 15$ GeV/c	11.8 GeV/c
$\lvert z \rvert < 60$ cm	(3.02±0.04) cm
t_0	(1.00±0.07) ns
Global Event Cuts	
raw $\not\!\!E_T > 40$ GeV	63.3 GeV $\phi(\not\!\!E_T) = 5.82$
[$\Sigma \text{E}_{\text{T}}$]	197.6 GeV
μ-stubs	BMU stub ($\eta = 0.92$, $\phi = 6.10$) from a track with $p_{_T} = 1.4$ GeV/c

Figure 64b shows little track activity. A track that points in direction of the $\not\!\!E_T$ is most probably misreconstructed. The track with $p_{_T} = 25.7$ GeV/c at $(\phi, \eta) = (-2, 1.7)$ most probably belongs to the jet.

The transverse mass of the photon and the $\not\!\!E_T$ is 101.8 GeV/c^2 which is consistent with a $W \rightarrow e\nu$ transverse mass hypothesis as shown in Fig. 65. As with the previous event, there is no phoenix track associated with the photon. As shown in Fig. 63, there are two well separated clusters in the CES associated to the photon. Both features indicate that the reconstructed photon may be an electron that emitted strong bremsstrahlung twice, early in the silicon tracking chamber so that no track can be reconstructed.

To summarize, this event appears to be a collision $W \rightarrow e\nu +$ jet event where the electron is misidentified as a photon and a wrong vertex was selected that causes the photon arrival time to be in the signal time window.

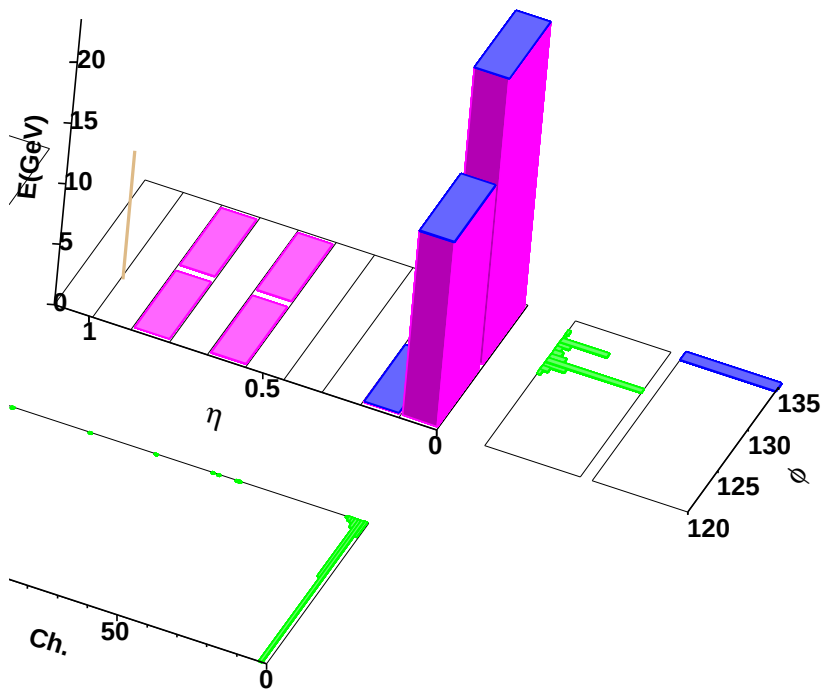

Figure 63: The CES energy distribution in the seed tower of the photon. While photons usually cause a single energy deposition, these two energy deposits most likely indicate an electron that emitted bremsstrahlung twice.

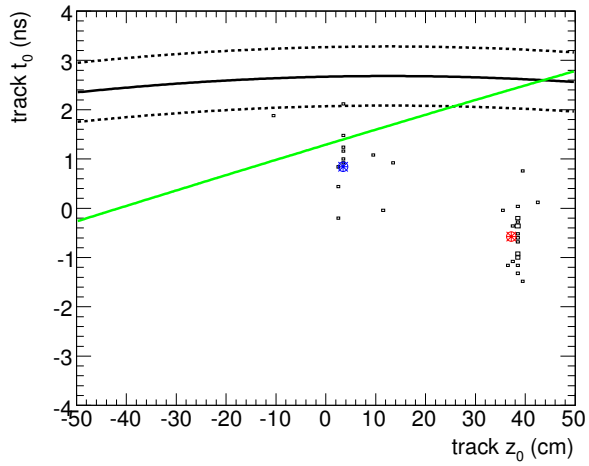

(a)

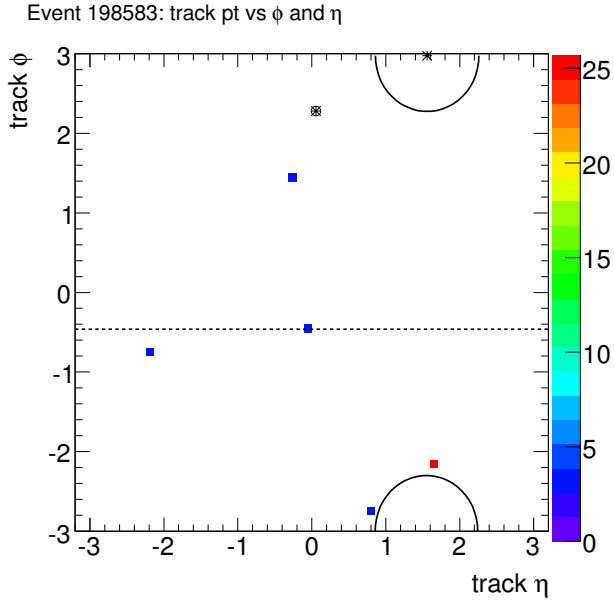

(b)

Figure 64: The same distributions as in Fig. 61, but for event 198583, 15031322; see that figure for detailed descriptions. The second vertex in this event that most likely produced both the photon and the jet is indicated in blue. The track that points to the $\not{E}_T$ is most probably misreconstructed. The track with $p_T = 25.7$ GeV/c at $(\phi, \eta) = (-2.0, 1.7)$ most probably belongs to the jet.

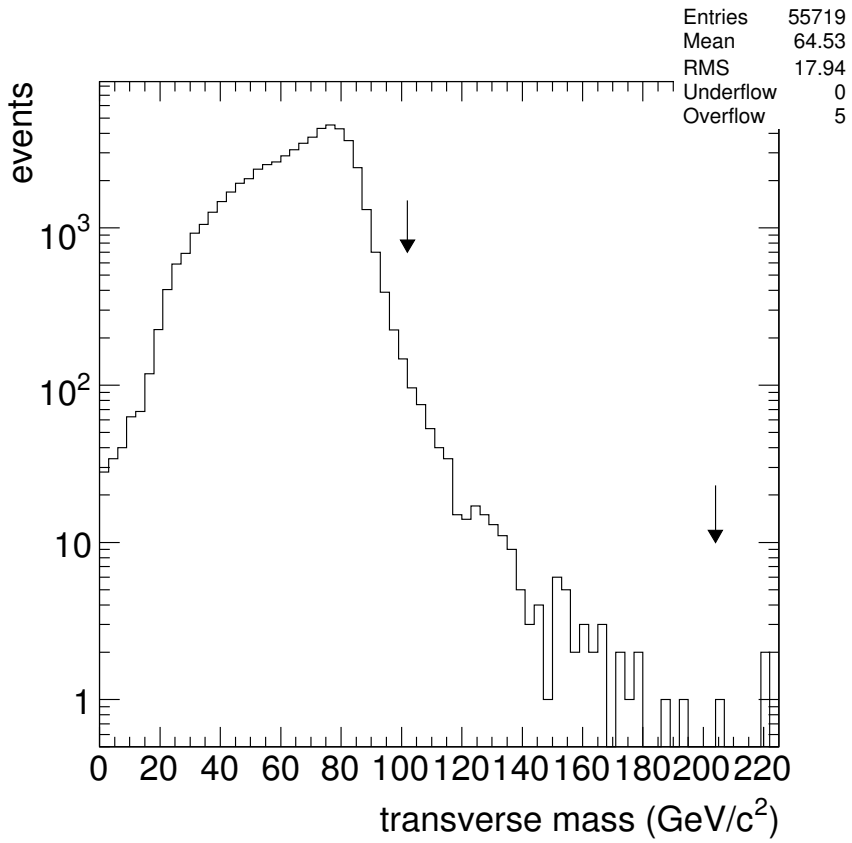

Figure 65: The distribution of the transverse mass of the electron and the $\not\!\!E_T$ in $W \to e\nu$ events simulated with the CDF MC sample used in Section III.G.2. Both events are indicated with arrows. While event 191534, 3062764 lies on the high tail with 204.8 GeV/c^2, event 198583, 15031322 is likely a $W \to e\nu +$ jets event with a value of 101.8 GeV/c^2.

B. Parametrization of the Acceptance × Efficiency

Since there is no evidence for new physics in our signal region, both an estimate of the GMSB cross section limits and a discussion of model-independent features of the sensitivity of this search are in order. This section describes a parametrization of the acceptance that allows (a) for smooth GMSB exclusion regions and (b) a comparison to production cross sections for any model that predicts long-lived, heavy, neutral particles that decay via the $\gamma + \not{E}_T$ event selection criteria and produce an additional jet. This is achieved by parametrizing the acceptance using variables that are independent of the GMSB specific event kinematics, such as the lifetime and the mass, coming from variations in the boost, of the decaying particle.

The total acceptance, $(A{\cdot}\epsilon)$, has been estimated as a function of both $\widetilde{\chi}_1^0$ mass and lifetime and can be parametrized using a fit over the region $65 < m_{\widetilde{\chi}} < 150$ GeV/c^2 and $0 < \tau_{\widetilde{\chi}} < 35$ ns. As described in Section I.B.2, there are several effects that cause the acceptance to vary as a function of both the $\widetilde{\chi}_1^0$ mass and lifetime. The dominant effects are the probability that (a) at least one $\widetilde{\chi}_1^0$ decays in the detector volume [40] to produce a photon that passes the kinematic selection criteria ($P_{\rm vol}$) and that (b) $t^{\gamma}_{\rm corr}$ is within the signal time window ($P_{\rm t}$). The latter effect is parametrized by requiring the $\widetilde{\chi}_1^0$ to decay within a timing window. The probability of these effects to happen independently as a function of $\tau_{\widetilde{\chi}}$ determine the functional form of $(A \cdot \epsilon) = P_{\rm vol} \cdot P_{\rm t}$, with minor modifications that are described below. A fit to the results in Table XVI

yields:

$$P_{\mathrm{t}} = (-0.0449877 + 8.69673 \cdot 10^{-3} m_{\widetilde{\chi}} - 3.49779 \cdot 10^{-5} m_{\widetilde{\chi}}^2) \cdot (1 - (1 - e^{-4.78942/(\tau_{\widetilde{\chi}}+1.21742)})^2) \quad (8.4)$$

$$P_{\mathrm{vol}} = (-0.254525 + 6.85926 \cdot 10^{-3} m_{\widetilde{\chi}} - 1.54730 \cdot 10^{-5} m_{\widetilde{\chi}}^2) \cdot (1 - e^{-(-0.625378+0.0647422 \cdot m_{\widetilde{\chi}})/(\tau_{\widetilde{\chi}}+0.842287)}) \quad (8.5)$$

where each function consists of two multiplicative terms: a mass-dependent term that determines the overall scale and a lifetime dependent term that has the functional form of the probability distributions described above. The small mass dependency of the overall scales and of the exponential term in P_{vol} both come from variations in the $\widetilde{\chi}_1^0$ boost with its mass [40]. A higher $\widetilde{\chi}_1^0$ boost can cause (a) the $\widetilde{\chi}_1^0$ to leave the detector with a higher probability given its lifetime and (b) the photon to be emitted at smaller angles relative to the $\widetilde{\chi}_1^0$ direction such that its arrival time becomes similar to a promptly produced photon. A variation in the boost is caused by a change in the shape of the p_T/m distribution of the $\widetilde{\chi}_1^0$ as shown in Fig. 66. For a $\widetilde{\chi}_1^0$ mass of 80 GeV/c^2 the distribution broadens and its maximum lies at a higher p_T/m compared to a mass of 40 GeV/c^2, yielding a greater fraction of high-p_T neutralinos and hence a loss in efficiency. For $m_{\widetilde{\chi}} \gtrsim 80$ GeV/c^2, the range considered for the fits, the maximum remains roughly the same and the distribution narrows, which in turn leads to a gain in efficiency. Another important, but small factor is the additive term in the denominator of both exponentials. This takes into account the effect that both acceptance and efficiency are not zero at low $\widetilde{\chi}_1^0$ lifetimes but instead dominated by the finite resolution of the $t_{\mathrm{corr}}^{\gamma}$ measurement that causes prompt photons to fluctuate into the signal time window.

The accuracy of the fit functions in Eqs. 8.4 and 8.5, defined as the relative

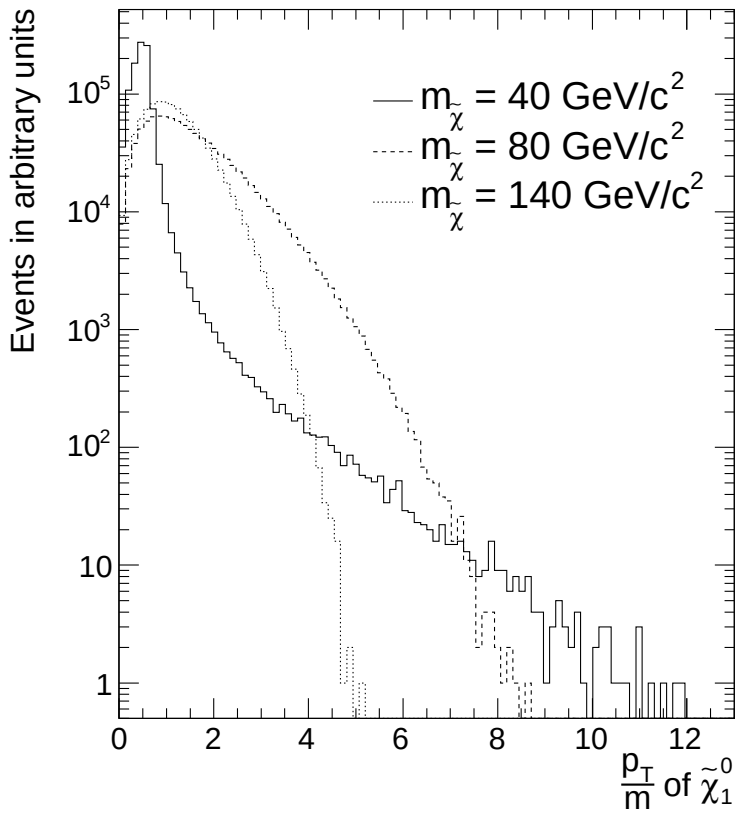

Figure 66: The p_T/m distribution of the $\widetilde{\chi}_1^0$ for $m_{\widetilde{\chi}} = 40$ GeV/c^2, 80 GeV/c^2 and 140 GeV/c^2. For a mass of 80 GeV/c^2 the maximum moves towards higher p_T/m and the distribution broadens compared to 40 GeV/c^2, yielding a greater fraction of high p_T neutralinos which either leave the detector or produce low $t^{\gamma}_{\rm corr}$ photons, and thus a loss in efficiency. For higher masses the maximum remains constant and the distribution narrows, leading to an efficiency gain at higher mass.

difference between the values of the fit-function and the direct estimation of $(A \cdot \epsilon)$, listed in Table XVI, of each GMSB point, is ∼10%. To further improve the accuracy such that it is well below the systematic uncertainty in Section VI.B a lifetime dependent correction term, P_{corr}, is introduced that is not further motivated other than to compensate the deviations:

$$P_{\text{corr}} = 1.04 - \frac{0.2}{55.0}\,\tau_{\widetilde{\chi}} - \frac{0.011}{0.06 + (1 - \tau_{\widetilde{\chi}})^2} \tag{8.6}$$

A comparison of the parametrization with the results in Table XVI is shown in Fig. 67. As the accuracy of the final fit shown in Fig. 67a is ∼4%, well below the systematic uncertainty (see Table XIII), this parametrization allows for an extrapolation of the expected acceptance and, hence, the expected cross section limit with a 4% accuracy to the total range of the considered GMSB parameter space. This accuracy gives confidence that the important effects are sufficiently understood to make model-independent statements. Both Figs. 67b and c show no residual tendency as a function of $\widetilde{\chi}_1^0$ lifetime or mass.

Figure 68 shows a comparison between fit functions and simulated acceptances as a function of lifetime for $\widetilde{\chi}_1^0$ masses of 67, 80, 94 and 113 GeV/c^2. The acceptance initially rises as more events contain a photon with a delayed t^{γ}_{corr} as a function of $\widetilde{\chi}_1^0$ lifetime, but falls as the fraction of $\widetilde{\chi}_1^0$'s decaying outside the detector begins to dominate. In the considered $\widetilde{\chi}_1^0$ mass region, the acceptance peaks at a lifetime of around 5 ns. The acceptance slightly rises as a function of the $\widetilde{\chi}_1^0$ mass due to a gain in kinematic acceptance from variations in the $\widetilde{\chi}_1^0$ boost.

The next section presents the exclusion regions.

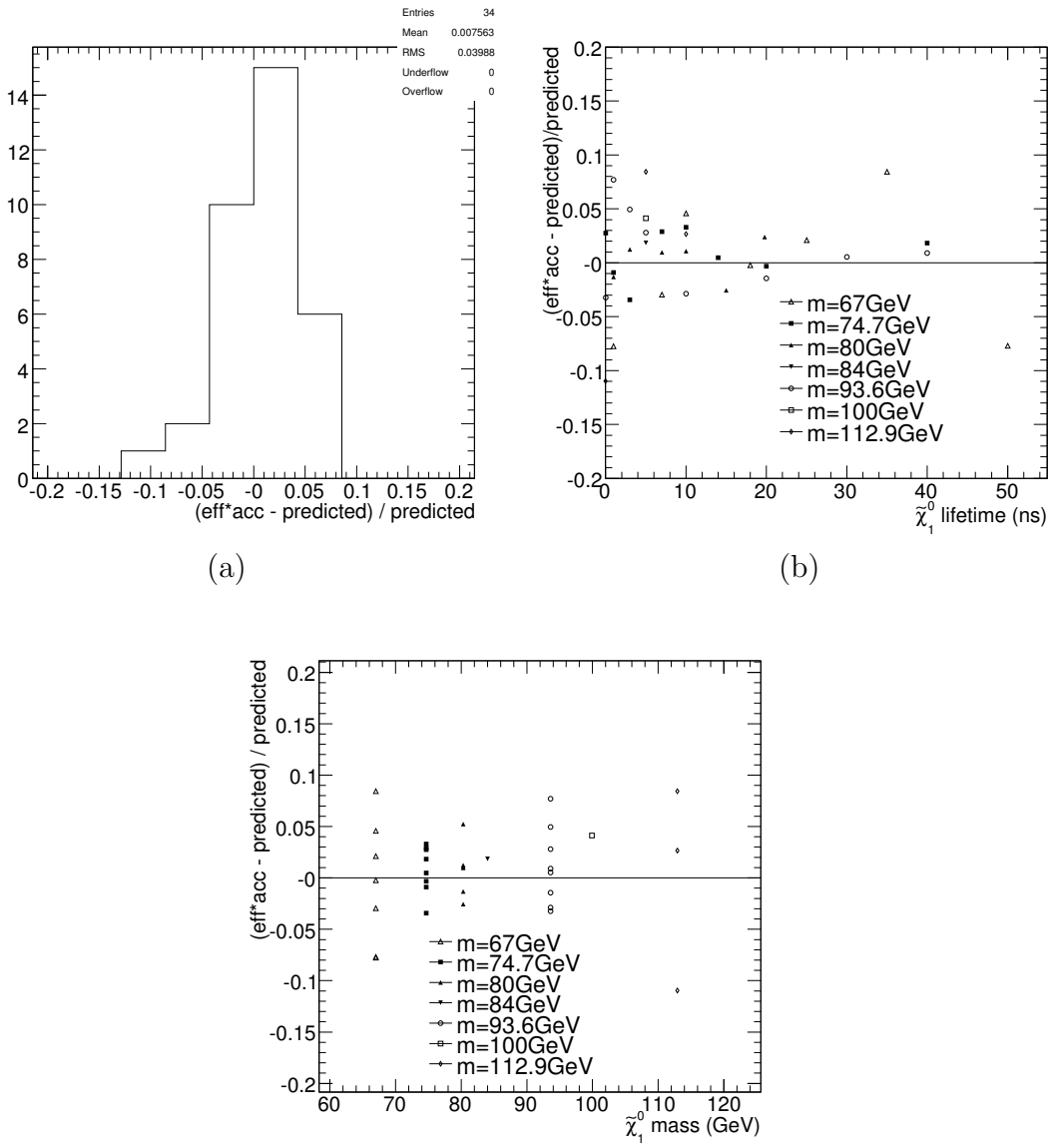

Figure 67: The relative difference of the $A \cdot \epsilon$ between the fit functions (predicted) and the MC simulation. As the fit appears to well model the simulation it is used to interpolate the simulated points for the cross section limits and the exclusion region. The overall RMS is $\sim 4\%$, well below the systematic uncertainty. Figures (b) and (c) show the relative difference as a function of $\tilde{\chi}_1^0$ lifetime and mass. There is no tendency towards lifetime or mass observed.

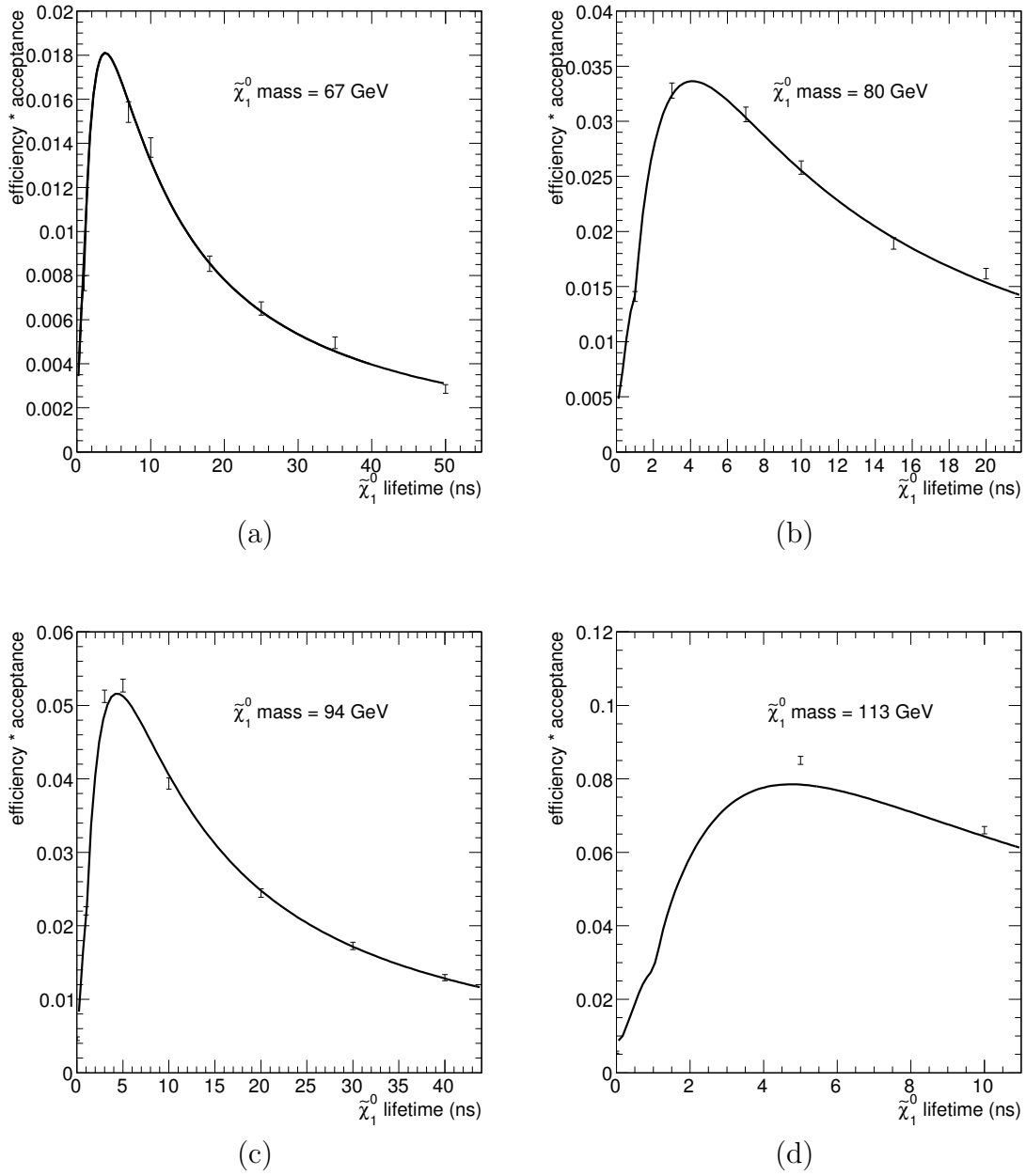

Figure 68: A comparison of the $A \cdot \epsilon$ between the fit functions and the MC simulation as a function of $\widetilde{\chi}_1^0$ lifetime for $\widetilde{\chi}_1^0$ masses 67 GeV/c^2 (a), 80 GeV/c^2 (b), 94 GeV/c^2 (c) and 113 GeV/c^2 (d). The acceptance is well modeled by the parametrization.

C. Model-Independent Cross Section Limits and GMSB Exclusion Regions

The $(A\cdot\epsilon)$-parametrization derived in the previous section can now be applied to show smooth, expected and observed GMSB exclusion regions as well as model-independent cross section limits. Figure 69 shows the expected and observed cross section limits along with the NLO production cross section as a function of $\widetilde{\chi}_1^0$ lifetime at a mass of 100 GeV/c^2 and as a function of $\widetilde{\chi}_1^0$ mass at a lifetime of 5 ns, close to the limit of the expected sensitivity. Indicated in green is the 6.5% uncertainty-band on the production cross section (see Table XIII). The yellow band shows the $\pm 1\sigma$ statistical variations of the expected cross section limit ($\sim$30%) using the data in Table XXI and the RMS definition in Eq. 7.3. The highest sensitivity is reached at a lifetime of $\sim$5 ns as the limit follows the shape of the $A \cdot \epsilon$ curves shown in Fig. 68. There is no exclusion of GMSB models with $\widetilde{\chi}_1^0$ lifetimes less than $\sim$1 ns as only few of the $\widetilde{\chi}_1^0$ have a long enough lifetime to produce delayed photons. However, most of the parameter space there is already excluded by searches in $\gamma\gamma + \not{E}_T$ [19]. While the acceptance increases (see Fig. 68) as a function of $\widetilde{\chi}_1^0$ mass the sensitivity goes down as the production cross section decreases rapidly.

Figure 70 shows the contours of constant 95% C.L. cross section upper limit based on the observed number of data events. The dominant features are (a) that for any $\widetilde{\chi}_1^0$ mass the sensitivity is highest for lifetimes of $\sim$5 ns, and (b) that the cross section limit goes down as either the mass or the lifetime increases. This figure allows for a sensitivity estimate to any proposed signal model that would lead to a delayed $\gamma + \not{E}_T + \geq 1$ jet final state, by comparing the shown expected cross section limit to any new production cross section. Finally, Fig. 71 shows the 95% C.L. exclusion region both for the expected and the observed number of events. Since the number

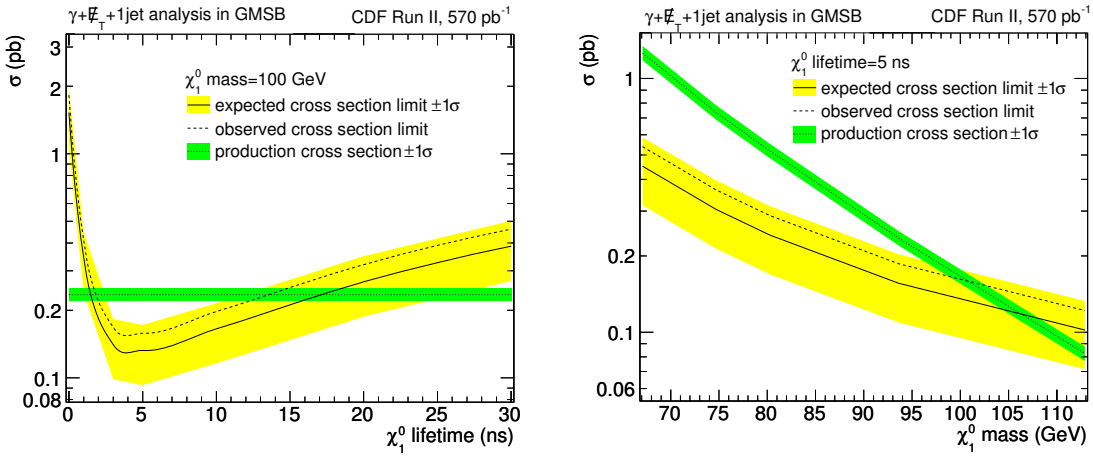

(a) (b)

Figure 69: The expected and observed cross section limits as a function of the $\widetilde{\chi}_1^0$ lifetime at a mass of 100 GeV/c^2 (a) and as a function of the $\widetilde{\chi}_1^0$ mass at a lifetime of 5 ns (b). Indicated in green is the 6.5% uncertainty-band for the production cross section (see Table XIII). Indicated in yellow is the variation in the expected limit due to the statistical uncertainty on the background prediction in the signal region (∼30%).

Table XXI: The 95% C.L. cross section limit as a function of the hypothetically observed number of events and the Poisson probability for this number of events based on the no-signal hypothesis. The expected limit and its variation are calculated as shown in [88] with Eqs. 7.2 and 7.3 using the optimized background expectation, acceptance and production cross section at an example GMSB point of $m_{\widetilde{\chi}}$ =100 GeV/c^2 and $\tau_{\widetilde{\chi}}$ =5 ns. With these numbers the expected cross section limit is 128 fb with an RMS on the limit of 42 fb, or ∼30%. This point has a production cross section of 0.162 pb and is excluded. Note that 2 events have been observed in this search.

N_{obs}	$\sigma_{obs}(N)$ (pb)	Probability
0	0.0799	0.287
1	0.120	0.358
2	0.153	0.224
3	0.196	0.0932
4	0.239	0.0291
5	0.280	0.00729

of observed events is above expectations, the observed limits are slightly worse than the expected limits. The $\widetilde{\chi}_1^0$ mass reach, based on the expected (observed) number of events is 108 GeV/c^2 (101 GeV/c^2), at a lifetime of 5 ns. The expected (observed) lifetime reach is 25 ns (21 ns) at the lowest simulated mass of 67 GeV. These limits, at large masses, extend well beyond those of LEP searches (using photon "pointing" methods [19]) and are currently the world's best.

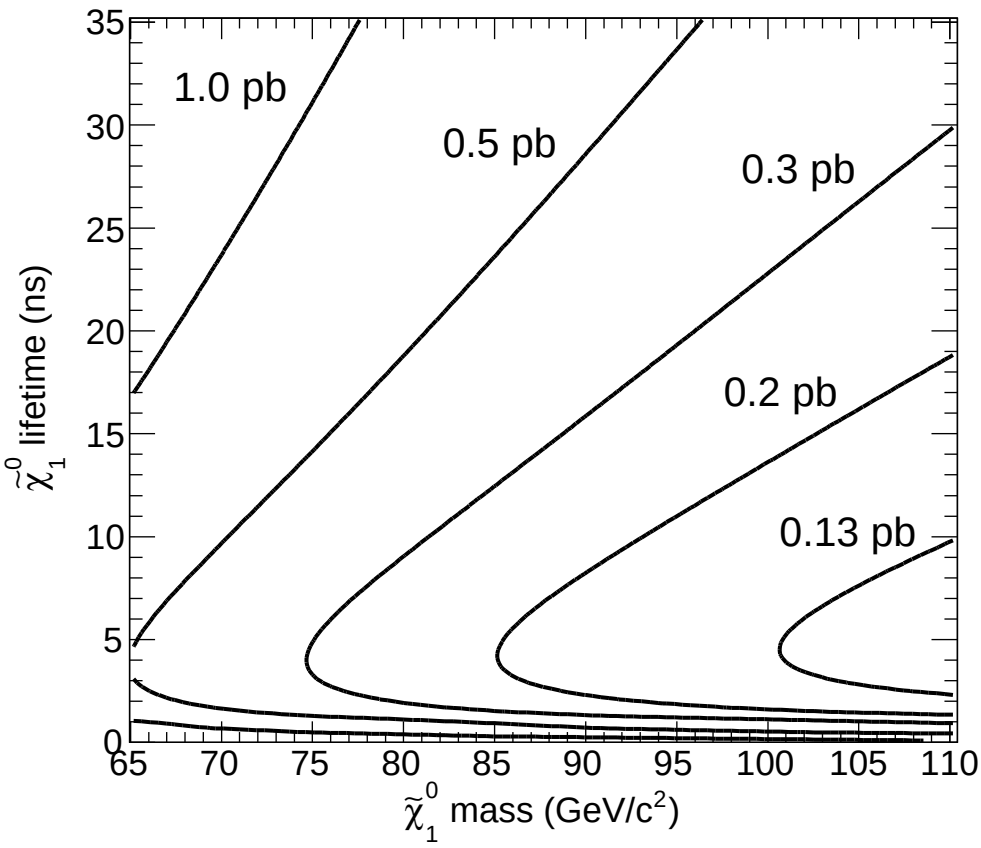

Figure 70: The contours of constant cross section limit, using the $A \cdot \epsilon$ interpolation, for the observed number of events.

While the $\widetilde{\chi}_1^0$ mass and lifetime limits are GMSB specific, a model-independent upper limit can be estimated on the number of events produced by any model that predicts events with a delayed $\gamma + \not\!\!E_T + \geq 1$ jet signature. This number, $N_{95}^{\rm obs}$, is

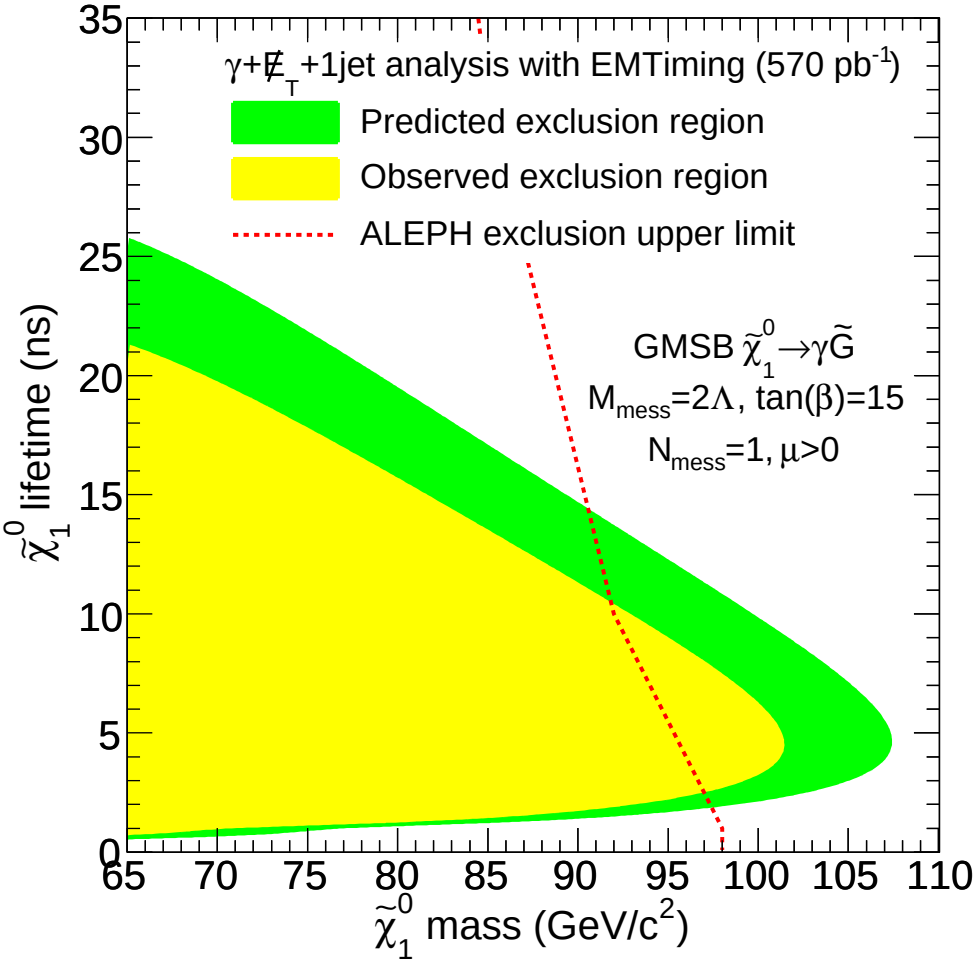

Figure 71: The expected and observed exclusion region using the interpolation function, along with the most stringent published LEP limits from ALEPH [19]. The highest mass reach of 108 GeV/c^2 (expected) and 101 GeV/c^2 (observed) is achieved at a lifetime of 5 ns.

defined as

$$N_{95}^{\text{obs}} = \sigma_{95}^{\text{obs}} \cdot \mathcal{L} \cdot (A \cdot \epsilon) \tag{8.7}$$

where σ_{95}^{obs} is the observed 95% C.L. cross section limit, $\mathcal{L}$ is the integrated luminosity, taken to be 570 pb^{-1}, and $(A \cdot \epsilon)$ is the acceptance, at any given GMSB parameter point. Using the data given in Table XVI, N_{95}^{obs} is estimated to be 5.5 events. As expected, this number is the same for all GMSB points.

CHAPTER IX

CONCLUSION

A. Summary of the Search

This dissertation has presented a search for heavy, neutral, long-lived particles that decay to photons in a sample of $\gamma + \not\!\!E_T + \geq 1$ jet events from $p\bar{p}$ collisions at $\sqrt{s} =$ 1.96 TeV using the CDF detector. Candidate events were primarily selected based on the delayed arrival time of the photon at the calorimeter as measured with the newly installed EMTiming system. In 570 pb^{-1} of data collected during 2004-2005 at the Fermilab Tevatron two events were found, consistent with the background estimate of 1.3±0.7 events. This result allows for setting quasi model-independent cross section limits and the exclusion region of a gauge mediated supersymmetry breaking model with $\widetilde{\chi}_1^0 \rightarrow \gamma\widetilde{G}$ in the $\widetilde{\chi}_1^0$ lifetime vs. mass plane, with a mass reach of 101 GeV/c^2 at $\tau_{\widetilde{\chi}} = 5$ ns. These results extend the world sensitivity to these models beyond those from LEP II [19]. As the search strategy does not rely on event properties specific to GMSB models, any delayed $\gamma + \not\!\!E_T + \geq 1$ jet signal can be excluded that would produce more than 5.5 events.

While this search extends the exclusion region only by a few GeV/c^2 for this GMSB model, this is an important region of parameter space where the $\widetilde{G}$ is predicted to be thermally produced in the early universe with a mass of 1-1.5 keV/c^2 as described in Section I.B.2.a. With a higher luminosity this search technique will be sensitive to this mass range as will be described in the next section.

B. Future Prospects

To investigate the prospects of a search at higher luminosity the expected cross section limit is calculated, assuming for simplicity that all backgrounds and their uncertainty fractions scale linearly with luminosity. While this assumption allows for a quick estimate it does not reflect the probable improvements in the background rejection methods or the worsening effects due to the higher instantaneous luminosity that could cause a higher fraction of events with a wrong vertex selection. The resulting background and cross section limit improvement along with the expected 95% C.L event limit, $N_{95}^{\rm exp}$, are shown in Table XXII for a GMSB example point at $m_{\widetilde{\chi}} = 100$ GeV/c^2 and $\tau_{\widetilde{\chi}} = 5$ ns. Figure 72 shows the expected exclusion region for a luminosity of 2 and 10 fb^{-1}. The figure suggests a further expansion of the exclusion region far beyond the LEP II limits. Also shown for comparison in this figure is the parameter space where the $\widetilde{G}$ is predicted to be thermally produced and to have a mass between 1 and 1.5 keV/c^2, calculated using Eq. 1.2. The figure suggests that this search technique will be sensitive to all of this important parameter space at 10 fb^{-1} luminosity for $\widetilde{\chi}_1^0$ masses of less than $\sim$140 GeV/c^2 and lifetimes of less than between 30 and 70 ns. The sensitivity could be improved even further by a photon pointing measurement at CDF that also complements the search method as discussed in App. F.

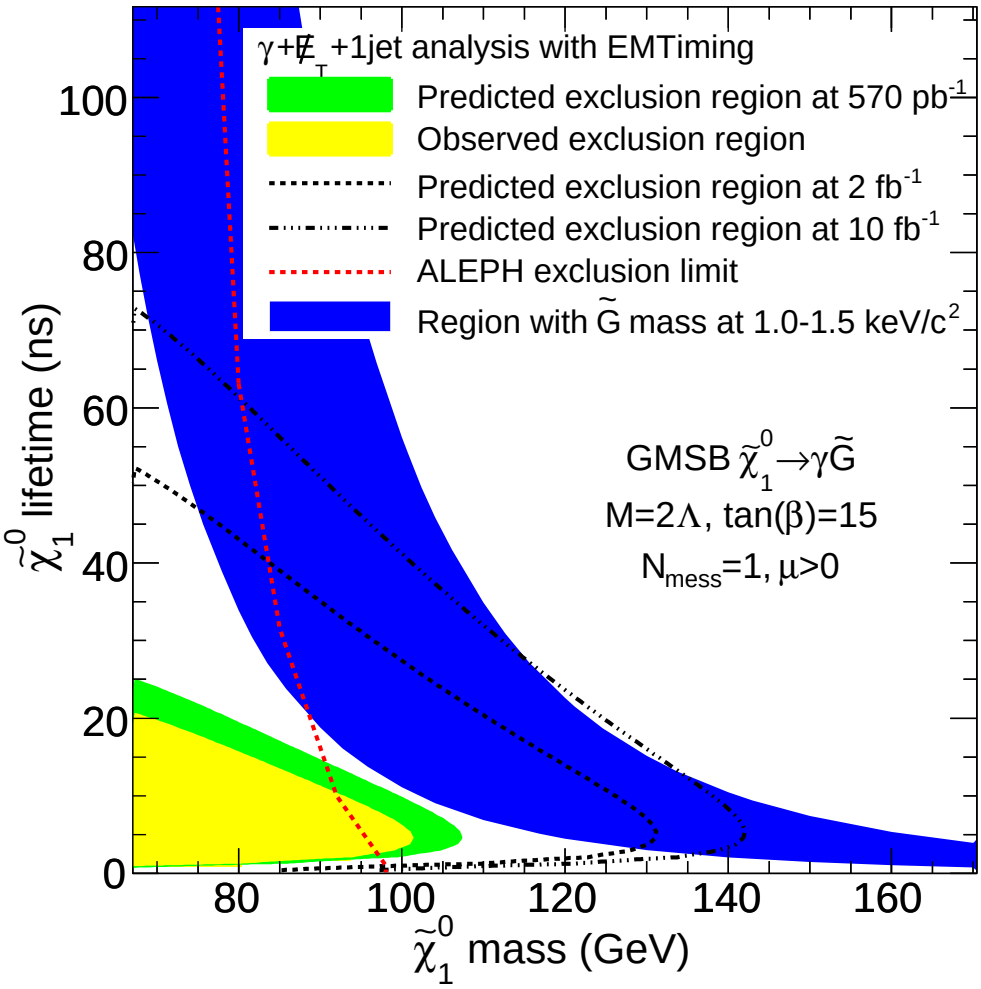

Figure 72: The dashed lines show the prediction of the exclusion limit after a scaling of the background prediction and the uncertainties for a luminosity of 2 fb^{-1} and 10 fb^{-1} respectively. The blue band shows the parameter space where the $\widetilde{G}$ mass is between 1 and 1.5 keV/c^2. A higher luminosity extends the sensitivity into this important parameter region.

Table XXII: The expected improvement for various luminosities for a GMSB example point at $m_{\widetilde{\chi}} = 100$ GeV/c^2 and $\tau_{\widetilde{\chi}} = 5$ ns assuming all backgrounds and their uncertainty fractions scale linearly with luminosity. The resulting exclusion region is plotted in Fig. 72.

Luminosity (fb^{-1})	Background	Factor of σ_{exp} Improvement	N_{95}^{exp}
0.570	1.3±0.7	1	4.60
2	4.3±2.3	0.46	7.44
10	21.9±11.6	0.0308	24.8

REFERENCES

[1] Particle Data Group, S. Eidelman *et al.*, Phys. Lett. B **592**, 1 (2004).

[2] J.H. Christenson, J.W. Cronin, V.L. Fitch, and R. Turlay, Phys. Rev. Lett. **13**, 138 (1964).

[3] K. Anikeev *et al.*, arXiv:hep-ph/0201071.

[4] S. Weinberg, *The Quantum Theory of Fields* (Cambridge University Press, Cambridge, UK, 1995-2000), Vols. 1-3.

[5] S. Martin, arXiv:hep-ph/9709356.

[6] Y. Ashie *et al.* (Super-Kamiokande Collaboration), Phys. Rev. Lett. **93**, 101801 (2004).

[7] M. Gonzalez-Garcia and Y. Nir, Rev. Mod. Phys. **75**, 345 (2003), and references therein.

[8] K. Hagiwara, A. Martin, D. Nomura and T. Teubner, Phys. Rev. D **69**, 093003 (2004) and Phys. Lett. B **649**, 173 (2007).

[9] G. Bennett *et al.* (Muon $(g-2)$ Collaboration), Phys. Rev. Lett. **92**, 1618102 (2004).

[10] C. Bennett *et al.*, Astrophys. J. Suppl. **148**, 1 (2003); N. Jarosik *et al.*, arXiv:astro-ph/0603452, submitted to Astrophys. J.

[11] G. Bertone, D. Hooperb and J. Silk, Phys. Rept. **405**, 279 (2005).

[12] R. Arnowitt and B. Dutta, New Astron. Rev. **49**, 143 (2005).

[13] D. Toback, Ph.D. thesis, University of Chicago, FERMILAB-THESIS-1997-36 (1997).

[14] J. Berryhill, Ph.D. thesis, University of Chicago, FERMILAB-THESIS-2000-02 (2000).

[15] At CDF, and other collider experiments, the collision occurs with no momentum in the plane transverse to the collision. By conservation of momentum the vector sum of the momenta of the final state particles must be zero in the transverse plane. Since the energies of most final state particles are measured by the detector, any imbalance of energy could indicate the presence of a particle, such a neutrino, which does not interact with the detector. This imbalance is known as missing transverse energy ($\not\!\!E_T$).

[16] S. Dimopoulos *et al.*, Phys. Rev. Lett. **76**, 3494 (1996).

[17] See for example M. Dine, A. Nelson, Phys. Rev. D **48**, 1277 (1993) or S. Ambrosanio, G. L. Kane, G. D. Kribs, S. P. Martin and S. Mrenna, Phys. Rev. D **54**, 5395 (1996).

[18] C. H. Chen and J. F. Gunion, Phys. Rev. D **58**, 075005 (1998).

[19] A. Heister *et al.* (ALEPH Collaboration), Eur. Phys. J. C **25**, 339 (2002); A. Garcia-Bellido, Ph.D. thesis, Royal Holloway University of London (2002) (unpublished), arXiv:hep-ex/0212024; also see M. Gataullin, S. Rosier, L. Xia and H. Yang, AIP Conf. Proc. **903**, 217 (2007). (2007); OPAL Collaboration, Proc. Sci. HEP2005 346 (2006); DELPHI Collaboration, Eur. Phys. J. C **38**, 395 (2005).

[20] M. Strassler and K. Zurek, arXiv:hep-ph/0604261; M. Strassler and K. Zurek, arXiv:hep-ph/0607160

[21] Concerning the notation, the superpartner of the SM particle is indicated by placing by a tilde above the letter.

[22] A. De Rujula, S. L. Glashow and U. Sarid, Nucl. Phys. B **333**, 173 (1990).

[23] F. Gabbiani, E. Gabrielli, A. Masiero and L. Silvestrini, Nucl. Phys. B **477**, 321 (1996); J. Ellis and D. Nanopoulos, Phys. Lett. B **110**, 44 (1982).

[24] There are various ongoing direct detection experiments. See Y. Ramachers, Nucl. Phys. Proc. Suppl. **118**, 341 (2003) for a review.

[25] See for example, R. Arnowitt, P. Nath, arXiv:hep-ph/9708254 and references therein.

[26] H. Baer *et al.*, FERMILAB-Pub-00/251-T, S. Dimopoulos *et al.*, SLAC-PUB-7236 (1996).

[27] If non-gauge interaction were involved, gauginos that only couple through SM gauge interactions could be lighter than the electroweak scale set by the SM Higgs scalars which is excluded by observation.

[28] J. L. Feng and T. Moroi, Phys. Rev. D **58**, 035001 (1998).

[29] B. C. Allanach *et. al.*, Eur. Phys. J. C **25**, 113 (2002).

[30] J. Feng, Phys. Rev. D **70**, 075019 (2004), and references therein.

[31] P. Bode, J. Ostriker and N. Turok, Astrophys. J. **556**, 93 (2001).

[32] L. Covi, J. Kim and L. Roszkowski, Phys. Rev. Lett. **82**, 4180 (1999).

[33] K. Choi and L. Roszkowski, AIP Conf. Proc. **805**, 30 (2006).

[34] E. Baltz *et al.*, J. High Energy Phys. **0305**, 067 (2003).

[35] M. Carena, *et al.*, arXiv:hep-ex/9712022.

[36] T. Sjöstrand, L. Lönnblad and S. Mrenna, arXiv:hep-ph/0108264 (2001); we use version 6.216.

[37] W. Beenakker *et al.*, Phys. Rev. Lett. **83**, 3780 (1999).

[38] T. Affolder *et al.* (CDF Collaboration), Phys. Rev. D **64**, 032001 (2001), T. Abe *et al.* (CDF Collaboration), Phys. Rev. Lett. **68**, 1104 (1992).

[39] Taus can decay into lighter leptons for example via $\tau^{\pm} \to e^{\pm}\nu_e\nu_\tau$ or $\tau^{\pm} \to \mu^{\pm}\nu_\mu\nu_\tau$ ("leptonically") and into one or more pions as $\tau^{\pm} \to \pi^{\pm}\nu_\tau$ or $\tau^{\pm} \to \pi^{\pm}\pi^{\mp}\pi^{\pm}\nu_\tau$ ("hadronically"). While there are more efficient ways at CDF to identify hadronic taus (see A. Safonov, Nucl. Phys. Proc. Suppl. 144, 323 (2005)), they can also be identified as jets [38]. A better tau identification may be a possible improvement for future GMSB searches in the $\gamma + \not\!\!E_T + \geq 1$ jet signature.

[40] P. Wagner and D. Toback, Phys. Rev. D **70**, 114032 (2004).

[41] D. Acosta *et al.* (CDF Collaboration), Phys. Rev. D **71**, 031104 (2005).

[42] V. Abazov *et al.* (D0 Collaboration), Phys. Rev. Lett. **94**, 041801 (2005).

[43] A. Abulencia *et al.* (CDF Collaboration), FERMILAB-PUB-07-075-E (2007), accepted for publication in Phys. Rev. Lett.

[44] Tevatron Accelerator Division, "Operations Rookie Books," http://www-bdnew.fnal.gov/operations/rookie_books/rbooks.html (accessed 2007).

[45] D. Acosta *et al.* (CDF Collaboration), Phys. Rev. D **71**, 032001 (2005).

[46] Fermilab Beams Division, Run II Handbook (1998), http://www-bd.fnal.gov/runII/index.html (accessed 2007).

[47] This expression refers to a data-acquisition run, which is not to be confused with a "collider run" between major machine upgrades that can take several years.

[48] A. Bhatti *et al.*, Nucl. Instrum. Methods Phys. Res., Sect. A **566**, 375 (2006).

[49] Fermilab Visual Media Services, Graphic Arts Gallery, http://www-visualmedia.fnal.gov (accessed 2007).

[50] We use a cylindrical coordinate system that defines z as the longitudinal axis along the proton beam axis, in which θ is the polar angle, ϕ is the azimuthal angle and $\eta = -\ln\tan(\theta/2)$. The west (east) side of the detector corresponds to the positive- (negative-)z side. In general, all kinematic quantities are defined from $z_{\text{vertex}} = 0$, unless a vertex has been reconstructed that defines the origin: $E_T = E\sin\theta$ and $p_T = p\sin\theta$ where E is the energy measured by the calorimeter and p the momentum measured in the tracking system. $\vec{\not{E}}_T = -\sum_i E_T^i \vec{n_i}$ where $\vec{n_i}$ is a unit vector that points from the interaction vertex to the ith calorimeter tower in the transverse plane. $\not{E}_T$ is the magnitude of $\vec{\not{E}}_T$.

[51] R. Blair *et al.* (CDF Collaboration), FERMILAB-PUB-96-390-E.

[52] CDF Run IIb Technical Documents, http://www-cdf.fnal.gov/run2b.html (accessed 2007).

[53] CDF Pictures Database, http://www-cdf.fnal.gov/events/pics.html (accessed 2007).

[54] Note that photons can start showering as far as $3X_0$ into the CEM as they interact statistically with the material via bremsstrahlung.

[55] J. Elias *et al.*, Nucl. Instrum. Methods Phys. Res., Sect. A **441**, 366 (2000); D. Acosta *et al.*, Nucl. Instrum. Methods Phys. Res., Sect. A **461**, 540 (2001).

[56] S. Klimenko, J. Konigsberg and T.M. Liss, FERMILAB-FN-0741 (2003).

[57] For a description of beam halo see R. Tesarek, CDF Report No. CDF-NOTE-5873 (2002) and P. Onyisi, CDF Report No. CDF-NOTE-6009 (2003), both unpublished. There are many early CDF Reports on cosmic ray background. For a recent discussion see M. Goncharov *et al.*, CDF Report No. CDF-NOTE-8409 (2006), unpublished.

[58] EMTiming homepage, http://hepr8.physics.tamu.edu/hep/emtiming/ (accessed 2007).

[59] M. Goncharov *et. al.*, Nucl. Instrum. Methods Phys. Res., Sect. A **565**, 543 (2006).

[60] Table II shows 4 less PMT channels than one would expect from the calculation. This is because the two towers that cover the region $75° < \phi < 90°$ and $0.77 < \eta < 1.0$ contain the solenoid cooling pipe ("chimney").

[61] M. Goncharov *et al.*, CDF Report No. CDF-NOTE-7515 (2005), unpublished.

[62] E. Gerchtein and M. Paulini, arXiv:physics/0306031.

[63] Y. Liu, Ph.D. thesis, Université de Genève, FERMILAB-THESIS-2004-37 (2004).

[64] Note that while α varies for the prompt electrons with the vertex position as described in Section III.C, the efficiency as a function of β is estimated by varying the CES X of the electron, assuming that a large CES X is equivalent of a large β. This allows for a maximum angle of $\sim 6^\circ \approx \arctan(20\text{cm}/183\text{cm})$ where 20 cm is the half-width of a CEM tower.

[65] R. Brun, F. Bruyant, M. Maire, A. C. McPherson, and P. Zanarini CERN Report No. DD/EE/84-1 (1987).

[66] R. Blair, CDF Report No. CDF-NOTE-1436 (1991), unpublished.

[67] Noise in this system is simulated using a Gaussian with a mean of 48 analog-to-digital conversion (ADC) units and RMS of 3.6 (6) for strips (wires) [98] and added to the output energies. The conversion factors from these ADC units to energies in GeV are 120.0480 for the strips and 240.3846 for the wires [98].

[68] The hypothesis has always been that GEANT3 does not properly model the keV level phenomenon which are important for gas detectors. In particular, long range effects from low energy Bremsstrahlung by electrons, subsequent re-absorption of the high energy bremsstrahlung photon and ionization at some distance from the photon shower. The cutoffs and cross sections were tuned for higher density ionization devices/detectors. This, however, is just a hypothesis. The standard simulation on the other hand, which is based on test beam data, has no straightforward way to deal with showers from vertices that lie at $(x, y) \neq (0, 0)$ and even the z variation is probably limited. (private communication with B. Blair)

[69] T. Müller *et al.*, CDF Report No. CDF-NOTE-6047 (2003), unpublished; J.-F. Arguin, B. Heinemann and A. Yagil, CDF Report No. CDF-NOTE-6238 (2003), unpublished.

[70] While there is no good reference for the standard track requirements, they are summarized at http://www-cdf.fnal.gov/internal/physics/joint_physics/instructions/ (accessed 2007).

[71] G. McLachlan and D. Peel, *Finite Mixture Models* (John Wiley & Sons Inc., Hoboken, US), ISBN 0471006262.

[72] M. Jones, B. Kephart and R. Vidal, CDF Report No. CDF-NOTE-5951 (2002), unpublished.

[73] For technical reasons we have decided not to show distributions of the raw time from the TDC banks.

[74] The conversion from ADC counts to energy is roughly: 1000 ADC counts $\simeq$ 3 GeV.

[75] G. Grindhammer, M. Rudowicz, and S. Peters, Nucl. Instrum. Methods Phys. Res., Sect. A **290**, 469 (1990).

[76] F. Abe *et al.* (CDF Collaboration), Phys. Rev. D **45**, 1448 (1992).

[77] Trigger towers encompass $0.2 \times 15°$ in η-ϕ space.

[78] P. Onyisi, CDF Report No. CDF-NOTE-6381 (2003), unpublished.

[79] A. Abulencia *et al.* (CDF Collaboration), FERMILAB-PUB-05-360-E, submitted to Phys. Rev. D.

[80] M. Albrow *et al.*, CDF Report No. CDF-NOTE-5926 (2002), unpublished.

[81] P. Simeon and D. Toback, CDF Report No. CDF-NOTE-7084 (2006), unpublished.

[82] F. Paige and S. Protopopescu, BNL Report BNL38034, 1986; F. Paige, S. Protopopescu, H. Baer and X. Tata, hep-ph/0001086. We used version 7.64 to generate the SUSY masses.

[83] CDF Jet and Energy Resolution Group, http://www-cdf.fnal.gov/internal/physics/top/jets/corrections.html (accessed 2007).

[84] CDF Joint Physics Group Agenda, Procedures for Estimating Uncertainties due to Initial and Final State Radiation, http://www-cdf.fnal.gov/internal/physics/joint_physics/agenda/20050527-minutes.html (accessed 2007). For a description of initial and final state radiation see Ref. [36] and references therein.

[85] O. Gonzalez and C. Rott, CDF Report No. CDF-NOTE-7051 (2005), unpublished; J. Pumplin *et al.*, J. High Energy Phys. **0207**, 012 (2002); J. Huston *et al.*, J. High Energy Phys. **0310**, 046 (2003).

[86] M. Griffiths *et al.*, CDF Report No. CDF-NOTE-8389 (2006), to be submitted to PRL.

[87] See e.g. W. Beenakker *et al.*, Nucl. Phys. B **492**, 51 (1997); Prospino 2.0, http://www.ph.ed.ac.uk/$\sim$tplehn/prospino/prospino.html (accessed 2007).

[88] E. Boos, A. Vologdin, D. Toback and J. Gaspard, Phys. Rev. D **66**, 013011 (2002). J. Conway, CERN Yellow Book Report No. CERN 2000-005 (2000), p. 247;

[89] J. Heinrich, CDF Report No. CDF-NOTE-7587 (2005), unpublished; J. Heinrich *et al.*, CDF Report No. CDF-NOTE-7117 (2004), unpublished.

[90] R. Culbertson *et al.*, CDF Report No. CDF-NOTE-8372 (2006), unpublished.

[91] B. Blair *et al.*, CDF Report No. CDF-NOTE-5830 (2002), unpublished.

[92] G. Apollinari, K. Goulianos, P. Melese and M. Lindgren, Nucl. Instrum. Methods Phys. Res., Sect. A **412**, 515 (1998).

[93] D. Ambrose *et al.*, CDF Report No. CDF-NOTE-6361 (2003), unpublished.

[94] T. Phillips, CDF Report No. CDF-NOTE-6277 (2003).

[95] Note that the plug EMTiming system simulation extrapolates the photon trajectory to the plug (PES) shower maximum subdetectors |z| = 185.4 cm.

[96] L. Balka *et al.*, Nucl. Instrum. Methods Phys. Res., Sect. A **267**, 272 (1988); F. Abe *et al.* (CDF Collaboration), Phys. Rev. Lett. **73**, 2662 (1994); D. Partos, Ph.D. thesis, Brandeis University, FERMILAB-THESIS-2001-21 (2001).

[97] K. Hagiwara *et al.*, Phys. Rev. D **66**, 010001 (2002).

[98] CDF Photon Group, CES and CPR geometry, http://www-cdf.fnal.gov/internal/physics/photon/docs/CES_CPR_geometry.html (accessed 2007).

APPENDIX A

EMTIMING ONLINE MONITORING RESULTS

This appendix shows the online monitoring results as they illustrate the performance of the EMTiming system. The monitoring helps control the quality of the system and its validation during data-taking in realtime ("ObjectMon"). Figure 73 shows the channel-by-channel fraction of all events with a time recorded by the TDC, if the sum of PMT energies in a CEM (PEM) tower is greater than 6.25 GeV (3.0 GeV) where the efficiency is expected to be 100%. Figure 74 shows the rate at which a timing hit has been recorded by the TDC in a tower with little energy deposited ("fake firings"). A run with pathologies has been purposely chosen for pedagogical reasons. Each pathology is described in the captions of those figures. While the rate of pathologies has been generally very low since installation (one broken channel in $\sim$20000 PMTs $\cdot$ month), the most common pathologies of channel failure is on the LEMO connector to the TB due to pulled wires or loosely connected LEMO connectors. If a failure occurs the channel is marked bad for the calibration tables.

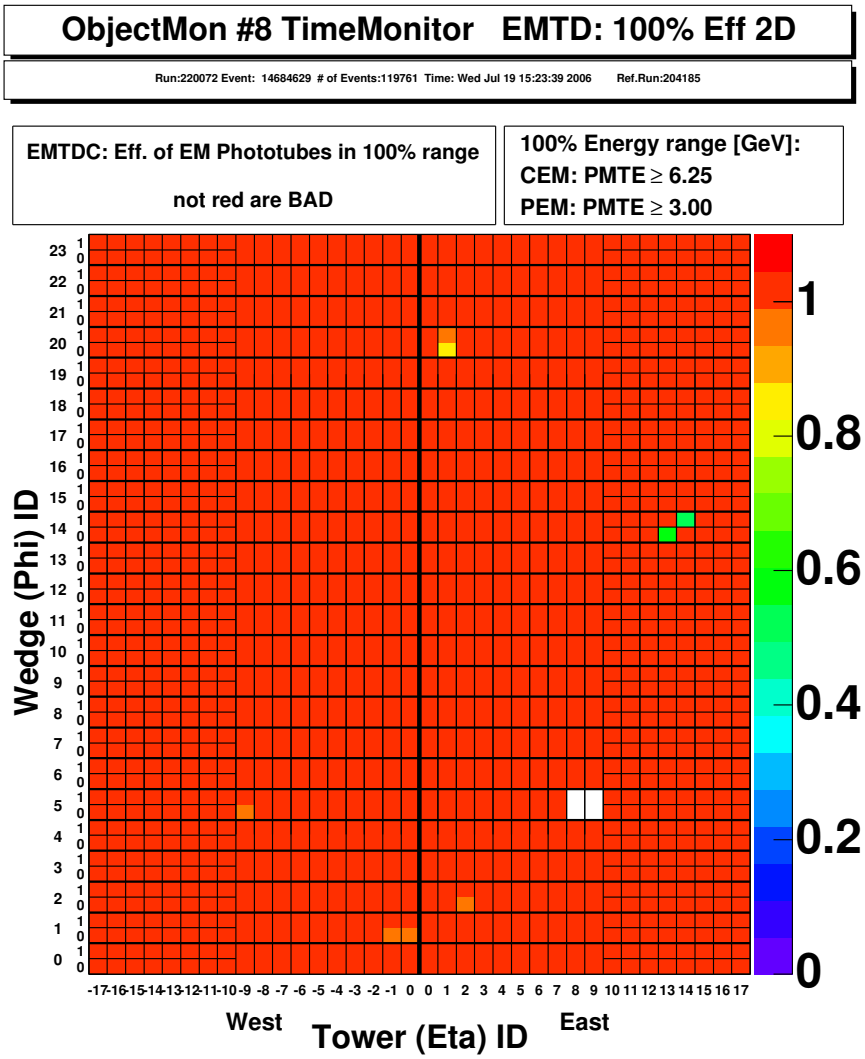

Figure 73: The fraction of all events with a time recorded in a tower with more than 6.25 GeV (3 GeV) energy deposited, as shown by the monitoring system. The y-axis shows the 24 wedges in ϕ numbered starting at $\phi = 0$; the x-axis shows the towers in η numbered starting at $\eta = 0$ from 0-9 (CEM) and from 10-17 (PEM) for each west and east side of the detector. This particular run shows two pathologies: The LEMOs into the TB of the PEM channels in the east towers 13 and 14 of wedge 14 are swapped which yields half the efficiency in either channel. The CEM channel in wedge 20, east tower 1 had a bad LEMO connection to the TB that causes a greater threshold width of the efficiency curve and in turn to worse efficiency in the lower energy bins. Note that the two white towers indicate the chimney.

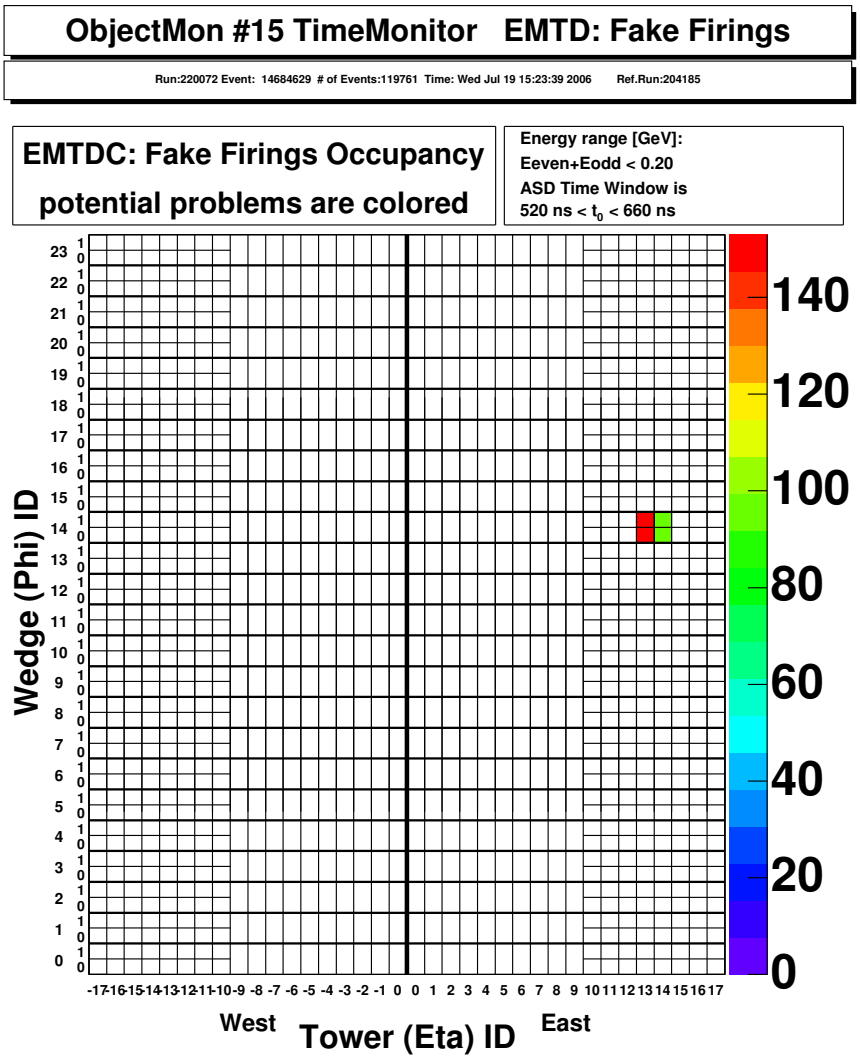

Figure 74: The rate at which an energy deposit of less than 0.2 GeV causes a time to be recorded in the TDC for each tower in the CEM and PEM ("fake firings"), as shown by the monitoring system for the same run as shown in Fig. 73. The only towers that show fake firings are the ones that contain the swapped LEMO cable-TB connections, and can be easily determined.

APPENDIX B

IDENTIFICATION VARIABLES FOR ELECTRONS

This appendix presents the standard CDF high-E_T electron selection criteria. Since electrons interact with the calorimeter similarly to photons, they are used to study the vertexing performance, the timing resolution measurement as well as the prompt background estimate. The electron identification criteria for both central and plug are reviewed in [79], and can be separated into requirements on the electron track in the COT (only for central electrons), the energy deposit in the calorimeter and the matching between the track and the calorimeter cluster. The requirements are summarized in Table XXIII for central and plug electrons separately.

Electrons in the central calorimeter are identified similarly to photons, in particular the calorimeter cluster requirements (fiduciality, energy isolation, transverse profile CES χ^2 test, ratio of hadronic to EM energy) are similar and the E_T measurement is identical to photons (see Section III.A). However, the $\frac{E_{\mathrm{Had}}}{E_{\mathrm{Em}}}$ is tighter than for photons as these can start showering up to $3X_0$ into the EM calorimeter. A lateral sharing variable, $Lshr$, compares the energy that the electron candidate deposits in neighboring towers in the same wedge to that expected from test beam data to help discriminate it from hadronic showers. The highest-p_T track is selected that is extrapolated to be within 3 cm in z (Δz) and a charge dependent distance in (r, ϕ) (Δx) of the CES shower position. The track must have at least three axial and stereo superlayers with >5 hits to ensure a good track quality, as described in Section III.F.2. The E/p requirement matches the track momentum to the calorimeter energy to reduce the misidentification due to conversions of $\gamma \to e^+e^-$. The track is required to originate from the most probable collision region, less than 60 cm away from the center of the detector.

The identification of plug electrons are substantially different from those of central electrons as the PEM and the CEM are different detectors and as the COT detector is not fully fiducial for tracks in this η region. Plug electron candidates deposit their energy in clusters (see Section III.A) of the plug EM detector (PEM) that are required to have an E_T of at least 15 GeV. The PEM consists of alternating scintillator and lead layers providing coverage in the region $1.1 < |\eta_{\rm det}| < 3.6$ and measuring particles with an energy resolution of $\frac{16\%}{\sqrt{E_T}} \oplus 1\%$. As an isolation requirement, the total transverse isolation energy in a cone of 0.4, $E_T^{\rm Iso}$, must be less than 10% of the cluster E_T. The $\frac{E_{\rm Had}}{E_{\rm Em}}$ is required to be less than 0.05, similar to central electrons. The $\chi^2_{3\times3}$ variable compares the energy distribution in a 3x3 array of PEM towers around the seed tower to the distribution expected from test beam data and must be less than 10. The electron candidate is required to have a cluster that is measured in the plug EM shower maximum detector (PES) [92] by two layers ("u" and "v") of 5 mm wide scintillating strips at a depth of $\sim 6X_0$ with a 45° crossing angle to each other. The energy ratio of 5 to 9 strips of the cluster for each layer separately must be at least 0.65. The PES cluster is fiducial if it has an η with magnitude within 1.2 and 2.8. A track is matched to the calorimeter energy deposit by selecting the highest-p_T track that is extrapolated to be within 3 cm of the PES cluster position.

Table XXIII: Central and plug electron ID requirements. Note that "q" is the charge of the electron.

Requirement
Central Electrons
$E_T > 20$ GeV
Fiducial: $\lvert X_{\rm CES}\rvert < 21$ cm && 9 cm $< \lvert Z_{\rm CES}\rvert < 230$ cm
$\frac{E_{\rm Had}}{E_{\rm Em}} < 0.055 + 0.00045 \cdot E$
$\chi^2_{\rm Strip} < 10$
$Lshr < 0.2$
$p_T > 10$ GeV
$E^{\rm Iso} < 0.1 \cdot E_T$
$-3 < \Delta x \cdot q < 1.5$ && $\lvert\Delta z\rvert < 3$
$\lvert z_0\rvert < 60$
$p_T > 50$ GeV or $0.5 < E/p < 2.0$
Track traverses $\geq$3 stereo and $\geq$3 axial COT superlayers with 5 hits each
Plug Electrons
$E_T > 15$ GeV
Fiducial: $1.2 < \lvert\eta_{\rm PES}\rvert < 2.8$
$\frac{E_{\rm Had}}{E_{\rm Em}} < 0.05$
$\chi^2_{3\times3} < 10$
$E_T^{\rm Iso} < 0.1 \cdot E_T$
$E^{\rm u}_{\rm PES}(5\times9) > 0.65$ && $E^{\rm v}_{\rm PES}(5\times9) > 0.65$
$\Delta R_{\rm trk} < 3$ cm

APPENDIX C

TRACK REQUIREMENTS AND CORRECTIONS FOR SIMULATED TRACKS

This appendix describes the track requirements used in this search as well as the corrections used for simulated tracks and their coding implementation. Also described is a systematic bias in the t_0 measurement that likely cause the non-Gaussian tails in Fig. 36c.

A. Track Requirements

This search uses the standard CDF requirements for COT tracks [70] with additional timing quality requirements to identify charged particles. Both are summarized in Table VI. They are:

- Tracks are required to have $p_T > 0.3$ GeV/c to ensure that their speed is sufficiently relativistic to be approximated by the speed of light, an assumption used in the tracking algorithms.

- Protons with $p_T > 0.3$ GeV/c that are non-relativistic ("slow protons") likely have a mismeasured t_0. They are rejected by requiring either the energy loss $(\frac{\mathrm{d}E}{\mathrm{d}x})$ as the track traverses the COT to be <20 keV/cm, if its curvature indicates a positive charge, or its p_T to be >1.4 GeV/c where the $\frac{\mathrm{d}E}{\mathrm{d}x}$ does not provide good separation between kaons, pions and protons [93].

- To ensure that the tracks traverse enough of the COT detector to be well measured, tracks are required to originate from $|z_0| < 70$ cm, near the center of the detector, and to have a well-measured z_0 with an uncertainty $\mathrm{Err}(z_0) < 1$ cm. Additionally, tracks are required to have $|\eta| < 1.6$ to be fiducial in the COT.

- Tracks are required to occur within a time window of $|t_0| < 40$ ns around a calibrated, average collision time, as tracks outside this time window are unlikely to be produced in a collision. The t_0 is also required to be well-measured ($0.05 < \mathrm{Err}(t_0) < 0.8$ ns).

- Tracks typically generate hits in many superlayer, compared to random hits from noise. To ensure a reliable track reconstruction and a well-measured p_T, tracks are required to have at least three axial and stereo superlayers with >5 hits.

B. Additional Corrections for Simulated Tracks

The standard CDF MC does not simulate the track t_0 and $\frac{\mathrm{d}E}{\mathrm{d}x}$ correctly, as they show dependencies on the track p_T and η and the angle θ, respectively.

As tracks are not included in the vertexing if their $\frac{\mathrm{d}E}{\mathrm{d}x}$ is consistent with a slow proton ($\frac{\mathrm{d}E}{\mathrm{d}x} > 20$ keV/cm), the simulation of the $\frac{\mathrm{d}E}{\mathrm{d}x}$ is critical for the GMSB acceptance estimate. The $\frac{\mathrm{d}E}{\mathrm{d}x}$ correction takes into account the varying amount of material that the trajectory crosses at higher θ:

$$\left(\frac{\mathrm{d}E}{\mathrm{d}x}\right)_{\mathrm{corr}} = (\frac{\mathrm{d}E}{\mathrm{d}x} - 12) \cdot (1 - 1.35 \log(\sin(\theta)))^{-1}. \tag{C.1}$$

The track t_0 shows in MC a charge-dependent correlation with the track p_T and η at low p_T. The track t_0 distributions are shown in Figs. 75 and 76 as a function of p_T and η for positively and negatively charged tracks separately. These effects are not entirely understood. Hypotheses for the t_0 variation as a function of p_T are that (1) at low p_T the $\frac{\mathrm{d}E}{\mathrm{d}x}$ requirement on the track is not a good discriminant to reject slow protons and biases the average track t_0 to larger values and (2) the drift of the charge in the gas of the COT to the sense wire is not well modeled for both track simulation

and reconstruction. Hypotheses for the t_0 variation as a function of η are that at $|\eta| > 1$ tracks traverse COT regions that have a lower reconstruction efficiency that are not well modeled. Those effects are not properly taken into account for simulated tracks. The variations for negative charged simulated tracks are parametrized with:

$$t_0^{corr} = t_0 - 0.55 \cdot \sqrt{\frac{1.5}{p_T}} + 0.1 - 0.01 \cdot (9 - 10 \cdot \eta^4) \tag{C.2}$$

The corrections for positively charged tracks with $p_T < 10$ GeV/c are:

$$\begin{aligned} t_0^{corr} = t_0 \quad &- \quad (\frac{2.56521 - 16.3752 \cdot p_T}{1 + e^{-p_T^{-1}-2}} + \frac{1.92549 + 2.21641 \cdot p_T}{1 + e^{p_T^{-1}-2}}) \\ &- \quad 0.01 \cdot (-2.64164 + 0.332608\eta \\ &\quad +4.15586\eta^2 + 3.64391\eta^3 + 2.28618\eta^4) \end{aligned} \tag{C.3}$$

C. Systematic Bias in the Track t_0 Measurement

The vertex t_0 resolution in Fig. 36(c) shows non-Gaussian tails at the 2.3σ level. This appendix shows that this is likely due to a systematic bias of the track t_0 measurement towards $t_0 = 0$ ns at large vertex collision times.

Figure 77 shows the difference between the reconstructed, simulated track t_0 and the true vertex t_0 as a function of the true vertex t_0 after the corrections that are described in App. C.B. There is a systematic bias towards having a $t_0 = 0$ ns that is present in MC and data due to tracking hits in the COT being associated to a track with the assumption that the vertex t_0 is 0 ns. With these biased hits the track t_0 is calculated [94]. The t_0 values of many tracks are then averaged to a vertex t_0. This effect is not corrected for as the fraction of the events on the non-Gaussian tail is low ($\sim$1%) with only a minor systematic error on the order of 0.3 ns at a vertex t_0 of 3 ns. Note that this does not affect the vertex t_0 calculation as shown with the Gaussian

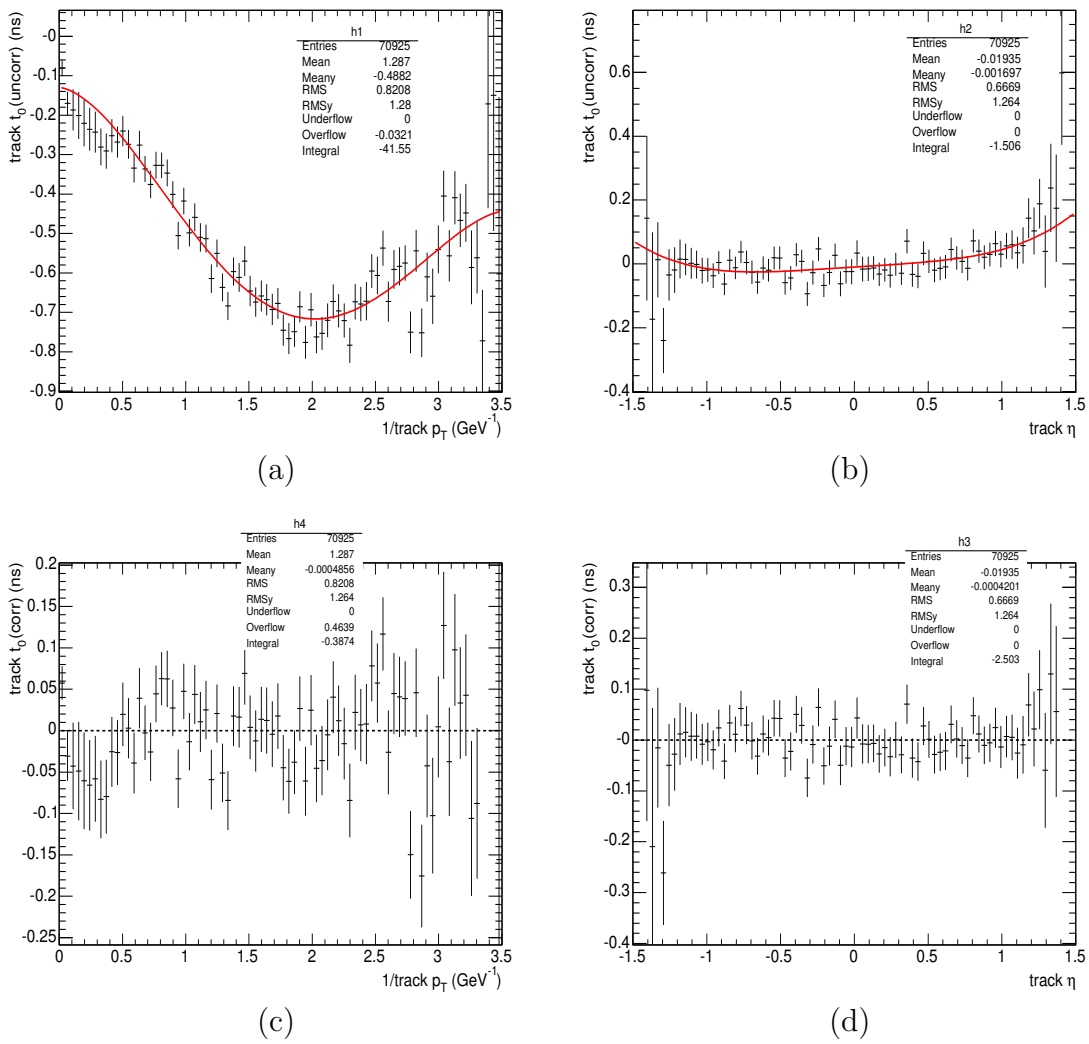

Figure 75: The mean t_0 of the negatively charged simulated tracks (*TStnTrack::T0Cot()*) as a function of (a) their $1/p_T$ before any corrections, (b) their η after applying the p_T dependent corrections. In (c) and (d) both distributions after both corrections are applied.

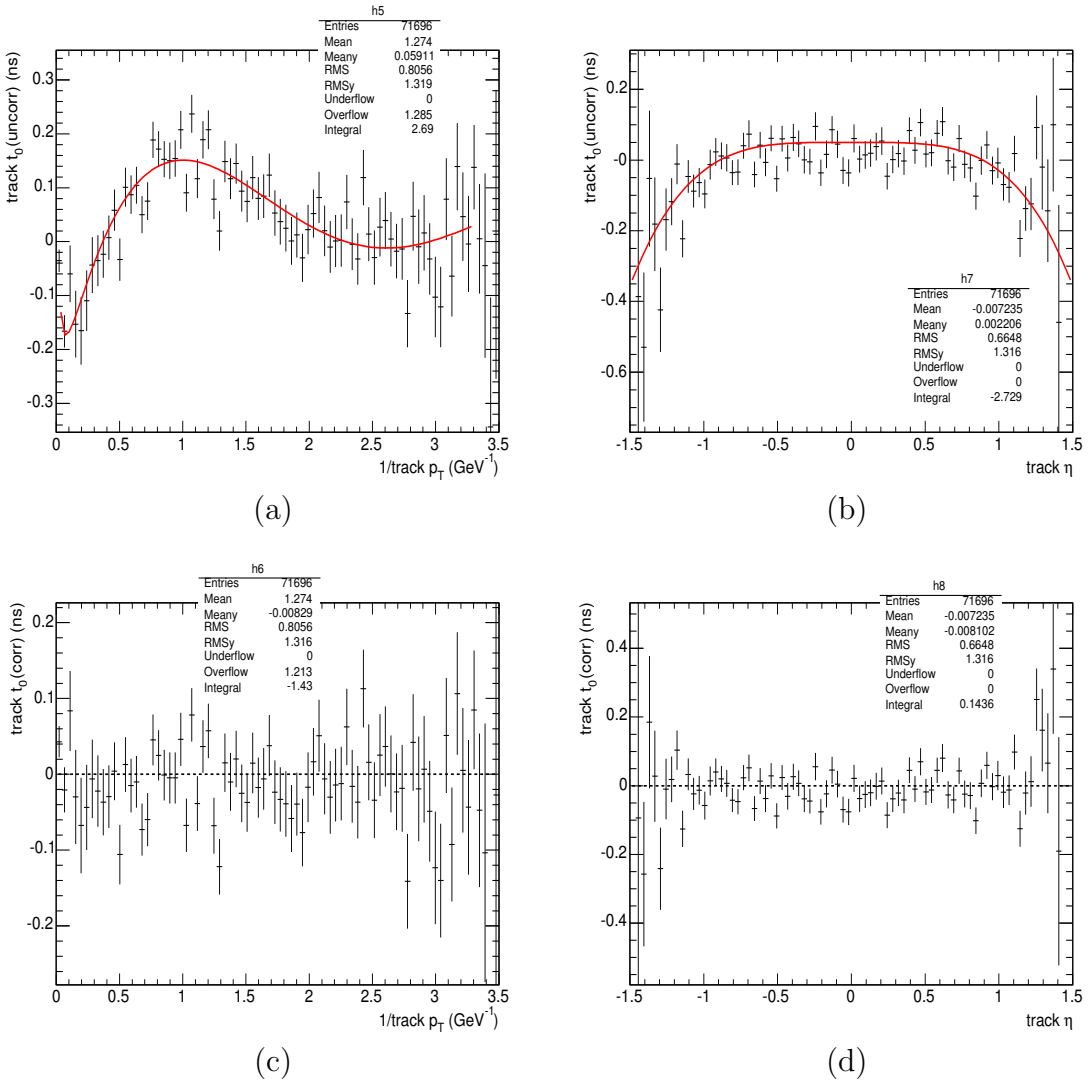

Figure 76: The same as in Fig. 75 but for positively charged simulated tracks.

distribution in Fig. 30.

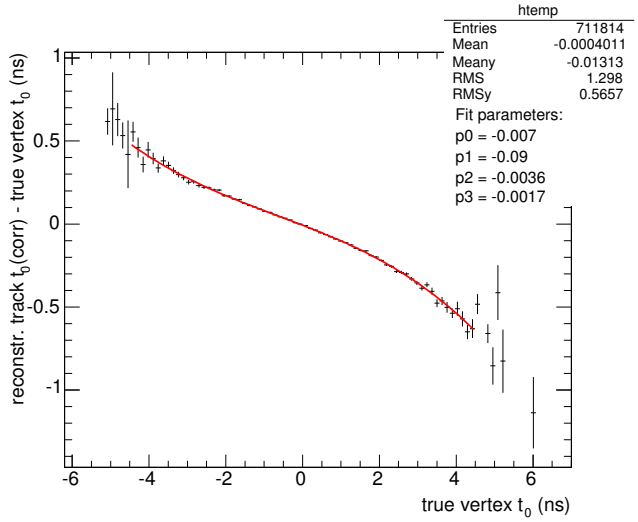

Figure 77: The difference between the reconstructed, simulated track t_0 and the true vertex t_0 as a function of the true vertex t_0 after the corrections that are described in App. C for all simulated tracks that pass the basic requirements in Table VI. The fit is made with a 3rd order polynomial. This effect is due to the biased hit selection towards 0 of the track reconstruction algorithm.

APPENDIX D

TIMING AND CORRECTIONS FOR PLUG PHOTONS

This appendix presents the corrected arrival time, $t_{\rm corr}$ (see Section III.G), of plug photons for use in future analyses. The $t^{\gamma}_{\rm corr}$ is calculated in the same way as for central photons with slight modifications.

As for central photons, all time distributions are produced using plug electrons from $W \to e\nu$ events that are required to pass the MET_PEM trigger requirements listed in Table XXVI, corresponding to an integrated luminosity of 145.7 pb^{-1}. In addition, each event is required to have $\not\!\!E_T > 25$ GeV, and at least one space-time vertex, reconstructed as described in Section III.F, with more than 2 tracks with a $\Sigma p_T^{\rm trk} > 2$ GeV/c, and $|z_0| < 60$ cm. A plug electron that passes the requirements listed in Table XXIII with an $E_T > 20$ GeV is required to match the vertex using $|z_{\rm track} - z_{\rm vertex}| < 5$ cm. Unlike for the central electrons in Section III.G, the track is not required to match the vertex in time, as a large fraction of the tracks are only reconstructed in the silicon detectors; the silicon detectors have a coverage that is larger in η than the COT but do not provide a time measurement of the track. This effectively allows the time distributions to have a larger secondary tail from incorrectly selected vertices as described in Section V.A. This effect only occurs in data events as the MC simulation, that uses the same event requirements as for data, does not generate multiple vertex events.

Figure 78 compares the time distribution from data after each correction to $W \to e\nu$ events simulated as described in Section III.G.4 with the same event requirements as the data. The contribution to the raw time of the RMS of each correction is summarized in Table XXIV. The uncertainties due to each effect are estimated using

the MC simulation. They are shown in Fig. 79 separately and are summarized in Table XXV. After all corrections the $t_{\rm corr}$ resolution for plug electrons from $W \to e\nu$ events with correctly selected vertex is 0.68 ns (0.65 ns) for MC (data), which is dominated by the intrinsic resolution (0.5 ns), the precision of the TDC output (0.29 ns) and the vertex t_0 resolution (0.25 ns). The RMS of the $t^{\gamma}_{\rm corr}$ distribution for data events with incorrectly selected vertex is 2.26 ns

Table XXIV: The RMS of the corrected time distribution after cumulatively correcting for the effects shown in the first column for PEM electrons taken from data and MC using $W \to e\nu$ samples (see Fig. 78) [73]. The last row shows the fully corrected RMS. The number in parentheses is the RMS from mismeasured vertex cases. Note that the RMS contribution from run-dependent corrections is 0.43 ns.

Correction	MC (ns)	Data (ns)
Before corrections (raw)	8.06	
Slewing (E-dependent)	1.61	1.76
Vertex t_0	0.97	1.04
Vertex Position	0.65	0.68 (2.26)

The $t_{\rm corr}$ of both plug and central photons are constructed as shown Eq. 3.8. As described in detail in Section III.G.1, the calibration corrections $C_{\rm calibs}$ comprises functions that are obtained from fits to inclusive jet data samples. Figure 80 shows both a slewing and a PMT asymmetry curve for an example PEM tower. In the PEM both PMTs lie in separate sub-towers that share no energy. While the slewing correction averages over those independent energy measurements and looks similar to the CEM (compare Fig. 37), the asymmetry curve for the PEM is a measure of cable length and PMT response differences.

As discussed in Section III.G.1, the tower-by-tower slewing calibrations averaged over the event-by-event vertex positions of the inclusive jet sample from which it was

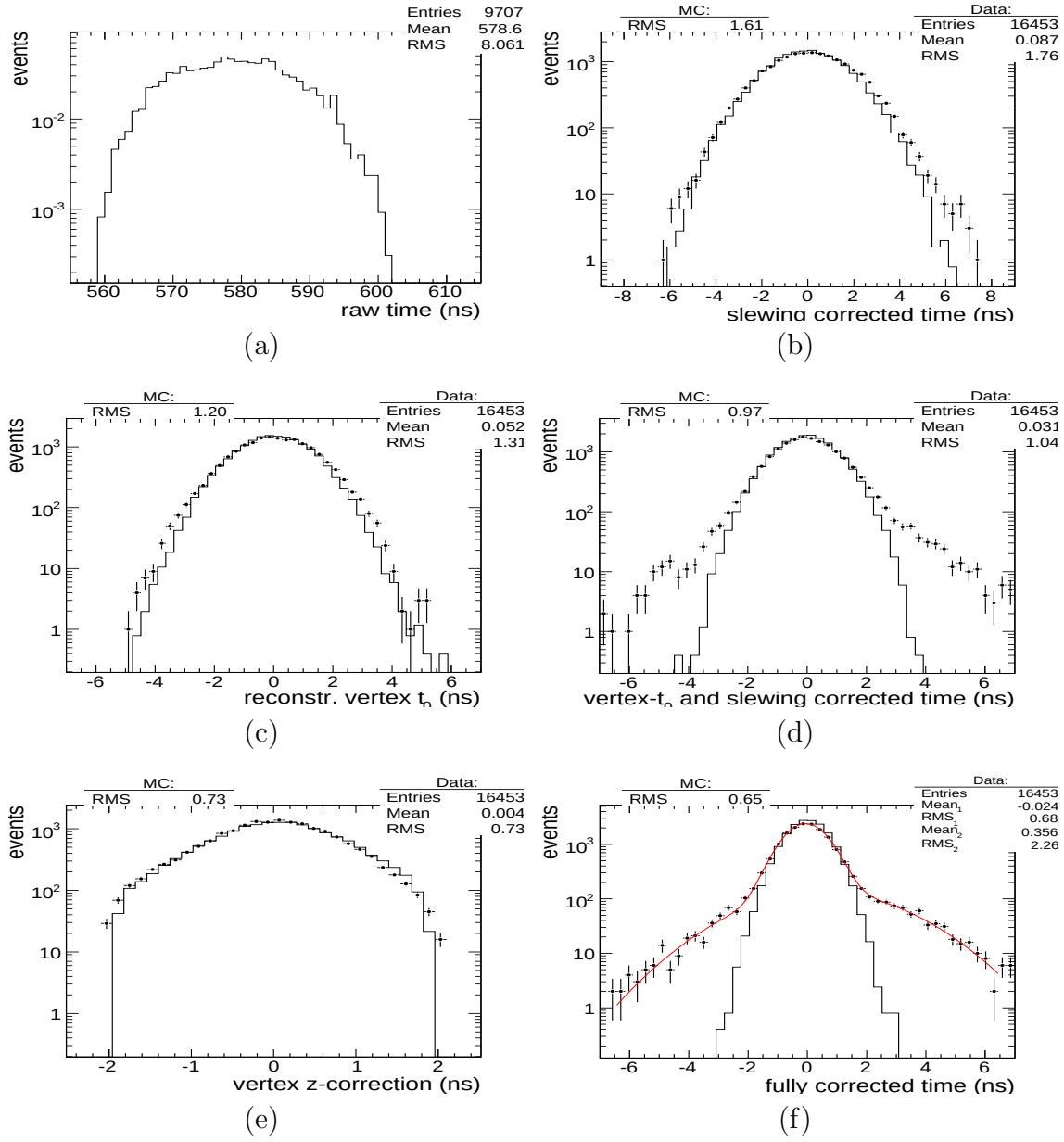

Figure 78: A comparison between MC (solid) and data (points) for the timing information for plug electrons from $W \to e\nu$ samples after cumulatively applying the various corrections (left side) and the corrections themselves (right side). For details see Fig. 35. In all cases the distributions are well centered around 0 and well described by the sum of two Gaussians. The primary Gaussian for the data and the MC agree well, the secondary Gaussian in the data distribution of (d) and (f) comes from picking a vertex that is not associated with the electron (not simulated in MC). The shift between the primary and the secondary Gaussian tail in (f) is suspected to come from the difference in vertex z-distributions between the actual W events and the events that cause the second vertex, as discussed in the text.

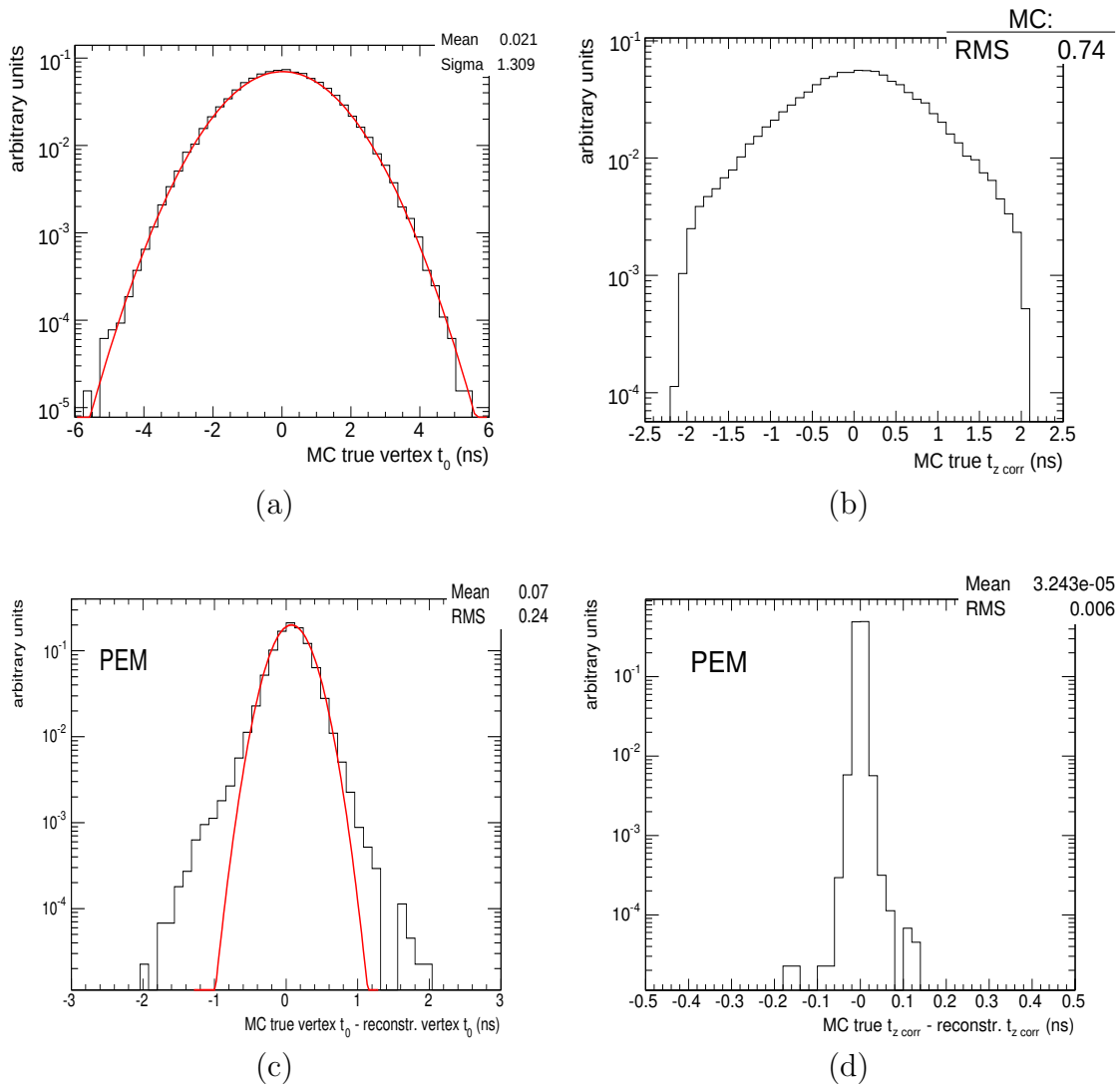

Figure 79: A MC simulation of the vertex time and position effects for plug electrons from a $W \rightarrow e\nu$ MC sample that contribute to the RMS of the "raw" time and their impact on the final timing resolution. Figure (a) shows the simulated vertex t_0 distribution (identical to Fig. 36a), and Fig. (b) shows the TOF correction. The contributions to the raw time RMS are 1.3 ns from the vertex t_0 and 0.74 ns from the TOF correction. Similarly, Figures (c) and (d) show the difference between the reconstructed vertex information and the true values; a measure of the final resolution of these quantities. The resolution of the vertex z measurement is negligible with 0.006 ns, the resolution of the vertex t_0 is 0.24 ns with non-Gaussian tails described in App. C.C, both similar to central electrons.

Table XXV: The contributions of physics and hardware effects for the plug, and the uncertainty of their corrections, to the RMS of the EMTiming system taken from a $W \to e\nu$ MC sample (see Figs. 79 and the MC histograms in 78). The dominant contribution is the slewing effect as part of the calibrations as described next.

Effect	Contribution to Raw RMS (ns)	Uncertainty of Correction (ns)
Slewing (energy dependent)	7.9	0.59
Vertex t_0	1.20	0.24
Vertex Position	0.73	<0.1
TDC integer conversion.	0.29	0.29
Total	8.06	0.65

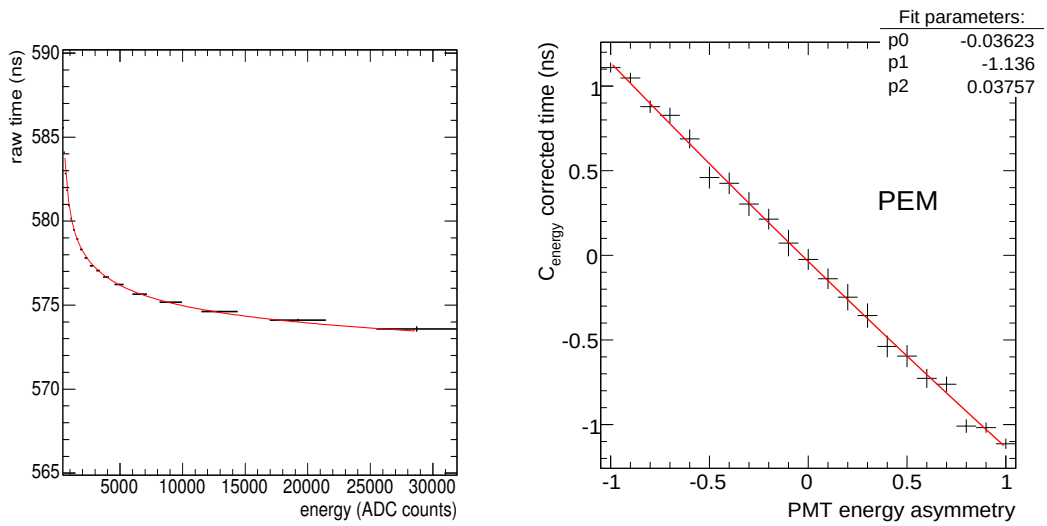

(a) (b)

Figure 80: The functional form (a) of the slewing correction as a function of the energy sum of the PMTs of adjacent towers (in ADC counts [74]) and (b) of the C_{energy}-corrected time as a function of the PMT energy asymmetry of an example tower in the PEM from an example run. In (a) the raw times are energy dependent due to the fixed height discrimination slewing of the ASD and lie between 560 ns and 590 ns for a prompt particle. The shape of the linear fit in (b) is due to the PMT/tower setup and is explained in the text.

made as the vertex reconstruction takes too much time to run on several 100,000 events with high track activity. As particles that deposit energy on one side of the detector are more likely to be produced at a vertex further away from this side, their EM tower position is correlated to their vertex position. If in addition a minimum E_T requirement is imposed on these particles then their average tower energy depends on the vertex position as well. As the vertex position is important for the t_{corr} calculation and as the correlation can be different between the calibration sample and the sample the correction is applied to, this causes an artificial correlation of the t_{corr} on the EM tower position and the EM energy. While this correlation is negligible for central particles, it is more important for plug particles as the vertex TOF correction has a bigger impact as described below. While for MC events the effect compensates as the slewing corrections are simulated by applying the exact same table reversely (see Section III.G.4), in data the effect is compensated offline with η- and energy-dependent corrections ("ring-corrections"). Figures 81 and 82 show the fully corrected time as a function of energy, tower and vertex position before and after applying the ring-corrections. The energy and ring-dependent offset f is calculated from W electrons and for the energy dependency (E) a fit to the calibration data is used with a ring-dependent slope parameter g: $f + \frac{g}{E}$. After all above corrections the timing distribution is centered at zero with an RMS of ∼1.76 ns, as shown in Fig. 78b and summarized in Table XXIV.

After the calibrations, the vertex-based t_0 and the TOF corrections are applied to the t_{corr} calculation. Figure 79a shows the typical distribution of the primary collision t_0, i.e. t_{vertex}, for the MC $W \to e\nu$ sample with the default $\sigma = 1.3$ ns. Figure 79c shows a comparison of the vertex reconstructed time vs. the true generated collision time. The RMS is a measure of the t_{vertex} resolution of the MC W sample which is 0.24 ns, roughly the same as for central electrons (see Section III.G.2). As in the

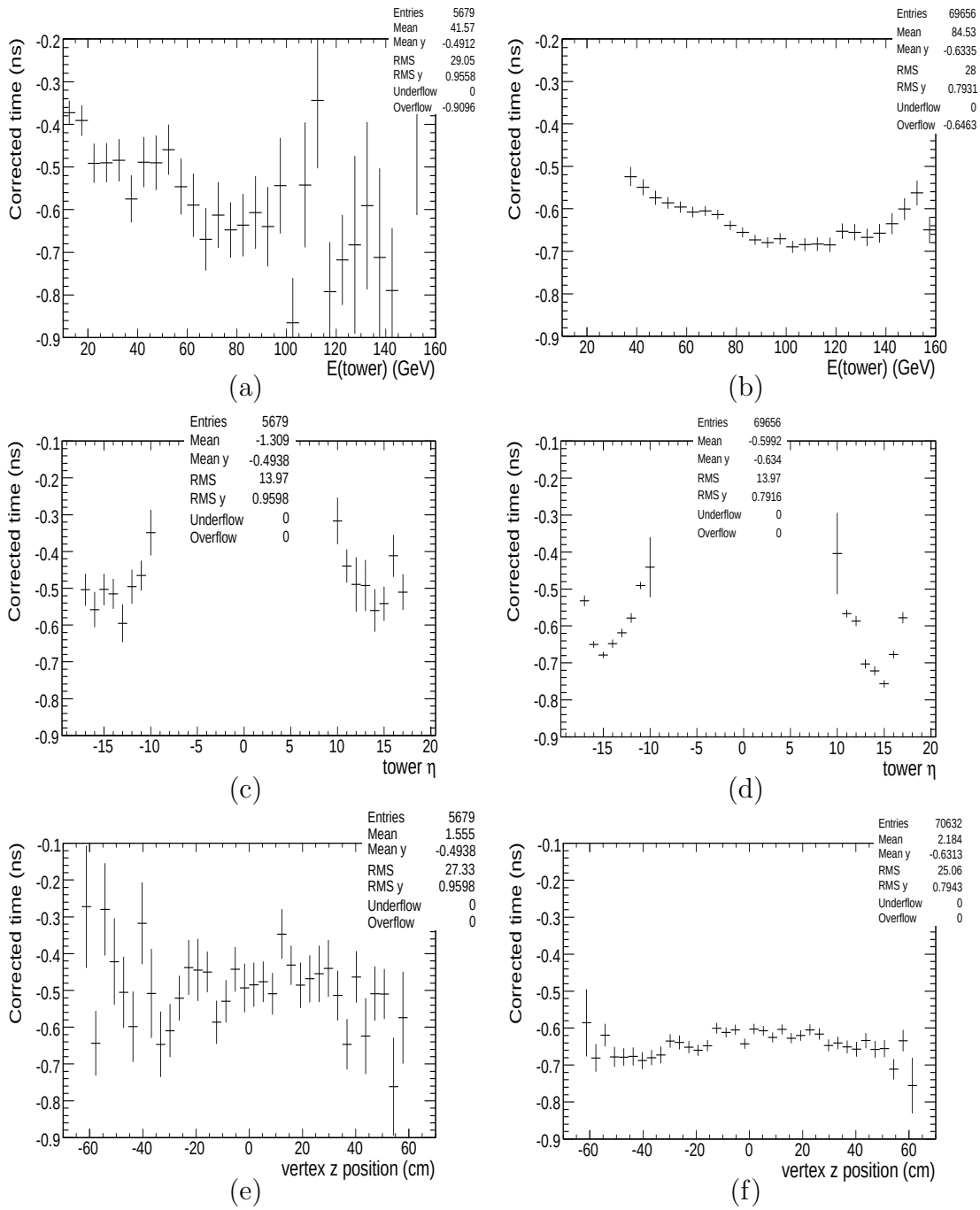

Figure 81: The fully corrected time before applying the "ring-corrections" as a function of tower energy, tower number (integrated over ϕ) and vertex position from a part of the calibration data on the left and plug electrons from $W \to e\nu$ events on the right side. Both samples show the same tendency as a function of those variables: the corrected time falls with energy and shows a u-shape as a function of tower number. It is flat as a function of vertex position.

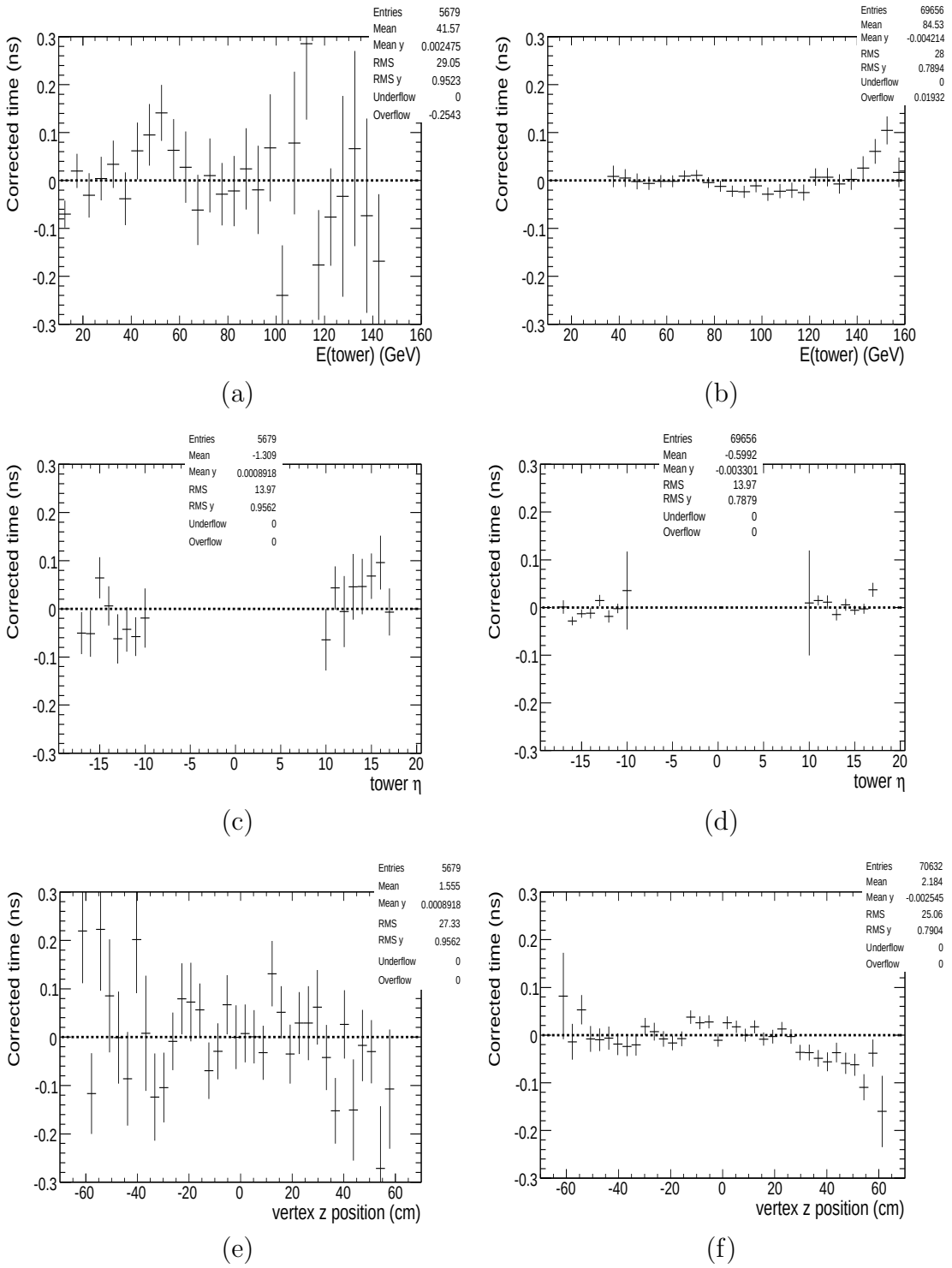

Figure 82: The t_{corr} after applying the "ring-corrections" as a function of tower energy, tower number (integrated over ϕ) and vertex position from part of the calibration sample on the left and plug electrons from $W \to e\nu$ events on the right side. All dependencies are resolved as the mean corrected time is well centered and all variations are within 0.2 ns.

central, this makes up the largest non-EMTiming contribution to the final resolution. The non-Gaussian tails in this distribution are due to the track t_0 calculation being biased towards a vertex t_0 of 0 ns as discussed in App. C.C. The reconstructed t_{vertex} distribution is shown in Fig. 78c and the time distribution after this and the slewing correction is shown in Fig. 35d with an RMS of 1.04 ns and begins to show a secondary Gaussian tail that is described below.

The arrival time is corrected for the TOF of the particle, C_{TOF}. Figure 79b shows the TOF correction needed to compensate for the collision position being different from $z = 0$ if the spread of the vertex position is $\sigma_z = 28$ cm, from the MC $W \to e\nu$ sample. The mean corrected TOF is centered at 0 with an RMS of 0.74 ns. This is larger than in the central as the particles traverse a larger distance in the detector to the plug calorimeter. Figure 36d shows the time difference of the TOF between the true and measured vertex z-position for the MC sample. The small RMS shows that the resolution of the TOF correction is negligible at 0.006 ns assuming that the vertex is correctly picked. The time distribution from the reconstructed vertex has an RMS of 0.73 ns as shown in Fig. 78e. After this correction Fig. 35f shows two Gaussians, corresponding to the right and wrong vertex selection as described in Section V.A. The RMS of the "fully corrected time" distribution is 0.68 ns (2.26 ns) for the right (wrong) vertex selection, as shown in Table XXIV.

The intrinsic EMTiming resolution that is used in the MC simulation (see Section III.G.4) for the plug part of the system can be estimated in the same way as described in Section III.G.3, using a sample of $Z \to ee$ events. Figure 83 shows the arrival time difference of the two decay electrons for events that (a) contain one central and one plug electron and (b) contain two plug electrons. The RMS is ∼0.85 ns, roughly the same as for the central (see Fig. 38), after correcting for the TOF. From this one gets a resolution of $\sigma_{\text{EMTiming}} = 0.84\ \text{ns}/\sqrt{2} = 0.59$ ns. After subtracting

off the contribution to the RMS from the TDC that rounds the time to integers ($1/\sqrt{12} \approx 0.29$ ns), and the resolution for the TOF correction (see Fig. 79d, negligible) one gets the same "intrinsic" EMTiming system resolution of 0.5 ns as in the central. If this value is put into the MC simulation, taking into account its slight variation as a function of energy derived from data (see Fig. 84) the data plots after each correction can be reproduced as shown in Fig. 78 which is a confirmation of its correctness for the EMTiming system in the plug.

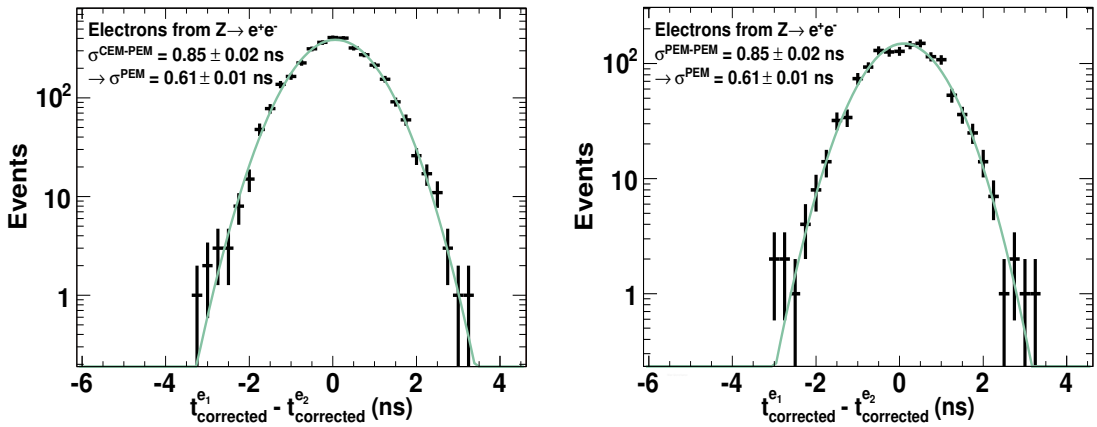

(a) (b)

Figure 83: The difference in the arrival times of the decay electrons, that both pass the requirements in Table XXIII, from a data sample of $Z \rightarrow ee$ events, corrected for the TOF but not the vertex t_0. The figures show the case when the electrons are CEM-PEM (a) and PEM-PEM (b). The distributions are centered at 0 ns with an RMS of ~0.84 ns which indicates an intrinsic EMTiming resolution of 0.84 ns/$\sqrt{2} \approx 0.59$ ns, the same as for the CEM (see Fig. 38).

While the MC simulation method described in detail in Section III.G.4 is the same for both the plug and central EMTiming system [95], it makes use of threshold functions obtained in calibrations from inclusive jet data samples that are different in CEM and PEM. These functions are used to simulate the efficiency turn-on of each tower by determining the probability of the energy deposited in a tower to produce

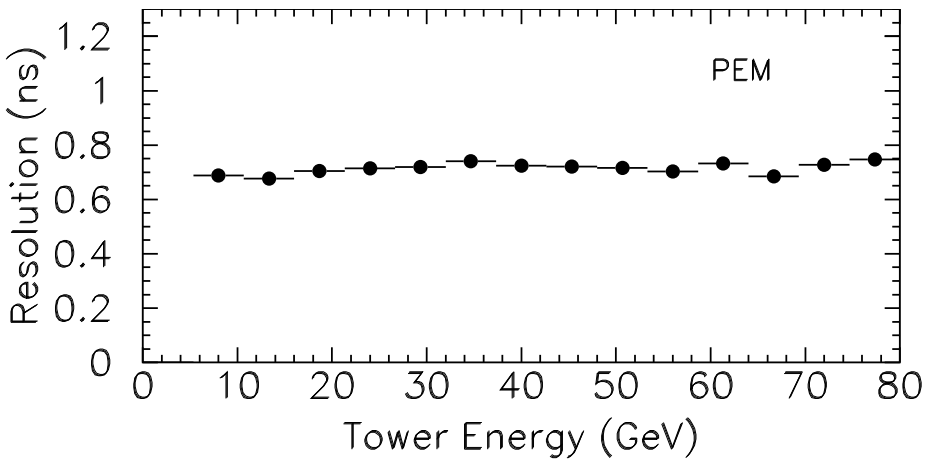

Figure 84: The RMS of the fully corrected arrival time versus the electron EM energy from a plug electron data sample produced with the requirements shown in App. B, but without the E_T requirement. This effect is simulated as described in the text.

a time recorded in the TDC. Figure 85 shows the hit efficiency dependence on the energy sum of the PMTs of an example tower in the PEM [74]. The threshold for all PEM towers lies consistently at ∼2 GeV deposited energy with widths of ∼0.5 GeV (see Section II.C).

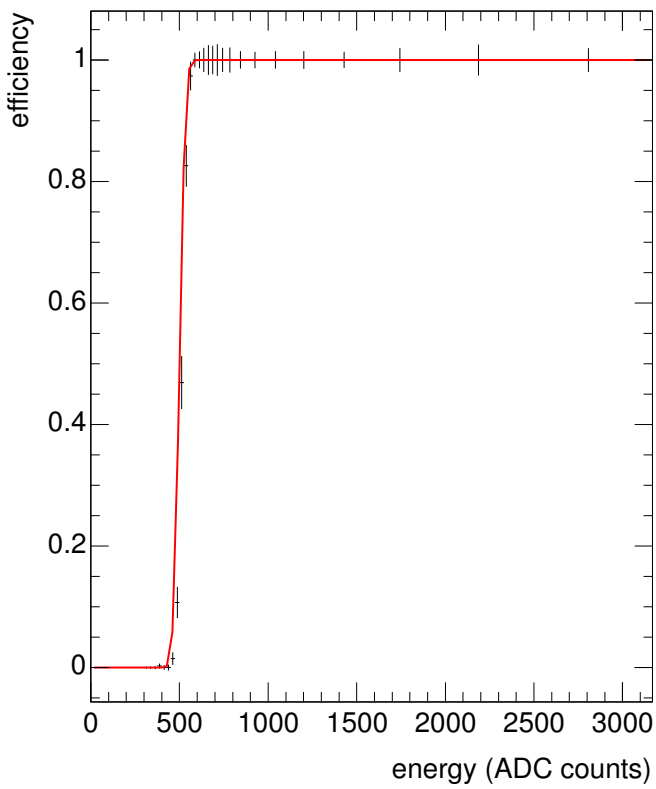

Figure 85: The functional form of the TDC efficiency as a function of energy sum of the PMTs of an example tower in the PEM in ADC counts [74] with the data of an example run. In this case the threshold is around 1.6 GeV for the energy sum and the width is around 0.5 GeV.

APPENDIX E

NON-COLLISION BACKGROUNDS FOR PLUG PHOTONS

This section describes the non-collision background shapes for a possible future search with plug photons in an inclusive $\gamma + \not\!\!E_T$ sample from the MET_PEM trigger with the requirements described in Table XXVI. As with the central detector, events containing photons can be separated into two classes: prompt collision events and non-collision events such as beam halo, cosmics and PMT spikes. As the time distribution of central collision photons is described in Section V.A and as App. D shows that with slight modifications to the timing corrections their time distribution has the same shape as plug photons, this section will focus on non-collision plug photons. While it has not been further investigated, it may be difficult to reject PMT spikes. As there is only one PMT in each plug tower, the PMT asymmetry requirement cannot be applied.

Figure 86 shows the time distribution for plug photons that pass the requirements in Table XXVII in events that have no reconstructed vertex. While the events at $\sim$0 ns are from collision sources, the events at -18 ns and $+18$ ns are from beam halo from the primary and satellite bunches as described in detail for central photons in Section V.B.1. The flat distribution above $\sim$20 ns is from cosmics which makes up $<$1.6% of the total sample.

As illustrated in Fig. 48a, the beam halo from the primary collision bunch has an arrival time of -18 ns ($\sim$0 ns) if it interacts with the plug calorimeter as it enters (leaves) the detector. Hence, beam halo background is potential major background contributing to a possible signal region at $\gtrsim$0 ns. A study of beam halo and cosmics events show no features that could separate them from collision photons. The main

Table XXVI: Triggers that contribute to the MET_PEM dataset and their requirements. Note that at Level 1 the central and plug requirements are *or*'d.

Trigger Type	Level 1	Level 2	Level 3
Photon	≥1 EM cluster Central $E_T > 8$ GeV $\frac{E_{\rm Had}}{E_{\rm Em}} < 0.125$ Plug $E_T > 8$ GeV $\frac{E_{\rm Had}}{E_{\rm Em}} < 0.0625$	$1.1 < \lvert\eta\rvert < 3.6$ $E_T > 20$ GeV $\frac{E_{\rm Had}}{E_{\rm Em}} < 0.125$ seed tower $E_T > 8$ GeV	≥1 plug EM cluster use cluster track for vertex, if avail. $E_T > 20$ GeV $\frac{E_{\rm Had}}{E_{\rm Em}} < 0.125$
$\not\!\!E_T$	$\not\!\!E_T > 15$ GeV		$\not\!\!E_T > 25$ GeV

Table XXVII: The selection requirement for plug photons. The requirements on the EM cluster are similar to plug electrons as shown in Table XXIII, but, instead of a track matching requirement, the cluster is required to have no high-p_T tracks pointing to it within a cone of 0.4.

Photon
$E_T > 20$ GeV
Fiducial: $1.2 < \lvert\eta_{\rm PES}\rvert < 2.8$ && PEM 3x3 fit tower
$\frac{E_{\rm Had}}{E_{\rm Em}} < 0.05$
$E^{\rm Iso}_{\rm R=0.4} < 2.0 + 0.02 \cdot (E_T - 20)$
$\Sigma p_{\rm T}$ of tracks in a 0.4 cone $< 2.0 + 0.005 \cdot E_T$
$E_{\rm PES} > 0.001$ GeV
$\chi^2_{3x3} < 10$
$E^u_{\rm PES}(5 \times 9) > 0.65$ && $E^v_{\rm PES}(5 \times 9) > 0.65$

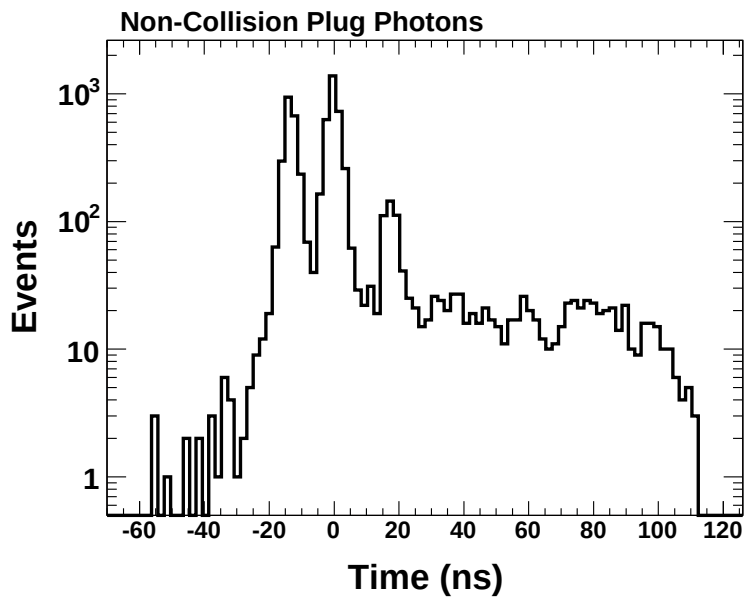

Figure 86: The time distribution of photon candidates in the MET_PEM sample that pass the photon ID requirements in Table XXVII in events that have no reconstructed vertex. Clearly one can separate collision events from beam halo and cosmics.

reason is that beam halo does not deposit energy in a series of towers as in the CEM. Instead it enters and leaves the plug calorimeter in an angle similar to high-η collision photons.

A method to estimate the contribution of beam halo to the region around $t_{\rm corr} \approx 0$ ns uses the correlation of the rate of beam halo events between both plug sides, as shown with the time distributions in Fig. 87. This indicates that the number of events in the region -18 ns is roughly the same as the number of events at $\sim$0 ns.

To summarize, as there are not as many handles to separate the various backgrounds as in the central region, cosmics and beam halo backgrounds cannot be well separated without timing information. While it has not been investigated further, the background contribution to a potential signal region at $\gtrsim$0 ns can be estimated as follows: (a) Cosmics are assumed to have a constant rate as a function of time, (b)

beam halo contribution to prompt events can be estimated from their rate at around -18 ns, and (c) the remaining prompt contribution can be estimated as in the central region using the same shapes from a $W \to e\nu$ event sample.

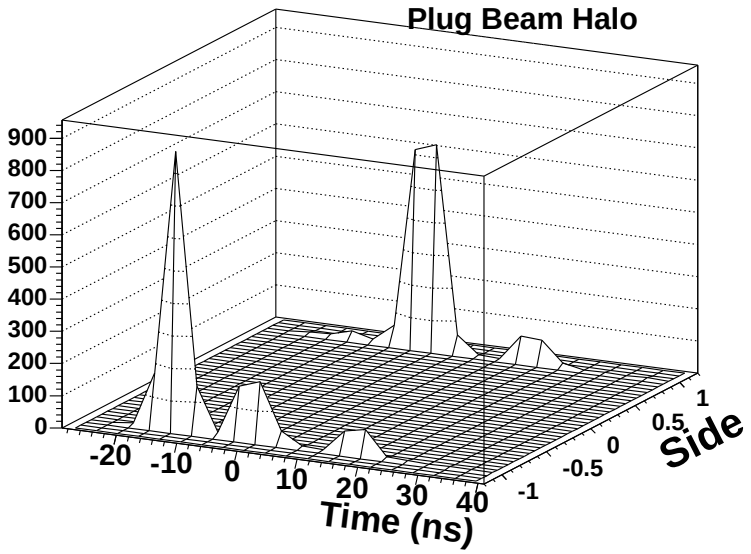

Figure 87: The time distribution of photon candidates in the MET_PEM sample that pass the requirements in Table XXVII for both sides of the detector. Clearly the time distribution peaks at $\sim$0 ns on the side where beam halo exits and at -18 ns where it enters the detector which helps estimating the beam halo contribution at $\sim$0 ns.

APPENDIX F

PHOTON POINTING AT CDF

As described in Section I.C and shown in Fig. 6, the ALEPH experiment has already searched for long-lived $\widetilde{\chi}_1^0$ that decay via $\widetilde{\chi}_1^0 \rightarrow \gamma\widetilde{G}$ and has excluded the low $\widetilde{\chi}_1^0$ mass region using a photon "pointing" method [19]. This method measures the photon direction and extrapolates it towards the center of the detector. If the distance of closest approach between this extrapolated trajectory and the beam axis ("impact parameter") as shown in Fig. 88 is significant, it can indicate that the photon was produced at a displaced vertex produced by a nanosecond lifetime particle.

In this section the search sensitivity to heavy, neutral, long-lived particles using the EMTiming system is compared to a potential photon pointing ability at CDF. While CDF has never used its calorimeter for a pointing measurement it is possible to use the position measurements from the central EM strip/wire gas chamber (CES) and the central pre-radiator gas chamber (CPR) in front of the calorimeter at CDF to measure two points along the photon trajectory and extrapolate them towards the beam axis to yield a measurement of the impact parameter [96]. While the CES is described in Section II.B, the CPR is a system of drift chambers between the EM calorimeter and the solenoid that uses the $1X_0$ solenoid material for, e.g., photon/π^0 discrimination on a statistical basis by measuring the conversion probability. While the CPR has no z-measurement ability, the ϕ information allows for a measurement of the impact parameter with an estimated resolution of 10 cm (see Table XXVIII). One of the primary reasons this has not been used is that the measurement probability is $\sim$65% as photons do not always convert in the solenoid material and deposit energy

in the CPR, with an angular dependence of:

$$P_C = 1 - e^{-(7N_{\rm rad})/(9\sin\theta)} \quad , \tag{F.1}$$

where $N_{\rm rad} = 1.072$ is the number of radiation lengths before the CPR, and θ is the angle with respect to the beam axis [97].

Table XXVIII: Photon pointing parameters for the CDF detector [96]. With this combination an impact parameter measurement may be possible with a resolution of 10 cm in the radial direction. The $\sigma^{\phi}_{\rm CES}$ and $\sigma^{\phi}_{\rm CPR}$ denote the resolution of CES and CPR in ϕ direction.

measurement only in radial direction	
Radius of CES	184.15 cm
Radius of CPR	168.29 cm
$\sigma^{\phi}_{\rm CES}$	2 mm
$\sigma^{\phi}_{\rm CPR}$	5 mm
$\rm N_{rad}$	1.072 $\rm X_0$

To estimate the sensitivity with a pointing method we consider a $\gamma + \not{E}_T + \geq$ 1 jet analysis. Figure 89 shows the distribution of simulated GMSB signal events as a function of impact parameter and $t^{\gamma}_{\rm corr}$ taking into account the measurement probability. There are roughly as many events in the region of low impact parameter and high $t^{\gamma}_{\rm corr}$ as there are at high impact parameter and low $t^{\gamma}_{\rm corr}$. Hence either method should have roughly the same effect on the exclusion region, as confirmed by Fig. 90, which shows the expected exclusion region in the mass-lifetime plane. While timing is better than pointing by itself, if pointing turns out to be feasible, a combination of the two would further improve the sensitivity.

Considered separately, a second advantage of timing is that it "filters" manifestly long-lifetime events, whereas the impact parameter selects also short lifetime-high mo-

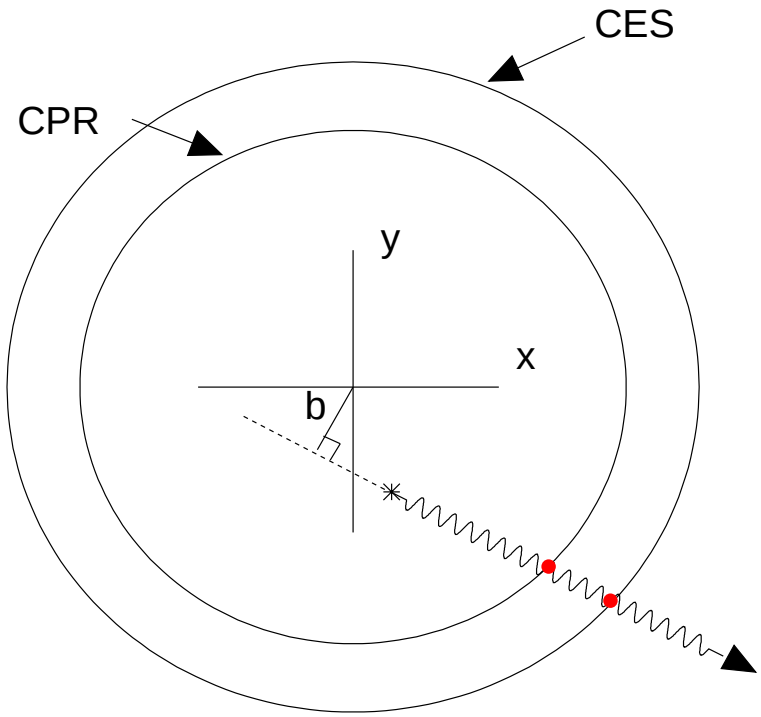

Figure 88: An illustration of the impact parameter b in a plane perpendicular to the beam (z) axis for a photon that is created at a displaced vertex indicated with a star. The impact parameter is basically the distance of closest approach of the extrapolated trajectory to the beam axis. The trajectory of the photon can be determined from its energy deposits in the CES and CPR detectors.

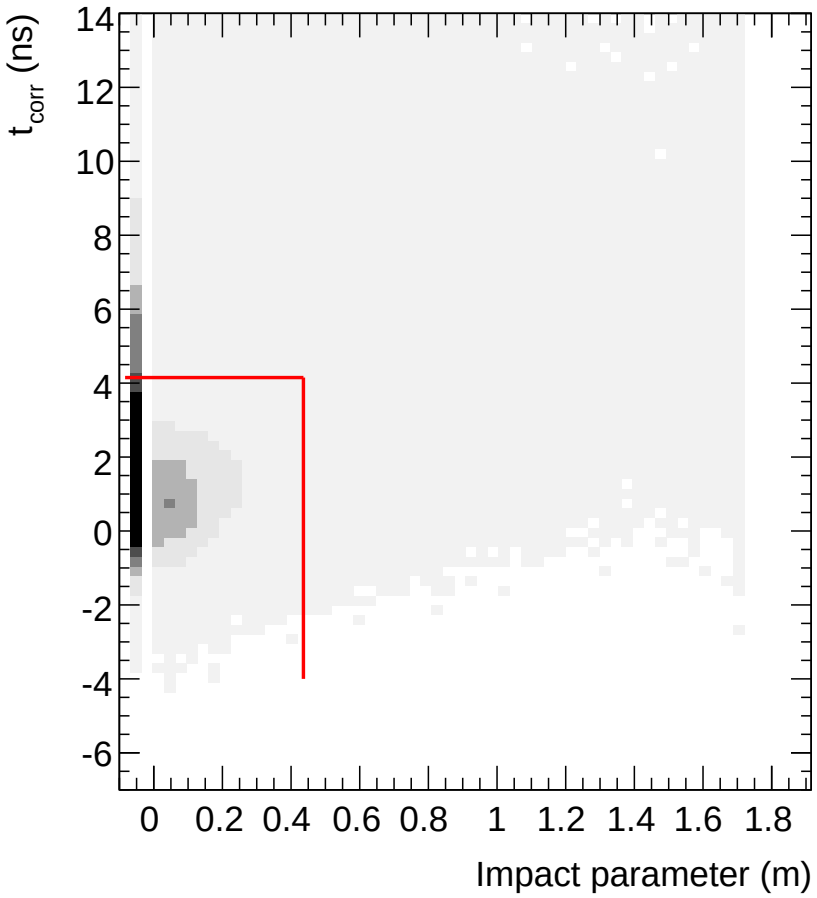

Figure 89: The relationship between $t_{\rm corr}$ and the impact parameter (b) of a photon from $\widetilde{\chi}_1^0 \to \gamma\widetilde{G}$ decays in a GMSB model with $m_{\widetilde{\chi}} = 110$ GeV/c^2 and $\tau_{\widetilde{\chi}} = 10$ ns. The solid lines show the selection requirements that give us the smallest 95% C.L. cross section limit in a $\gamma + \not\!\!E_T +$ jets analysis. The photons without impact parameter measurement are assigned a $b < 0$ m. Due to the low cut on the impact parameter there are about as many events in the low-$t_{\rm corr}$ high-b as in the high-$t_{\rm corr}$ low-b region. This leads to a similar efficiency for a pure b-cut compared to a pure $t_{\rm corr}$ cut. The combined restriction leads to improved signal sensitivity.

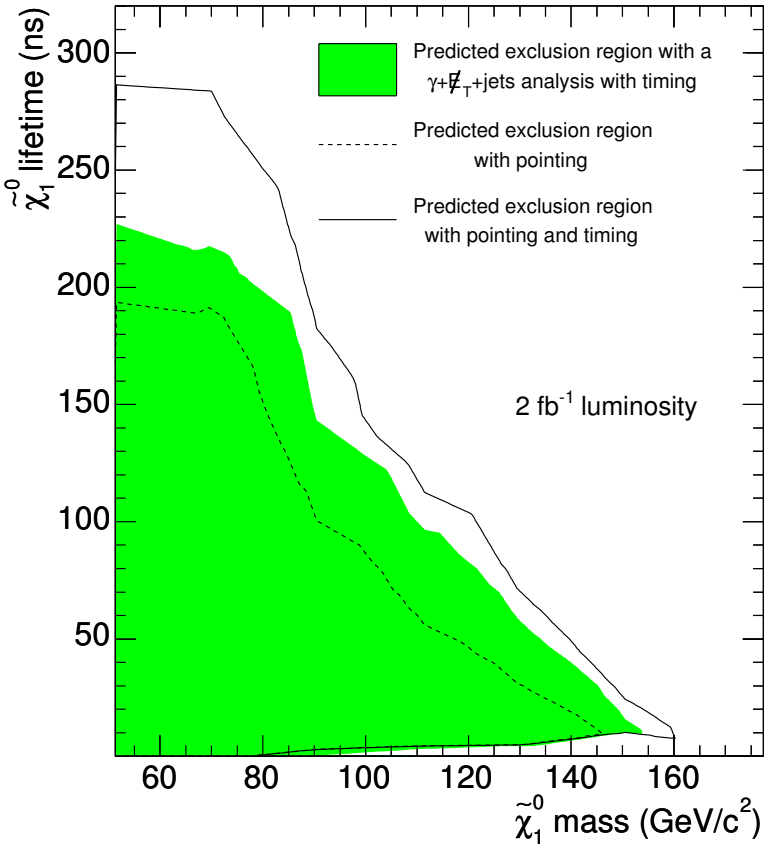

Figure 90: A comparison of the expected exclusion regions as a function of $\widetilde{\chi}_1^0$ mass and lifetime for the GMSB model at 2 fb^{-1} luminosity for a $\gamma + \not{E}_T + \geq 1$ jet analysis with photon pointing and timing. While timing generally yields a higher sensitivity than pointing, both methods would, if available and combined, extend the exclusion region further than either of them alone.

mentum events. Another possible advantage of the combination is that if there is an excess, we could draw more information about the individual events, for instance determine the direction of the photon. With the x-y-direction of the photon momentum measured by the CPR/CES system, the EMTiming system can be used to measure the z component, if we assume the neutralino boost to be ~ 1.0 which is typically the case. Or, the pointing could provide z and x-y components, one could possibly determine the position of the vertex and thus the decay time. However, with a time resolution of 1.0 ns the photon vertex position resolution would be roughly 50 cm.

VITA

Peter Wagner was born in 1978 in Koblenz, Germany. He graduated from Immanuel Kant Gymnasium Boppard with the Abitur in 1998. He attended the Johannes Gutenberg University in Mainz where he majored in physics and specialized in theoretical physics from 1998 to 2001. He got his B.S. in Physics in 2000. He joined Texas A&M University in Fall 2001. In the Fall of 2002 he began working as a part of the CDF collaboration in experimental particle physics. His permanent mailing address is Department of Physics, TAMU MS4242, College Station, TX 77483.

The typist for this dissertation was Peter Wagner.